Photoproduction of J/ψ Mesons at Medium and Low Elasticities at HERA

DISSERTATION

zur Erlangung des Doktorgrades
des Fachbereichs Physik
der Universität Hamburg

vorgelegt von

Katja Krüger

aus München

Hamburg
2001

Gutachter der Dissertation:	Prof. Dr. B. Naroska
	Prof. Dr. F.-W. Büßer
Gutachter der Disputation:	Prof. Dr. B. Naroska
	Prof. Dr. R.-D. Heuer
Datum der Disputation:	3. 4. 2001
Dekan des Fachbereichs Physik und Vorsitzender des Promotionsausschusses:	Prof. Dr. F.-W. Büßer

Abstract

An analysis of the photoproduction ($Q^2 < 1\,\mathrm{GeV}^2$) of J/ψ mesons at medium and, for the first time, at low elasticities z is presented. The muonic decay channel is used to select the J/ψ mesons. The data have been collected with the H1 detector at the electron-proton collider HERA and correspond to an integrated luminosity of $40\,\mathrm{pb}^{-1}$.

In the medium elasticity region the total photoproduction cross section as a function of the photon-proton centre-of-mass energy $W_{\gamma p}$ and the single differential cross sections as functions of the elasticity z, the transverse momentum squared of the J/ψ meson $p_{t,\psi}^2$ and the fractional gluon momentum inside the proton x_g are extracted. The analysis covers the kinematic range $0.3 < z < 0.9$, $60 < W_{\gamma p} < 180\,\mathrm{GeV}$ and $p_{t,\psi}^2 > 1\,\mathrm{GeV}^2$. The results are in agreement with previous HERA measurements where such measurements exist. Theoretical predictions in the next-to-leading order Colour Singlet Model can describe the data. The $W_{\gamma p}$ dependence favours a gluon density in the proton which rises slowly towards small x_g, e.g. MRS(A') [1].
The double differential cross section in $p_{t,\psi}^2$ and z is extracted and the decay angle distributions of the J/ψ mesons in two elasticity regions are studied. No evidence for significant colour octet contributions is found in any of the distributions studied.

The analysis of the low elasticity region aims to measure the contributions from resolved photon processes to J/ψ photoproduction. The kinematic region is $0.05 < z < 0.45$, $120 < W_{\gamma p} < 260\,\mathrm{GeV}$ and $p_{t,\psi}^2 > 1\,\mathrm{GeV}^2$. The total photoproduction cross section as a function of $W_{\gamma p}$ and the differential cross sections as a function of z and $p_{t,\psi}^2$ are extracted. Contributions from resolved photon processes improve the agreement of the simulation and of theoretical predictions with the data compared to direct photon-gluon fusion alone. Due to large uncertainties in the normalization of the colour singlet prediction for resolved photon processes no statement on colour octet contributions is possible.

Kurzfassung

In dieser Arbeit wird eine Analyse der Photoproduktion ($Q^2 < 1\,\mathrm{GeV}^2$) von J/ψ Mesonen bei mittleren und kleinen Elastizitäten z vorgestellt. Zur Selektion der J/ψ Mesonen wird der myonische Zerfallskanal verwendet. Die Daten wurden mit dem H1 Detektor am Elektron-Proton-Speicherring HERA aufgezeichnet und entsprechen einer integrierten Luminosität von $40\,\mathrm{pb}^{-1}$.

Im Bereich mittlerer Elastizität werden der totale Photoproduktionswirkungsquerschnitt als Funktion der Photon-Proton-Schwerpunktenergie $W_{\gamma p}$ und die einfach differentiellen Wirkungsquerschnitte als Funktionen der Elastizität z, des Quadrats des Transversalimpulses des J/ψ Mesons $p_{t,\psi}^2$ und des Impulsbruchteils des Gluons im Proton x_g bestimmt. Die Analyse deckt den kinematischen Bereich $0.3 < z < 0.9$, $60 < W_{\gamma p} < 180\,\mathrm{GeV}$ und $p_{t,\psi}^2 > 1\,\mathrm{GeV}^2$ ab. Die Ergebnisse sind in Übereinstimmung mit früheren Messungen sofern

solche existieren. Theoretische Vorhersagen in nächstführender Ordnung im Colour Singlet Modell beschreiben die Daten. Die $W_{\gamma p}$-Abhängigkeit bevorzugt eine Gluondichte im Proton, die langsam zu kleinen Werten von x_g ansteigt, wie z.B. MRS(A') [1].
Der doppelt differentielle Wirkungsquerschnitt in $p_{t,\psi}^2$ und z wird bestimmt, und die Zerfallswinkelverteilung der J/ψ Mesonen in zwei Elastizitätsbereichen wird untersucht. Es werden keine Hinweise auf signifikante Colour Octet Beiträge gefunden.

Die Analyse im Bereich kleiner Elastizität hat die Messung von Beiträgen mit aufgelösten Photonen zur Photoproduktion von J/ψ Mesonen zum Ziel. Der kinematische Bereich ist $0.05 < z < 0.45$, $120 < W_{\gamma p} < 260\,\mathrm{GeV}$ und $p_{t,\psi}^2 > 1\,\mathrm{GeV}^2$. Es werden der totale Photoproduktionswirkungsquerschnitt als Funktion von $W_{\gamma p}$ und die einfach differentiellen Wirkungsquerschnitte als Funktionen von z und $p_{t,\psi}^2$ bestimmt. Beiträge von Prozessen mit aufgelösten Photonen verbessern die Übereinstimmung der Simulation und der theoretischen Vorhersagen mit den Daten im Vergleich zu direkter Photon-Gluon-Fusion allein. Wegen großer Unsicherheiten in der Normierung der Colour Singlet Vorhersagen für Prozesse mit aufgelösten Photonen ist keine Aussage über Colour Octet Beiträge möglich.

Contents

Introduction

The HERA collider and its experiments offer the possibility to study high energy physics in electron-proton collisions. The physics program comprises a large number of fields including, for example, the measurement of the structure functions of the proton, the photon and the pion, tests of perturbative and non-perturbative quantum chromodynamics and electroweak theory and the study of diffractive phenomena.

Quantum chromodynamics (QCD) is a field theory which successfully describes the strong interaction of quarks and gluons. Perturbative QCD allows for precise predictions, but is only applicable in the presence of a 'hard scale', e.g. high energies of the interacting particles. The production of heavy quarks (*charm, bottom*) is of special interest since the mass of the quarks provides a scale for the application of perturbative QCD. The dominant production mechanism for heavy quarks at HERA is direct photon-gluon fusion. The electron acts as a source of quasi-real photons which interact with a gluon from the proton via a $q\bar{q}$ pair. This process is directly sensitive to the gluon density inside the proton.

The cross section for *charm* production is much higher than that for *bottom* quarks due to the smaller mass of the *charm* quark. In order to distinguish the *charm* production from the large background originating from light quarks, *up, down* and *strange*, charmed mesons like the $D^{*\pm}$ ('open charm') or bound *charm-anticharm* states like the J/ψ meson are used. The J/ψ meson can be easily identified and triggered in the H1 detector via its muonic decay mode.

There are several models which describe the production of $c\bar{c}$ pairs and the transition from the $c\bar{c}$ to the J/ψ meson. Until 1992 the data on J/ψ meson production in lepton-hadron and hadron-hadron collisions were in agreement with the 'Colour Singlet Model' (CSM). The CSM is based on the idea that only $c\bar{c}$ states with the same quantum numbers as the J/ψ are allowed to evolve into a J/ψ meson. The analysis of the data collected in the 1992-93 run of the Tevatron, however, showed that the cross section of J/ψ and also $\psi(2s)$ production in $p\bar{p}$ collisions is underestimated by the CSM by more than an order of magnitude. A new approach, the 'Colour Octet Model' (COM) based on an effective field theory called non-relativistic quantum chromodynamics (NRQCD), was introduced which can accommodate a larger production rate. It includes more intermediate $c\bar{c}$ states than the CSM which are allowed to evolve into a J/ψ meson. This also has consequences for J/ψ production in other processes, e.g. at HERA. The first predictions of the COM for the photoproduction of J/ψ mesons at HERA showed poor agreement with the data.

In the meantime, however, additional theoretical efforts have led to several ideas that improve the agreement.

At HERA different production mechanisms are possible, such as direct production or by 'resolved' photons. The elasticity z which corresponds to the relative photon energy transferred to the J/ψ meson is often used to distinguish regions where these are expected to dominate. In this thesis the analysis is performed in two regions of elasticity. In the medium z region, $0.3 < z < 0.9$, the direct photon-gluon fusion process is expected to dominate and high statistics results in a sensitivity to the gluon density in the proton. Most of the more recent predictions in the COM expect a very small contribution from the additional $c\bar{c}$ states in this range. In the second elasticity region, $0.05 < z < 0.45$, processes with so-called 'resolved' photons are expected to play a major role. In these processes the photon acts like a hadron and only a fraction of its energy takes part in the interaction with the gluon from the proton. Resolved photon processes have been measured in the production of light quarks, but J/ψ production has not yet been identified in such processes. The differences between the predictions of the CSM and the COM are more significant in the low z region than at medium z.

In the work described here an overview over the HERA collider and the H1 detector is given in the first chapter. The focus lies on the detector components relevant for this analysis, including the trigger system. In the second chapter, after an introduction into the kinematics of electron-proton scattering, different models for J/ψ production are discussed. The Monte Carlo simulations used to correct the data for detector effects are presented in the third chapter, which also contains a study of the resolution in the reconstruction of kinematic variables. Chapter four describes the data selection and investigates the efficiencies in the two elasticity regions. The results of the analyses in the medium and the low elasticity region are presented in chapters five and six. The Monte Carlo simulation used for the efficiency determination is compared to data. The cross sections are extracted and compared to theoretical predictions. The results are summarized in the final chapter and an outlook is given.

Chapter 1

HERA and the H1 Detector

The data used for this analysis were taken using the H1 detector at the electron-proton collider HERA. In the following a short overview of HERA and the most relevant components of the H1 experiment is given.

1.1 HERA

The HERA collider (fig. 1.1) at the DESY laboratory in Hamburg consists of two separate accelerators, one for protons and one for electrons or positrons. It has a circumference of 6.4 km. From 1994 until 1997 positrons were used as beam particles because of the better beam lifetime. After an improvement of the vacuum, electrons were collided during 1998 and the first half of 1999. Afterwards positrons were utilized again. Since the autumn of the year 2000 a major luminosity upgrade program has been in progress.

The lepton beam is operated at an energy of 27.5 GeV. At the beginning of 1998 the proton beam energy was increased from 820 GeV to 920 GeV, corresponding to centre-of-mass energies of $\sqrt{s} \approx 300$ GeV and $\sqrt{s} \approx 318$ GeV. The beams collide at two interaction regions in the Northern and Southern experimental halls, where the multi-purpose detectors H1 and ZEUS are located. In the Eastern hall the HERMES experiment uses the electron beam for studies of the spin structure of the nucleons, while HERA–B in the Western hall studies B-mesons produced in collisions of the HERA protons with wire targets.

The beam particles are stored in 'bunches' with a bunch crossing interval of 96 ns (corresponding to 10.4 MHz). A small number of non-colliding 'pilot bunches' are used for background studies. The typical lifetime of the proton beam is 100 h, whereas the typical lifetimes of the lepton beams are only about 10 h for positrons and 6 h for electrons. In contrast to positrons electrons can recombine with the ions of the residual gas in the beam pipe. This is the explanation for their shorter beam lifetime.

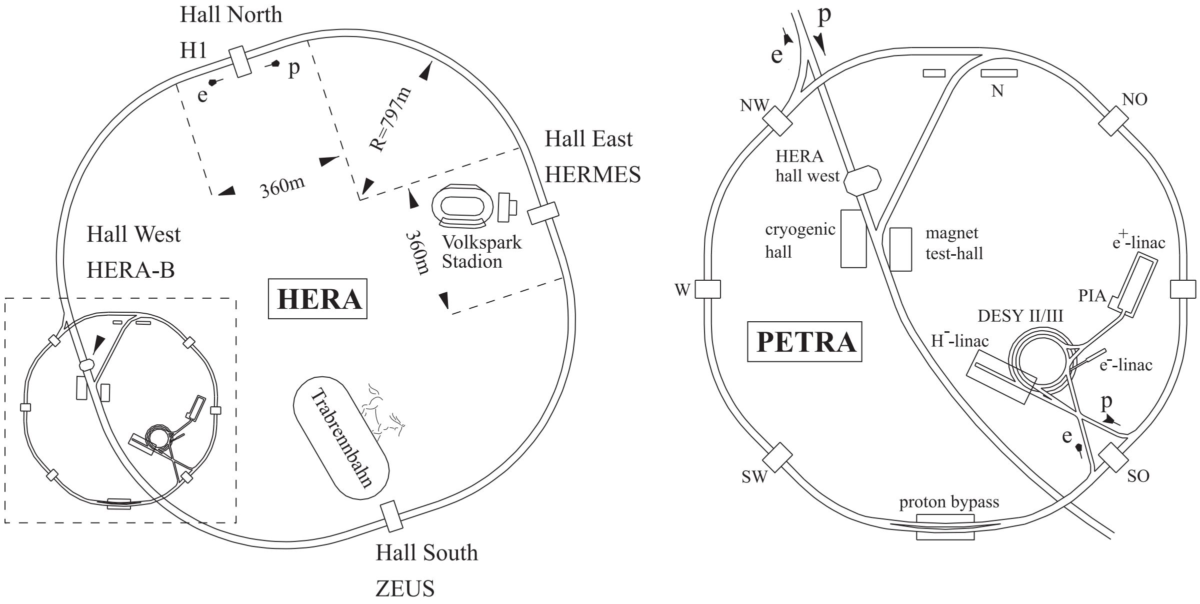

Figure 1.1: *The HERA collider with the four experiments H1, ZEUS, HERMES and HERA–B on the left and its pre-accelerators on the right.*

1.2 H1 Detector

The H1 detector is a typical multi-purpose collider experiment. A schematic side-view is shown in figure 1.2. To take into account the asymmetric beam energies the instrumentation is enhanced in the direction of the proton beam. Both the tracking detectors and the main calorimeter are located inside the superconducting coil that produces the magnetic field for the momentum measurement. This layout reduces the dead material in front of the calorimeter. The right-handed coordinate system used within the H1 collaboration has its origin in the nominal interaction point with the z-axis pointing in the proton beam (or 'forward') direction and the x-axis pointing towards the centre of HERA. The polar angle ϑ is measured with respect to the z-axis, the azimuthal angle φ to the x-axis. A detailed description of the H1 detector can be found in [2]. In the following only the detector components most relevant for this analysis are discussed.

1.2.1 Tracking Detectors

The H1 tracking system consists of two main parts, the central and the forward tracking detectors. For this analysis mainly the Central Tracking Detector (CTD) is used, because it provides a much better momentum resolution which is important for the reconstruction of the invariant mass of the J/ψ meson from its decay muons. Additional tracks may also be found in the Forward Tracking Detector (FTD). In the backward region the Backward Drift Chamber (BDC) in front of the SpaCal and the Backward Silicon Tracker (BST) complement the H1 tracking system. Both BDC and BST are not used in this analysis.

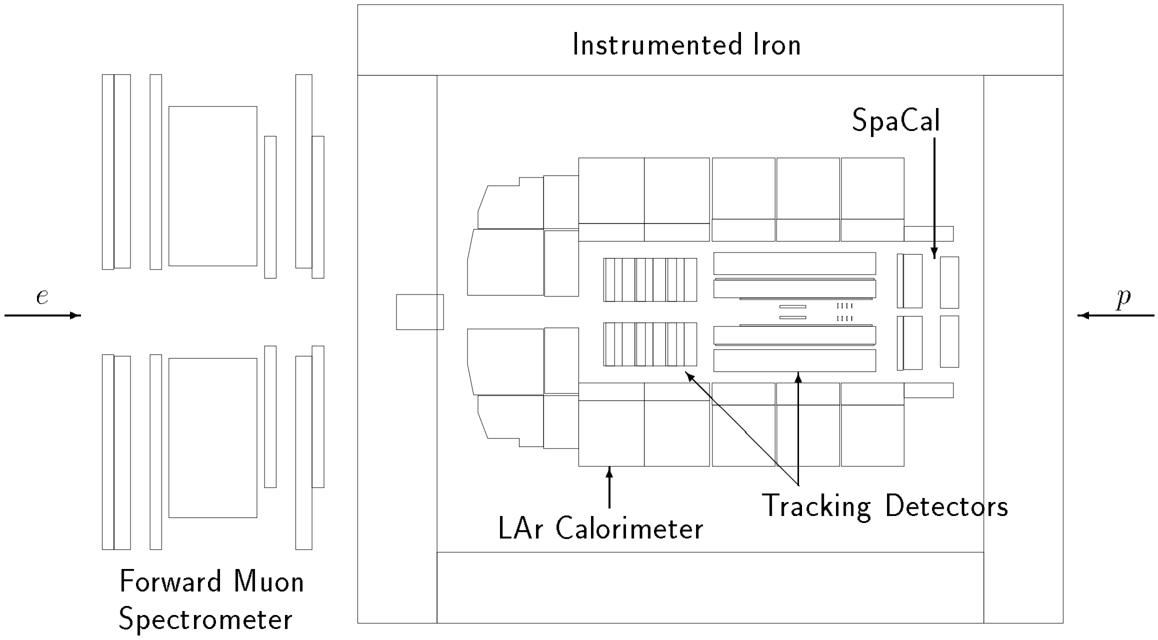

Figure 1.2: *A schematic side-view of the H1 detector*

Central Tracking Detector

The Central Tracking Detector (CTD) consists – radially from inside out – of the Central Silicon Tracker (CST), the Central Inner Proportional chamber (CIP), the Central Inner z-drift chamber (CIZ), the inner Central Jet Chamber (CJC1), the Central Outer z-drift chamber (COZ), the Central Outer Proportional chamber (COP), and the outer Central Jet Chamber (CJC2). It covers a polar angular range of $20° \lesssim \vartheta \lesssim 160°$ and provides a good momentum, angular and vertex resolution.

The central jet chambers, CJC1 and CJC2, yield the most important information for the track reconstruction of the CTD. They consist of 30 (60) drift cells respectively with 24 (32) sense wires strung parallel to the beam axis. The drift cells are tilted with respect to the radial direction to improve the resolution and to avoid track ambiguities. The spatial resolution of the CJC in the $r\varphi$ plane is $\sigma_{r\varphi} = 170\,\mu$m, the momentum resolution $\sigma_{p_t}/p_t^2 = 0.01/$GeV. The sense wires are read out at both ends, and the z coordinate is measured by charge division with a resolution of $\sigma_z = 22\,$mm. During the year 1997 the hit efficiency in the lower half of CJC2 was slowly deteriorating. The complete CJC was therefore rewired between the data taking periods 1997 and 1998.

The measurement of the z-coordinate is improved with the central z-drift chambers CIZ and COZ. They consist of rings containing sense wires strung perpendicular to the beam axis. A z-resolution of $\sigma_z \approx 300\,\mu$m is achieved. The central proportional chambers, CIP and COP, are equipped with pad cathodes, which are segmented in z and φ: 60×8 for the CIP and 18×16 for the COP. They provide a fast signal used for trigger purposes only (see section 1.2.5).

Forward Tracking Detector

The Forward Tracking Detector (FTD) covers a polar angular range of $5° \lesssim \vartheta \lesssim 30°$. It consists of three supermodules segmented each in three planar drift chambers, a MWPC (Multi Wire Proportional Chamber), a transition radiator and finally a radial drift chamber. For the track measurement only the planar and radial drift chambers are used. The transition radiators are designed for the separation of electrons and pions. The MWPCs serve for trigger purposes and complement the polar angular coverage of the central proportional chambers.

1.2.2 Calorimeters

The two main calorimeters of the H1 detector are the liquid argon calorimeter in the central region and the SpaCal in the backward region, which replaced a purely electromagnetic calorimeter (BEMC) in 1995. The main purpose of the backward calorimeter is the identification and measurement of the scattered electron up to photon virtualities of $Q^2 \lesssim 100\,\text{GeV}$, while the liquid argon calorimeter can detect the electron at higher virtualities and measure the hadronic final state. In the forward direction the liquid argon calorimeter is complemented by the PLUG calorimeter. In 1998, the VLQ calorimeter was installed in the extreme backward region to detect scattered electrons at very low virtualities ($0.15 \lesssim Q^2 \lesssim 0.4\,\text{GeV}$).

Liquid Argon Calorimeter

The polar angular coverage of the Liquid Argon calorimeter (LAr) is $4° \lesssim \theta \lesssim 153°$. It is a non-compensating sampling calorimeter with lead as absorber in the electromagnetic part and stainless steel in the hadronic part. It is subdivided into about 45000 cells. The depth of the electromagnetic section varies between 20 and 30 radiation lengths X_0, the total depth corresponds to values between five and eight hadronic interaction lengths λ. The energy resolution of the LAr is $\sigma_E/E \approx 12\%/\sqrt{E[\text{GeV}]} \oplus 1\%$ for electrons and $\sigma_E/E \approx 50\%/\sqrt{E[\text{GeV}]} \oplus 2\%$ for pions. In this analysis the LAr is used to reconstruct kinematic variables and to identify muons via their signature as a minimal ionizing particle. Between the data taking periods 1997 and 1998 the analog calorimeter electronics were upgraded. This reduced the noise, made lower trigger and readout thresholds possible and thus led to an improved muon identification efficiency.

SpaCal

The SpaCal, a 'spaghetti' type lead scintillating-fibre calorimeter complements the LAr in the region $158° \lesssim \theta \lesssim 178°$ and is able to measure the scattered electron down to $Q^2 \approx 1\,\text{GeV}^2$. It consists of 1192 cells in the electromagnetic part and 143 cells in the hadronic part. The electromagnetic section of the SpaCal has an energy resolution of $\sigma_E/E \approx 7.5\%/\sqrt{E[\text{GeV}]} \oplus 1\%$. The energy resolution of the hadronic section is $\sigma_E/E \approx 30\%/\sqrt{E[\text{GeV}]} \oplus 7\%$. The SpaCal is used here to veto events with higher photon virtualities and to detect the 'photon remnant' (see chapter 2).

1.2.3 Muon Detectors

The H1 detector has two subdetectors designed for the identification of muons, the Central Muon Detector (CMD) or 'instrumented iron', and the Forward Muon Detector (FMD). In this analysis only the central muon detector is used because it has a higher acceptance.

Central Muon Detector

The iron return yoke for the flux of the magnet coil is instrumented with limited streamer tubes of $1\,\text{cm} \times 1\,\text{cm}$ cross section. Eight single layers and one double layer are installed between 10 iron layers (fig. 1.3). On the inside and the outside of the iron yoke three additional detector layers, the so called 'muon boxes', improve the track measurement. Layers 3, 4, 5, 8 and 12 are used for trigger purposes. The resolution of the position measurement reaches about 3 to 4 mm perpendicular to the direction of the limited streamer tubes. In order to provide a two-dimensional measurement five layers are equipped with strip electrodes glued perpendicular to the sense wire direction. This results in a resolution of 10 to 15 mm. The other eleven layers are equipped with pad electrodes, which can be used to resolve track ambiguities and to detect hadronic energy leaking from the LAr and SpaCal calorimeters.

The central muon detector is divided into 64 modules arranged in four parts (fig. 1.4), the backward endcap ($130° \lesssim \vartheta \lesssim 175°$), the backward and the forward barrel ($35° \lesssim \vartheta \lesssim 130°$) and the forward endcap ($5° \lesssim \vartheta \lesssim 35°$). For the trigger the endcap modules are grouped into inner (modules $6-11$ and $54-59$) and outer parts. The sense wires are oriented along the z-axis in the barrel and along the x-axis in the endcaps. The track reconstruction in the CMD uses local coordinates for the different detector parts and endcap track segments are not linked with barrel track segments.

Forward Muon Detector

The Forward Muon Detector (FMD) covers the polar angular region $3° \lesssim \vartheta \lesssim 17°$. It is a spectrometer consisting of three double layers of drift chambers in front of and behind a toroidal magnet. It provides identification and momentum measurements for muons with $p \gtrsim 5\,\text{GeV}$. Since the momentum threshold is high compared to the typical momenta of the J/ψ decay muons (see chapter 3) and there is no overlap with the polar angle coverage of the CTD, the FMD is not used in this analysis.

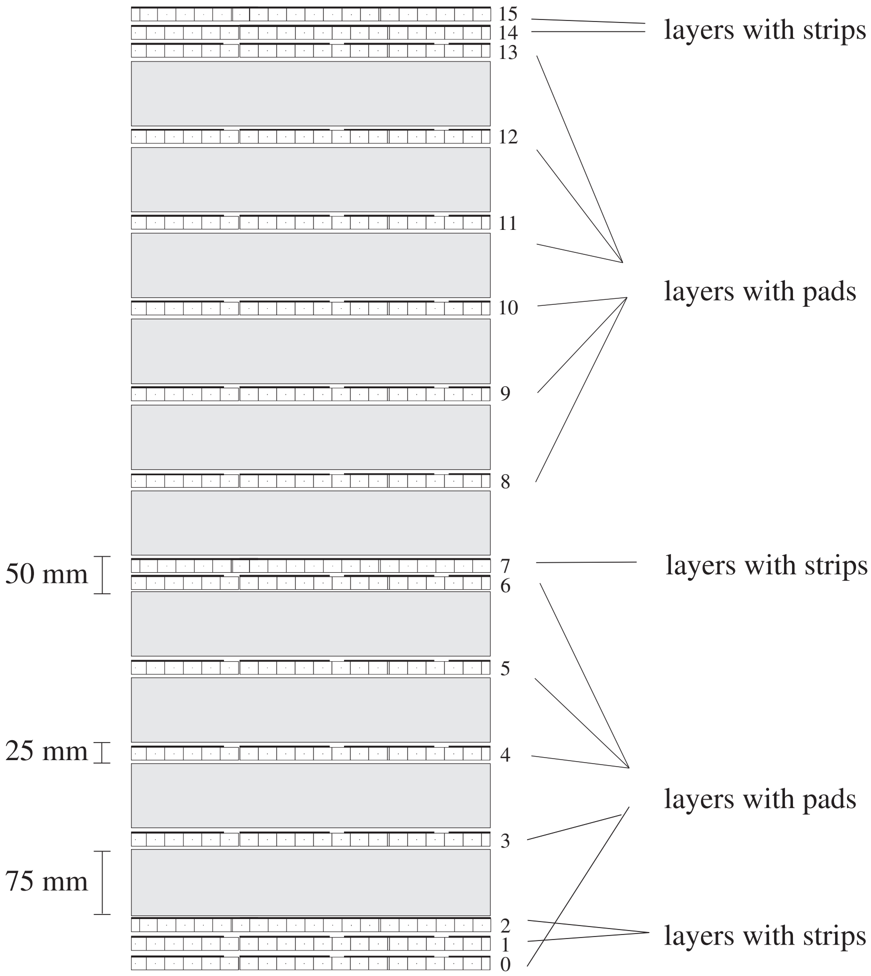

Figure 1.3: *Cross section of the Central Muon Detector.*

1.2.4 Luminosity System

The H1 luminosity system is located downstream from the H1 detector in the direction of the electron beam. It measures the luminosity during data taking by detecting the electron and the photon from the Bethe–Heitler process $e\,p \to e\,p\,\gamma$. The Bethe–Heitler process is a purely electromagnetic process which is well understood. In the offline reconstruction only the photon measurement is used, yielding a precision of better than 2%. The luminosity system consists of a Photon Detector (PD) at $-103\,\mathrm{m}$ and several Electron Taggers (ET). The Electron Tagger at $-33\,\mathrm{m}$ is utilized in the online luminosity measurement. In addition the electron taggers can detect scattered electrons at very small angles corresponding to photon virtualities $Q^2 < 0.01\,\mathrm{GeV}^2$.

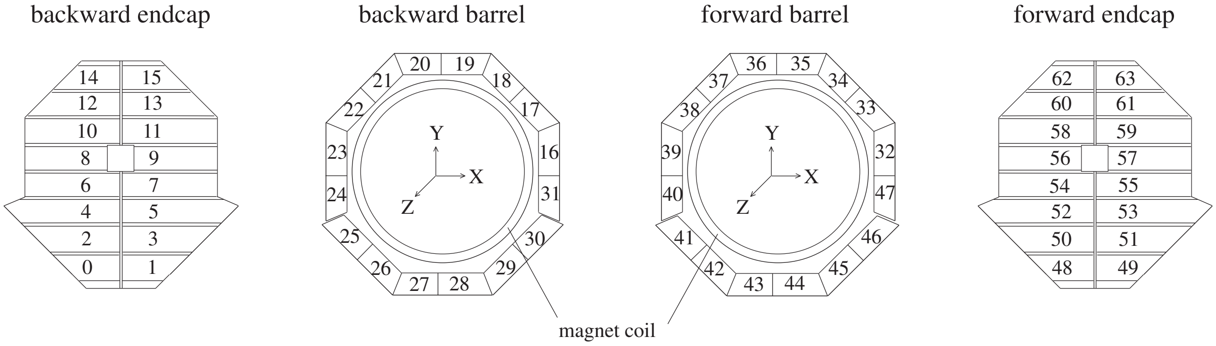

Figure 1.4: *Layout of the 64 modules of the instrumented iron.*

1.2.5 Trigger System

At HERA the expected rate of interesting physics events is much smaller than the background arising from interactions of the proton beam with the beam pipe or with residual gas and from cosmic ray muons. In addition the time interval of 96 ns between two bunch crossings is too short to read out the complete detector. A trigger system with four levels (L1, L2, L4 and L5) aims to record the interesting events efficiently and to minimize the dead time. Trigger levels L1 and L2 are online hardware triggers, while L4 is an online software trigger. Events passing these three trigger levels are stored as 'raw data' on tapes. Short data taking periods with the same detector and running conditions are grouped into 'runs'. A full reconstruction (L5) is performed offline. An additional software trigger L3 is foreseen, but has not been realized so far.

First Trigger Level L1

The first level trigger L1 is pipelined to buffer drift times, read out times and cable delays. Logical combinations of 192 (256 since 1998) 'trigger elements' of the subdetectors form 128 'subtriggers'. If an event is accepted by at least one subtrigger a 'L1 keep' signal stops the pipelines. L1 typically reduces the event rate from ~ 100 kHz to ~ 2 kHz.

Depending on run and background conditions the level 1 subtriggers are prescaled to control the output rate. Subtriggers prescaled with a factor d accept only every d'th event fulfilling the subtrigger conditions. The trigger decision before prescaling is called 'raw subtrigger', afterwards 'actual subtrigger'. The effect of the prescaling is accounted for by weighting the events in the data (for a detailed description see [3]). To make the statistical error as small as possible the weights are not calculated run-wise, but a luminosity weighted average w_j over a period with unchanged trigger definitions is used.

Defining r_{ij}, d_{ik} and $\mathcal{L}_k$ as follows:

$$\begin{aligned} r_{ij} &= \begin{cases} 1 & : \text{ if raw subtrigger } i \text{ is set in event } j \\ 0 & : \text{ otherwise} \end{cases} \\ d_{ik} &= \text{prescaling factor of subtrigger } i \text{ in run } k \\ \mathcal{L}_k &= \text{integrated luminosity of run } k \end{aligned}$$

The probability P_{jk} that at least one of the N_{subtr} used has accepted the event is calculated according to:

$$P_{jk} = 1 - \prod_{i=1}^{N_{subtr}} \left(1 - \frac{r_{ij}}{d_{ik}}\right).$$

The triggering probability of an event is then averaged over the full run range as follows:

$$w_j = \frac{\sum_{k=1}^{N_{runs}} \mathcal{L}_k}{\sum_{k=1}^{N_{runs}} \mathcal{L}_k P_{jk}}.$$

In table 1.1 the trigger element conditions of the subtriggers used in the medium z analysis (S15, S19, S22) and in the low z analysis (S19, S22, S56) are listed. The meaning of the trigger elements is explained in the following.

S15	`DCRPh_Thigh` && `zVtx_Mu_D` && `(Mu_Bar`‖`Mu_ECQ)`
S19	`DCRPh_CNH` && `zVtx_sig1` && `Mu_Bar`
S22	`DCRPh_CNH` && `zVtx_sig1` && `Mu_ECQ`
S56	`DCRPh_Ta` && `(SPCLe_IET>1`‖`SPCLe_IET_Cen_2)` && `Mu_Any`

Table 1.1: *Definition of the L1 subtriggers used in this analysis. Additional veto conditions against beam background are omitted.*

DCRPh Trigger In the central jet chamber ten of the 56 sense wire layers of are used for the `DCRPh` trigger (7 in CJC1 and 3 in CJC2). By comparison with predefined masks in the $r\varphi$ plane the numbers of track candidates with low ($450 \lesssim p_t \lesssim 800\,\mathrm{MeV}$) or high ($p_t \gtrsim 800\,\mathrm{MeV}$) transverse momentum is counted. This is done separately for negative and positive charges. The trigger element `DCRPh_Ta` requires at least one track with a $p_t \gtrsim 450\,\mathrm{MeV}$, `DCRPh_Thigh` at least one with a $p_t \gtrsim 800\,\mathrm{MeV}$. `DCRPh_CNH` is an abbreviation for `DCRPh_Tc && DCRPh_Tneg && DCRPh_Thigh` corresponding to a minimum of three tracks, at least one negative track and at least one with a transverse momentum $p_t \gtrsim 800\,\mathrm{MeV}$.

zVtx Trigger The `zVtx` trigger uses the information of the central proportional chambers, CIP and COP, and of the first layer of the Forward Proportional Chamber

(FPC) to provide a rough determination of the z-position of the event vertex. At least three out of four possible pad signals on a straight line in the rz plane are combined into 'rays' whose origins on the z-axis are filled into the 'z-vertex histogram'. This histogram has 16 bins in the range of ± 44 cm around the nominal interaction point. Of the variety of trigger elements provided by this system `zVtx_Mu_D` and `zVtx_sig1` are used in this analysis. Both require a significant peak in the z-vertex histogram. The conditions of `zVtx_Mu_D` are not as 'hard' as those of `zVtx_sig1`. The element `zVtx_t0` demands only one entry in the histogram and is often used as a veto against non-ep background.

SpaCal Trigger The SpaCal trigger produces energy sums in two separate branches according to whether the arrival time of particles corresponds to nominal ep interactions (ToF) or to upstream background (AToF). The 'inclusive electron trigger' (IET) uses the highly segmented ToF branch to compare the energy in a trigger tower of 16 electromagnetic SpaCal cells to three adjustable thresholds. A sliding window technique reduces losses due to edge effects and allows localization of the cluster. The trigger elements are formed in an inner (IET_Cen, $R < 16$ cm) and an outer ($R > 16$ cm) region of the SpaCal. The trigger elements `SPCLe_IET>1` and `SPCLe_IET_Cen_2` both use the medium threshold corresponding to 2 GeV in all data taking periods relevant for this analysis. In the AToF branch coarse energy sums are formed that are used to veto non-ep background.

Muon Trigger The muon (or iron) trigger uses five layers of the central muon detector (see section 1.2.3). The coincidence conditions differ between the detector regions. In the barrel (`Mu_Bar`) two of the innermost four trigger layers are required. In the backward endcap (inner `Mu_BIEC` and outer `Mu_BOEC`) and the forward outer endcap (`Mu_FOEC`) three out of five layers are required and in the forward inner endcap (`Mu_FIEC`) four out of five layers. In addition trigger elements demanding two coincidences in the backward (`Mu_2_BIoOEC`) or forward (`Mu_2_FIoOEC`) endcap exist. The trigger elements are combined into a coincidence in the outer endcaps (`Mu_ECQ=Mu_BOEC||Mu_2_BIoOEC||Mu_FOEC`) and into a signal covering the complete CMD (`Mu_Any=Mu_BIEC||Mu_BOEC||Mu_Bar||Mu_FOEC||Mu_FIEC`).

Two main sources contribute to the efficiency of the iron trigger. The single layer efficiency of the streamer tubes of $\sim 80\%$ is stable and rather well known and contributes also to the reconstruction efficiency of tracks in the CMD. Because of drift times of the order of 100 ns and cable delays the track reconstruction uses the hits of four successive bunch crossings. This is however not possible for the trigger since it would increase the rate drastically. Only hits in two time windows of 96 ns are considered, and a sophisticated system of signal stretching and delays is used to set the trigger bit only in the first bunch crossing of the coincidence [4]. The 'timing inefficiency' introduced varies between modules and data taking periods. In the context of this analysis a method was developed to determine the timing inefficiency module by module based on 'analysis-level' data ('Data Summary Tapes' DST, see end of this chapter), where no information about single hits is available any more (appendix A). The advantage of this method is the possibility to study long periods of data taking easily. In addition all effects influencing the trigger efficiency like imperfections of the hardware are taken into account, not only timing effects. This improves the agreement of the simulation with the data and reduces the systematic error.

Second Trigger Level L2

The second trigger level uses neural networks (L2NN) and topological correlations (L2TT) to reduce the event rate to about 50 Hz. The information of the subdetectors used to form the L1 trigger elements can be analyzed in more detail because of the longer time available for the decision. A maximum of thirty-two L2 trigger elements can be logically combined with one or more L1 subtriggers. Usually they are used to verify the decision of a specific high-rate subtrigger. The 'L2 keep' signal starts the readout of the detector. For this analysis the reduction of the rate of subtrigger S15 by the neural net is important [5]. The most relevant input quantities stem from the `zVtx`, the `DCRPh` and the muon trigger. The energy in the inner forward part of the LAr calorimeter also allows a good distinction between physics and background. From the training of the network with preselected inelastic J/ψ candidates as physics sample an efficiency of about 90% at a background rejection of about 80% is expected.

Fourth Trigger Level L4

The fourth trigger level is a multi-processor farm that reduces the rate to about 10 Hz. In 1996 and 1997 a trigger verification was done on trigger level 4 which mimicked the L1 subtrigger conditions. For the `DCRPh` and `zVtx` trigger elements a CJC track fulfilling certain quality criteria was required. The trigger elements of the instrumented iron were validated by a reconstructed track in the central muon detector which had to match a CTD or FTD track in ϑ and φ ('muon matching'). In 1996 at least one validated subtrigger was sufficient to pass L4. In 1997 a scheme consisting of 'hard scales' and 'final-state finders' was added. If an event did not fulfil any of the hard scales, like a track with high transverse momentum, for example, or a high energy cluster in the calorimeter, it had to pass one of the finders, depending on the verified subtriggers. For several subtriggers with trigger elements of the instrumented iron this finder was again the muon matching [6].

During the data taking period 1998 the trigger verification in its original sense was removed and the classification, which had been done on L5 before, was replaced by the hard scales and the finders. For J/ψ production class 16, defined by the 'high mass finder', is the relevant class (for the definition see appendix B). Events which do not fulfil any of the final-state or hard scale class conditions are downscaled as 'soft physics'.

Offline Reconstruction L5

For the offline reconstruction the software package H1REC is used. Based on the final calibration, energy deposits in the calorimeters are merged to clusters, and tracks are reconstructed and linked between different tracking detectors. Until 1997 the events were assigned to several physics classes (J/ψ candidates with two identified muons to class 24) and then stored with the full detector information on 'production output tapes' (POT) and in a reduced format ('data summary tape', DST) on disk. Events not assigned to any class were not kept on POT or DST. This procedure reduced the number of events by about a factor of 2.

Since the classification was taken over by L4 in 1998, no rejection of events was done on L5. The reconstruction with final calibration constants was, however, retained, together with the POT and DST storage.

<table>
<tr><th></th><th>1996</th><th>1997</th><th>1999</th></tr>
<tr><td rowspan="2">L4</td><td>trigger
verification</td><td>trigger
verification</td><td></td></tr>
<tr><td></td><td>hard scales
& finders</td><td>hard scales
& finders
classification (class 16)</td></tr>
<tr><td rowspan="2">L5</td><td colspan="3">final reconstruction</td></tr>
<tr><td>classification (class 24)</td><td>classification (class 24)</td><td></td></tr>
</table>

Table 1.2: *Overview over trigger levels L4 and L5 in 1996 to 1999*

Chapter 2

Charmonium Production

After a brief introduction of HERA kinematics and the charmonium system, the inelastic production J/ψ mesons is discussed. This will be done in two steps. First inelastic production mechanisms for heavy quark pairs and their relevance in the two analysis regions are described. Then two models for the formation of the J/ψ meson from the $c\bar{c}$ state are presented. The diffractive production of J/ψ mesons which is considered as background for this analysis is described after that. In the last section the main goals of the analysis of J/ψ photoproduction in the two regions of the elasticity are discussed.

2.1 Kinematics

The interaction between an electron and a proton can be described via the exchange of an electroweak gauge boson γ, Z^0 (neutral current, NC) or W^+, W^- (charged current, CC):

$$\text{a) } e^{\pm}\, p \rightarrow e^{\pm}\, X \quad (\text{NC}) \qquad\qquad \text{b) } e^{\pm}\, p \rightarrow \overset{(-)}{\nu_e}\, X \quad (\text{CC}).$$

A generic Feynman diagram is shown in figure 2.1. The main kinematic variables used to describe this process are the virtuality Q^2 of the exchanged boson, the square of the total centre-of-mass energy s, the Lorentz invariant scaling variable y and the centre-of-mass energy of the boson-proton system $W_{\gamma p}$:

$$Q^2 = -q^2 = -(k-k')^2 \tag{2.1}$$
$$s = (k+P)^2 \tag{2.2}$$
$$y = \frac{q \cdot P}{k \cdot P} \tag{2.3}$$
$$W_{\gamma p} = \sqrt{(q+P)^2} \tag{2.4}$$

where k, k', P and q denote the four momenta of the incoming and the scattered electron, the incident proton and the exchanged boson respectively. In the proton rest frame y is the fraction of the electron energy transferred to the photon.

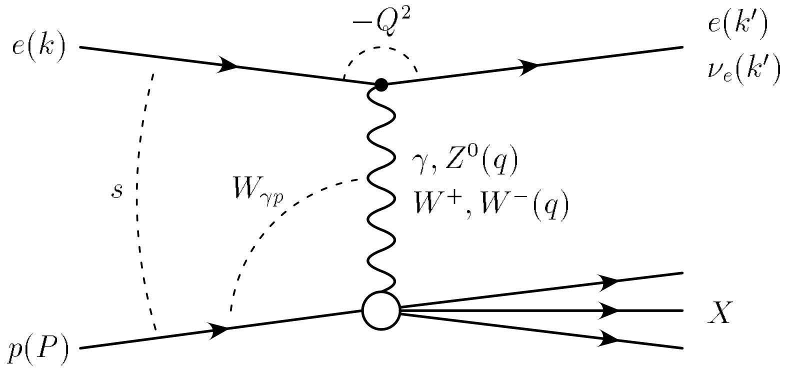

Figure 2.1: *Feynman diagram for electron-proton scattering. The particles' four-momenta are given in brackets.*

The virtuality Q^2 is used to distinguish two kinematic ranges: deep inelastic scattering (DIS, $Q^2 \gtrsim 1\,\mathrm{GeV}^2$), where at H1 the electron is scattered into the main detector, and photoproduction ($Q^2 \lesssim 1\,\mathrm{GeV}^2$), where the scattered electron escapes through the beampipe or can be detected in one of the electron taggers. The exchange of the weakly interacting gauge bosons Z^0, W^+, W^- is suppressed by a factor $Q^2/(Q^2 + M^2_{Z,W})$ with respect to photon exchange and therefore negligible at small virtualities. To leading order the interaction can be described as arising from a photon-proton scattering interaction where the electron is the source of a photon flux (equivalent photon approximation, [7]):

$$\sigma_{ep} = \int_{y_{min}}^{y_{max}} \mathrm{d}y \int_{Q^2_{min}}^{Q^2_{max}} \mathrm{d}Q^2 \, f_{\gamma/e}(y, Q^2)\, \sigma_{\gamma p}(y, Q^2) \;, \tag{2.5}$$

where $\sigma_{\gamma p}$ denotes the photon-proton cross section. $f_{\gamma/e}(y, Q^2)$, the flux of transversely polarized photons, is given by

$$f_{\gamma/e}(y, Q^2) \;=\; \frac{\alpha}{2\pi\, y\, Q^2}\left(1 + (1-y)^2 - 2m_e^2 \frac{y^2}{Q^2}\right) \;. \tag{2.6}$$

The integration limits on the virtuality are given by the kinematic minimum and the analysis region:

$$Q^2_{min} \;=\; m_e^2 \frac{y^2}{1-y} \quad \text{and} \tag{2.7}$$

$$Q^2_{max} \;=\; 1\,\mathrm{GeV}^2 \;. \tag{2.8}$$

For small Q^2 the dependence of the photon-proton cross section on y and Q^2 is much smaller than the dependence of the photon flux. Thus it is possible to treat $\sigma_{\gamma p}$ as a constant and bring it out in front of the integral. The photon-proton cross section can be expressed with the integrated photon flux $\Phi_{\gamma/e}$ as

$$\sigma_{\gamma p} = \sigma_{ep}/\Phi_{\gamma/e} \tag{2.9}$$

$$\text{where} \quad \Phi_{\gamma/e} = \int_{y_{min}}^{y_{max}} dy \int_{Q^2_{min}}^{Q^2_{max}} dQ^2 \, f_{\gamma/e}(y, Q^2) \;. \tag{2.10}$$

This relation is used to extract photoproduction cross sections from the measured electron-proton cross sections.

2.2 Charmonium System

The J/ψ is the lightest vector meson in the *charmonium* family, which comprises all bound *charm-anticharm* pairs (fig. 2.2). It has a mass of $m_\psi = 3.09687 \pm 0.00004\,\mathrm{GeV}$ [8] and the same quantum numbers as the photon, $J^{PC} = 1^{--}$. The spectroscopic notation for the spin, the orbital angular momentum and the total angular momentum is $^3S_1$. The extremely small decay width of $\Gamma_\psi = 87 \pm 5\,\mathrm{keV}$ can be explained firstly by the fact that the obvious decay mode into two charmed mesons (D mesons) is forbidden because of energy conservation. All other decay modes are suppressed by the Zweig rule [9]. Decays via one or two gluons are impossible due to colour and C-parity conservation. For the analyses which will be presented here the decay via a virtual photon into two muons $J/\psi \to \mu^+\,\mu^-$ is utilized which has a branching ratio of only $5.88 \pm 0.10\%$ [8], but leads to a clean signature in the detector.

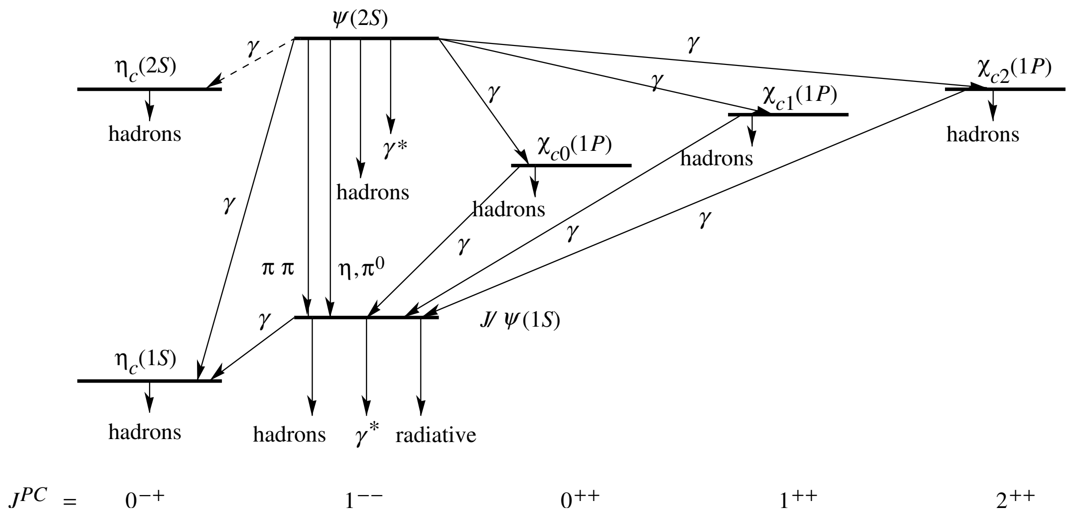

Figure 2.2: *The charmonium system (from [8])*

The J/ψ meson was discovered in 1974 simultaneously by two groups: Aubert et al. [10] reported an enhancement in the $e^+\,e^-$ invariant mass spectrum of the reaction $p\,Be \to e^+\,e^- + X$ at the Brookhaven National Laboratory while Augustin et al. [11] observed a sudden rise in the $e^+\,e^-$ annihilation cross section at the SPEAR machine in Stanford.

The mass of the first radial excitation of the J/ψ , the $\psi(2s)$ meson, is $m_{\psi(2s)} = 3.68596 \pm 0.00009\,\mathrm{GeV}$ [8] and therefore still below the threshold of $D\bar{D}$ production. It has a decay width of $\Gamma_{\psi(2s)} = 277 \pm 31\,\mathrm{keV}$. More than 50% of its decays include a J/ψ which leads to significant background contributions for direct J/ψ production. Another possibility is the direct decay into two muons with a branching ratio of $0.77 \pm 0.17\%$.

The three P wave states χ_{c0}, χ_{c1} and χ_{c2} have masses between the J/ψ and the $\psi(2s)$ meson. Their spectroscopic notation is ${}^3P_0$, ${}^3P_1$ and ${}^3P_2$. All χ_c mesons can decay into a J/ψ meson via emission of a photon, but with rather different branching ratios ($BR(\chi_{c0} \to J/\psi\,\gamma) = 0.66 \pm 0.18\%$, $BR(\chi_{c1} \to J/\psi\,\gamma) = 27.3 \pm 1.6\%$ and $BR(\chi_{c2} \to J/\psi\,\gamma) = 13.5 \pm 1.1\%$).

2.2.1 Kinematic Variables in J/ψ Production

If a J/ψ meson is produced in an electron-proton interaction, additional variables can be defined. The elasticity z is used to distinguish different production mechanisms:

$$z = \frac{p_\psi \cdot P}{q \cdot P}\,, \tag{2.11}$$

where p_ψ is the four momentum of the J/ψ meson. In the proton rest frame the elasticity is the fraction of the photon energy transferred to the J/ψ meson.

Another way to differentiate between production mechanisms is via the polarization of the J/ψ meson, which can be measured via the decay angular distribution in the muonic decay mode $J/\psi \to \mu^+\mu^-$. This distribution can be parameterized in the J/ψ rest frame as

$$\frac{\mathrm{d}\sigma}{\mathrm{d}\Omega\,\mathrm{d}y} \propto 1 + \lambda(y)\cos^2\vartheta^* + \mu(y)\sin 2\vartheta^*\cos\varphi^* + \frac{\nu(y)}{2}\sin^2\vartheta^*\cos 2\varphi^*, \tag{2.12}$$

where y stands for a set of variables and the angles ϑ^* and φ^* denote the polar and the azimuthal angle of the positive decay muon with respect to a coordinate system defined in the J/ψ rest frame. In the following the *recoil* or *s-channel helicity* frame will be used, where the z-axis is defined to lie along the direction of the J/ψ three-momentum in the photon-proton centre-of-mass frame. Figure 2.3 illustrates the definition of φ^* and ϑ^* in the helicity frame.

In the case of limited statistics it is reasonable to study each decay angle separately. The integration of formula 2.12 leads to

$$\frac{\mathrm{d}\sigma}{\mathrm{d}\cos\vartheta^*\,\mathrm{d}y} \propto 1 + \lambda(y)\cos^2\vartheta^* \tag{2.13}$$

$$\text{and}\quad \frac{\mathrm{d}\sigma}{\mathrm{d}\varphi^*\,\mathrm{d}y} \propto 1 + \frac{\lambda(y)}{3} + \frac{\nu(y)}{3}\cos 2\varphi^*. \tag{2.14}$$

In figure 2.4 the decay angular distributions are shown for some typical values of the parameters λ and ν (for the choice of the values compare table 2.3). Good precision of the data is needed especially to restrict ν.

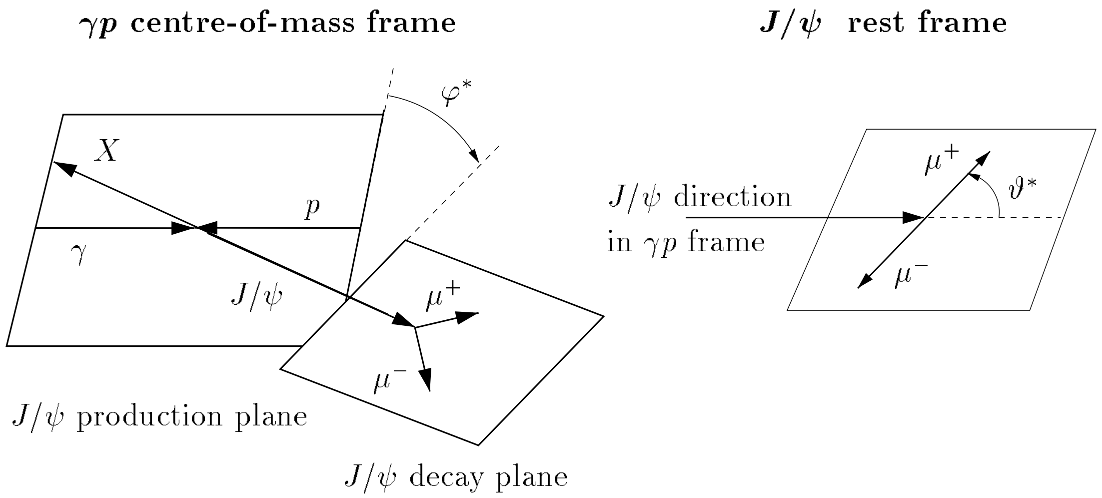

Figure 2.3: *Illustration of the decay angles φ^* and ϑ^* in the helicity frame for the muonic decay $J/\psi \to \mu^+\mu^-$. φ^* is the azimuthal angle of the positive decay muon and corresponds to the angle between the J/ψ production and decay planes. ϑ^* is the polar angle of the μ^+.*

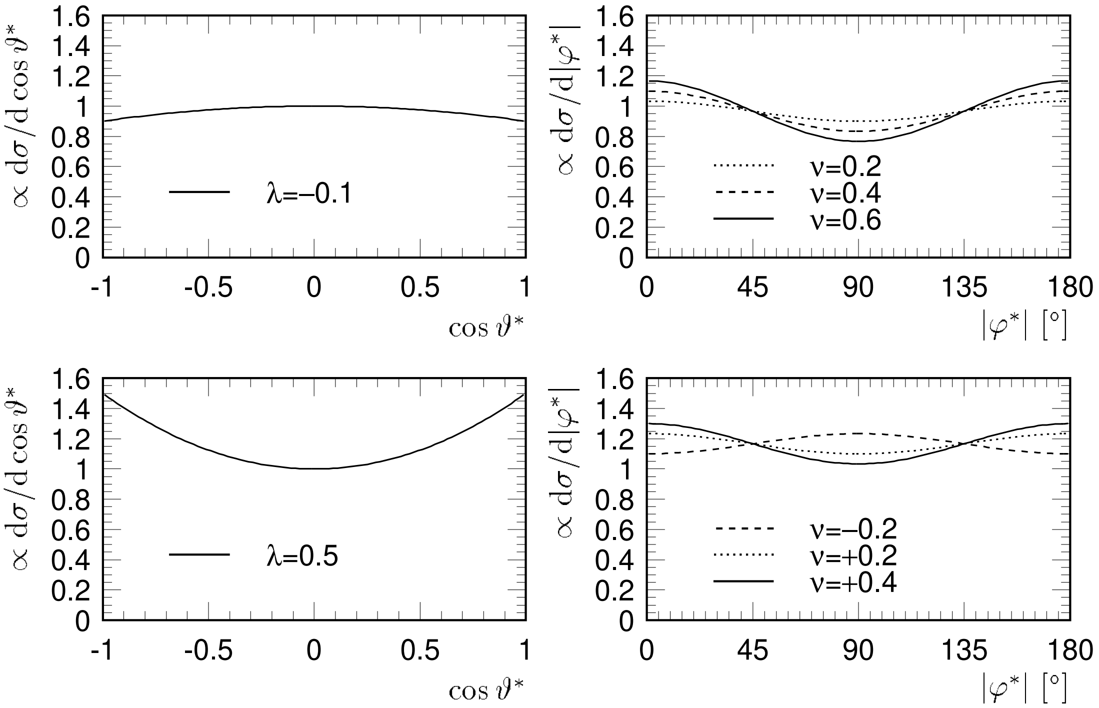

Figure 2.4: *Example of the decay angle distributions for typical values of the parameters λ and ν. For the plots on the right the values of λ from the left are used.*

2.3 Models for Inelastic Production of J/ψ Mesons

In this section two models for the inelastic production of J/ψ mesons are discussed. Both assume factorization into the production of a $c\bar{c}$ pair which can be calculated in perturbative QCD (pQCD) and the evolution into the bound J/ψ state. Therefore the production mechanisms for heavy quark pairs in electron-proton scattering and their relevance in the two analysis regions are discussed first. The Colour Singlet Model (CSM) and the approach within non-relativistic QCD (NRQCD) are explained subsequently. Finally a recently proposed addition to the models is presented, the possibility of gluons inside the proton with intrinsic transverse momentum.

2.3.1 Inelastic Production of Heavy Quark Pairs

Two classes of inelastic production mechanisms of heavy quark pairs are important at HERA, the direct photon-gluon fusion and resolved photon processes. The generic Feynman diagram for direct photon-gluon fusion in leading order, $\mathcal{O}(\alpha_s)$, is shown in figure 2.5.

The photon and a gluon from the proton fuse via a virtual c quark. The fractional gluon momentum inside the proton is denoted x_g:

$$p_g = x_g\, P \ .$$

The gluon content of the proton is described by a parton density function (PDF). Since the total momentum of the photon enters the production of the heavy quark pair, this reaction is kinematically possible at comparatively small centre-of-mass energies of the

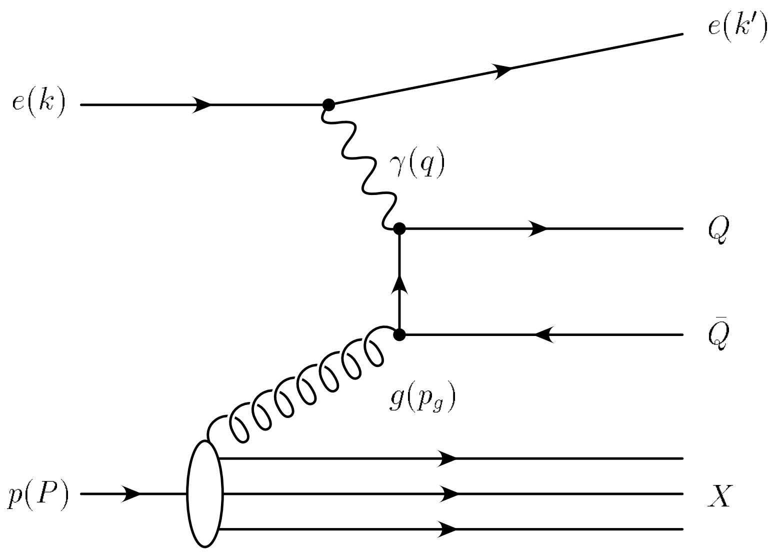

Figure 2.5: *Feynman diagram for direct photon-gluon fusion in leading order, $\mathcal{O}(\alpha_s)$. The particles' four-momenta are given in brackets.*

photon-proton system. If a J/ψ meson is formed in this process, the elasticity z which is a measure for the photon energy transferred to the J/ψ lies typically at medium to large values.

The second class of production mechanisms consists of resolved photon processes, where a photon with very small virtuality behaves like a hadron and interacts via its partonic content. In this case the fractional parton momentum inside the photon is denoted x_γ:

$$g = x_\gamma \, q \ .$$

The partonic content of the photon can be described by a photon PDF. For higher orders the separation into direct and resolved processes must be handled with care because some of the direct terms may be included in the photon PDF.

The dominating process for heavy quark production at HERA with a resolved photon is the gluon-gluon fusion, for which a generic Feynman diagram in leading order, $\mathcal{O}(\alpha_s^2)$, is shown in figure 2.6. Typically a photon remnant is produced in addition to the proton remnant X in this process. Because of the small photon virtuality Q^2 the photon remnant lies in the direction of the electron. Since only a fraction of the photon momentum takes part in the heavy quark production high photon-proton centre-of-mass energies are needed to produce charm quarks. If a charmonium is formed the elasticity z is typically small.

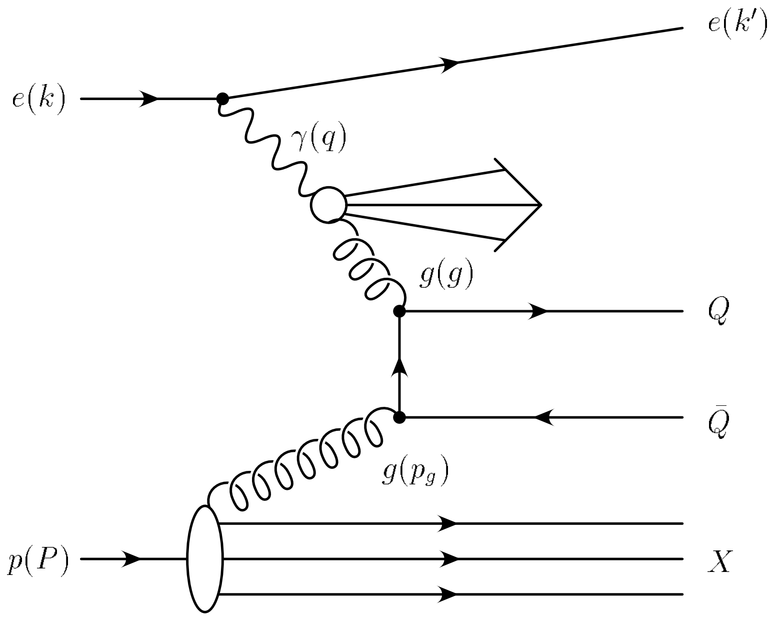

Figure 2.6: *Feynman diagram for gluon-gluon fusion in leading order, $\mathcal{O}(\alpha_s^2)$, as an example for a process with a resolved photon. The particles' four-momenta are given in brackets.*

2.3.2 Colour Singlet Model

The Colour Singlet Model (CSM) was developed from 1980 onwards. The main theoretical predictions for the hadro- and electro-production of charmonia are from Chang [12], Berger and Jones [13] and Baier and Rückl [14]. The Colour Singlet Model assumes that only $c\bar{c}$ pairs with the same quantum numbers as the meson contribute significantly to charmonium production. In direct photon-gluon fusion therefore an additional gluon is needed to produce a colour singlet state. In gluon-gluon fusion, a gluon or a photon is needed to conserve the angular momentum and parity of the J/ψ. The generic Feynman diagrams for J/ψ photoproduction in the CSM in leading order are shown in figure 2.7. The coupling of the J/ψ meson to the $c\bar{c}$ pair is determined by the radial wave function at the origin $|R_\psi(0)|$ which can be calculated from its measured leptonic decay width $\Gamma_{l\bar{l}}$:

$$\mathrm{d}\sigma(J/\psi + X) \propto \mathrm{d}\hat{\sigma}(c\bar{c}[\underline{1},{}^3S_1] + X) \cdot |R_\psi(0)|^2 \tag{2.15}$$

$$\Gamma_{l\bar{l}} = 4\, e_q^2\, \alpha^2\, \frac{|R_\psi(0)|^2}{m_\psi^2} \left(1 - \frac{16\,\alpha_s}{3\,\pi}\right) \tag{2.16}$$

The colour singlet state of the $c\bar{c}$ pair is marked by $\underline{1}$, and ${}^3S_1$ is the spectroscopic notation for the spin, the orbital angular momentum and the total angular momentum. The QCD correction to the leptonic decay width (term in brackets) increases $|R_\psi(0)|$ by about a factor of 2 compared to the lowest order and reduces the discrepancy in the normalization which was originally observed. The dependence of the cross section on the charm quark mass $\sigma \propto \Gamma_{l\bar{l}}/m_c^3$ introduces another large normalization uncertainty [13].

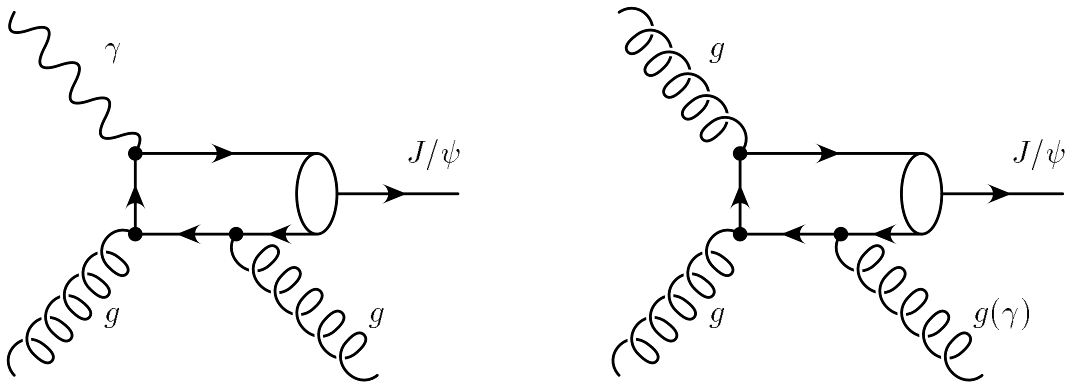

Figure 2.7: *Feynman diagrams for J/ψ photoproduction in the Colour Singlet Model in a) direct photon-gluon fusion and b) gluon-gluon fusion. The $c\bar{c}$ pair is produced in the colour and angular momentum state of the J/ψ.*

The CSM has large predictive power, because the only non-perturbative parameter for J/ψ production is $|R_\psi(0)|$ which is independent of the production process. On the other hand, the factorization as assumed in (2.15) is not proven. In addition cross sections for P-wave states like the χ_c show infra-red divergences in the CSM.

The next-to-leading order (NLO) terms of the colour singlet $c\bar{c}$ cross section in photon-gluon fusion $\mathrm{d}\hat{\sigma}(\gamma g \to c\bar{c}[\underline{1},{}^3S_1] + X)$ were calculated in 1995 by Krämer [15]. Previously it had been assumed that the NLO corrections would only change the normalization by a so called k factor which turned out to be approximately 2. The NLO calculation, however, showed that this is not the case. The p_t spectrum of the J/ψ meson is much harder if the NLO terms are included. For hadroproduction no NLO computation is available at present.

Although the Colour Singlet Model is able to describe inelastic J/ψ photoproduction at HERA [16, 17] and fixed target muoproduction (EMC, NMC) [18, 19], it fails to describe prompt[1] J/ψ and $\psi(2s)$ production in $p\bar{p}$ collisions at the Tevatron (CDF) [20]. A mismatch in the normalization of more than one order of magnitude was observed (fig. 2.8).

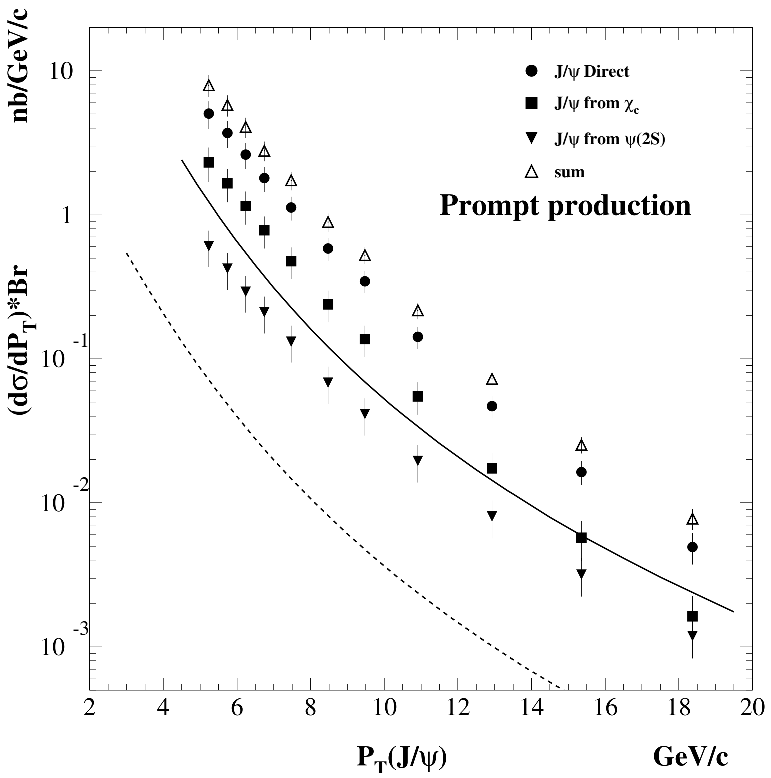

Figure 2.8: *Differential cross section* $\mathrm{d}\sigma/\mathrm{d}p_t$ *times the branching ratio* $BR(J/\psi \to \mu^+\mu^-)$ *for prompt* J/ψ *production in* $p\bar{p}$ *collisions measured by CDF [20]. The data are divided into directly produced* J/ψ *mesons (circles) and those originating from* χ_c *(squares) and* $\psi(2s)$ *(filled triangles) decays. The dashed line is a prediction in the CSM for the direct part, the full line the sum of colour singlet and colour octet contributions to the decay* $\chi_c \to J/\psi\,\gamma$ *[21].*

[1] 'Prompt' indicates charmonia which are produced directly at the interaction vertex, not by decays of B hadrons.

2.3.3 NRQCD/Colour Octet Model

In the Colour Octet Model (COM) colour octet states of the $c\bar{c}$ pair can also contribute to charmonium production via the emission of soft gluons. In 1995 a general factorization formalism based on non-relativistic QCD (NRQCD) was developed by Bodwin, Braaten and Lepage [22]. Effects of the scale m_c and those of lower scales such as $m_c v$ with the typical relative momentum v of the quarks in the charmonium state are separated. The general form of the J/ψ production cross section is a sum over all colour and angular momentum states n of the $c\bar{c}$ pair :

$$\mathrm{d}\sigma(J/\psi + X) = \sum_n C_n(c\bar{c}[n] + X) \cdot \langle \mathcal{O}_n^{J/\psi} \rangle \tag{2.17}$$

The C_n are short-distance parton cross sections for producing a $c\bar{c}$ pair with vanishing relative momentum. They correspond to parts of Feynman diagrams where all internal lines are off-shell by amounts of order m_c or larger. Therefore they are calculable in pQCD. The long-distance non-perturbative factors $\langle \mathcal{O}_n^{J/\psi} \rangle$ are called 'Colour Octet Matrix Elements' (COMEs) and describe the formation of the J/ψ meson from the $c\bar{c}$ pair. They correspond to those parts of the Feynman diagrams where the internal lines are off-shell by amounts much less than m_c. They scale with a power of v ($v^2 \approx 0.25$ for charmonium). In the non-relativistic limit, $v \to 0$, the formula 2.15 of the Colour Singlet Model is recovered.

The most general form of formula 2.17 contains an infinite number of non-perturbative COMEs and thus has no predictive power. This can be changed by truncating the expansion to a low order in v. For J/ψ production the leading order term is the colour singlet one $\langle \mathcal{O}^{J/\psi}[\underline{1},{}^3S_1] \rangle$ scaling with v^3. The following order scales with v^7 and consists of $\langle \mathcal{O}^{J/\psi}[\underline{8},{}^1S_0] \rangle$, $\langle \mathcal{O}^{J/\psi}[\underline{8},{}^3S_1] \rangle$ and $\langle \mathcal{O}^{J/\psi}[\underline{8},{}^3P_J] \rangle$.

The Colour Octet Matrix Elements cannot be calculated perturbatively, but they are assumed to be universal. Therefore it should be possible to determine their values from one experiment and make predictions for other production processes. The lowest order J/ψ COMEs have been extracted by fitting the differential cross section $\mathrm{d}\sigma/\mathrm{d}p_t$ in $p\bar{p}$ collisions as measured by the CDF collaboration. The dominant term at large p_t is gluon fragmentation via a $[\underline{8},{}^3S_1]$ state. For $\langle \mathcal{O}^{J/\psi}[\underline{8},{}^1S_0] \rangle$ and $\langle \mathcal{O}^{J/\psi}[\underline{8},{}^3P_J] \rangle$ only the value of a linear combination can be determined (see table 2.1), which is mainly sensitive to the measurement at small p_t.

Cano-Coloma and Sanchis-Lozano take higher order effects approximately into account for the extraction of the COMEs from CDF data [24]. The Monte Carlo generator PYTHIA is used to estimate the effects of multiple gluon radiation. While the result for $\langle \mathcal{O}^{J/\psi}[\underline{8},{}^3S_1] \rangle$ turns out to be only about a factor of 2 lower including the higher order corrections, the value of the linear combination of $\langle \mathcal{O}^{J/\psi}[\underline{8},{}^1S_0] \rangle$ and $\langle \mathcal{O}^{J/\psi}[\underline{8},{}^3P_J] \rangle$ is reduced by an order of magnitude. Kniehl and Kramer confirmed this result with an updated CDF measurement [25]. They parameterized the ratio of the higher order cross section to the leading order one as a function of the transverse momentum of the J/ψ meson. The predictions for inelastic J/ψ photoproduction at HERA were updated with the new COMEs.

Colour Octet Matrix Element	value [GeV^3]	scaling order
$\langle \mathcal{O}^{J/\psi}[\underline{8},^3S_1]\rangle$	$(6.6 \pm 2.1) \times 10^{-3}$	$m_c^3 v^7$
$\frac{\langle \mathcal{O}^{J/\psi}[\underline{8},^3P_0]\rangle}{m_c^2} + \frac{\langle \mathcal{O}^{J/\psi}[\underline{8},^1S_0]\rangle}{3}$	$(2.2 \pm 0.5) \times 10^{-2}$	$m_c^3 v^7$

Table 2.1: *Colour Octet Matrix Elements extracted from the fits to prompt J/ψ production at the Tevatron by Cho and Leibovich [23].*

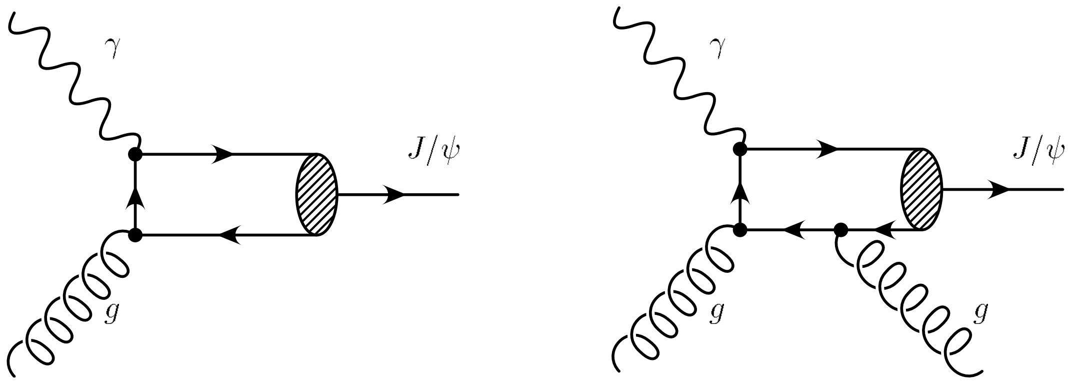

Figure 2.9: *Feynman diagrams for J/ψ photoproduction in direct photon-gluon fusion in the Colour Octet Model in a) leading order $\mathcal{O}(\alpha_s)$ and b) next-to-leading order $\mathcal{O}(\alpha_s^2)$. The $c\bar{c}$ pair can be in a colour singlet or colour octet state. It evolves into the J/ψ via emission of soft gluons.*

At HERA the colour octet term which is of leading order in α_s is the fusion of a photon and a gluon without emission of additional hard gluons (fig. 2.9a). In photoproduction the photon is nearly co-linear with the beam electron. In the co-linear approach the gluon inside the proton is assumed to follow the proton direction. Thus the J/ψ meson cannot have large transverse momentum if it is the only particle produced. A cut $p_t > 1\,\mathrm{GeV}$ is believed to remove the leading order contribution completely. One of the next-to-leading order, $\mathcal{O}(\alpha_s^2)$, diagrams (fig. 2.9b) is similar to the CSM diagram with the difference, that other colour and angular momentum states are allowed for the $c\bar{c}$ pair. The $[\underline{8},^3S_1]$ state has the same kinematics as the colour singlet term, but the COME is suppressed by a factor v^4. Therefore it can be neglected in view of the normalization uncertainty of the CSM. For the $[\underline{8},^1S_0]$ and the $[\underline{8},^3P_J]$ state additional diagrams with t-channel exchange of a gluon contribute. Therefore their perturbative cross sections C_n depend differently on p_t and z. They are expected to dominate at high values of z at HERA, where the distinction from diffraction is not clear. Predictions based on the first COMEs extracted from CDF data (for the values used in the numerical analysis see table 2.2) showed a steep rise towards high z starting already at $z \approx 0.7$. This could not be confirmed experimentally (fig. 2.10). Using the higher-order improved COMEs the Colour Octet contributions are expected to dominate only above $z = 0.9$ which means that previous analyses and the medium z analysis presented here are not sensitive to them due to the restriction in z.

The colour octet contributions to resolved photon processes are expected to increase the cross section at low z significantly, an order of magnitude based on the first COMEs (fig. 2.10) or about a factor of 3 based on the higher-order improved COMEs. This effect is searched for in the low z analysis.

One prediction of NRQCD which can be used to check the consistency of the approach is the polarization of prompt J/ψ and $\psi(2s)$ at the Tevatron. The colour octet gluon fragmentation should dominate the cross section at large p_t and the charmonium state tends to inherit the transverse polarization of the gluon. Therefore the deviations from a total transverse polarization of the charmonium state should become smaller with rising p_t. The CDF measurements, however, do not show this behaviour, neither for the prompt J/ψ (fig. 2.11a) nor for the $\psi(2s)$ (fig. 2.11b).

Colour Octet Matrix Element	value [GeV^3]	scaling order
$\langle\mathcal{O}^{J/\psi}[\underline{1},{}^3S_1]\rangle$	1.16	$m_c^3v^3$
$\langle\mathcal{O}^{J/\psi}[\underline{8},{}^3S_1]\rangle$	10^{-2}	$m_c^3v^7$
$\langle\mathcal{O}^{J/\psi}[\underline{8},{}^1S_0]\rangle$	10^{-2}	$m_c^3v^7$
$\langle\mathcal{O}^{J/\psi}[\underline{8},{}^3P_0]\rangle/m_c^2$	10^{-2}	$m_c^3v^7$

Table 2.2: *Colour Octet Matrix Elements used for the prediction of inelastic J/ψ photoproduction at HERA by Krämer [26].*

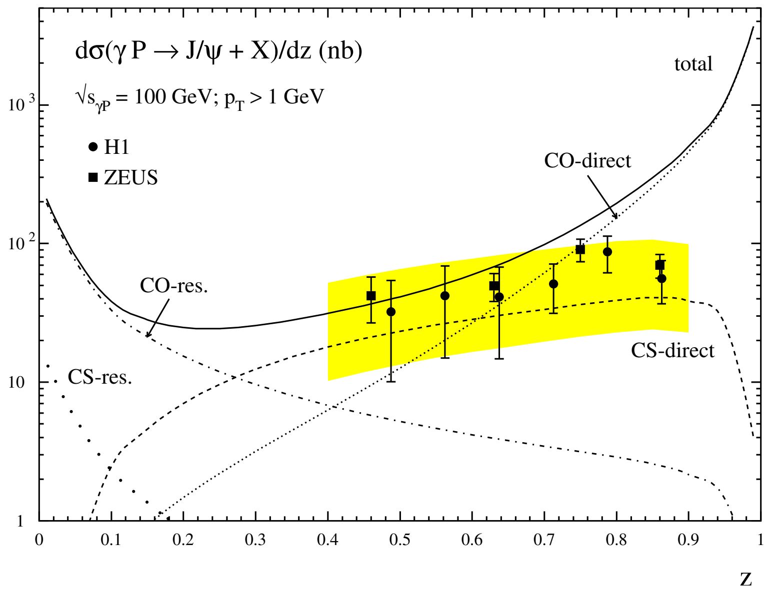

Figure 2.10: *Colour singlet (CS) and colour octet (CO) contributions to the differential cross section $\mathrm{d}\sigma/\mathrm{d}z$ for inelastic J/ψ photoproduction at HERA calculated by Krämer [26]. GRV parton density functions with $\Lambda^{(4)} = 200\,\mathrm{MeV}$ and $m_c = 1.5\,\mathrm{GeV}$ are used. The shaded band reflects the normalization uncertainty of the direct colour singlet contribution due to a variation of m_c ($1.35 < m_c < 1.55\,\mathrm{GeV}$) and α_s ($200 < \Lambda^{(4)} < 400\,\mathrm{MeV}$).*

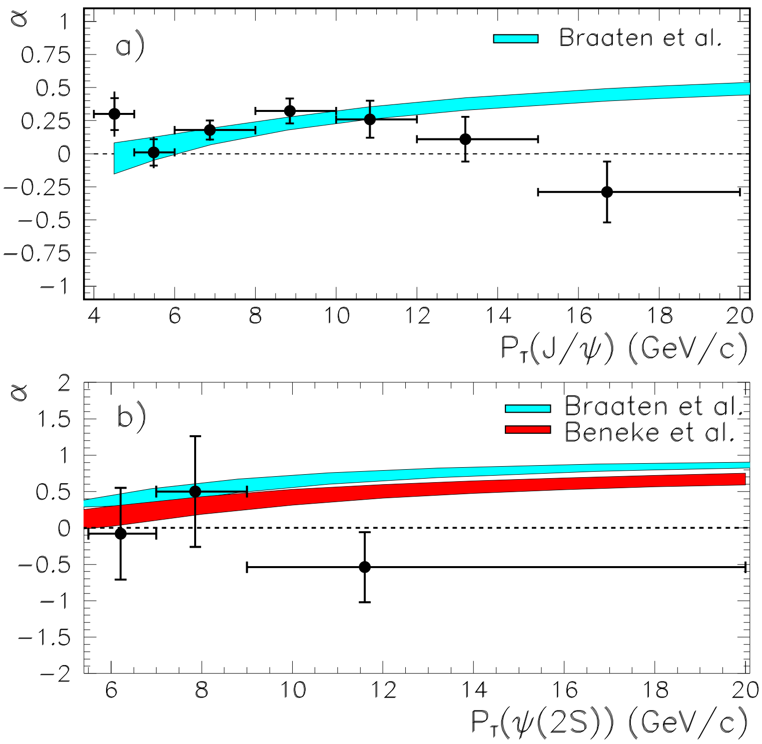

Figure 2.11: *The polarization parameter α (equivalent to λ in this analysis) for a) prompt J/ψ and b) prompt $\psi(2s)$ production in $p\bar{p}$ collisions measured by CDF [27]. Unpolarized mesons have $\alpha = 0$, whereas $\alpha = +1$ or -1 correspond to fully transverse or fully longitudinal polarizations respectively. The shaded bands show NRQCD predictions [28, 29].*

Beneke, Krämer and Vänttinen proposed to measure the polarization of the J/ψ also in photoproduction to clarify the relative importance of colour octet production mechanisms [30]. A large uncertainty in the predictions for photoproduction is the fact, that in the endpoint region $z \approx 1$ the energy transfer in the non-perturbative transition from the $c\bar{c}$ pair to the J/ψ meson is neglected. A smearing in a region of the order of $v^2 \approx 0.25$ is expected. This affects the normalized decay angular distributions to a lesser extent than the differential cross section $\mathrm{d}\sigma/\mathrm{d}z$ if they do not have a strong z dependence in the region affected by the smearing. The predictions for the z dependence of the polarization parameters λ and ν are shown in figure 2.12. In the region of intermediate elasticities ($0.3 < z < 0.6$) both models expect the value of λ to be near to zero. ν is expected to lie at about 0.6 in the CSM and between 0.15 and 0.4 in the COM. At higher elasticities ($0.6 < z < 0.9$) the CSM predicts λ to rise to 0.8, while in the COM it depends on the choice of parameters as to whether a slower rise or a flat behaviour is expected. The prediction for ν falls to 0.1 (CSM) or to values between 0.0 and -0.6 (COM). Estimates for the mean values of λ and ν are listed in table 2.3. The resulting decay angle distributions are shown in figure 2.4.

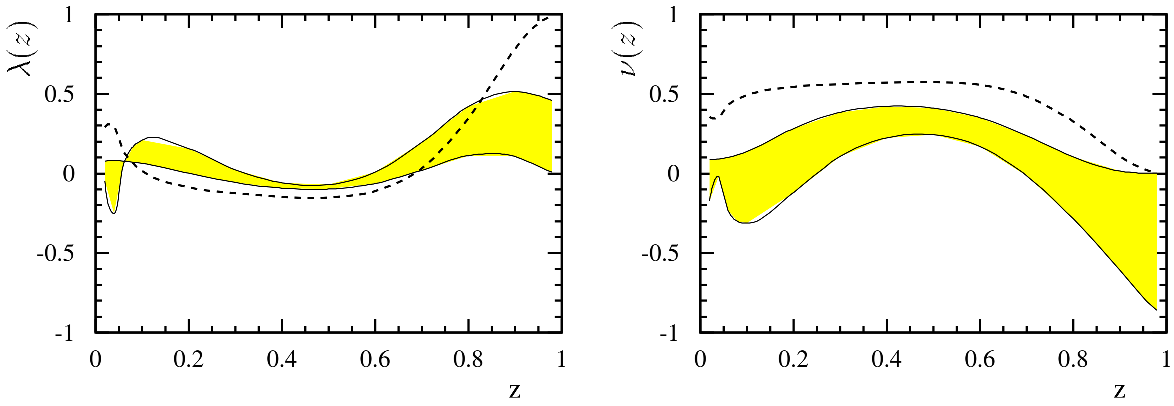

Figure 2.12: *Polarization parameters λ and ν for inelastic J/ψ photoproduction as a function of the elasticity z ($W_{\gamma p} = 100\,\mathrm{GeV}$, $p_t > 1\,\mathrm{GeV}$) [30]. The dashed line is the prediction in the Colour Singlet Model. The shaded area shows the NRQCD prediction bounded by two choices of parameters, with $\langle \mathcal{O}^{J/\psi}[\underline{8},{}^1S_0]\rangle = 0$ and $\langle \mathcal{O}^{J/\psi}[\underline{8},{}^3P_0]\rangle / m_c^2 = 0$ respectively.*

z region	λ CSM	λ COM	ν CSM	ν COM
$0.3 < z < 0.6$	-0.1	-0.1	0.6	$0.2 - 0.4$
$0.6 < z < 0.9$	0.5	$0.0 - 0.5$	0.4	$-0.2 - 0.2$

Table 2.3: *Estimates of the mean values of the polarization parameters λ and ν in two regions of the elasticity z.*

2.3.4 Intrinsic k_T

One possible explanation for the fact, that the Colour Octet Matrix Elements fitted to the Tevatron data do not describe the elasticity distribution at HERA, could be the effect of soft physics at small values of p_t (and large z). This can be parameterized by including transverse momentum smearing of the partons inside the proton. Sridhar, Martin and Stirling studied the effect of the parton transverse momentum k_T on the J/ψ distributions at the Tevatron and at HERA [31]. For three different values of the mean intrinsic transverse momentum, $\langle k_T \rangle = 0.0, 0.7, 1.0\,\mathrm{GeV}$, the Colour Octet Matrix Elements are extracted from CDF data (table 2.4), where all fits are comparable in quality. With rising $\langle k_T \rangle$ the value of the linear combination of the COMEs $\langle \mathcal{O}^{J/\psi}[\underline{8},{}^3P_0]\rangle$ and $\langle \mathcal{O}^{J/\psi}[\underline{8},{}^1S_0]\rangle$, which is responsible for the strong rise at large z at HERA, is reduced. The resulting z distributions for inelastic J/ψ photoproduction are shown in figure 2.13. The k_T smearing significantly reduces the cross section at large z, mainly due to the smearing function itself, but also due to the different COMEs. This may indicate that inelastic J/ψ photoproduction, especially at high elasticities, does not provide a clean test of NRQCD.

$\langle k_T \rangle$	$\langle \mathcal{O}^{J/\psi}[\underline{1},{}^3S_1] \rangle$	$\langle \mathcal{O}^{J/\psi}[\underline{8},{}^3S_1] \rangle$	$\frac{\langle \mathcal{O}^{J/\psi}[\underline{8},{}^3P_0] \rangle}{m_c^2} + \frac{\langle \mathcal{O}^{J/\psi}[\underline{8},{}^1S_0] \rangle}{3}$
0.0	0.81	$(1.26 \pm 0.33) \times 10^{-2}$	$(3.14 \pm 0.58) \times 10^{-2}$
0.7	0.98	$(1.35 \pm 0.30) \times 10^{-2}$	$(2.82 \pm 0.47) \times 10^{-2}$
1.0	1.41	$(1.50 \pm 0.29) \times 10^{-2}$	$(2.35 \pm 0.39) \times 10^{-2}$

Table 2.4: *Colour Octet Matrix Elements (in* GeV^3*) extracted from the fits to prompt* J/ψ *production at the Tevatron for different values of the mean intrinsic transverse momentum* $\langle k_T \rangle$ *[31].*

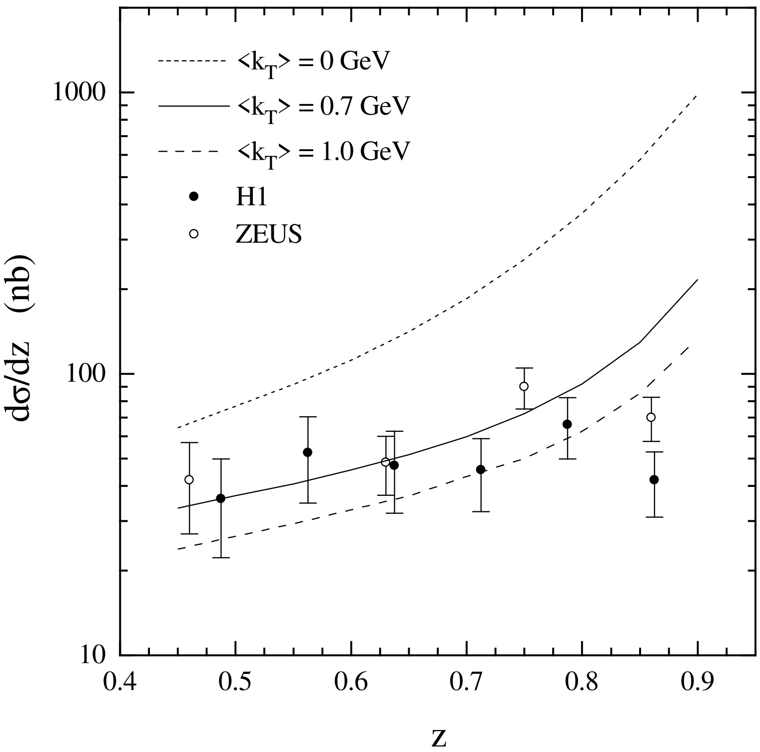

Figure 2.13: *Model predictions for three choices of the intrinsic transverse momentum distribution for the differential cross section* $\mathrm{d}\sigma/\mathrm{d}z$ *of* J/ψ *photoproduction [31].*

Very recently it was shown by Yuan and Chao that the k_T factorization approach by Hägler et al. [32], which also allows for intrinsic k_T of the partons inside a particle, could explain the CDF polarization measurement [33]. The transverse momentum spectrum of the J/ψ in the prediction is changed in such a way, that even at $p_t = 20\,\mathrm{GeV}$ gluon fragmentation could not be the dominant production process. The polarization effect should then only be visible at substantially higher transverse momenta.

2.4 Diffraction

For high values of the elasticity z ($z \gtrsim 0.95$) diffractive processes dominate the production of J/ψ mesons. Two processes are distinguished (fig. 2.14): elastic scattering $\gamma p \to J/\psi\, p$ where the proton stays intact, and proton dissociation $\gamma p \to J/\psi\, X$, where the proton breaks up. Diffraction is described only very briefly here because the main focus of the analysis lies on the inelastic production processes and diffractive processes enter only as a background.

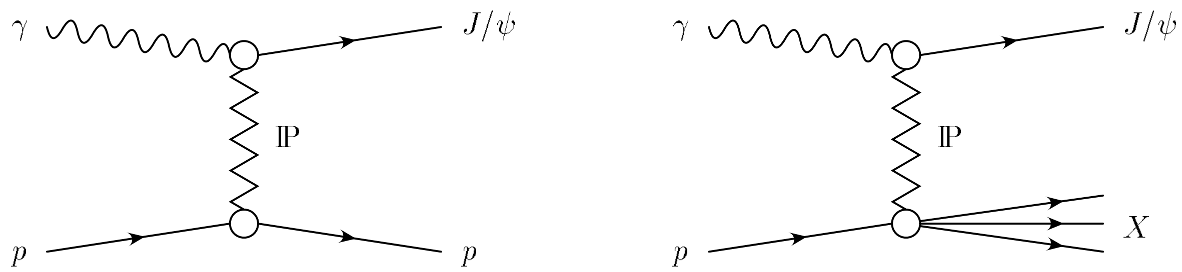

Figure 2.14: *Feynman diagrams for diffractive J/ψ photoproduction: a) elastic and b) proton dissociative diffraction.*

Diffraction can be described within different frameworks. In the Vector Meson Dominance Model (VDM) the photon fluctuates into a vector meson before the interaction with the proton takes place. The scattering of the vector meson and the proton is described within Regge theory via exchange of a pomeron $\mathbb{P}$, a colourless object with the quantum numbers of the vacuum. While Regge theory can reproduce the cross sections for light meson production such as ρ [34] and ϕ [35], the $W_{\gamma p}$ dependence of the J/ψ photoproduction cross section shows a much steeper behaviour than expected with a single universal pomeron behaviour [36].

Models based on perturbative QCD which predict a steeper rise should be applicable in the presence of a hard scale, like high values of Q^2 or a heavy mass of the vector meson. In pQCD based models the interaction between the photon and the proton factorises into three parts: the fluctuation of the photon into a $q\bar{q}$ pair, the interaction by exchange of a 'reggeized' gluon ladder (with the quantum numbers of the vacuum) and the formation of the vector meson.

Not only the diffractive production of J/ψ mesons but also of $\psi(2s)$ mesons is a significant background for inelastic J/ψ production. In the decay mode $\psi(2s) \to J/\psi\, \pi^+\, \pi^-$ the pions can lead to a lower reconstruction of z and therefore to the wrong assumption of an inelastic event. In addition to the elasticity z the transverse momentum squared of the J/ψ meson $p_{t,\psi}^2$ can be used to distinguish diffractive from inelastic processes because the cross section for diffraction falls much more steeply with $p_{t,\psi}^2$ than the inelastic cross section.

2.5 J/ψ Production at HERA: Open Problems

As explained in section 2.3.3, at the Tevatron contributions from intermediate $c\bar{c}$ pairs in colour octet states can explain the size of the J/ψ production cross section at the price of introducing several new free parameters [20]. Independent confirmation might come from J/ψ production in ep interactions. The colour octet terms which are most important at HERA correspond, however, to the low p_t region at the Tevatron where the extraction of the Colour Octet Matrix Elements is difficult.

At HERA several regions of the elasticity z are distinguished for the analysis of J/ψ production. The influence of colour octet contributions varies in these elasticity regions.

At high elasticities, $z \gtrsim 0.9$, the colour octet contributions to photon-gluon fusion are expected to be much larger than the cross section in the Colour Singlet Model. It is, however, experimentally very difficult, if not impossible, to distinguish the inelastic colour octet contributions from diffractive processes. This is made even more difficult by the fact that there is at present no model of the effect of the soft gluons which are emitted when the coloured $c\bar{c}$ pair evolves into an observable J/ψ state.

In the region of medium elasticities, $0.4 \lesssim z \lesssim 0.9$, the diffractive background is expected to be much smaller than at high z, especially with a restriction in the transverse momentum squared of the J/ψ meson. For the dominant production process, photon-gluon fusion, colour octet contributions were originally thought to exceed the colour singlet ones at $z \gtrsim 0.7$. Since this could not be confirmed experimentally, several ideas (see section 2.3.4) were developed which can explain the fact, that the colour octet contributions are small for $z \lesssim 0.9$. With increased statistics which is available now a more detailed search for colour octet signatures is possible. If they are confirmed to be very small it can be tried to restrict the gluon density in the proton via its influence on the cross sections in the Colour Singlet Model.

At low elasticities, $z \lesssim 0.4$, large contributions from processes with resolved photons to the inelastic J/ψ production are expected. Experimentally the problems are a small detector acceptance (see next chapter) and large non-resonant background originating from hadrons mis-identified as muons. It is impossible to include the decay mode $J/\psi \rightarrow e^+e^-$ because there are no efficient triggers for events with high track multiplicities and low-energy electrons. Up to now the statistics was too small to allow a definitive statement on contributions from processes with resolved photons. An analysis in this elasticity region therefore has the goal to establish the existence of contributions from resolved photoproduction and to measure the order of magnitude of the cross section. This is especially interesting because the Colour Octet Model predicts cross sections up to one order of magnitude larger than the Colour Singlet Model.

Chapter 3

Monte Carlo Simulation

The Monte Carlo simulation of physics processes is used to correct measured data for detector effects, to estimate contributions from background processes and to compare cross sections with different models. The simulation process is divided into three levels. On generator level the programs produce four-vectors of particles according to a given cross section. The decay of unstable particles and the interaction of particles with the detector is simulated in the second step (with the program package H1SIM [37] based on GEANT [38]), where the detector response and the trigger decision is also derived. The output is then processed by the same reconstruction software as the data.

For the analysis three Monte Carlo generators are used: EPJPSI for the simulation of J/ψ production via direct photon-gluon fusion and resolved photon processes, CASCADE, which includes the initial state parton evolution according to the CCFM equation, and DIFFVM for the determination of background originating from diffractive J/ψ and $\psi(2s)$ production. In this chapter, the generators are described and the effect of basic cuts on the J/ψ decay muons for different simulations is discussed. Then a study of the quality of the reconstruction of some kinematic variables is presented, as the elasticity z, the photon-proton centre-of-mass energy $W_{\gamma p}$ and the fractional gluon momentum of the proton x_g.

3.1 EPJPSI

EPJPSI [39] simulates the production of J/ψ mesons in high energy γp, ep, μp, $p\bar{p}$ and pp collisions. The relevant production mechanisms for the presented analysis are direct photon-gluon fusion, gluon-gluon fusion as the dominant process for resolved photons and production and decay of B and χ_c mesons. The simulation of direct photon-gluon fusion (EPJPSI-direct) and gluon-gluon fusion in processes with resolved photons (EPJPSI-resolved) is used to correct the data for detector effects and to calculate cross sections. They will be discussed in more detail.

In EPJPSI the interaction between an electron and proton is described via photon exchange in the equivalent photon approximation [7]. The parton density functions (PDF) for the proton and the photon can be chosen from the PDFLIB [40]. In this analysis MRS(A') [1] for the proton and GRV92 LO [41] for the photon are used as standard PDFs. The scale for the evaluation of the parton density functions can be chosen as m_ψ^2 (default, used for this analysis), $m_\psi^2 + p_{t,\psi}^2$ and the centre-of-mass energy squared $\hat{s}$ of the particles taking part in the hard interaction. The matrix elements of the production processes are calculated in leading order in α_s. The value of the strong coupling constant is fixed at $\alpha_s = 0.3$ in this analysis. Alternatively it can be calculated according to the one-loop formula $\alpha_s(\mu) = \frac{6\pi}{(33-2\cdot n_f)\cdot\ln(\mu/\Lambda)}$. For MRS(A') with $n_f = 4$ free flavours and $\Lambda = 231\,\mathrm{MeV}$ this would result in $\alpha_s = 0.29$ at a scale of $\mu = m_\psi$. Higher order QCD effects are taken into account using a parton shower approach with a backward evolution from the hard scattering process to the initiating parton according to the Altarelli–Parisi equations. The hadronisation is performed using the Lund string model by the JETSET package [42].

An overview over the predicted elasticity dependence of different inelastic J/ψ production mechanisms is shown in figure 3.1. The direct photon-gluon fusion dominates the J/ψ production in the region of medium to high elasticities. At low elasticities $z \lesssim 0.2$ gluon-

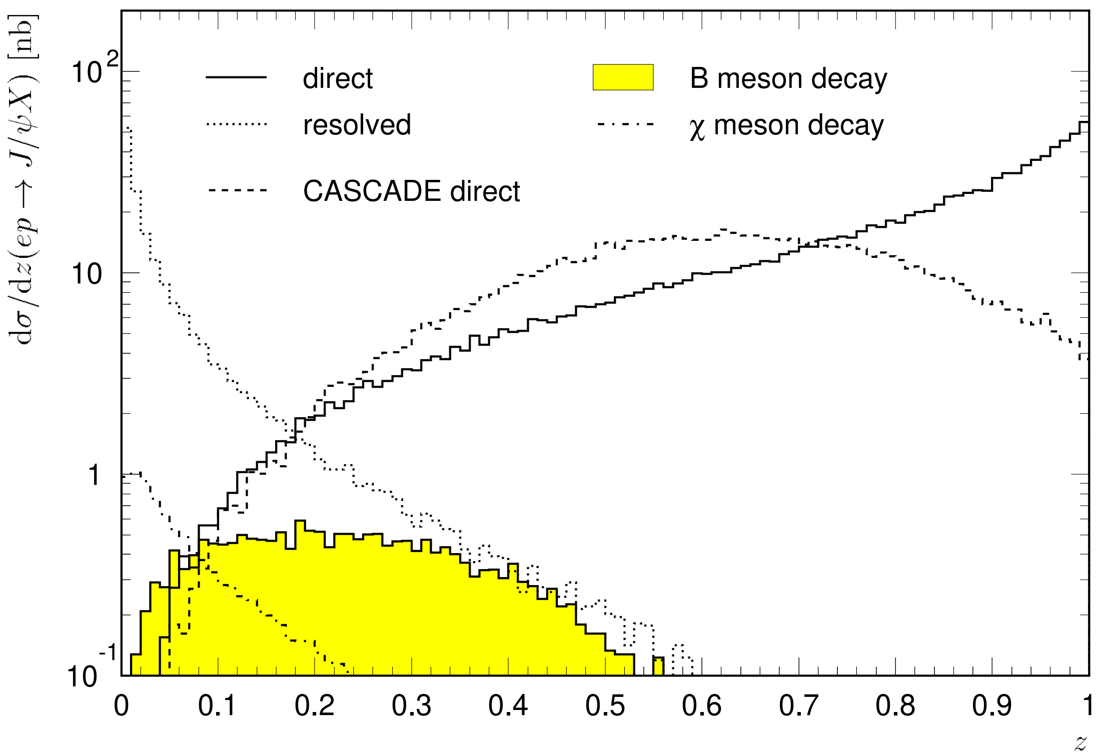

Figure 3.1: *The differential electron-proton cross section for different J/ψ production mechanisms as a function of the elasticity z in the photoproduction domain $Q^2 < 1\,\mathrm{GeV}^2$. The proton beam energy is $E_p = 820\,\mathrm{GeV}$. All histograms except the dashed one (CASCADE direct) are calculated with EPJPSI. The contribution from the decay of B-mesons is normalized to the cross section measured by H1 [43]. For the χ_c meson decay a cut $p_{t,\chi} > 1\,\mathrm{GeV}$ was applied.*

gluon fusion in resolved photon events is the most important process. The J/ψ production via the decay of χ_c mesons behaves similar as gluon-gluon fusion, but the cross section is predicted to be more than an order of magnitude smaller. The χ_c mesons are produced in resolved photon events via gluon-gluon fusion or in a quark-gluon reaction. The difference in the event topology between J/ψ mesons originating from χ_c decays and those formed in the gluon-gluon fusion process is the presence of an additional low-energy photon which is very difficult to identify in the detector. Therefore no distinction between these processes is made. In chapter 6 an estimate on the size of the χ_c contribution can be found. The J/ψ production via the decay of B mesons is considered as a source of resonant background to the low z analysis ($0.05 < z < 0.45$). The dominant process for B meson production is direct photon-gluon fusion. The J/ψ production cross section via decay of B mesons in figure 3.1 is normalized to the $b\bar{b}$ cross section measured by H1 [43]. The cross section calculated by EPJPSI in leading order is roughly a factor of 2 lower.

3.1.1 Direct Photon-Gluon Fusion (EPJPSI-direct)

The calculation of J/ψ production in direct photon-gluon fusion is performed according to [13] in the Colour Singlet Model. Relativistic corrections due to a relative motion of the quarks inside the J/ψ meson can be taken into account [44]. These corrections lead to a rise at high z (fig. 3.1) in contrast to the breakdown at $z = 1$ due to vanishing phase space predicted by [13]. In the region of the medium z analysis ($0.3 < z < 0.9$) direct photon-gluon fusion is expected to dominate inelastic J/ψ production. For lower elasticities resolved photoproduction becomes more important, but a significant contribution from the direct process remains down to $z \approx 0.1$.

The coupling of the J/ψ meson to the $c\bar{c}$ pair is determined from a leptonic decay width of $\Gamma_{l\bar{l}} = 5.4\,\mathrm{keV}$ including QCD corrections. The value of the charm mass, which has a strong influence on the normalization of the cross section, is $m_c = m_\psi/2$.

One of the goals of the analysis of inelastic J/ψ photoproduction is the determination of the gluon density in the proton. Therefore the influence of different gluon density functions on the generated cross sections is studied in figure 3.2. For the more recent parameterizations, GRV98 LO [45], CTEQ5L [46] and MRST LO [47], HERA measurements of the total inclusive structure function F_2 were used to restrict the gluon density. All gluon densities show a steeper rise than MRS(A') towards small fractional gluon momenta x_g inside the proton (fig. 3.2 a, at a scale $\mu^2 = m_\psi^2$). The shown region, $-3.1 < \log_{10}(x_g) < -1.9$, corresponds to events within the acceptance of the H1 detector. In the cross section as a function of the elasticity z the gluon density is reflected in the normalization, but the shape is very similar for all parton density functions (fig. 3.2 b). In $W_{\gamma p}$, not only the normalization, but also the shape is influenced by the proton PDF. This can be seen in figure 3.2 d), where the cross sections are normalized to 1 in the bin from 60 to 80 GeV. The steeper the gluon density the shallower is the decrease of the electron-proton cross section with $W_{\gamma p}$. If it is converted into a photon-proton cross section, the steepest gluon density corresponds to the steepest rise of the cross section with $W_{\gamma p}$. For the elasticity z (fig. 3.2 e) the influence of the proton PDF on the shape is very small, for the transverse

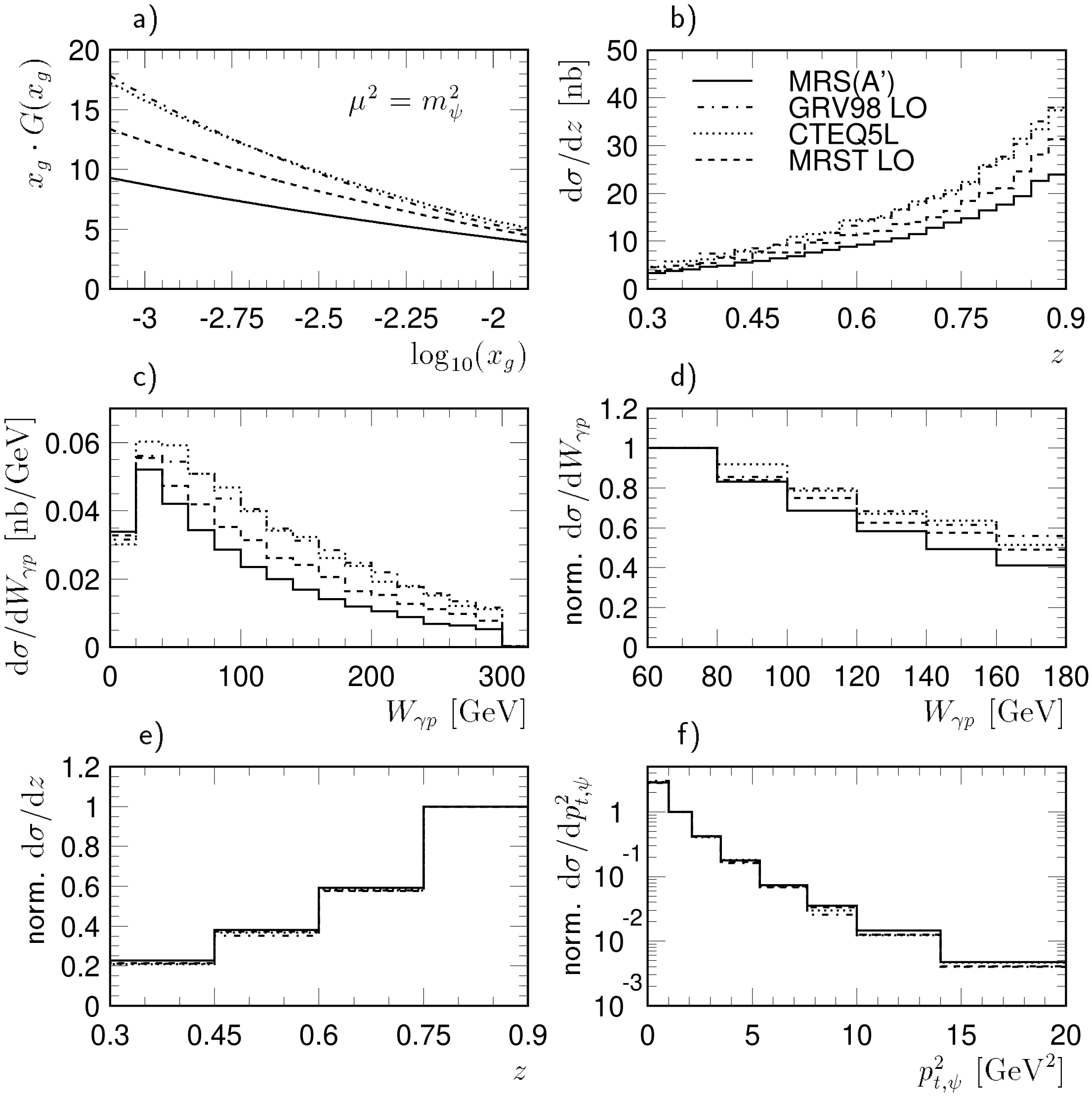

Figure 3.2: *a) Parameterizations of the gluon density in the* **proton**: *MRS(A') ('default', full line), GRV98 LO (dotted), CTEQ5L (dash–dotted) and MRST LO (dashed). EPJPSI predictions for the electron-proton cross section of direct photon-gluon fusion as functions of b) z and c) $W_{\gamma p}$ in the kinematic region $Q^2 < 1\,\mathrm{GeV}^2$ and $0.3 < z < 0.9$. The shapes of the cross sections are compared by normalizing them in one bin: d) $W_{\gamma p}$ between 60 and 80 GeV, e) z between 0.75 and 0.9 and f) $p_{t,\psi}^2$ between 1 and 2.125 GeV^2.*

momentum squared of the J/ψ meson $p_{t,\psi}^2$ (fig. 3.2 f) the influence is smaller than for $W_{\gamma p}$ but not negligible.

Figure 3.3 shows the correlation of the elasticity z and the polar angle ϑ_μ of the J/ψ decay muons with the photon-proton centre-of-mass energy $W_{\gamma p}$. The J/ψ mesons originating from direct photon-gluon fusion are predominantly produced at high z and small $W_{\gamma p}$ (fig. 3.3 a). Towards lower z and higher $W_{\gamma p}$ the number of J/ψ decreases significantly. Since $W_{\gamma p}$ and ϑ_μ are strongly correlated (fig. 3.3 b), the polar angular acceptance of the H1 detector ($20° < \vartheta_\mu < 160°$) restricts the accessible $W_{\gamma p}$ region.

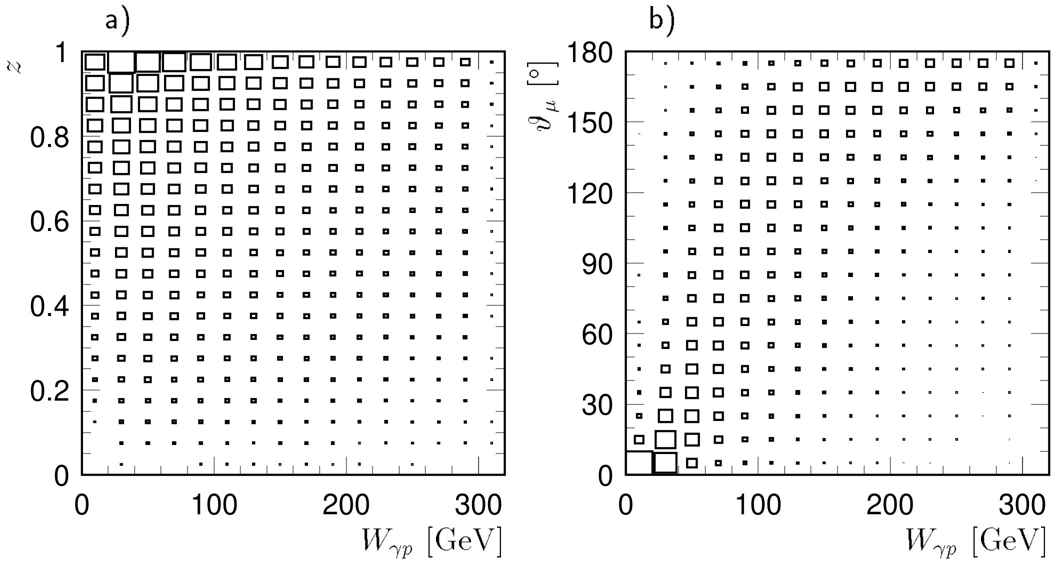

Figure 3.3: *Correlation a) between the photon-proton centre-of-mass energy $W_{\gamma p}$ and the elasticity z and b) between $W_{\gamma p}$ and the polar angle ϑ_μ of the decay muons for direct photon-gluon fusion in photoproduction generated with EPJPSI.*

The restriction of the polar angle of the decay muons to $20° < \vartheta_\mu < 160°$ is necessary to ensure a good momentum resolution of the measurement in the tracking chambers. In the medium z analysis the momentum of the muons has to fulfil $p_\mu > 1.1\,\mathrm{GeV}$ to reduce the background from hadrons mis-identified as muons. The influence of these requirements on several observables is studied in figure 3.4.

Since most of the decay muons are produced in the forward or backward directions, the restriction to the central region has a large impact on other quantities. It affects muons with high momenta and rejects nearly all events below $W_{\gamma p} = 40\,\mathrm{GeV}$ and above $W_{\gamma p} = 200\,\mathrm{GeV}$. The momentum of the muons peaks at around half the J/ψ mass with a long tail towards higher values. In the J/ψ rest system both muons have $p^*_\mu \approx m_\psi/2$, which is smeared out by the boost to the laboratory frame. The momentum requirement rejects up to 25% of the central muons. This behaviour is reflected in $W_{\gamma p}$, where primarily events at intermediate values are rejected. Neither of the muon requirements, however, change the shape of the elasticity distribution.

Since a significant direct photon-gluon fusion contribution is expected at small elasticities, the influence of the restrictions used in the low z analysis, $20° < \vartheta_\mu < 140°$ and $p_\mu > 0.8\,\mathrm{GeV}$, is studied for $z < 0.45$ (fig. 3.5). The generated polar angle and momentum distributions of the decay muons and the $W_{\gamma p}$ distribution are similar to the medium z range (fig. 3.4). The elasticity shows a steeper rise at very low values ($z < 0.15$). The reduced upper limit on ϑ_μ increases the impact of the polar angle restriction, while the softened cut on the momentum has less impact. The $W_{\gamma p}$ distribution after both restrictions is shifted about 20 GeV towards higher values compared to the medium z region.

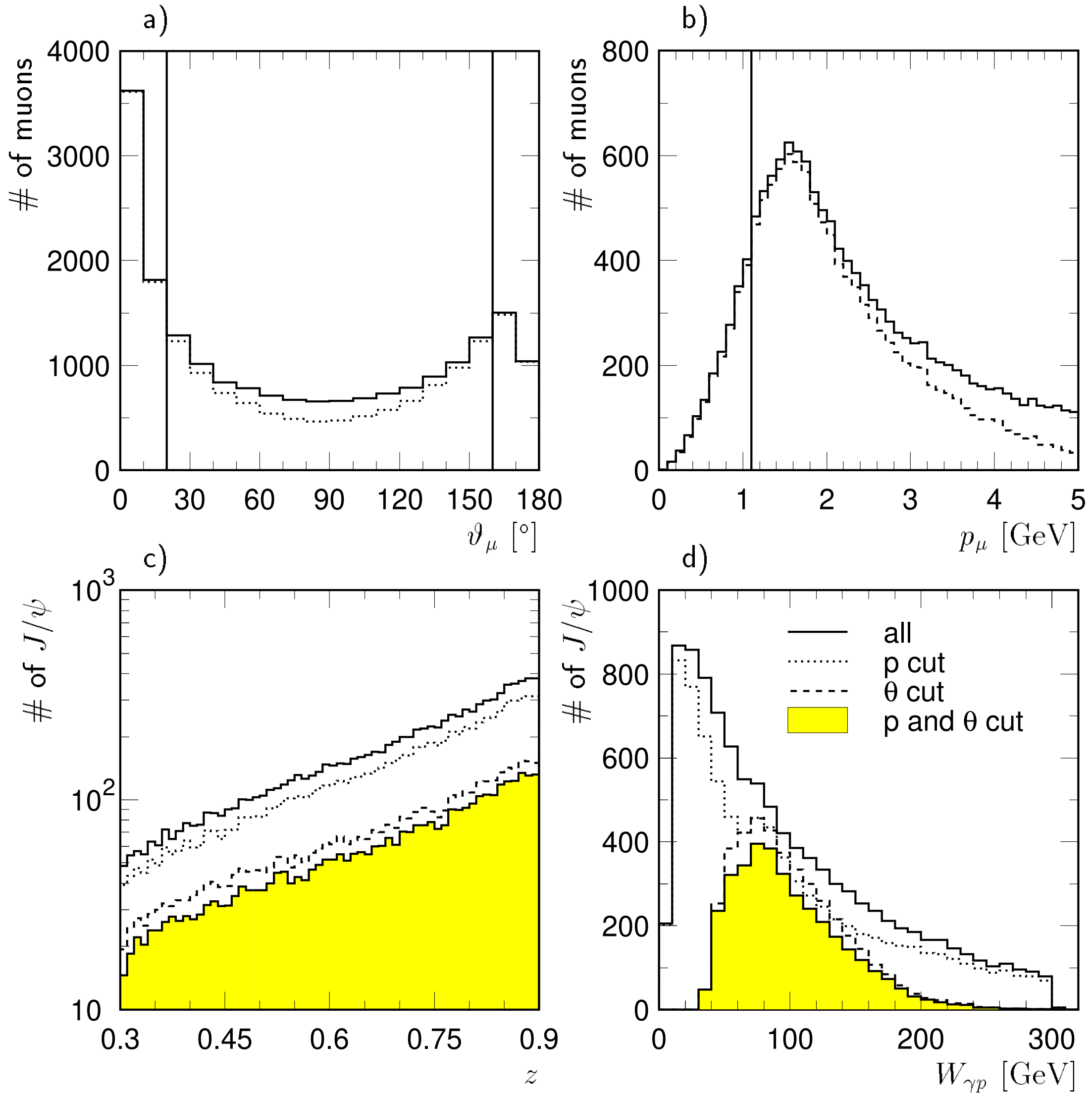

Figure 3.4: *Influence of the restrictions* $p_\mu > 1.1\,\mathrm{GeV}$ *(dotted line),* $20° < \vartheta_\mu < 160°$ *(dashed line) and the logical AND of both (shaded histogram) on a) the polar angle* ϑ_μ*, b) the momentum* p_μ *of the decay muons, c) the elasticity* z *and d)* $W_{\gamma p}$*. The kinematic range is* $Q^2 < 1\,\mathrm{GeV}^2$ *and* $\mathbf{0.3 < z < 0.9}$*. The distributions correspond to 10000 events generated with EPJPSI in direct photon-gluon fusion.*

3.1.2 Resolved Photoproduction (EPJPSI-resolved)

The resolved photoproduction of J/ψ mesons is dominated by gluon-gluon fusion via the subprocesses $gg \to J/\psi\, g$ and $gg \to J/\psi\, \gamma$. The cross section of the second subprocess is about a factor 5 lower than the cross section of $gg \to J/\psi\, g$. Both cross sections are calculated in the Colour Singlet Model. Since the gluon has the same quantum numbers as the photon except for the colour, the matrix elements differ from direct photon-gluon fusion only by colour factors and coupling constants. In addition the parton density of the photon is taken into account.

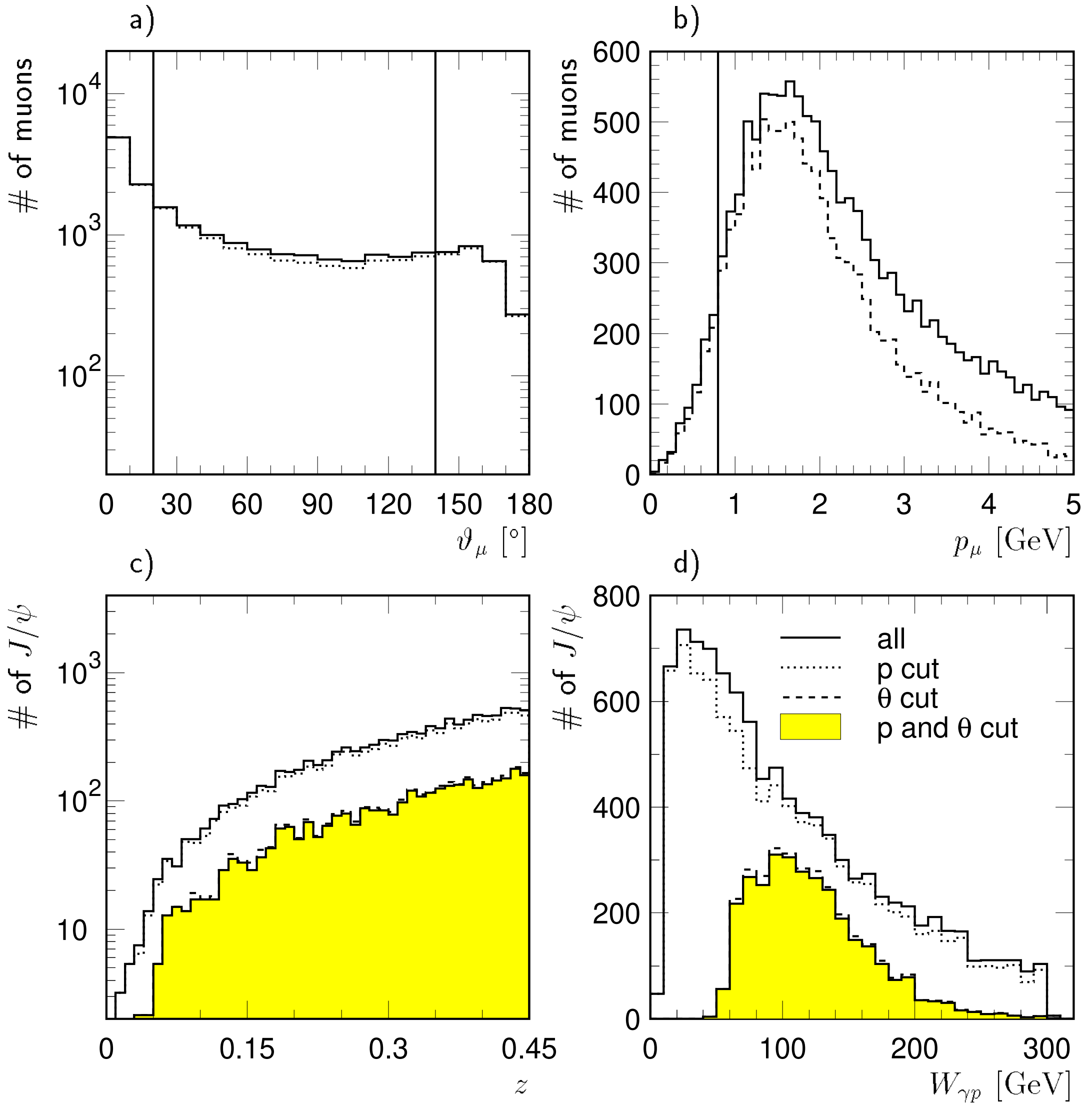

Figure 3.5: *Influence of the restrictions $p_\mu > 0.8\,\mathrm{GeV}$ (dotted line), $20° < \vartheta_\mu < 140°$ (dashed line) and the logical AND of both (shaded histogram) on a) the polar angle ϑ_μ, b) the momentum p_μ of the decay muons, c) the elasticity z and d) $W_{\gamma p}$. The kinematic region is $Q^2 < 1\,\mathrm{GeV}^2$ and* $\boldsymbol{z < 0.45}$. *The distributions correspond to 10000 events generated with EPJPSI in direct photon-gluon fusion.*

The knowledge of the gluon density in the photon is less accurate than that of the proton. The influence of different parameterizations of the gluon density in the photon on the electron-proton cross section of gluon-gluon fusion with resolved photons is studied in figure 3.6. Nearly all gluon densities show a shallower rise towards small x_γ than GRV92 LO which is used in the analysis. GAL [48] and SAS1D [49] are compared to GRV92 LO here. As an example of a function which rises more steeply LAC1 [50] is shown, which is already ruled out by measurements. The shown x_γ range, $\log_{10}(x_\gamma) > -2$, corresponds to the values accessible via resolved photoproduction of J/ψ mesons. LAC1 leads to a different z dependence, all other cross sections differ mainly in the normalization. In the analysis the region below $z = 0.05$ is excluded, which reduces the differences even further.

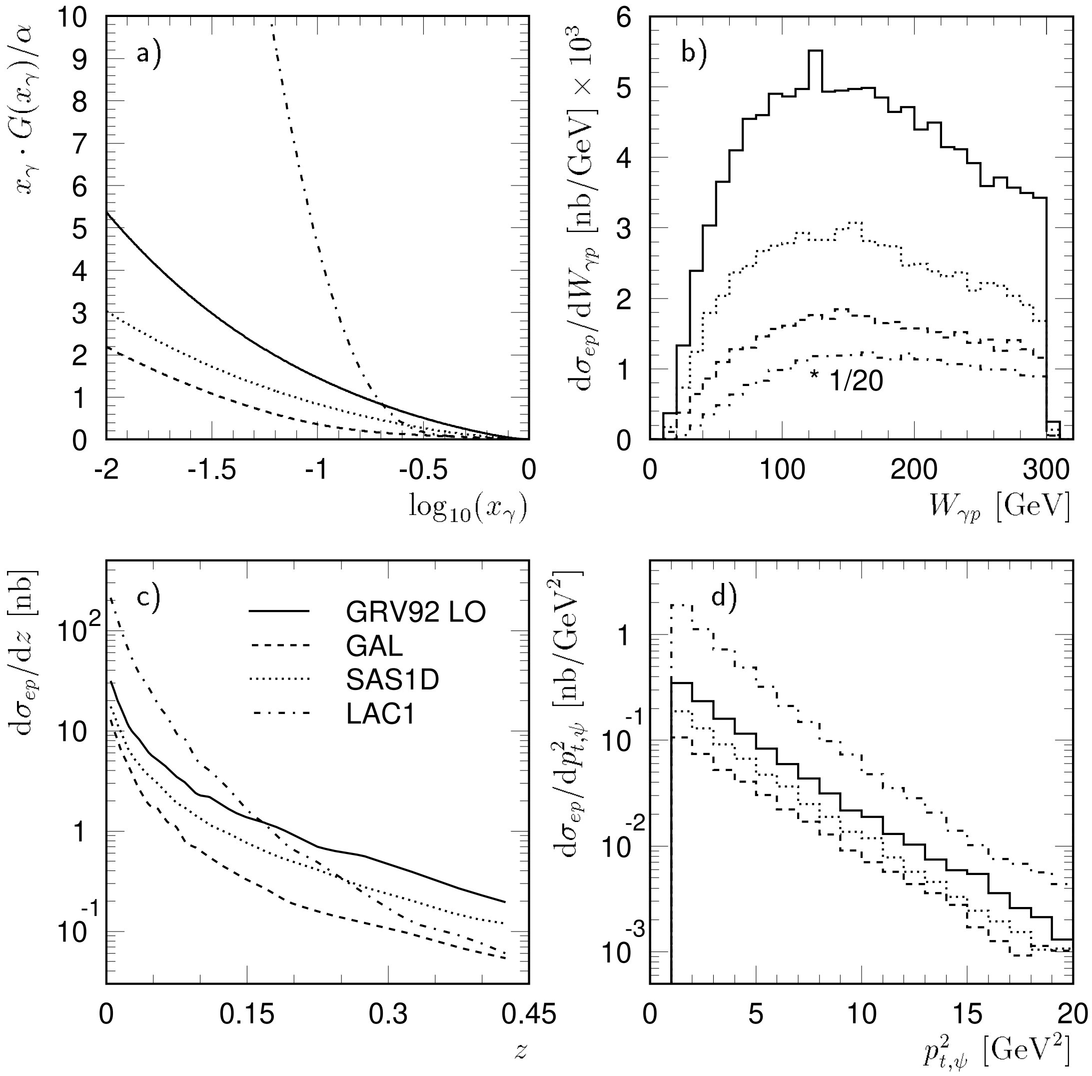

Figure 3.6: *a) Parameterizations of the gluon density in the* **photon**. *Predictions of EPJPSI for the electron-proton cross section of gluon-gluon fusion with resolved photons as functions of b) $W_{\gamma p}$, c) z and d) $p^2_{t,\psi}$ in the kinematic region $Q^2 < 1\,\mathrm{GeV}^2$, $z < 0.45$ and $p^2_{t,\psi} > 1\mathrm{GeV}^2$. The 'standard' GRV92 LO (full line) is compared to GAL (dashed) and SAS1D (dotted). LAC1 (dash–dotted) is already ruled out, but used as an example for a steeper rise towards small x_γ.*

In processes with resolved photons J/ψ mesons can also be produced via the decay of χ_c mesons. In this case gluon-gluon fusion is again the dominating subprocess, but significant contributions from a quark on the proton side and a gluon on the photon side and vice versa are expected. Since the total contribution of χ_c decays to J/ψ production in resolved photon processes is small, the gluon-gluon fusion simulation is used to correct the data. Here only the differences between the two production mechanisms are studied.

In figure 3.7 the distributions of the elasticity z, the photon-proton centre-of-mass energy $W_{\gamma p}$, the the transverse momentum squared of the J/ψ meson $p^2_{t,\psi}$ and the polar angle ϑ_μ

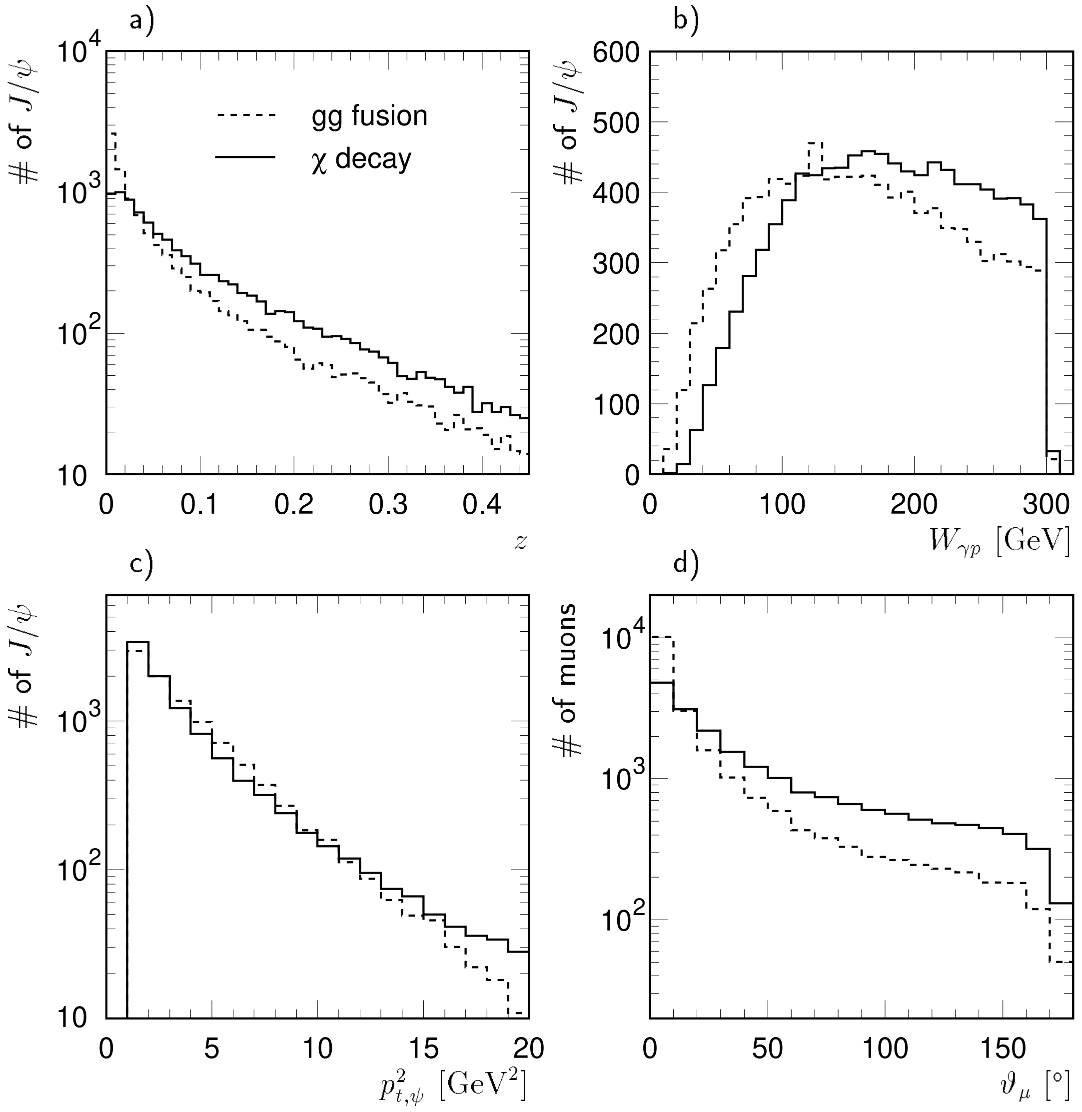

Figure 3.7: *Comparison between J/ψ mesons produced in resolved photon processes by gluon-gluon fusion (dashed line) and by decay of χ_c mesons (full line) for $p^2_{t,\psi} > 1\,\mathrm{GeV}^2$. a) elasticity z, b) $W_{\gamma p}$, c) $p^2_{t,\psi}$ and d) polar angle ϑ_μ of the decay muons.*

of the decay muons are shown. Since a cut $p^2_{t,\chi} > 1\,\mathrm{GeV}^2$ on the transverse momentum of the χ_c meson is applied in EPJPSI, $p^2_{t,\psi} > 1\,\mathrm{GeV}^2$ is required in both processes for consistency. The peak at very low elasticities is less pronounced in χ_c decays than it is for gluon-gluon fusion. Above $z = 0.1$ the shapes are very similar. The higher mean $W_{\gamma p}$ reflects the higher mass of the χ_c mesons which has to be produced. The $p^2_{t,\psi}$ distribution shows only small differences at high values. In χ_c decays the decay muons of the J/ψ mesons are not as strongly peaked in the forward direction as in gluon-gluon fusion. This leads to a different acceptance of the cut on ϑ_μ for the two processes.

With the present statistics, where the aim is to establish that J/ψ mesons are produced in resolved photoproduction processes and to measure the order of magnitude of the cross section, all these differences are not so important. For a more precise measurement the size of the contribution from χ_c decays has to be known. Since the ϑ_μ distribution differs mainly in the region outside of the detector acceptance, it cannot be used to distinguish the processes. An identification of the low-energy photon will be needed to reconstruct the χ_c mesons.

Processes with resolved photons differ from direct photon-gluon fusion not only in the elasticity. While direct photon-gluon fusion occurs predominantly at high elasticities and small $W_{\gamma p}$, gluon-gluon fusion events have very low z at medium to high $W_{\gamma p}$ (fig. 3.8 a). The correlation between $W_{\gamma p}$ and the polar angle of the decay muons is much smaller in gluon-gluon fusion, nearly all muons lie in the very forward region (fig. 3.8 b).

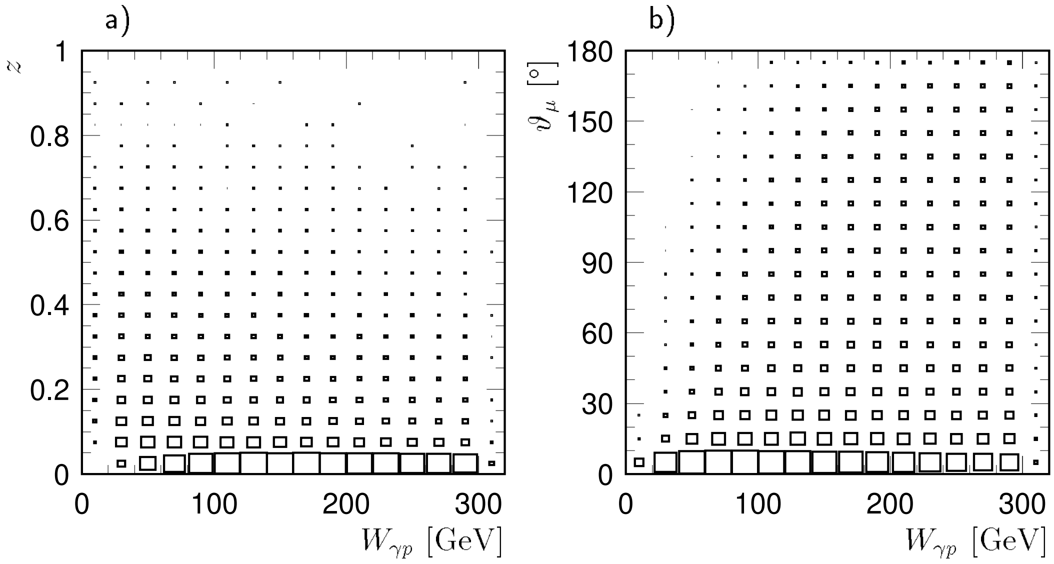

Figure 3.8: *Correlation a) between $W_{\gamma p}$ and the elasticity z and b) between $W_{\gamma p}$ and the polar angle ϑ_μ of the decay muons for gluon-gluon fusion in resolved photoproduction generated with EPJPSI.*

Since a two component simulation consisting of gluon-gluon fusion and direct photon-gluon fusion is used to correct the data in the low z analysis, the influence of the muon requirements, $20° < \vartheta_\mu < 140°$ and $p_\mu > 0.8\,\mathrm{GeV}$, on J/ψ mesons produced via gluon-gluon fusion is studied in figure 3.9. In contrast to the direct photon-gluon fusion simulation in the same elasticity region (fig. 3.5), the polar angular distribution of the decay muons is peaked much stronger in the forward region outside of the detector acceptance. The muon momentum is higher on average, but since the cut of 0.8 GeV is rather low the effect of the cut is small for both production mechanisms. The events at very small elasticities $z < 0.02$, where the cross section is highest, are nearly all rejected by the ϑ_μ cut. For the direct process this region contributes only very little to the total cross section. The generated $W_{\gamma p}$ distribution in resolved photoproduction is not peaked at around 30 GeV, as in the direct process, but has a very broad maximum around 120 GeV. In resolved processes a higher value of $W_{\gamma p}$ is needed on average, because only a part of the photon momentum enters the production of the J/ψ meson. The effect of the cut on the polar angle of the decay muons is rather different from the direct photon-gluon fusion case.

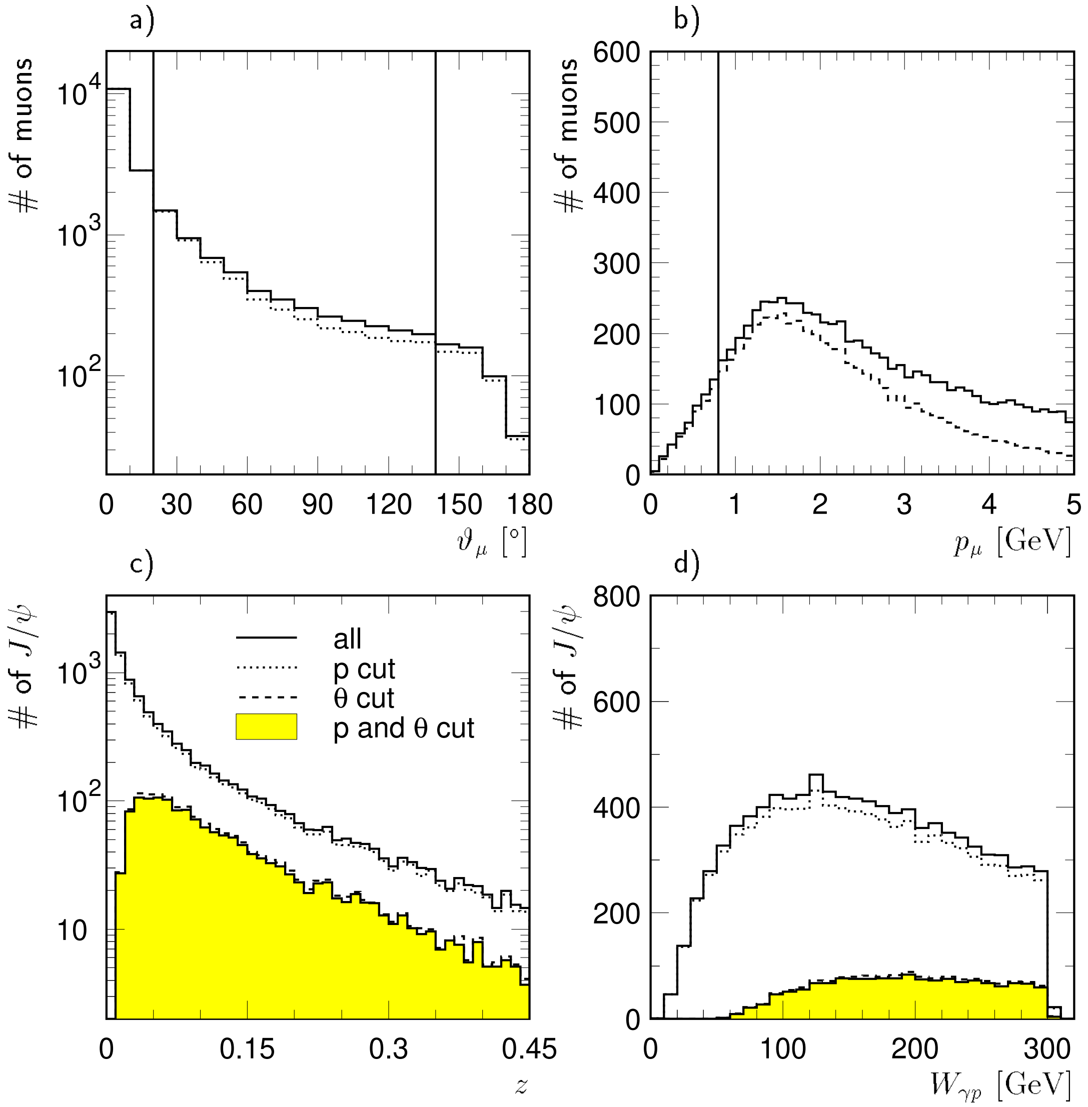

Figure 3.9: *Same as figure 3.5, but for 10000 events generated with EPJPSI via gluon-gluon fusion in resolved photoproduction. The kinematic region is* $Q^2 < 1\,\mathrm{GeV}^2$ *and* $\boldsymbol{z < 0.45}$.

While the $W_{\gamma p}$ region from 60 to 200 GeV shows a significant number of events passing this cut for direct photon-gluon fusion, in the resolved process this region starts at around 100 GeV and goes up to the kinematic limit.

3.2 CASCADE

The Monte Carlo generator CASCADE [51] simulates photoproduction of heavy quarks and deep inelastic scattering processes. The direct photoproduction of J/ψ mesons is implemented using the Colour Singlet Model in leading order. There are two conceptual differences with respect to EPJPSI: The matrix elements for the hard scattering process allow for a non-zero gluon virtuality on the proton side ('off-shell' gluon), and the evolution of the initial state parton shower is performed according to the Ciafaloni–Catani–Fiorani–Marchesini (CCFM) equation. For large momentum fractions of the gluon inside the proton the standard Altarelli–Parisi equations are recovered, while for small fractions the CCFM equation is equivalent to the Balitskii–Fadin–Kuraev–Lipatov (BFKL) evolution equation. In an initial state gluon cascade evolving according to the CCFM equation the gluons are ordered according to their angle with respect to the incoming proton. In the case of the Altarelli–Parisi equations the ordering is according to the transverse momentum of the gluons, for the BFKL evolution according to their fractional momentum.

Since the gluon inside the proton can have a transverse momentum relative to the proton, an unintegrated (or k_t dependent) gluon density is implemented in CASCADE. The free parameters are fixed by a comparison with the inclusive structure function F_2. Predictions for processes which are sensitive to the region of small gluon momentum fractions, such as the forward jet production at HERA, show reasonable agreement with the measurement [51].

Since CASCADE uses off-shell matrix elements for hard scattering processes, the relativistic corrections to the J/ψ cross section as implemented in EPJPSI cannot be applied. At present no calculation for the corrections to the off-shell matrix elements is available.

Despite the difference between CASCADE and EPJPSI at high elasticities, which is due to relativistic corrections, the correlation between $W_{\gamma p}$ and z is similar (fig. 3.10 in comparison to fig 3.3 a). A similar behaviour as in EPJPSI is also seen in the correlation between $W_{\gamma p}$ and the polar angle ϑ_μ of the decay muons (fig. 3.10 b). Forward muons correspond to small, backward muons to large values of $W_{\gamma p}$.

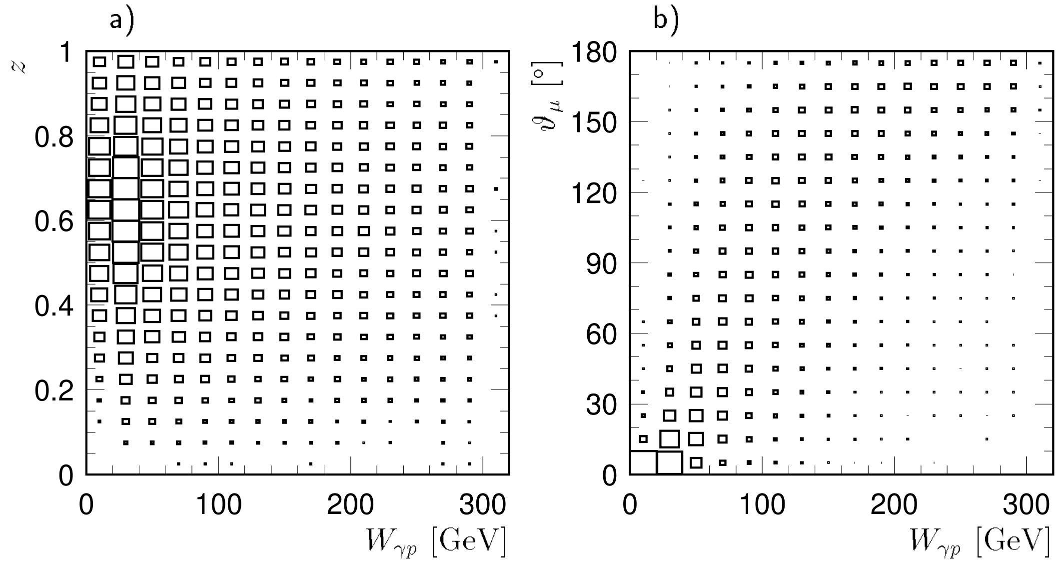

Figure 3.10: *Correlation a) between $W_{\gamma p}$ and the elasticity z and b) between $W_{\gamma p}$ and the polar angle ϑ_μ of the decay muons for direct photon-gluon fusion in photoproduction generated with CASCADE.*

Further differences between EPJPSI and CASCADE can be seen in the $W_{\gamma p}$ and the $p_{t,\psi}^2$ distributions (fig. 3.11). The peak at low photon-proton centre-of-mass energies is even more pronounced in CASCADE than in EPJPSI. The steeper fall-off towards higher $W_{\gamma p}$ has its origin in a shallower rise of the photon-proton cross section. The $p_{t,\psi}^2$ behaviour of CASCADE is harder than that of EPJPSI and resembles the prediction of the next-to-leading order calculation [15].

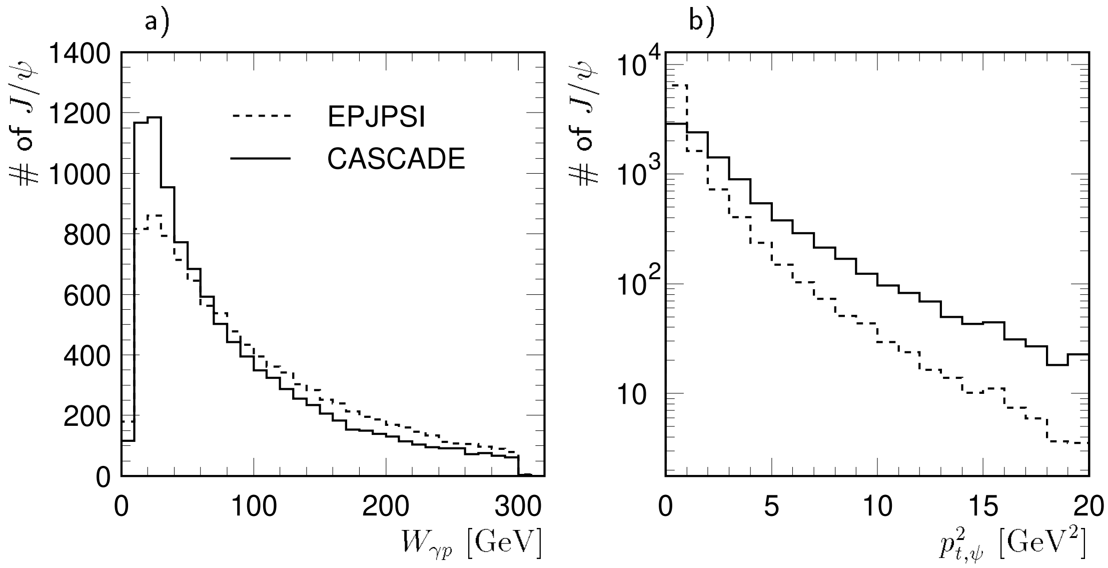

Figure 3.11: *Comparison of a) $W_{\gamma p}$ and b) $p_{t,\psi}^2$ between direct photon-gluon fusion simulated by EPJPSI (dashed line) and CASCADE (full line). The distributions correspond to 10000 events.*

3.3 DIFFVM

The generator DIFFVM [52] describes diffractive vector meson production in ep collisions. It is based on Regge theory and the Vector Meson Dominance Model. Both elastic scattering and proton dissociation can be simulated. DIFFVM is used to check the simulation of the muon identification in the LAr calorimeter and the instrumented iron. For the medium z analysis the background from diffractive J/ψ and $\psi(2s)$ production is estimated with the help of DIFFVM. The slope parameter b, which describes the exponential decrease of the cross section with the four-momentum transfer at the proton vertex, is set to $4.80\,\mathrm{GeV}^{-2}$ for the elastic and $1.60\,\mathrm{GeV}^{-2}$ for the proton dissociative process. For the photon-proton cross section of J/ψ production a value of 61.0 nb at $W_{\gamma p} = 95.0\,\mathrm{GeV}$ is used with a behaviour proportional to $W_{\gamma p}^{0.96}$. The $\psi(2s)$ cross section was assumed to be 15% of the J/ψ cross section in agreement with an earlier H1 measurement [53]. All values have been confirmed by a newer, larger statistics measurement [54].

3.4 Reconstruction of Kinematic Variables

For the reconstruction of the kinematics the Jacquet–Blondel method [55] is used. Neglecting the proton mass, y can be calculated from the electron beam energy E_e and the energies E and longitudinal momenta p_z of the hadronic final-state particles according to

$$y_{JB} = \frac{1}{2E_e} \sum_{had} (E - p_z) \ . \tag{3.1}$$

Since $(E - p_z)$ is small for particles at small polar angles, this reconstruction method is rather insensitive to particle losses through the beampipe in the forward direction of the detector. On the other hand a scattered electron in the backward part of the detector wrongly included in the hadronic final state spoils the result completely.

Using y_{JB} and neglecting electron and proton mass, the photon-proton centre-of-mass energy $W_{\gamma p}$, the elasticity z and the fractional gluon momentum inside the proton x_g can be calculated as

$$\begin{aligned}
W_{\gamma p} &= \sqrt{y_{JB}\, s - Q^2} \ \approx \ \sqrt{y_{JB}\, s}\ , && (3.2)\\
z &= \frac{y_\psi}{y_{JB}} && (3.3)\\
\text{with} \quad y_\psi &= \frac{1}{2E_e} \sum_{J/\psi} (E - p_z) && (3.4)\\
\text{and} \quad x_g &= \frac{1}{y_{JB}\, s} \left(\frac{\left(p^*_{t,\psi}\right)^2}{z\,(1-z)} + \frac{m_\psi^2}{z} + Q^2 \right) \approx \frac{1}{y_{JB}\, s} \left(\frac{p^2_{t,\psi}}{z\,(1-z)} + \frac{m_\psi^2}{z} \right) . && (3.5)
\end{aligned}$$

The second parts of equations 3.2 and 3.5 are valid only for photoproduction. For the reconstruction of y_ψ the decay muons of the J/ψ meson are used. $p^*_{t,\psi}$ is the transverse momentum squared of the J/ψ meson in the photon-gluon centre-of-mass system. In photoproduction it can be approximated by the transverse momentum squared in the laboratory frame since the photon is nearly co-linear with the electron and the gluon with the proton. Formula 3.5 is valid for x_g only in leading order.

For the determination of y_{JB} the momenta of all hadronic final-state particles have to be known. For charged particles the measurement in the tracking chambers is usually more accurate than the one in the calorimeter, while neutral particles are only detected in the calorimeters. Therefore both detectors are used, and to avoid double counting the regions in the calorimeter behind tracks are excluded from the summing. For resolved photon processes the contributions from the photon remnant in the backward calorimeter SpaCal are needed for a good reconstruction of y_{JB}. Special care has to be taken to exclude the scattered electron. This has been studied in a previous analysis [56], and the same method is adopted here. The innermost cells of the electromagnetic and the hadronic part of the SpaCal are excluded from the summation in order to avoid contributions from scattered electrons with showers only partially contained in the SpaCal.

In order to study the reconstruction of $W_{\gamma p}$, z and x_g, EPJPSI-direct and EPJPSI-resolved are used. Only events passing all selection requirements (see chapter 4) are included.

Since these cuts are different in the two analysis regions, a comparison of reconstructed and generated values is performed for each z range separately.

Medium z

In figure 3.12 the reconstruction of the elasticity z in the medium z analysis range is studied. The difference between the reconstructed and the generated value in the analysis bins is shown in figures a) – d). The standard deviation is nearly independent of the z bin. The reconstructed mean value is about 0.02 too high at low elasticities and about 0.03 too low at high z (fig. e). The comparison of the relative values (fig. f) shows that the constant absolute resolution leads to a worse relative resolution at low z than at high z. The size of the z bins is chosen to be of the order of the resolution, more precisely the bin size is chosen so that more than half of the events reconstructed in a bin are also generated there. Considering the statistics available for this analysis a smaller bin size would be preferable.

The difference between the reconstructed and the generated value of $W_{\gamma p}$ is shown in figure 3.13 a) – f). The standard deviation increases from 5.5 GeV at low $W_{\gamma p}$ to 8.3 GeV at high $W_{\gamma p}$. For the relative differences a decrease is observed. In all but the last bin $W_{\gamma p}$ is reconstructed on average about 2 GeV too high. The bin size of 20 GeV lies well above the resolution.

Figure 3.14 a) – f) shows the difference between the reconstructed and the generated value of $\log_{10}(x_g)$. The standard deviation increases slightly from the lowest to the highest analysis bin. At low x_g the reconstructed values are on average too high, at high x_g too low. The bin size of 0.2 in $\log_{10}(x_g)$ is of the order of the resolution. Due to the fact that $\log_{10}(x_g)$ is negative, the relative differences as a function of $\log_{10}(x_{gen})$ show an inverse behaviour compared to the absolute differences.

Low z

In the region of the low z analysis the resolution in z is better than in the medium z range (fig. 3.15). The standard deviation increases from 0.02 to 0.04. The bin sizes are well above the resolution, they were chosen to 'see' a J/ψ signal above background in each bin. The fact that the shift of the mean value is below 0.02 (or 5%) in all bins shows the good quality of the reconstruction. Since small values have to be reconstructed the relative differences are biggest in the lowest z bin.

Figure 3.16 shows that the $W_{\gamma p}$ reconstruction becomes more difficult at large $W_{\gamma p}$. Both the relative and the absolute differences between reconstructed and generated values increase. With the statistics available for this analysis the resolution is no problem, because the highest $W_{\gamma p}$ bin has to be large to find a J/ψ signal. The mean is shifted 4% at most, to higher values at low $W_{\gamma p}$ and to lower values at high $W_{\gamma p}$.

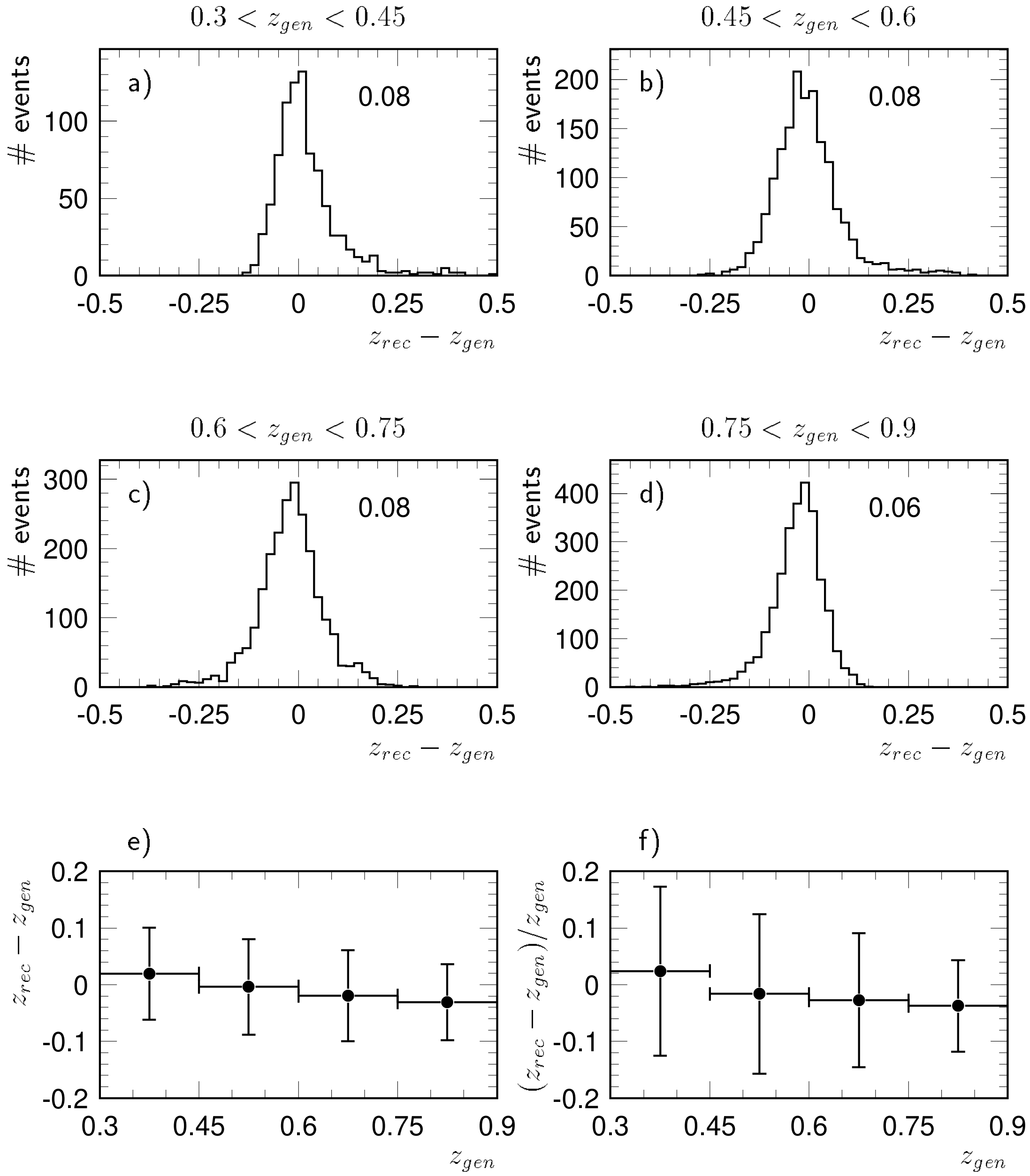

Figure 3.12: *Resolution of z in the region of the* **medium** *z analysis. a) – d) Difference between the reconstructed z_{rec} and the generated z_{gen} value in the analysis bins. The numbers indicated in the plots are the standard deviations of the distributions. e) Means and standard deviations of the distributions above as a function of z_{gen}. f) Same as e) but for the relative difference.*

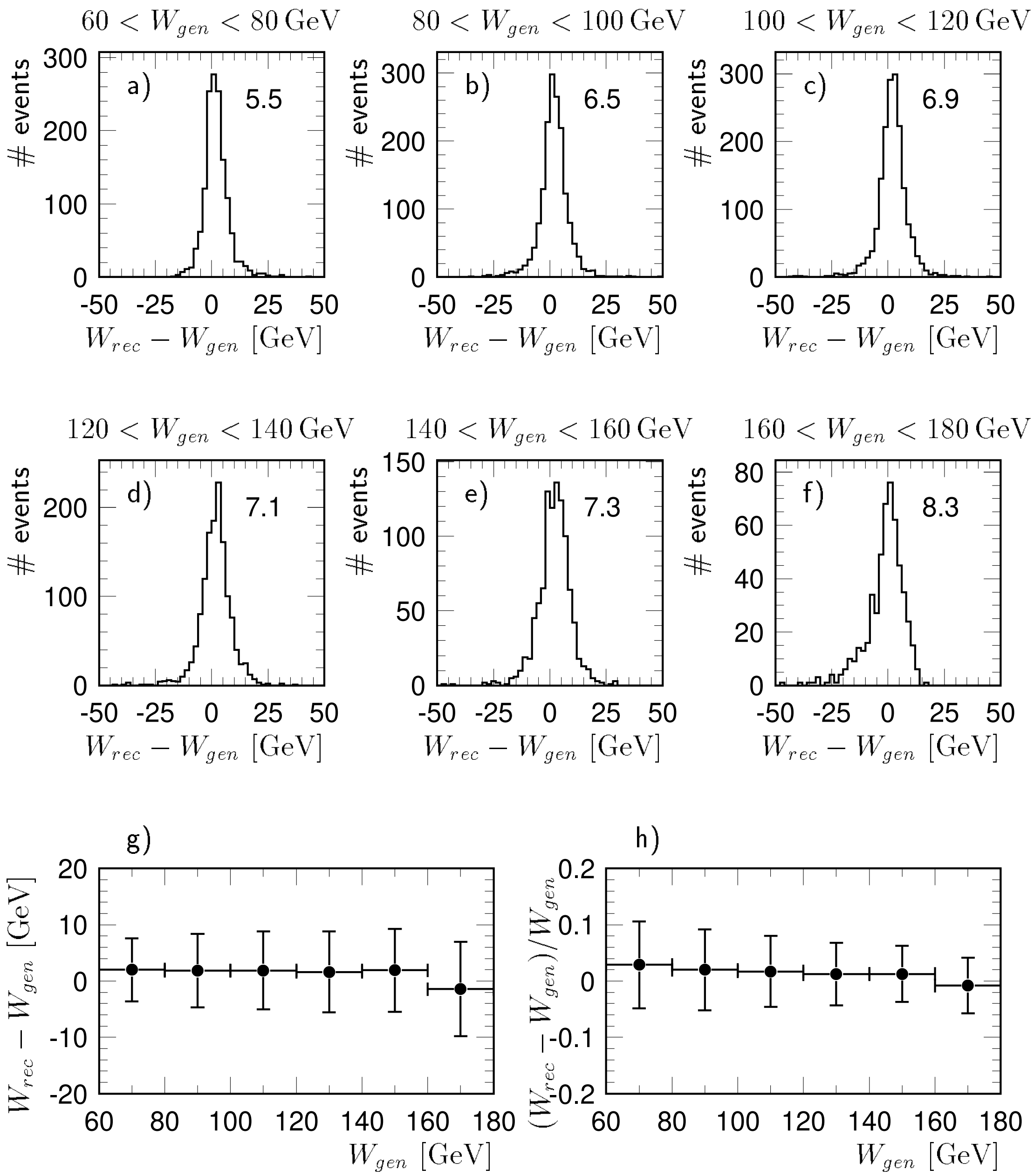

Figure 3.13: *Resolution of $W_{\gamma p}$ in the region of the* **medium** *z analysis. Explanations see figure 3.12.*

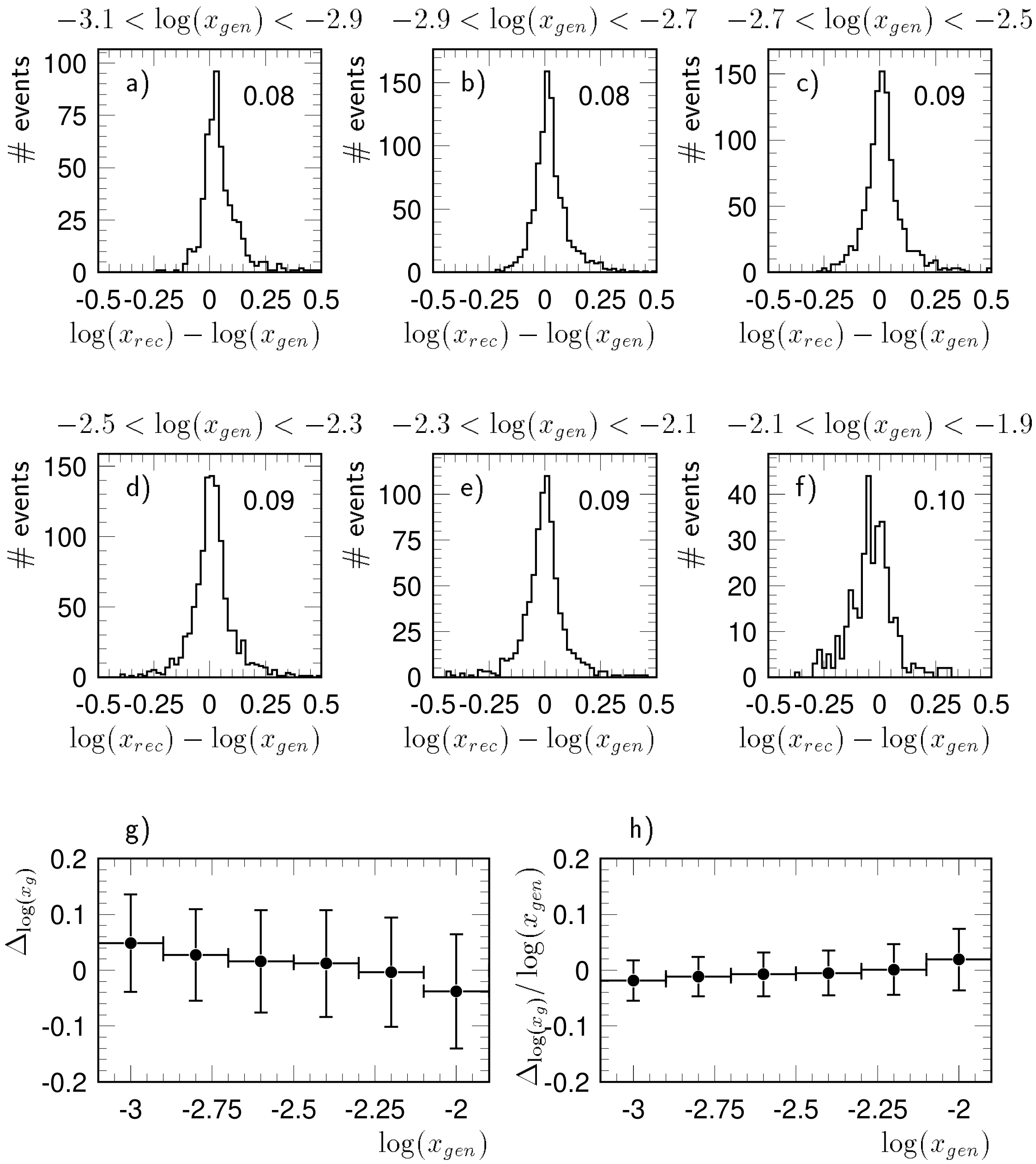

Figure 3.14: *Resolution of* $\log_{10}(x_g)$ *in the region of the* **medium** z *analysis. The abbreviation* $\Delta_{\log(x_g)} = \log_{10}(x_{rec}) - \log_{10}(x_{gen})$ *is used. Explanations see figure 3.12.*

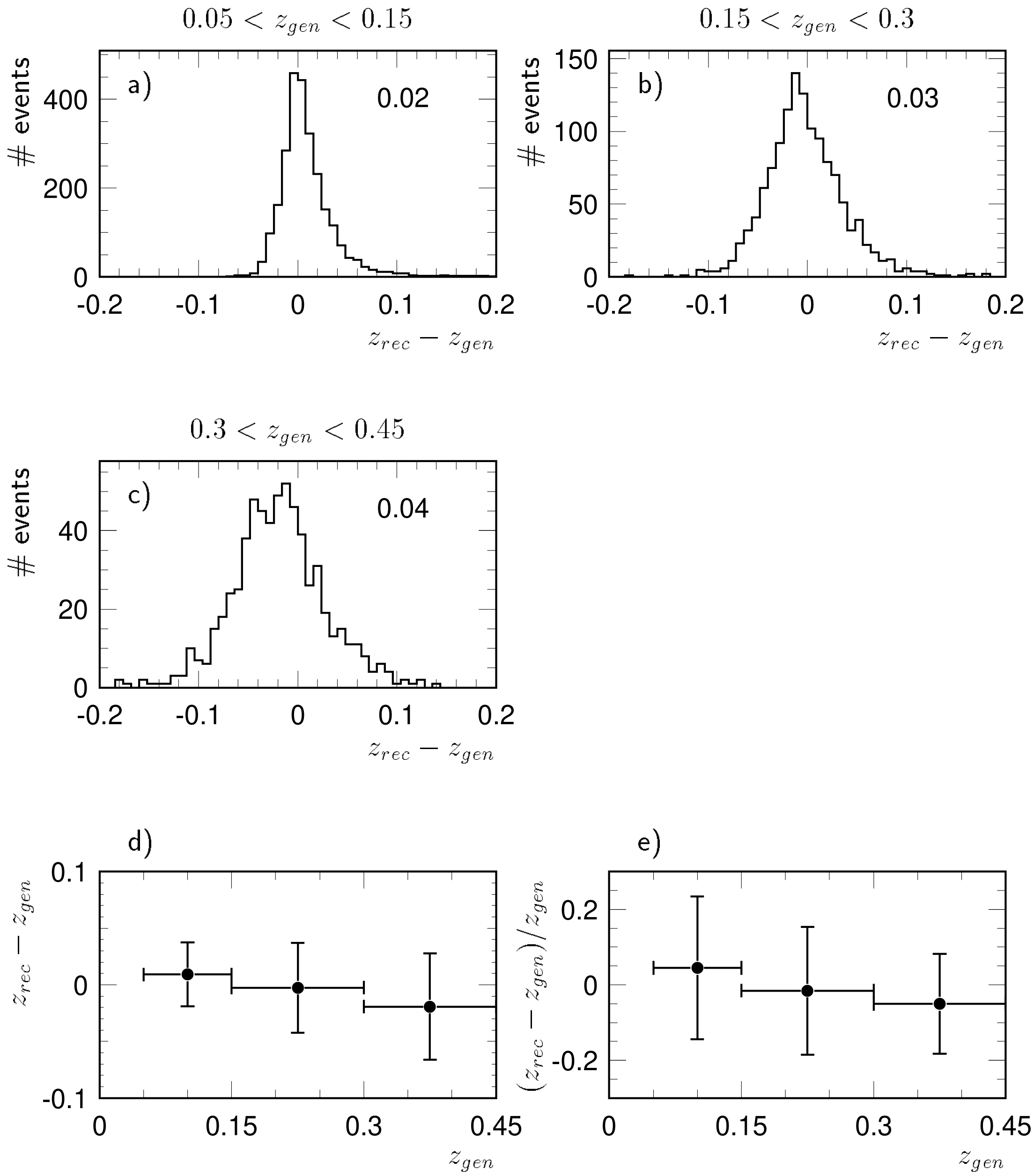

Figure 3.15: *Resolution of z in the region of the* **low** *z analysis. Explanations see figure 3.12.*

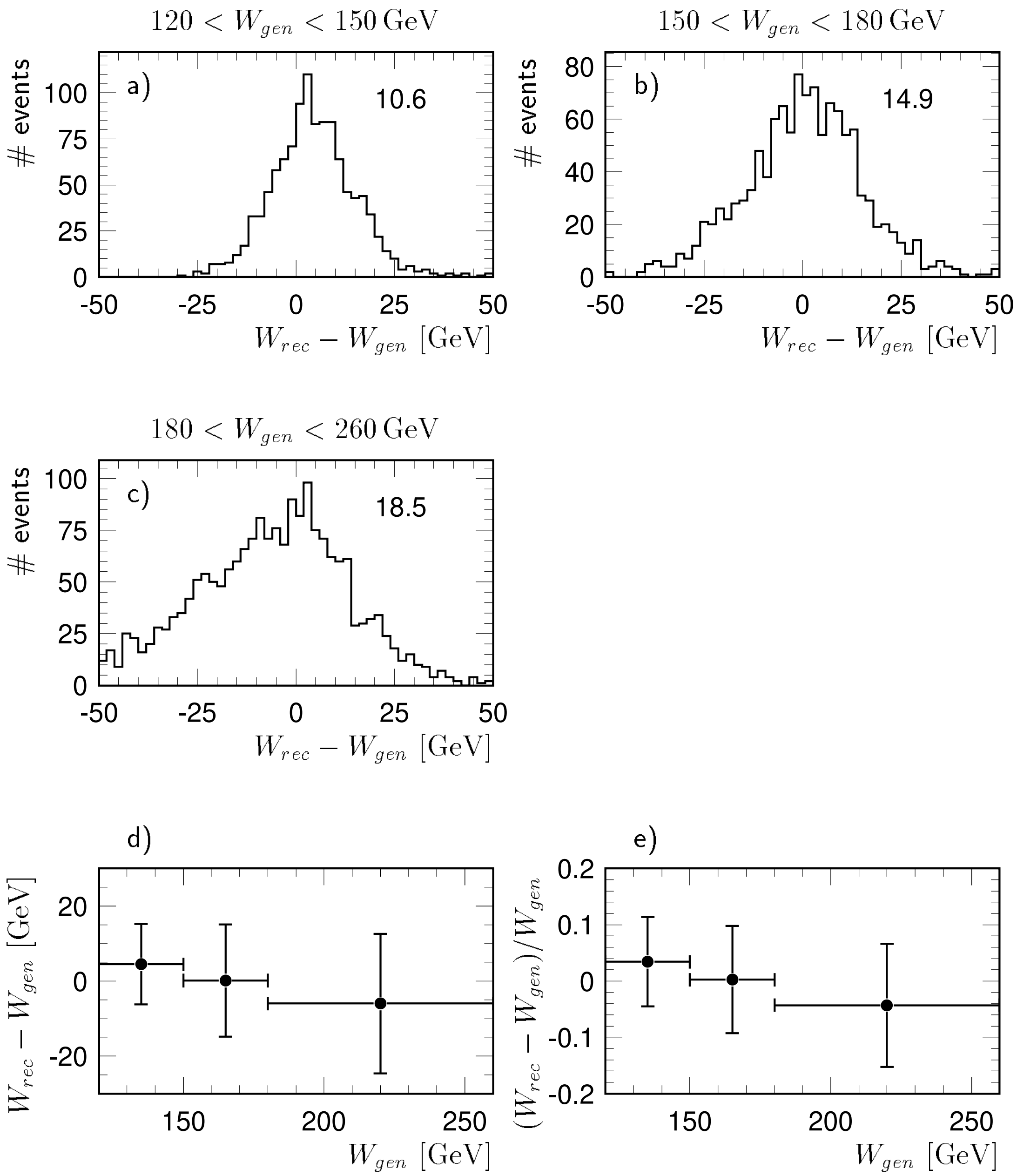

Figure 3.16: *Resolution of $W_{\gamma p}$ in the region of the* **low** *z analysis. Explanations see figure 3.12.*

Chapter 4

Data Selection

In this chapter the selection for the two analyses at medium and low z will be described. In the first section the preselection which is common to both analyses will be presented. The selection and the efficiencies of the cuts which are different will then be discussed.

4.1 Preselection

The basis of both analyses is a preselected sample of events with two identified muons in the CMD or the liquid argon calorimeter. Only those data taking periods are considered, where all relevant detector components were operational. For the selection of tracks and identification of muons a software package developed by Lee West (appendix C) is used.

4.1.1 Run Selection

During data taking the slow control status of all components of the H1 detector is logged approximately every 10 seconds. For the analysis and for efficiency determination only data where the following detector components were operational was used:

- central jet chambers (CJC1 and CJC2)
- central proportional chambers (CIP and COP)
- forward proportional chambers (FPC)
- liquid argon calorimeter (LAr)
- spaghetti calorimeter (SpaCal)
- central muon detector (CMD)
- Time-of-flight system (ToF)

		1996	1997	1999 e^-	1999 e^+	sum
proton beam energy	[GeV]	820	820	920	920	
$\mathcal{L}$ prod. by HERA	[nb^{-1}]	15600	31490	18320	17280	82690
$\mathcal{L}$ delivered to H1	[nb^{-1}]	14460	30010	17420	16180	78070
$\mathcal{L}$ H1 on tape	[nb^{-1}]	9870	24960	15684	14273	64787
$\mathcal{L}$ H1 G and M runs	[nb^{-1}]	9605	21611	14812	13341	59369
$\mathcal{L}$ phases 2 - 4	[nb^{-1}]	9232	17075	12207	11163	49677
$\mathcal{L}$ medium z	[nb^{-1}]	6439 ±114	13794 ±207	9693 ±126	9200 ±138	**39126** **$\pm$585**
$\mathcal{L}$ low z	[nb^{-1}]	6439 ±114	15826 ±237	10138 ±131	9566 ±143	**41969** **$\pm$625**

Table 4.1: *Integrated luminosities 1996 to 1999 [57].*

- luminosity system (Lumi)

During the year 1998 HERA was operated with electrons instead of positrons. The higher beam-induced background caused several problems especially in the tracking detectors and resulted in a very small amount of integrated luminosity available for the presented analysis. The data taking period 1998 is hence omitted. At the end of years 1997 and 1999 special data with different trigger settings (so-called 'minimum bias runs') were taken. These are not used for the analyses presented here. In October 1999 one wire in the inner central jet chamber (CJC1) broke and caused a 'hole' of approximately 20° in φ. Therefore all data after run 257601 are excluded.

An additional run selection is done to exclude data where other hardware problems, such as trigger settings not properly loaded, caused inefficiencies. Because of the different subtriggers required for the two analyses this leads to differing selections.

In order to avoid data taking regions where the used subtriggers had high prescale factors, trigger phase 1 is excluded in the medium z analysis. For the low z analysis this is only true for the year 1996. In 1997 and 1999 the SpaCal trigger S56 is used which has a prescale of 1 in all phases. Therefore trigger phase 1 is not excluded in these data taking periods.

4.1.2 Track and Muon Selection

The J/ψ meson is identified via its muonic decay mode. The selection is based on events with two identified muons. Since low elasticities are correlated with a high number of tracks, the combinatorial background for only one identified muon would be too high. In the data taking periods 1996 and 1997 class 24 is used, which demands at least one reconstructed lepton. Since this classification was performed during the offline reconstruction ('trigger level 5') it is 100 percent efficient if the selection cuts are at least as tight as the classification. In 1999 the classification was performed online already on trigger level 4. The new lepton class 16 (see appendix B) has a small inefficiency because the online reconstruction cannot use the final calibration. These efficiencies are discussed later in sections 4.2.3 and 4.3.3.

To resolve the ambiguities of the track reconstruction in several tracking detectors the track selection of a software package developed by Lee West (appendix C and [58]) is used. This package also provides a muon selection which is based on the track selection. The muons can either be identified by their minimal-ionizing signature in the liquid argon calorimeter or by reconstructing a track in the central or the forward muon detector. For the muons identified in the calorimeter a classification into 'poor', 'medium' and 'good' ($Q_c = 1, 2, 3$) quality is done (for details see [59, 60]).

The data selection in the two different z ranges is optimized for the dominant production processes. Because this results in different cuts on the decay muons, the efficiencies of the muon identification will be discussed for both selections separately.

4.2 Selection of J/ψ Mesons at Medium z

The main focus of the analysis of J/ψ production in the region $0.3 < z < 0.9$ is direct photon-gluon fusion. Three main contributions to the total analysis efficiency will be examined: the acceptance, the selection efficiency and the trigger efficiency. The acceptance is given by the cut on the polar angle and the momentum of the decay muons, the selection efficiency consists of the efficiency of all other selection cuts including the muon identification. The detector simulation is based on direct photon-gluon fusion events generated with the EPJPSI package (see section 3.1.1).

In order to reduce background originating from J/ψ and $\psi(2s)$ mesons produced in diffractive processes (see section 5.3) a cut on the transverse momentum squared of the J/ψ meson $p_{t,\psi}^2$ is applied for the photon-proton centre-of-mass energy $W_{\gamma p}$ and the elasticity z.

4.2.1 Acceptance

To ensure a good measurement of the momentum of the decay leptons, their polar angle is restricted to the acceptance region of the central tracking detector, $20° < \vartheta_\mu < 160°$. Identification of particles as muons in the LAr calorimeter is only possible for momenta $p_\mu > 0.8\,\mathrm{GeV}$. In the instrumented iron the minimum momentum is higher. For the lowest z region of this analysis ($0.3 < z < 0.45$) a significant improvement of the J/ψ signal in the di-muon mass spectrum is found by increasing this momentum cut. An optimal value between signal enhancement and acceptance loss was found for $p_\mu > 1.1\,\mathrm{GeV}$. The resulting acceptance, determined with a direct photon-gluon fusion Monte Carlo, is shown in figure 4.1 as a function of the γp centre-of-mass energy. For low $W_{\gamma p}$ a strong rise is observed. To avoid uncertainties in this region, a minimum $W_{\gamma p}$ of 60 GeV is demanded. For the upper cut a value of 180 GeV is chosen which corresponds to half of the maximum value of the acceptance. The position of the maximum acceptance depends slightly on the energy of the incoming proton.

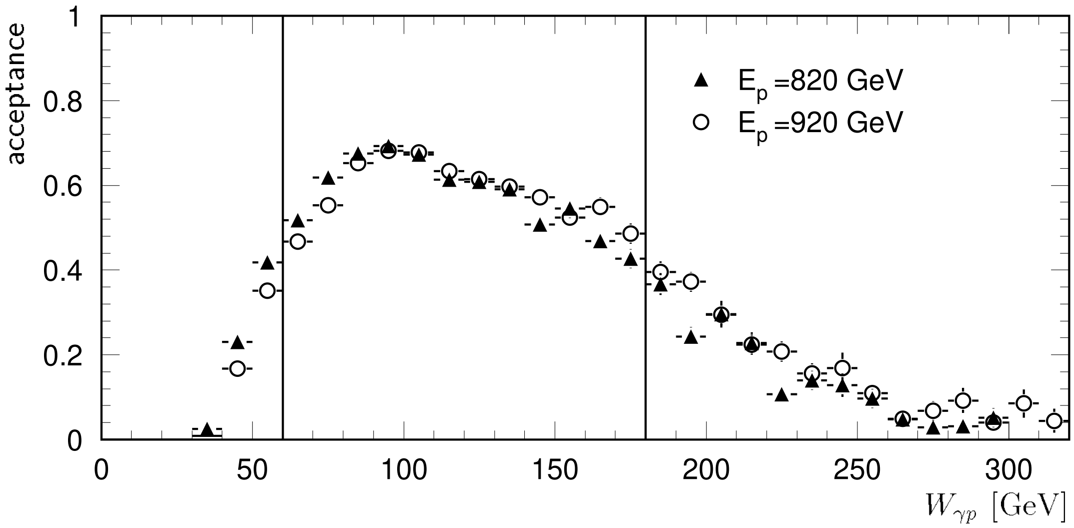

Figure 4.1: *Acceptance of* $20° < \vartheta_\mu < 160°$ *and* $p_\mu > 1.1\,\mathrm{GeV}$ *as a function of* $W_{\gamma p}$ *for direct photon-gluon fusion (EPJPSI-direct). The kinematic range is restricted to* $Q^2 < 1\,\mathrm{GeV}^2$, $0.3 < z < 0.9$ *and* $p_{t,\psi}^2 > 1\,\mathrm{GeV}^2$. *The lines show the* $W_{\gamma p}$ *region which is chosen for the analysis. The higher proton beam energy of* 920 GeV *in 1999 with respect to* 820 GeV *in 1996 and 1997 causes a shift of the maximum acceptance to slightly higher* $W_{\gamma p}$ *values.*

4.2.2 Selection Efficiency

Photoproduction events are selected by rejecting events with electromagnetic energy clusters above 8 GeV in the SpaCal or the LAr calorimeter. This restricts the photon virtuality to $Q^2 < 1\,\mathrm{GeV}^2$. Furthermore the energy deposited in the veto layer of the electromagnetic SpaCal has to be less than 1 GeV to exclude events where the shower of the scattered electron is only partially contained in the SpaCal. In figure 4.2 a) the energy distribution of the scattered electron is illustrated for the EPJPSI-direct simulation for photoproduction ($Q^2 < 1\,\mathrm{GeV}^2$) and non-photoproduction events. Only events with a scattered electron inside the main H1 detector with an energy of at least 1 GeV are considered. At an energy of about 8 GeV the same number of events is reached in both data sets. The Q^2 distribution of the selected photoproduction events ($E' < 8\,\mathrm{GeV}$, $E_{veto} < 1\,\mathrm{GeV}$) is shown in figure 4.2 b). Almost no events with $Q^2 > 1\,\mathrm{GeV}^2$ pass the photoproduction cuts, but for events which have a Q^2 just below $1\,\mathrm{GeV}^2$ the cuts are not very efficient.

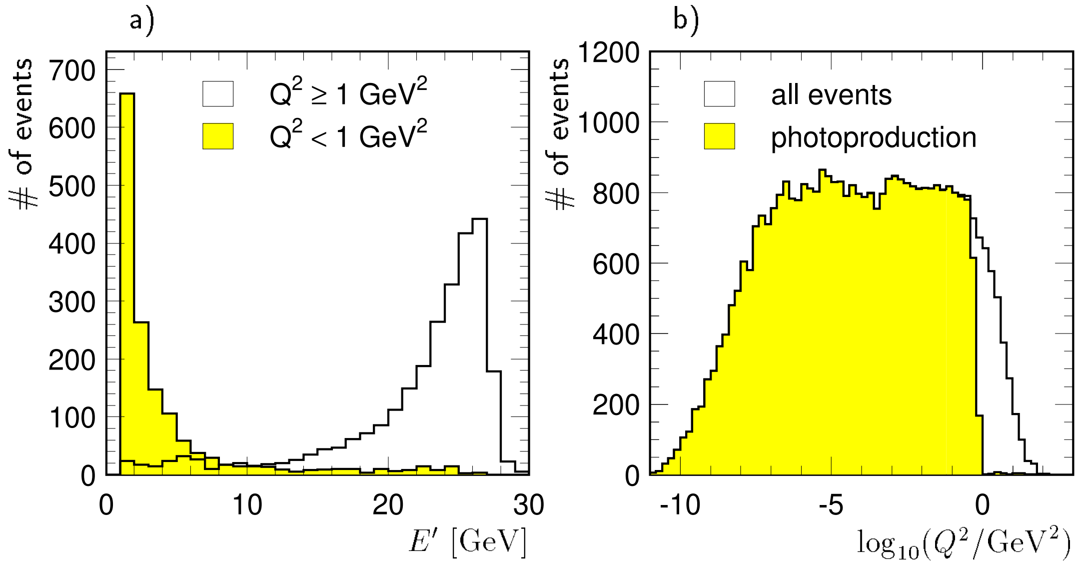

Figure 4.2: *a) Energy of the scattered electron E' for direct photon-gluon fusion events with $Q^2 > 1\,\mathrm{GeV}^2$ (open histogram) and $Q^2 < 1\,\mathrm{GeV}^2$ (shaded histogram). A cut at $8\,\mathrm{GeV}$ removes the main part of the events at higher Q^2. b) Q^2 distribution of all events (open histogram) and of the events with $E_{veto} < 1\,\mathrm{GeV}$ and no scattered electron in the main detector or $E' < 8\,\mathrm{GeV}$ if there is a candidate for the scattered electron (shaded histogram).*

The decay particles of the J/ψ meson both have to be identified as muons in the H1 detector. The corresponding tracks have to be reconstructed in the central or the forward tracking detector within $20° < \vartheta_\mu < 160°$ fulfilling the standard cuts of the Lee West track selection code (appendix C). In addition a minimum momentum of $p_\mu > 1.1\,\mathrm{GeV}$ is required as already mentioned. One of the muons must be identified in the barrel or the outer endcaps of the central muon detector to fulfil the requirements of the triggers which are used for this analysis. The other muon may be identified in the central muon detector or in the LAr calorimeter.

The muon identification efficiency is determined by tagging the event with one identified muon and studying the other track. To compare the identification efficiencies between data and detector simulation quasi-elastic J/ψ events are used. Exactly two 'good' tracks with opposite charges in the central or forward tracking detector are required. At least one of them has to be identified as a muon in the instrumented iron or the LAr calorimeter ($Q_c = 3$). To have no bias for the central muon detector an independent subtrigger without iron conditions (mostly electron tagger and SpaCal subtriggers) is required. Cosmic ray muons are rejected by a cut on the opening angle of the tracks. The resulting data sample shows a clean J/ψ signal in the invariant mass distribution of the two tracks.
After a cut on the J/ψ mass region ($2.9 < M < 3.3\,\mathrm{GeV}$) the data sample contains mainly J/ψ mesons produced via elastic and proton-dissociative diffraction, but also photon-gluon fusion events at high z. For the comparison a simulation of diffractive (DIFFVM) and photon-gluon fusion (EPJPSI-direct) events is used. Since the identification efficiency depends on ϑ_μ, the relative normalization of the two simulation contributions is chosen to fit the ϑ_μ distribution of the data.

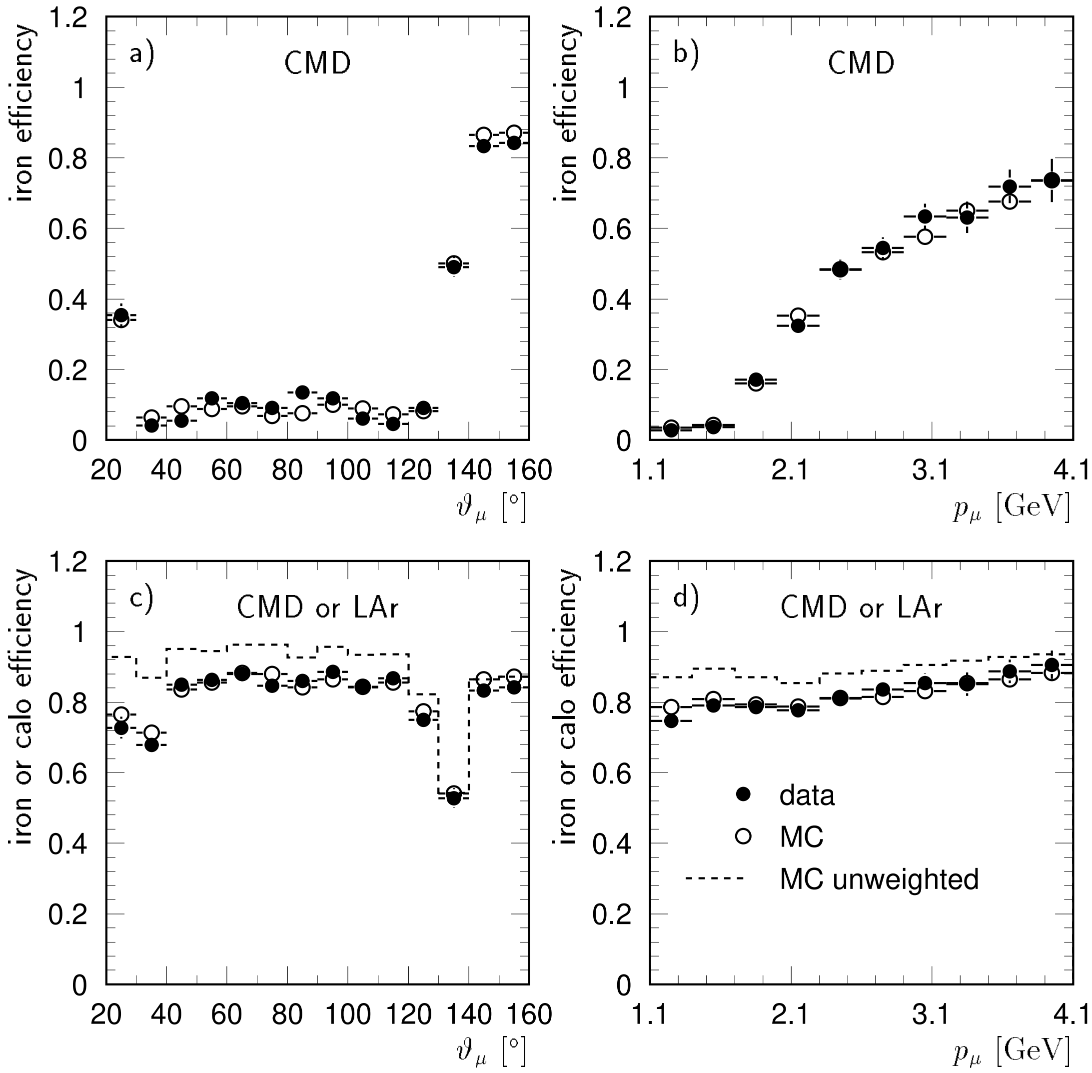

Figure 4.3: *Muon identification efficiency in the Central Muon Detector (CMD, upper plots) and in the CMD or the LAr calorimeter (lower plots) for 1999 data and simulation. For details of the data sets see text. In the simulation the calorimeter identification efficiency is reweighted to match the data.*

The muon identification efficiencies for the 1999 data and the simulation are shown in figure 4.3 as a function of the polar angle ϑ_μ and the momentum p_μ. As in previous analyses the calorimeter identification in the Monte Carlo simulation is found to be more efficient than in data [60, 61]. Therefore the efficiency is reweighted in the simulation to match the data as a function of ϑ. Because of hardware changes in the LAr calorimeter in the year 1998 which improved the identification efficiency in the forward region by $\sim 19\%$ two weighting functions for 1996/1997 and 1999 are determined. The muon identification efficiency in the instrumented iron is rather low in the central region ($30° \lesssim \vartheta \lesssim 130°$) of the detector and for low momenta. By using the LAr calorimeter in addition the identification efficiency is significantly improved. The remaining differences between data and simulation are considered in the systematic error (see section 5.3).

In order to select inelastic J/ψ events in addition to the upper cut on z at least three good tracks (including the muons) originating from the primary vertex are required. This excludes J/ψ mesons produced via elastic diffraction and reduces proton-dissociative diffraction. Furthermore it reduces the background of J/ψ mesons originating from diffractively produced $\psi(2s)$ decaying via $\psi(2s) \to J/\psi\, \pi^+\pi^-$, because these pions have small momenta and therefore low detection probabilities.

The selection efficiency resulting from the cuts described in this subsection is presented in figure 4.4 as a function of the photon-proton centre-of-mass energy $W_{\gamma p}$, the elasticity z and the transverse momentum squared of the J/ψ meson $p_{t,\psi}^2$ for a direct photon-gluon fusion Monte Carlo simulation in the Colour Singlet Model. The efficiency for a proton

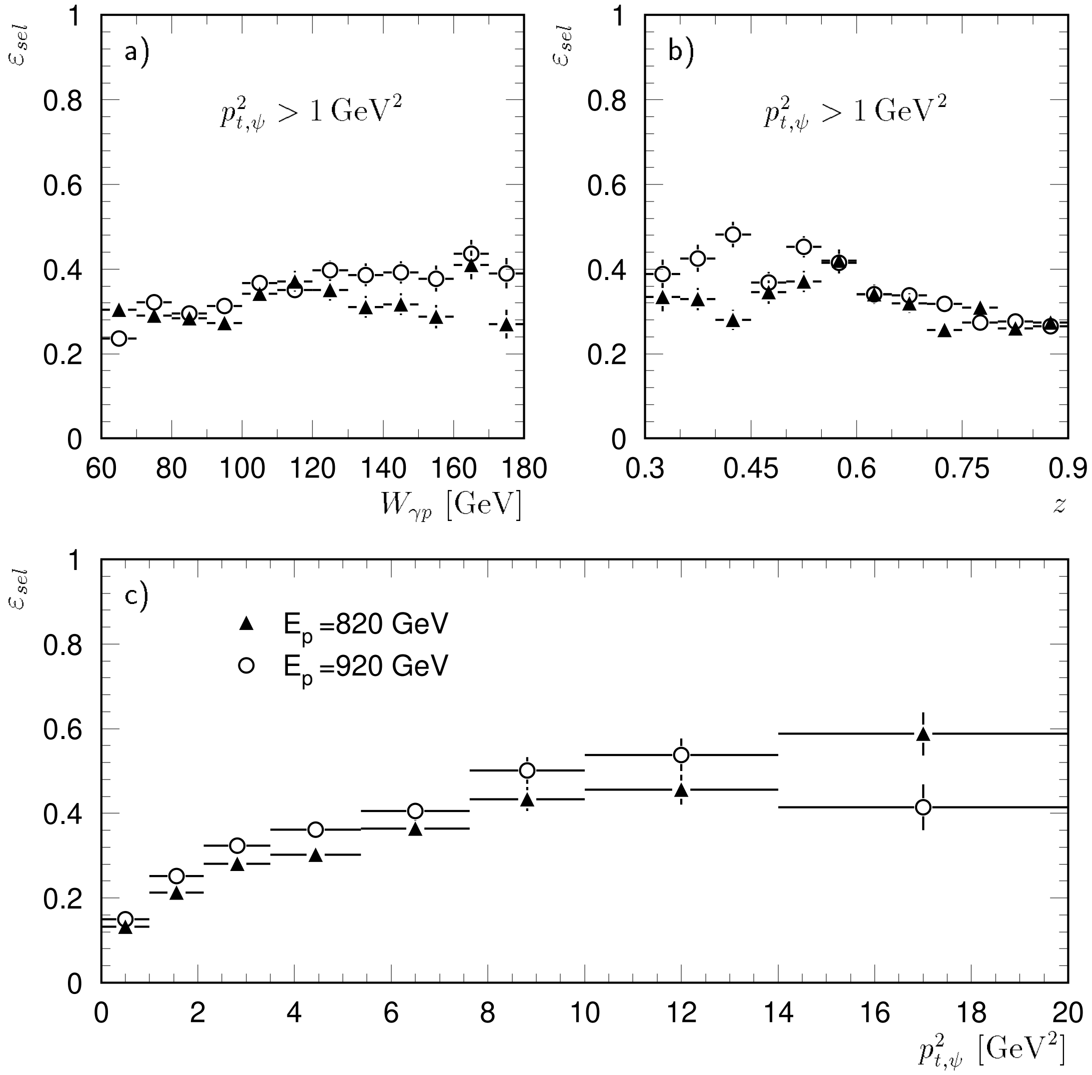

Figure 4.4: *Selection efficiency for EPJPSI-direct in the kinematic region* $0.3 < z < 0.9$, $60 < W_{\gamma p} < 180\,\mathrm{GeV}$ *and* $Q^2 < 1\,\mathrm{GeV}^2$. *The efficiency for a proton energy of* $E_p = 920\,\mathrm{GeV}$ *(circles, used in 1999) is higher than for* $E_p = 820\,\mathrm{GeV}$ *(triangles, used in 1996 and 1997).*

energy of $E_p = 920\,\mathrm{GeV}$ as used in 1999 is higher than for $E_p = 820\,\mathrm{GeV}$, corresponding to 1996 and 1997. Besides the higher mean momentum of muons and additional particles leading to higher identification probabilities the improved calorimeter identification and the higher efficiency of the CJC which was rewired in 1998 contribute to this effect. While the efficiency is only slowly rising with $W_{\gamma p}$ and decreasing with z, it depends strongly on $p_{t,\psi}^2$. For this reason it is important that the $p_{t,\psi}^2$ distribution agrees between data and the Monte Carlo simulation which is used to correct the data. The direct photon-gluon fusion simulation shows a steeper decrease than the data (see section 5.2.1), thus it is reweighted.

4.2.3 Trigger Efficiency

During the data taking period 1996 the most efficient subtriggers are S19 and S22 which cover the barrel region and the outer endcaps of the instrumented iron. In June 1997 a new subtrigger, S15, with relaxed track requirements on trigger level 1 was put into operation. To keep the trigger rate at an acceptable level it uses a neural net on trigger level 2 trained to select inelastically produced J/ψ mesons (for details see [5]). In this section the determination of the trigger efficiencies and the resulting values will be discussed.

Trigger Level 1

The subtriggers which are used in this analysis contain trigger elements of three different detector systems: the `DCRPh` derived from CJC informations, the `zVtx` from the proportional chambers and iron triggers. Because of low statistics it is not possible to determine the trigger efficiency in the data with completely independent subtriggers. The efficiency of each relevant trigger element will be compared between data and detector simulation instead and the trigger efficiency of the simulation will then be used.

The most important subtriggers which contain no trigger elements of the `DCRPh` or the `zVtx` trigger are based on an energy deposition of the scattered electron in the SpaCal. Therefore the photoproduction cuts are not imposed on the data set used for the efficiency determination. In addition the muon identification is slightly relaxed to increase statistics: The muon identified in the CMD may also lie in the inner endcaps. All other selection criteria are not changed with respect to the analysis. The trigger efficiency of the track trigger elements mainly depends on the number of tracks in the event which is approximated by the number of good tracks N_{good}. In figures 4.5 and 4.6 the efficiency of the trigger elements `DCRPh_CNH`, `DCRPh_Thigh`, `zVtx_sig1` and `zVtx_Mu_D` is shown as a function of N_{good}, the elasticity z and the transverse momentum squared of the J/ψ meson $p_{t,\psi}^2$. Data and simulation are compatible within the errors. There is, however, a tendency, that the simulation is slightly more efficient than the data for `DCRPh_Thigh` and `zVtx_Mu_D` and vice versa for `DCRPh_CNH` and `zVtx_sig1`. This will be used to estimate the systematic error (section 5.3).

In order to study the efficiency of the trigger elements of the instrumented iron events containing exactly one track in the central muon detector are selected. This iron track has

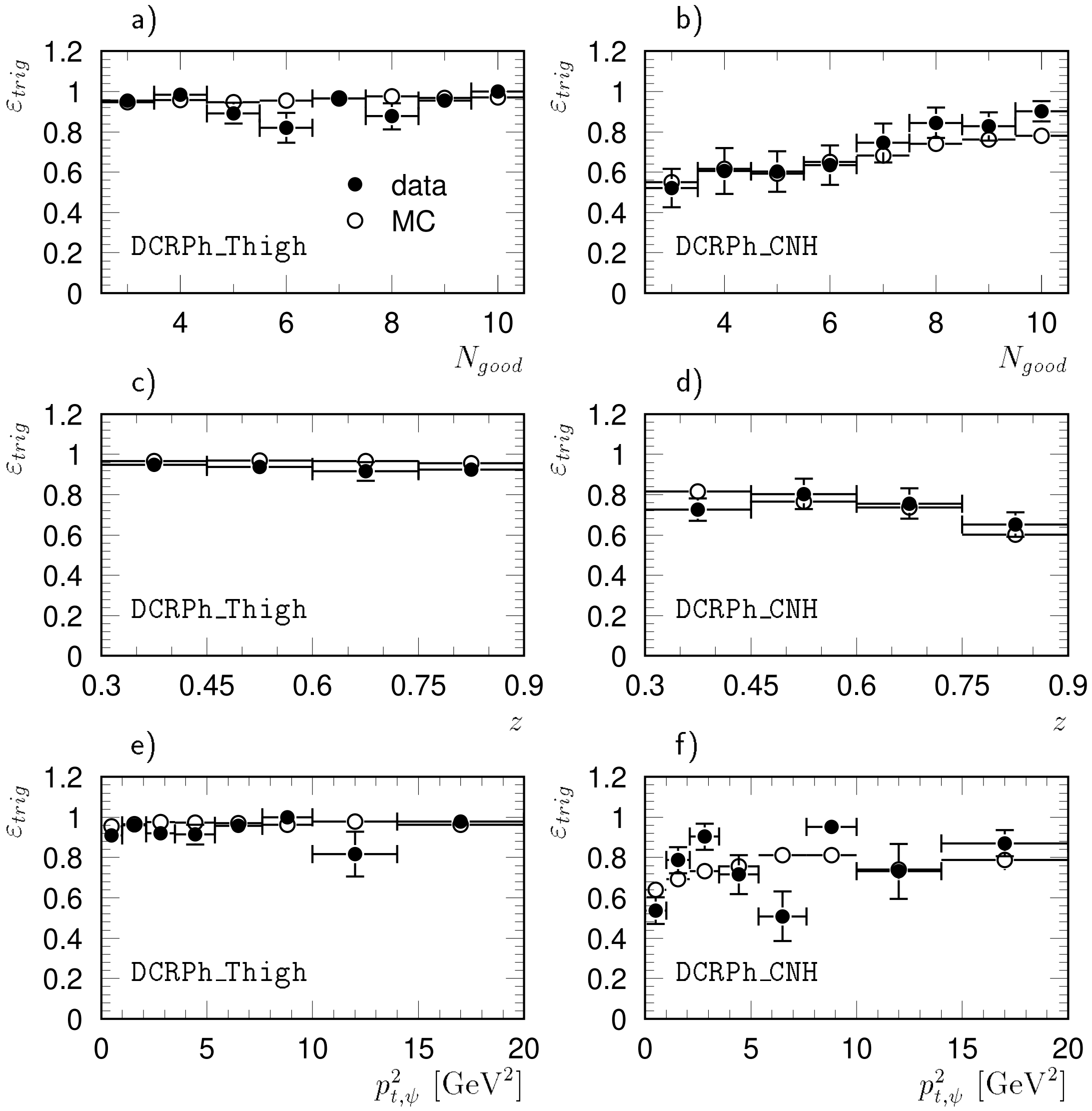

Figure 4.5: *Trigger efficiency of a) the trigger element* DCRPh_CNH *and b) the trigger element* DCRPh_Thigh *as a function of the number of good tracks N_{good}. The trigger efficiencies as a function of the elasticity z and the transverse momentum squared of the J/ψ meson $p_{t,\psi}^2$ are shown for the same trigger elements in c) and d) and e) and f) respectively.*

to belong to an identified muon and has to lie in the acceptance of the studied detector part. The independent subtriggers are mainly SpaCal and electron tagger triggers as well as track triggers designed for elastic J/ψ production. Therefore the photoproduction conditions as well as the upper z cut and the requirement of at least three good tracks are omitted. To reduce cosmic ray muons a cut on the difference in the polar angle and in the azimuthal angle is imposed on events with exactly two tracks. All other selection cuts are the same as in the analysis. In figure 4.7 the trigger efficiency of the combination Mu_Bar||Mu_ECQ is displayed as a function of the polar angle ϑ_μ (a) and the momentum p_μ (b) of the muon identified in the central muon detector. The data are well described by the Monte Carlo simulation. This agreement is due to fixing several problems in the detector simulation of the CMD and the determination of the timing inefficiencies of each

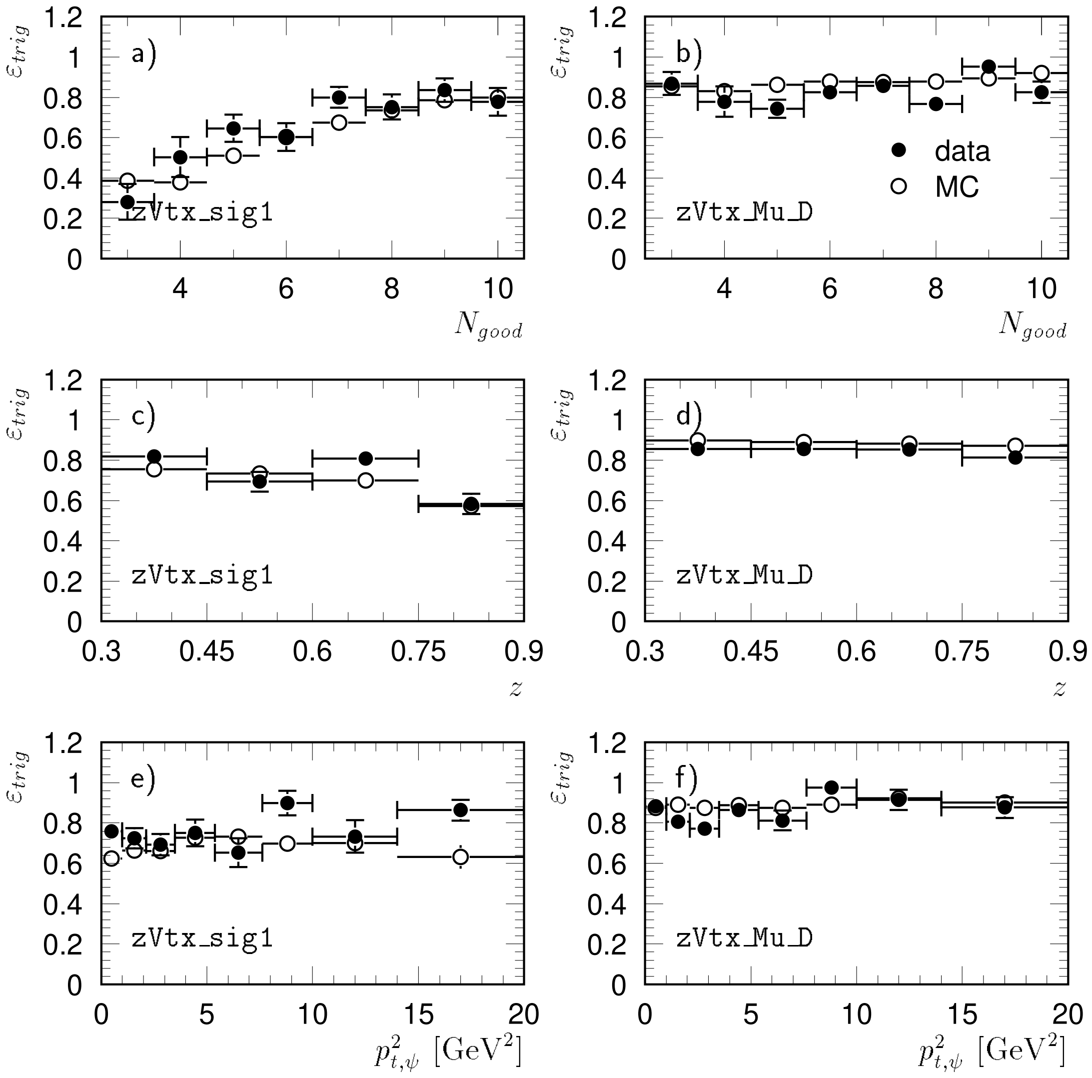

Figure 4.6: *Trigger efficiency of a) the trigger element* `zVtx_sig1` *and b) the trigger element* `zVtx_Mu_D` *as a function of the number of good tracks N_{good}. The trigger efficiencies as a function of the elasticity z and the transverse momentum squared of the J/ψ meson $p_{t,\psi}^2$ are shown for the same trigger elements in c) and d) and e) and f) respectively.*

module of the CMD. In a previous analysis a discrepancy of up to 25% was found [62].

Level 1 Prescaling

Depending on run and background conditions the level 1 triggers are prescaled to control the output rate. The subtriggers which are used in this analysis have high prescaling factors during trigger phase 1 as mentioned above. Trigger phase 1 is therefore excluded from the analysis. For the other trigger phases the effect of the prescaling is very small. It is accounted for by weighting the events in the data with a luminosity weighted average prescaling factor (see section 1.2.5). For subtriggers S15, S19 and S22 the deviation of

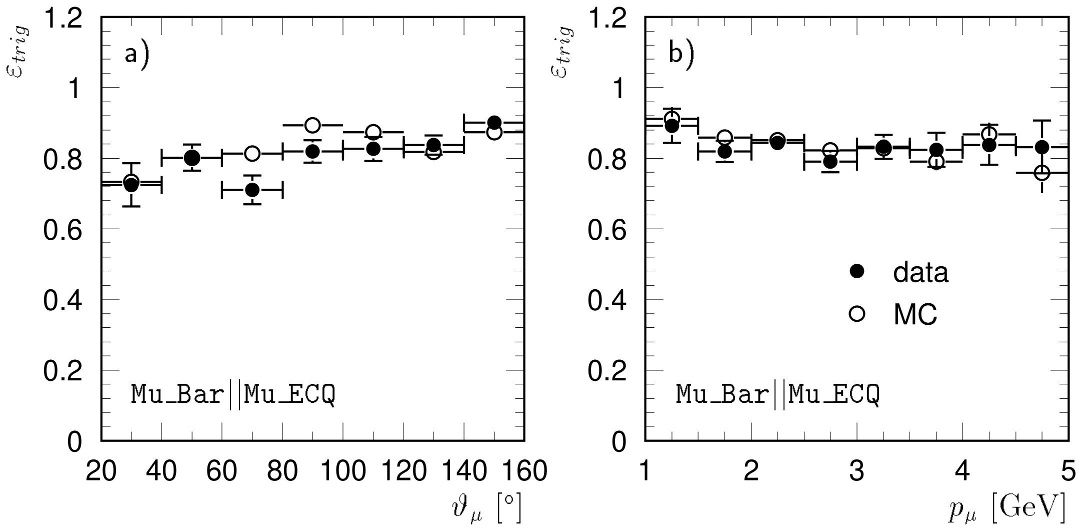

Figure 4.7: *Trigger efficiency of the trigger elements* `Mu_Bar` *and* `Mu_ECQ` *as a function of a) the polar angle ϑ_μ and b) the momentum p_μ of the muon identified in the instrumented iron. For the analysis subtrigger* S15 *or the combination* S19||S22 *is used, therefore* `Mu_Bar||Mu_ECQ` *is studied instead of the single trigger elements.*

the weights from 1 is always less than 2%.

Trigger Level 2

Subtrigger S15, which is used in this analysis in the second part of the data taking period 1997 and in 1999, is validated by a neural net on trigger level 2. It uses input quantities from the `zVtx`, the `DCRPh`, the LAr calorimeter and the CMD trigger systems. To train the neural network, candidate events for inelastic J/ψ production from the years 1995 and 1996 triggered by S19 or S22 were used. In addition S87 can be used as an independent trigger for the efficiency determination of the net. S87 contains electron tagger trigger conditions which are only efficient for certain regions in $W_{\gamma p}$. This has to be modelled by acceptance functions in the Monte Carlo. In addition to the selection criteria of the analysis the level 1 trigger conditions of S15 are required. The efficiency of the neural net is shown in figure 4.8 as a function of the photon-proton centre-of-mass energy $W_{\gamma p}$, the elasticity z and the transverse momentum squared of the J/ψ meson $p_{t,\psi}^2$. Reasonable agreement between the data and the EPJPSI-direct simulation is found for $W_{\gamma p}$ and $p_{t,\psi}^2$, while deviations are observed in z. In order to estimate the systematic error the simulated efficiency is reweighted in z to match the data (see section 5.3).

Trigger Level 4

In **1996 and 1997** a trigger verification was performed on trigger level 4 which mimicked the L1 subtrigger conditions. For the `DCRPh` and `zVtx` trigger elements a 'good' CJC

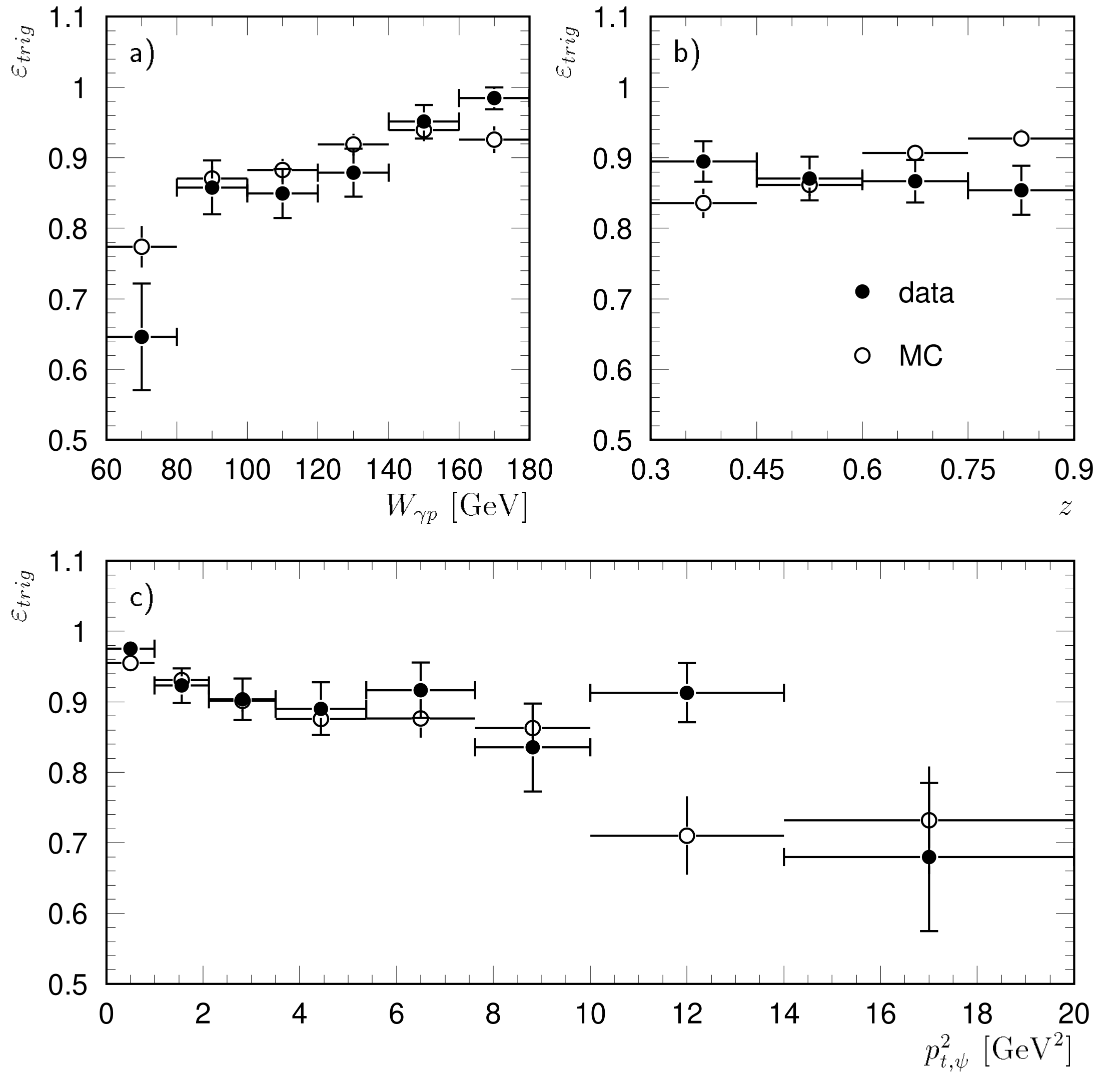

Figure 4.8: *The trigger efficiency of the neural net validating subtrigger* `S15` *on trigger level 2 as a function of a)* $W_{\gamma p}$*, b)* z *and c)* $p_{t,\psi}^2$ *in data (filled circles) and the EPJPSI-direct simulation (open circles). The independent subtriggers are S19, S22 and S87.*

track was required. The trigger elements of the instrumented iron were validated by a reconstructed track in the central muon detector which had to match a CTD or FTD track in ϑ and φ ('muon matching'). This last requirement caused an inefficiency on trigger level 4 especially for subtriggers containing the `Mu_Bar` condition, such as S19. The efficiency is determined from the data with events that have iron-independent L4 verified subtriggers. While in 1996 this was sufficient for events to pass L4, in 1997 they had to fulfil in addition a 'hard scale' or to pass a so-called 'final-state finder', which was again the muon matching for several subtriggers containing iron conditions.

In order to make sure that a hard scale condition is fulfilled the L4 efficiency is with events which contain at least one track with $p_t > 2.1\,\mathrm{GeV}$ (the L4 hard scale cut was $p_t > 2.0\,\mathrm{GeV}$). The resulting efficiency of the L4 trigger verification for S19 is $\varepsilon_{\mathrm{L4,S19}} =$

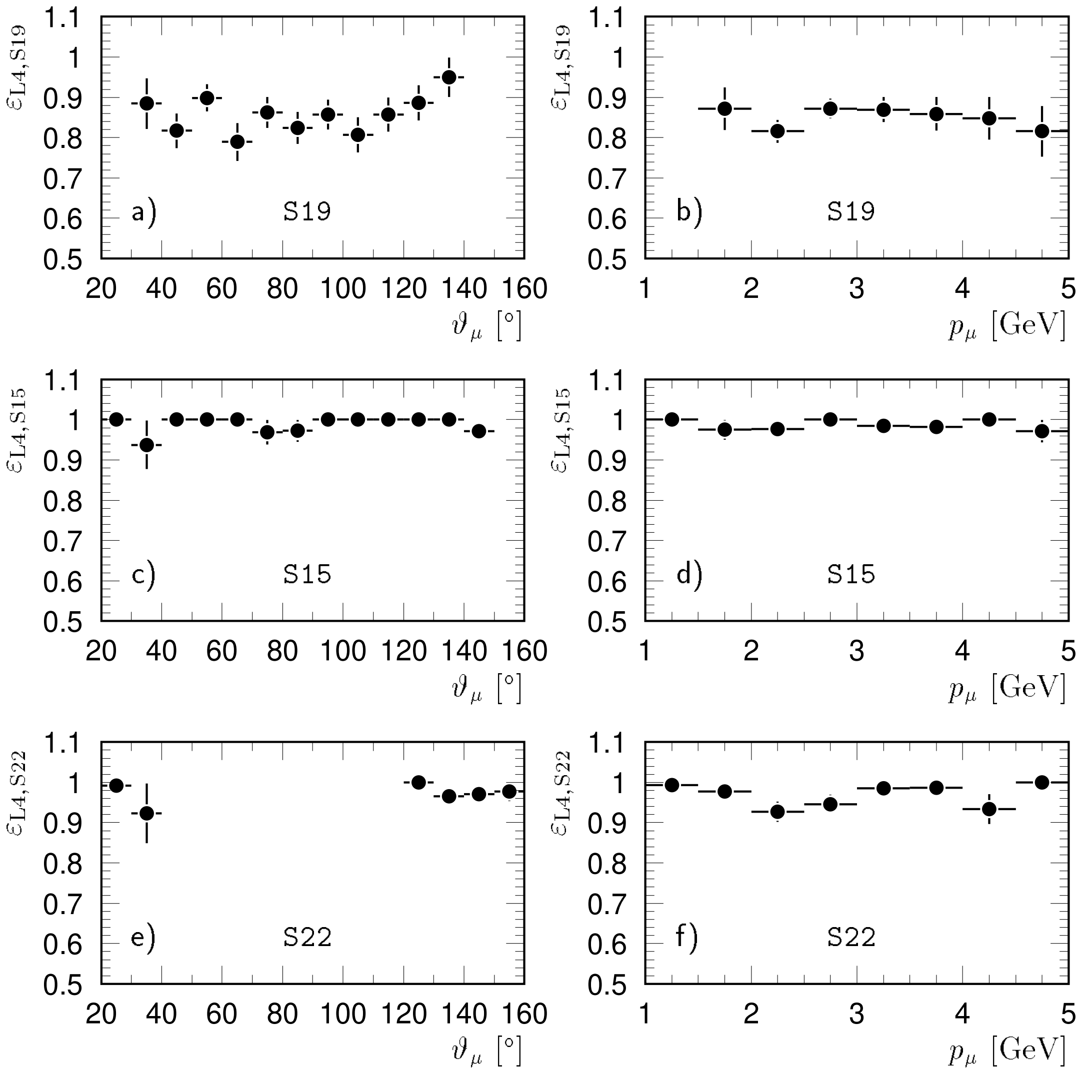

Figure 4.9: *The efficiency of the* **trigger verification on level 4** *in the data taking periods 1996 and 1997 for a) subtrigger* `S19`*, c) subtrigger* `S15` *and e) subtrigger* `S22` *as a function of the polar angle ϑ_μ of the muon identified in the central muon detector. The verification efficiency as a function of the momentum p_μ of the muon is shown for the same subtriggers in b), d) and f).*

84.6% ± 1.3% (in addition to the L1 trigger element efficiency) and nearly independent of the polar angle ϑ_μ and the momentum p_μ of the track identified in the central muon detector (fig. 4.9 a,b). Since L4 is not simulated for Monte Carlo events this is taken into account as a global weight for events which were accepted by S19 only. The efficiencies for S15 and S22 are much higher (fig. 4.9 c – f, $\varepsilon_{\mathrm{L4,S15}} = 98.6\% \pm 0.5\%$ and $\varepsilon_{\mathrm{L4,S22}} = 97.2\% \pm 0.5\%$) and are therefore not corrected but accounted for in the systematic error.

During the data taking period **1998** the L4 scheme was completely changed. The trigger verification in its original sense was removed and the classification, which had been done on L5 before, was replaced by the hard scales and the finders. This causes some small inefficiencies because the online reconstruction cannot use the final calibration values for several detector components. For J/ψ production, class 16, defined by the 'high mass finder', is the relevant class. Events which are not classified by the high mass finder can be saved by other final state or hard scale classes. If this is not the case they are downscaled as 'soft physics'. This means that for a downscale factor n only each nth event is written to tape with weight n. Thus it is possible to calculate the classification efficiency $\varepsilon_{\mathrm{L4}}$ as:

$$\varepsilon_{\mathrm{L4}} = \sum_{\text{selected events in class 16}} weights \Big/ \sum_{\text{all selected events}} weights$$

In total 3 events are found in 1999 which fulfil the selection cuts but are not accepted by the high mass finder, two with weight 1 and one with weight 20. This results in a L4 efficiency of $\varepsilon_{\mathrm{L4}} = 98.3\% \pm 1.5\%$ which is again considered in the systematic error.

Total Trigger Efficiency

After having established agreement of the simulation of the trigger elements with data, the total trigger efficiency (including the L4 verification) as calculated in EPJPSI-direct for three different setups is shown in figure 4.10: the combination S19||S22 with a proton beam energy of 820 GeV and S15 with a 820 GeV and a 920 GeV proton beam. It is studied for events passing all selection cuts as described above. S15 is more efficient than S19||S22 especially for lower photon-proton centre-of-mass energies $W_{\gamma p}$, higher elasticities z and small values of the transverse J/ψ momentum squared $p_{t,\psi}^2$. These regions correspond to events with lower charged particle multiplicities, where the track trigger elements used in S19 and S22 (`DCRPh_CNH` and `zVtx_sig1`) have a lower efficiency than those used in S15 (`DCRPh_Thigh` and `zVtx_Mu_D`). The difference in the efficiency of S15 for the different proton beam energies is small.

4.2.4 Selected Data Sample

The number of events which remain after applying the cuts described before are listed in table 4.2. The invariant mass spectrum of the muon pairs corresponding to the final selection (last row) in the elasticity range $0.3 < z < 0.9$ is shown in figure 4.11. The unlike-sign pairs show a clear J/ψ signal, whereas the like-sign distribution is flat. The unlike-sign spectrum is fitted with a function taken to be a superposition of a Gaussian for the J/ψ meson and a straight line for the non-resonant background. The background is fitted up to a mass of 3.55 GeV to avoid the region where a possible $\psi(2s)$ signal ($M_{\psi(2s)} = 3.68596$ GeV [8]) would appear. The J/ψ mass determined from this fit is only slightly lower than the nominal value $M_{J/\psi} = 3.09687$ GeV [8] (within 2 standard deviations). The width $\sigma_\psi = 58.3$ MeV is dominated by the resolution of the tracking chambers. In total the fit yields 773 ± 33 J/ψ mesons in the peak. If the number of J/ψ mesons is calculated as described in the next chapter, a value of 801 ± 32 is obtained.

To control the stability in time the rate of selected events per integrated luminosity is studied in $\sim$ 1pb^{-1} bins of the integrated luminosity (fig. 4.12). In 1996 and the first part of 1997 the combination of the subtriggers S19 and S22 is used which is less efficient than S15. For this reason the rate is lower. During 1997 the central jet chamber was slowly degrading and was therefore rewired after the data taking. This results in a small difference in rate between 1997 and 1999. For the periods where the rate is expected to be constant the values are compatible with this expectation.

	1996	1997	1999 e$^-$	1999 e$^+$	sum
events on DST	23.2 mio.	31.0 mio.	17.3 mio.	21.9 mio.	93.4 mio.
class 24 / 16	1.3 mio.	2.2 mio.	1.9 mio.	0.9 mio.	6.3 mio.
≥ 2 muons, $M_{\mu\mu} > 2\,\mathrm{GeV}$, HV & run selection	45442	87985	80894	73923	288244
$\mu^+\mu^-$, $p_\mu > 1.1\,\mathrm{GeV}$, $20° < \vartheta_\mu < 160°$	10817	21259	27360	22924	82360
photoproduction	8597	16978	23782	19858	69215
$\lvert z_{\mathrm{vertex}}\rvert < 40\,\mathrm{cm}$, $N_{good} \geq 3$, ≥ 1 muon id. in CMD	1547	3773	3678	3002	12000
$0.3 < z < 0.9$	573	1433	1681	1288	4975
$2.9 < M_{\mu\mu} < 3.3\,\mathrm{GeV}$	227	555	468	418	1668
$60 < W_{\gamma p} < 180\,\mathrm{GeV}$	426	1137	1098	841	3502
$2.9 < M_{\mu\mu} < 3.3\,\mathrm{GeV}$	186	468	375	346	1375
trigger	308	807	832	604	2551
$2.9 < M_{\mu\mu} < 3.3\,\mathrm{GeV}$	129	327	299	279	1034
prescale weighted	311.2	807.5	841.6	605.1	2565.4
$2.9 < M_{\mu\mu} < 3.3\,\mathrm{GeV}$	130.0	327.2	302.5	279.5	1039.2

Table 4.2: *Numbers of selected events for the* **medium z** *analysis 1996 to 1999.*

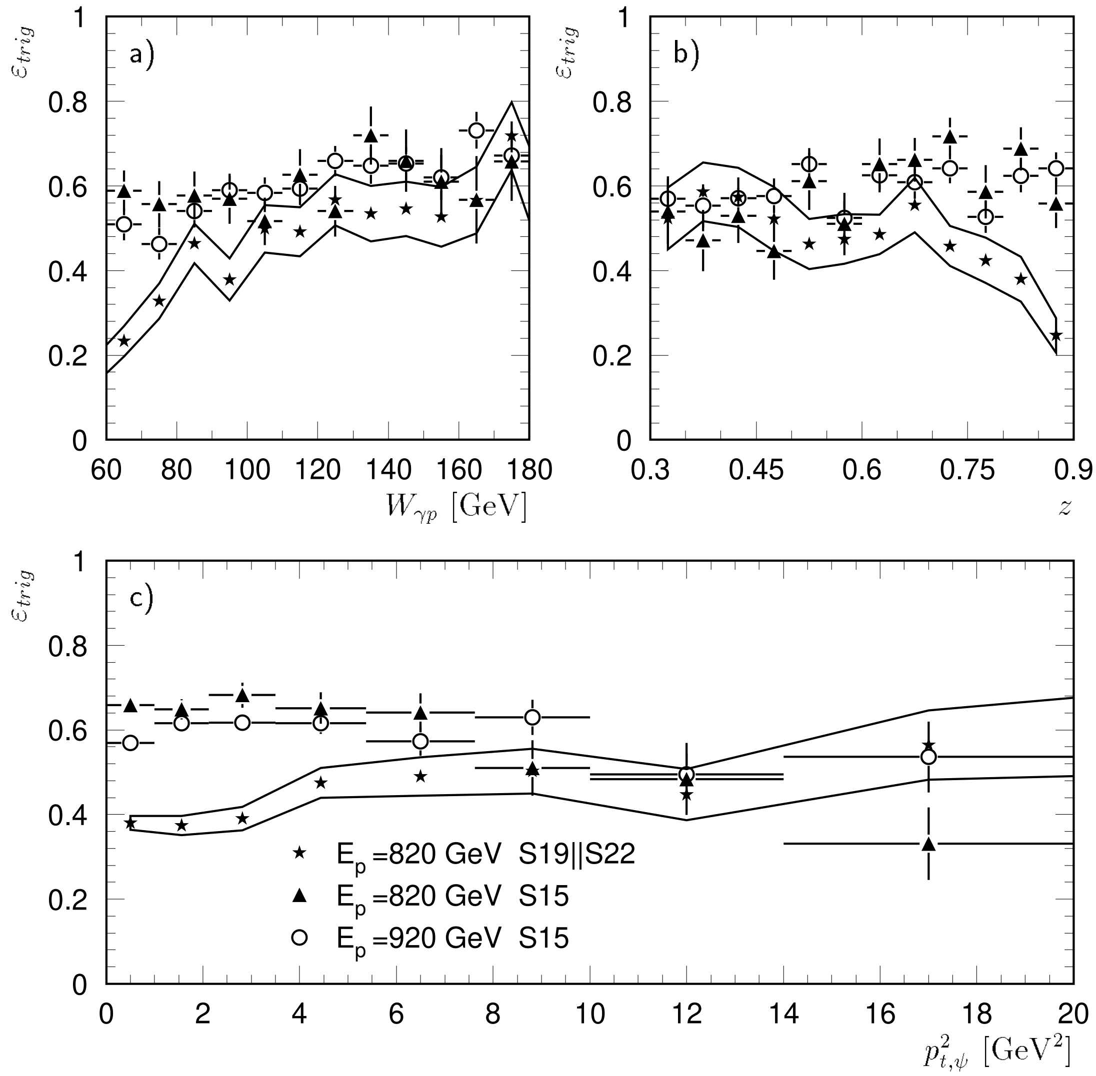

Figure 4.10: *The total trigger efficiency for three different setups: the combination* S19||S22 *with a proton beam energy of* 820 GeV *(stars with error band) corresponding to the data taking period 1996 and the first part of 1997, S15 with* 820 GeV *proton beam (triangles) corresponding to the second part of 1997 and S15 with a proton beam energy of* 920 GeV *(circles) corresponding to 1999 conditions. Events from EPJPSI-direct are used which have passed all selection cuts described above. The efficiency is shown as a function of a)* $W_{\gamma p}$*, b)* z *and c)* $p^2_{t,\psi}$*.*

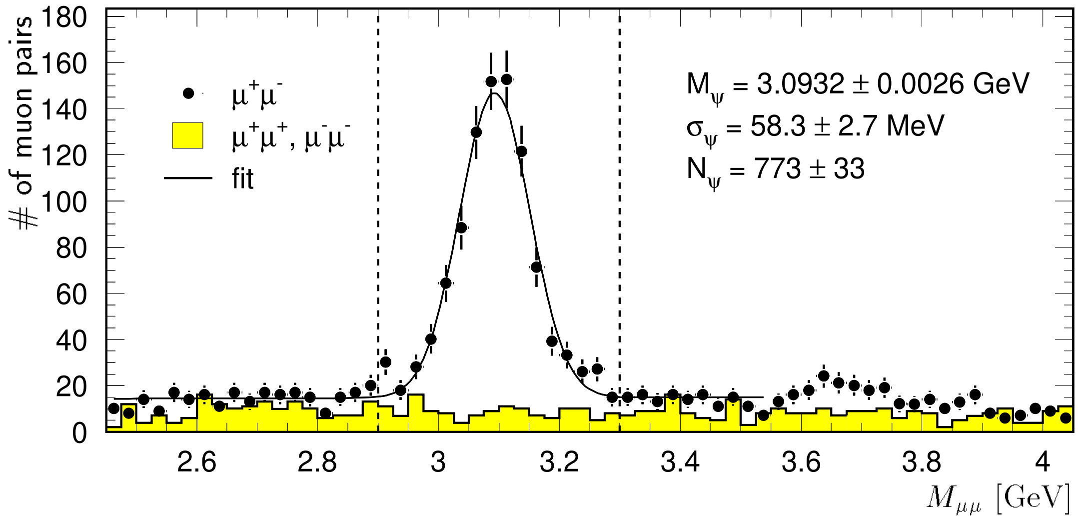

Figure 4.11: *The invariant mass distribution of the muon pairs for the medium z selection. The unlike-sign spectrum is fitted with a Gaussian for the J/ψ mesons plus a straight line for the non-resonant background ($\chi^2/\mathrm{NDF} = 1.33$). The fitted values for the J/ψ mass and width and for the number of J/ψ mesons are given.*

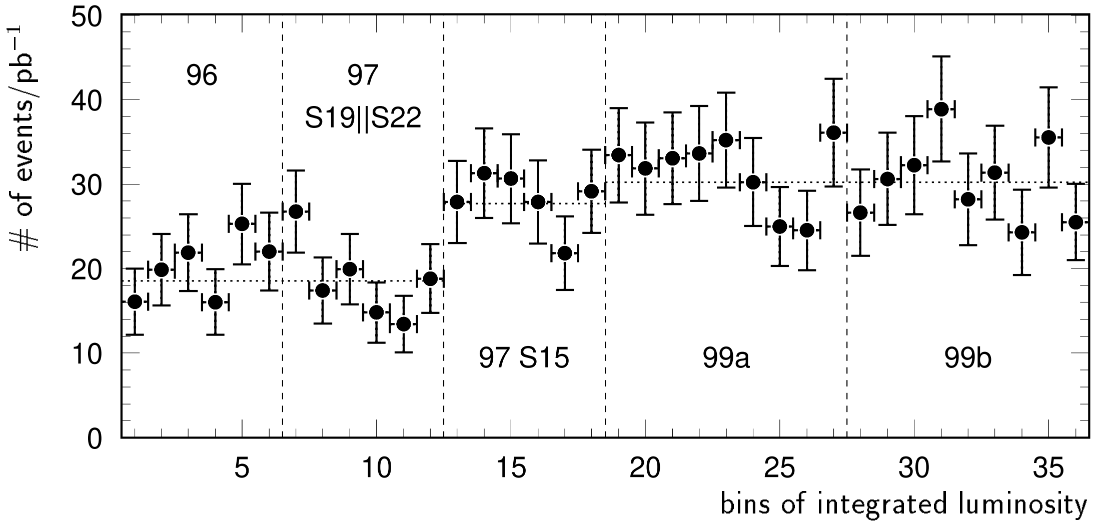

Figure 4.12: *The number of selected events per integrated luminosity in $\sim 1\,\mathrm{pb}^{-1}$ bins. Only events with unlike-sign muon pairs in the J/ψ mass region $2.9 < M_{\mu\mu} < 3.3\,\mathrm{GeV}$ are used. The different data taking periods are indicated by the dashed lines. In 1997 the trigger requirements of this analysis are changed from* S19||S22 *to* S15. *The fits with a constant for periods with the same running conditions* (96+97_1/97_2/99) *are represented as dotted lines* ($\chi^2/\mathrm{NDF} = 0.95/0.54/0.67$).

4.3 Selection of J/ψ Mesons at Low z

Production of J/ψ mesons in the region of small elasticities, $z < 0.45$, is expected to proceed at least partially through resolved photon processes. Therefore the total efficiency will be discussed mainly for gluon-gluon fusion, which dominates the resolved photon processes. The efficiencies which are used to correct the selected data are determined with simulations of gluon-gluon fusion (EPJPSI-resolved, see section 3.1.2) and direct photon-gluon fusion (EPJPSI-direct, see section 3.1.1). The relative normalization of the contributions is discussed in section 6.2.1.

4.3.1 Acceptance

As for the analysis at medium z, the decay muons of the J/ψ have to be detected in the acceptance region of the central tracking detector. At low elasticities, however, the J/ψ only has a small fraction of the photon momentum. This results in small polar angles of the J/ψ and its decay particles. At large polar angles the non-resonant background originating from hadrons mis-identified as muons exceeds the expected J/ψ signal by orders of magnitude. Therefore the polar angle of the decay muons is restricted to $20° < \vartheta_\mu < 140°$. On the other hand the momentum cut is chosen to be as low as possible for the muon identification, $p_\mu > 0.8\,\mathrm{GeV}$, in order to improve the acceptance.

In addition to the requirements for the decay leptons a cut on the transverse momentum of the J/ψ meson, $p_{t,\psi}^2 > 1\,\mathrm{GeV}^2$, is applied to enhance the J/ψ signal in the data. This cut is not corrected for, but treated as a restriction in the kinematic range of the analysis. It affects the polar angle and momentum distributions of the decay muons and is therefore taken into account for the acceptance and efficiency calculation.

In the kinematic region of the low z analysis the acceptance does not only depend on $W_{\gamma p}$ but also depends strongly on z. For very low values of z the acceptance tends towards zero (fig. 4.13 a). To avoid large uncertainties arising from an extrapolation to this region, the analysis is restricted to the range $0.05 < z < 0.45$. The acceptance in this region is shown in figure 4.13 b) as a function of $W_{\gamma p}$. A cut $W_{\gamma p} > 120\,\mathrm{GeV}$ avoids the area where the acceptance is below half of its maximum value. No systematic difference is seen for the two proton beam energies. The acceptance for direct photon-gluon fusion has a similar dependence on z (not shown in figure 4.13) but its maximum is at much lower $W_{\gamma p}$ values. Since the aim of this analysis is to establish the existence of contributions to J/ψ production via resolved photon processes, the cuts are chosen to optimise the acceptance for these processes.

4.3.2 Selection Efficiency

Photoproduction events are selected with the same requirements as in the medium z range, i.e. no electromagnetic cluster with energy greater than 8 GeV detected in the

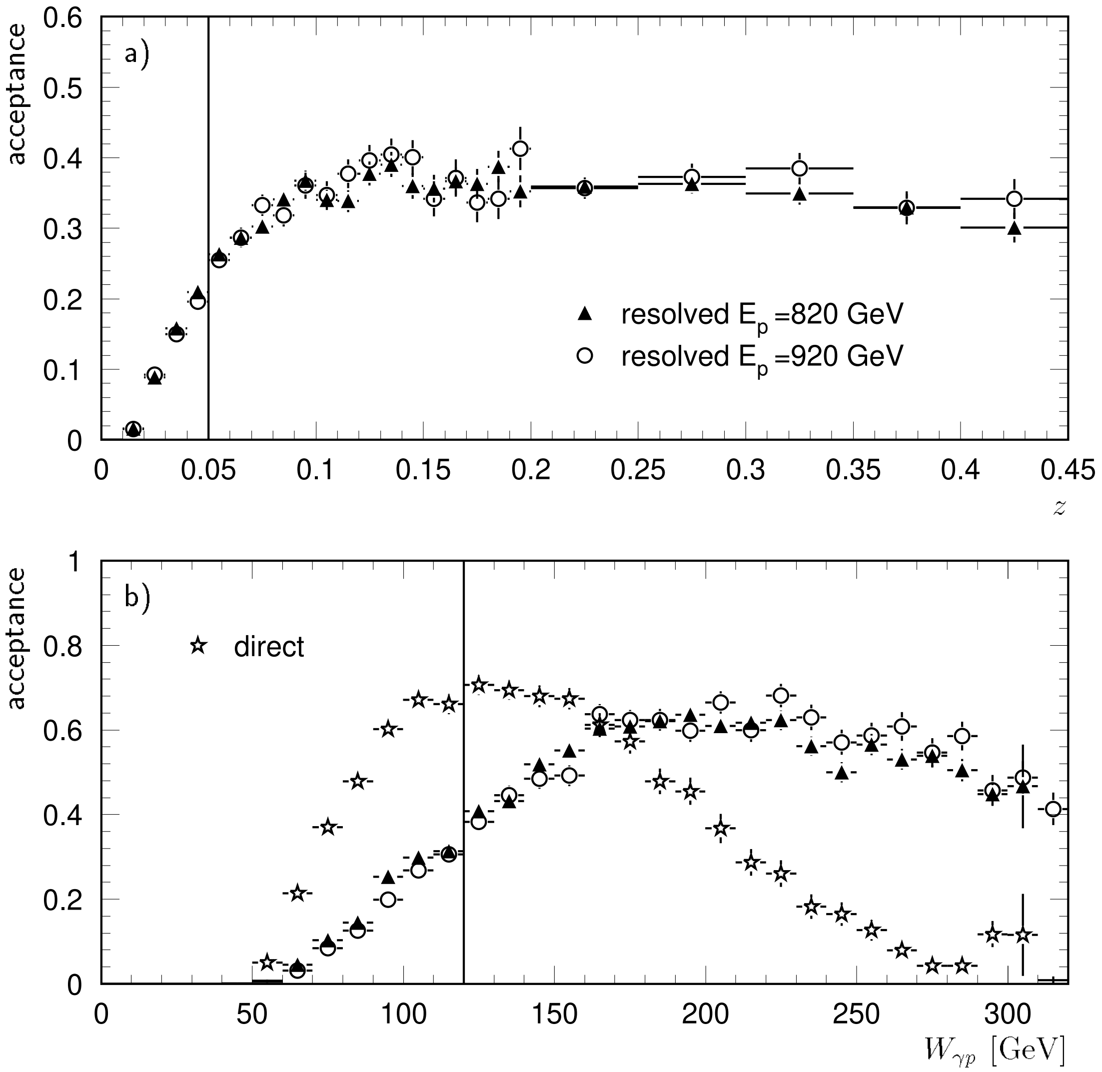

Figure 4.13: *a) The acceptance of the cuts* $20° < \vartheta_\mu < 140°$ *and* $p_\mu > 0.8\,\mathrm{GeV}$ *as a function of* z *for resolved photon processes in the range* $Q^2 < 1\,\mathrm{GeV}^2$ *and* $p_{t,\psi}^2 > 1\,\mathrm{GeV}^2$. *To avoid large uncertainties in the extrapolation to very low* z*, the analysis is restricted to* $z > 0.05$. *b) The acceptance as a function of* $W_{\gamma p}$ *in the kinematic range* $Q^2 < 1\,\mathrm{GeV}^2$, $p_{t,\psi}^2 > 1\,\mathrm{GeV}^2$ *and* $0.05 < z < 0.45$. *The vertical line shows the lower* $W_{\gamma p}$ *cut (*$W_{\gamma p} > 120\,\mathrm{GeV}$*).*

calorimeters, and the energy in the veto layer of the SpaCal smaller than 1 GeV. Since the photon remnant can lead to an electromagnetic cluster in the SpaCal, the value of the energy cut should be as high as possible. In figure 4.14 the effect of a veto on electromagnetic clusters with energies above a value E_{cut} is studied as a function of E_{cut} for a gluon-gluon fusion simulation with resolved photons and a direct photon-gluon fusion simulation (both with a proton beam energy of $E_p = 820\,\mathrm{GeV}$). Clusters with an energy of less than 1 GeV are not stored on DST as candidates for the scattered electron, which means that a cut of $E_{cut} = 1\,\mathrm{GeV}$ corresponds to no reconstructed (stored) cluster. In the direct case this requirement is fulfilled by more than 95% of the events in photoproduction, while for the resolved Monte Carlo simulation an efficiency of 95% is only reached above $E_{cut} = 6\,\mathrm{GeV}$. For $E_{cut} = 8\,\mathrm{GeV}$ the simulations of both processes show nearly the same efficiency.

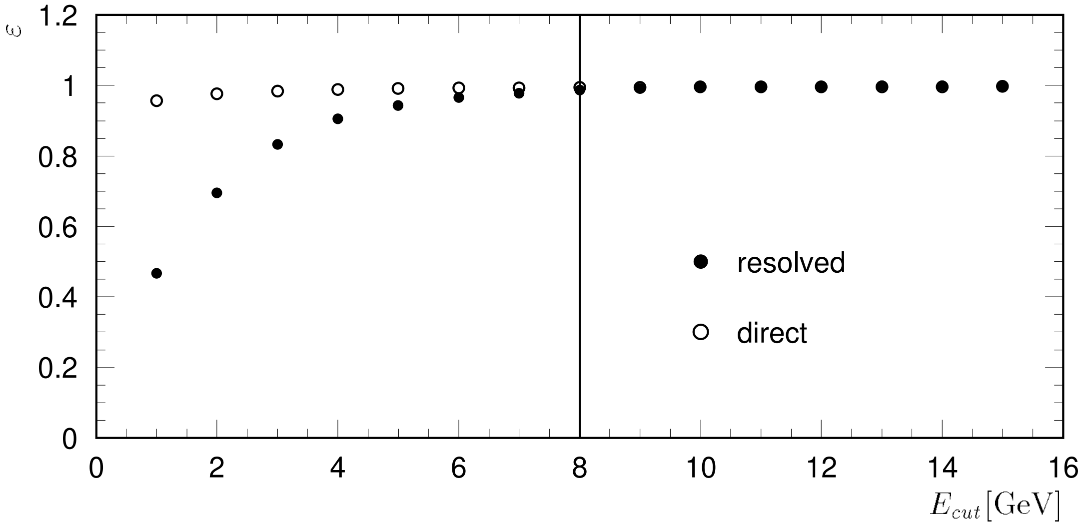

Figure 4.14: *Efficiency of the veto on electromagnetic clusters with energies above a value E_{cut}, which is applied to select photoproduction events, as a function of E_{cut} for a gluon-gluon fusion simulation with resolved photons and a direct photon-gluon fusion simulation. The kinematic region is restricted to $Q^2 < 1\,\mathrm{GeV}^2$. $E_{cut} = 1\,\mathrm{GeV}$ corresponds to events with no reconstructed electromagnetic cluster. For the analysis $E_{cut} = 8\,\mathrm{GeV}$ is chosen.*

As in the medium z analysis both decay particles have to pass the Lee West track selection ($20° < \vartheta_\mu < 140°$ and $p_\mu > 0.8\,\mathrm{GeV}$) and be identified as muons with the standard requirements. At least one muon has to be identified in the central muon detector because all triggers require elements of the instrumented iron. Since subtrigger S56 contains the trigger element `Mu_Any`, in contrast to the medium z analysis also the inner endcaps of the CMD are used.

In principle two methods can be used to check the muon identification in the simulation. The second method will be chosen here.

1. The identification in the LAr calorimeter can be probed using muons already identified in the instrumented iron and vice versa. This is statistically limited, because the identification efficiencies of the LAr calorimeter and the CMD are very complementary in ϑ_μ (fig. 4.15).

2. The identification efficiency can be studied with events which are known to have two muons and are tagged by the identification of one muon. The muonic decay mode of J/ψ mesons is suited for this method. It is necessary, however, to know which track in an event is the second muon, which is a problem for events with high track multiplicities.

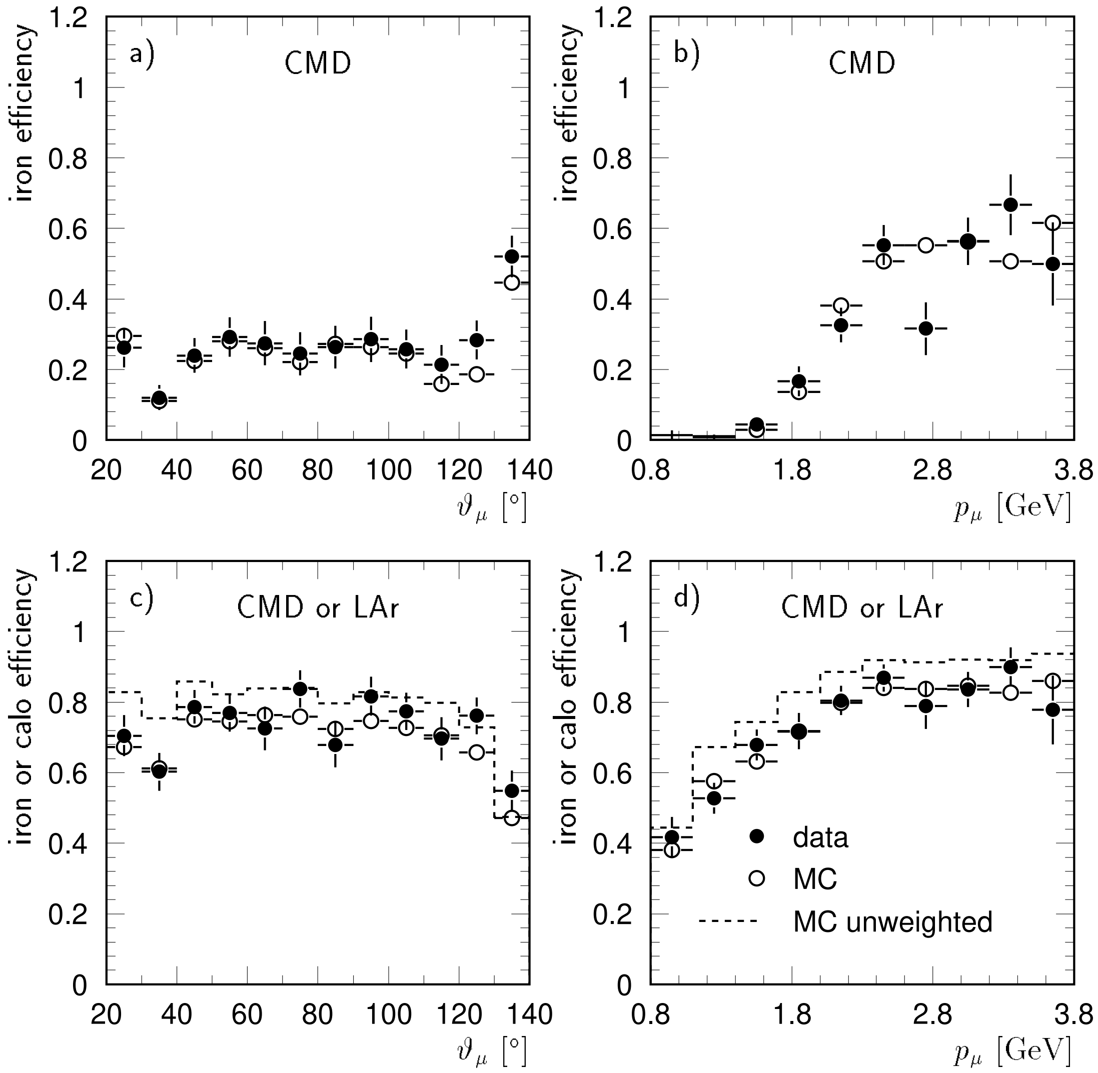

Figure 4.15: *Muon identification efficiency in the Central Muon Detector (CMD, upper plots) and in the CMD or the LAr calorimeter (lower plots) for 1996 and 1997. The simulation before (dashed line) and after (open circles) ϑ_μ dependent reweighting of the calorimeter identification efficiency with the function determined in the medium z analysis is compared to data (filled circles). For details of the data sets see text.*

In figure 4.15 the muon identification efficiency in the Central Muon Detector and in the LAr calorimeter or the CMD determined with the second method is compared between data and a two component Monte Carlo simulation.
In practice in the data the number of tracks has to be restricted to exactly two in order to select a clean J/ψ sample with one identified muon. For more tracks the combinatorial background is too high. The selection of events with two good tracks fulfilling $20° < \vartheta < 140°$ and $p > 0.8\,\mathrm{GeV}$, one of them identified as muon in the LAr calorimeter ($Q_c = 3$) or in the CMD leads to a quasi-elastic J/ψ sample similar to the one used for the determination of the identification efficiency for the medium z analysis. A cut on the J/ψ mass region and the requirement of an independent subtrigger are also applied. The

efficiency is determined by dividing the number of events where the second track is also identified as a muon by the total number of quasi-elastic events.
A two component simulation consisting of gluon-gluon fusion with resolved photons and direct photon-gluon fusion is used. For an inelastic simulation at low z, especially for the resolved photon processes, exactly two good tracks cannot be required since the track multiplicities are high. On the other hand in the simulation it is known which particle is the second muon, so that the requirement of exactly two good tracks is not needed. For the efficiency determination events with at least two tracks and one identified muon are used. The same p, ϑ and muon identification cuts as in the data are applied. The identification efficiency is calculated by dividing the number of events, where the second generated muon is found as a track and identified as a muon, divided by the number of events where the track is found.
For the comparison of the efficiencies the data sample and the simulation should be as similar as possible in the observables that the muon identification efficiency depends upon. The most important observable is the polar angle ϑ_μ. The relative normalization of the simulations is therefore chosen to fit the ϑ_μ distribution in the data. In addition the analysis cut on the transverse momentum squared of the J/ψ meson, $p_{t,\psi}^2 > 1\,\mathrm{GeV}^2$, is applied both in the quasi-elastic data sample and in the simulation, since it influences both the polar angle and the momentum distributions of the decay muons. This requirement reduces the statistics in comparison to the medium z analysis.
Despite the differences in the datasets mentioned above reasonable agreement between data and simulation is found (fig. 4.15). The remaining differences of the identification efficiency in the LAr calorimeter can be corrected with same weighting function determined in the medium z analysis. A possible influence of energy depositions in the LAr calorimeter in the vicinity of the muon or of additional tracks in the event is not observed in the simulation and has not been studied in the data.

In parallel to the medium z analysis at least three good tracks originating from the primary vertex are demanded. In figure 4.16 the resulting selection efficiency is shown as a function of the photon-proton centre-of-mass energy $W_{\gamma p}$, the elasticity z and the transverse momentum squared of the J/ψ meson $p_{t,\psi}^2$ for a resolved photon Monte Carlo simulation. As in the medium z analysis the efficiency for a proton energy of $E_p = 920\,\mathrm{GeV}$ is higher than for $E_p = 820\,\mathrm{GeV}$. The requirement $W_{\gamma p} < 260\,\mathrm{GeV}$ restricts the analysis to the plateau region of the selection efficiency in $W_{\gamma p}$. In the range $120 < W_{\gamma p} < 260\,\mathrm{GeV}$ the selection efficiency is nearly flat in z, while it increases with increasing $p_{t,\psi}^2$. The simulation of direct photon-gluon fusion shows a similar behaviour in the regions where the statistics is large (small $W_{\gamma p}$, high z and small $p_{t,\psi}^2$).

4.3.3 Trigger Efficiency

Similar to the medium z range the most efficient subtriggers in 1996 are S19 and S22 which cover the barrel region and the outer endcaps of the instrumented iron. At the beginning of the 1997 data taking period a dedicated resolved photon trigger, S56, was added. It uses the energy deposition of the photon remnant in the SpaCal. Therefore it is possible to include all regions of the CMD and to reduce the track requirement in the trigger. On

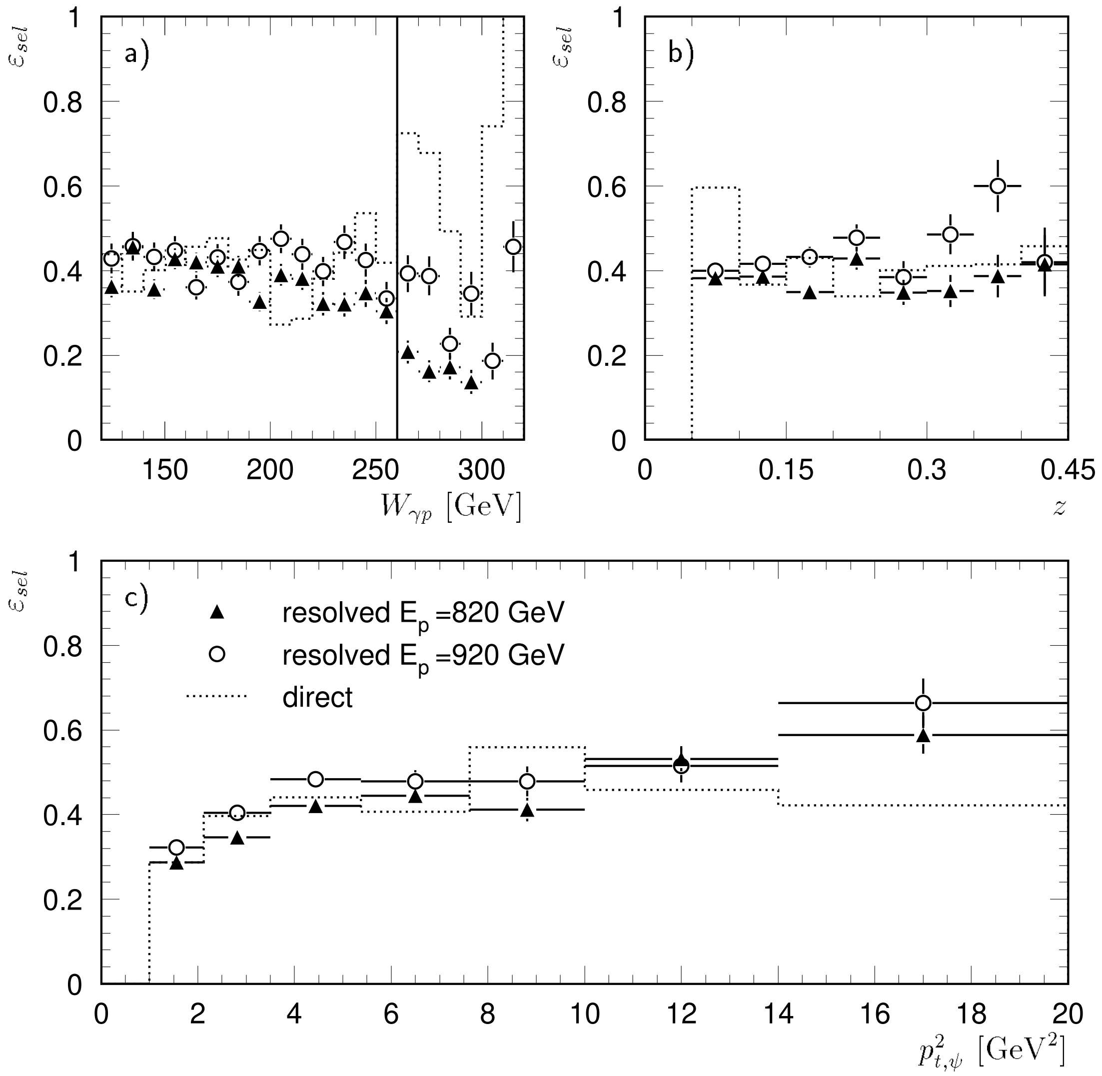

Figure 4.16: *Selection efficiency for EPJPSI-resolved and EPJPSI-direct in the kinematic region* $0.05 < z < 0.45$, $Q^2 < 1\,\mathrm{GeV}^2$ *and* $p^2_{t,\psi} > 1\,\mathrm{GeV}^2$. *The requirement* $W_{\gamma p} < 260\,\mathrm{GeV}$ *restricts the analysis to the plateau region of the selection efficiency of EPJPSI-resolved (a). The selection efficiency as a function of b) z and c) $p^2_{t,\psi}$ is displayed for* $120 < W_{\gamma p} < 260\,\mathrm{GeV}$.

the other hand only about a half of the simulated events in resolved photoproduction at low z (and nearly no event originating from direct photon-gluon fusion) show such an energy deposition, so S56 is used in addition to S19 and S22.

Trigger Level 1

A comparison of the trigger efficiencies in data and simulation is performed as in the medium z analysis. For this analysis track trigger elements of the `DCRPh` and the `zVtx` systems are used as well as trigger elements from the SpaCal and the instrumented iron.

Again the results of the simulation are used to extract the cross sections. The differences between data and simulation are taken into account in the systematic error (see section 6.3).

The track trigger elements relevant to this analysis are DCRPh_Ta (S56), DCRPh_CNH and zVtx_sig1 (S19 and S22), which are studied in the low z region as a function of the number of good tracks N_{good} and the elasticity z (fig. 4.17). Since most of the independent triggers are based on an energy deposition of the scattered electron in the SpaCal, the photoproduction requirements are not imposed on the data set used to determine the track trigger efficiencies. All other analysis cuts are applied. Reasonable agreement between the simulation and the data is found.

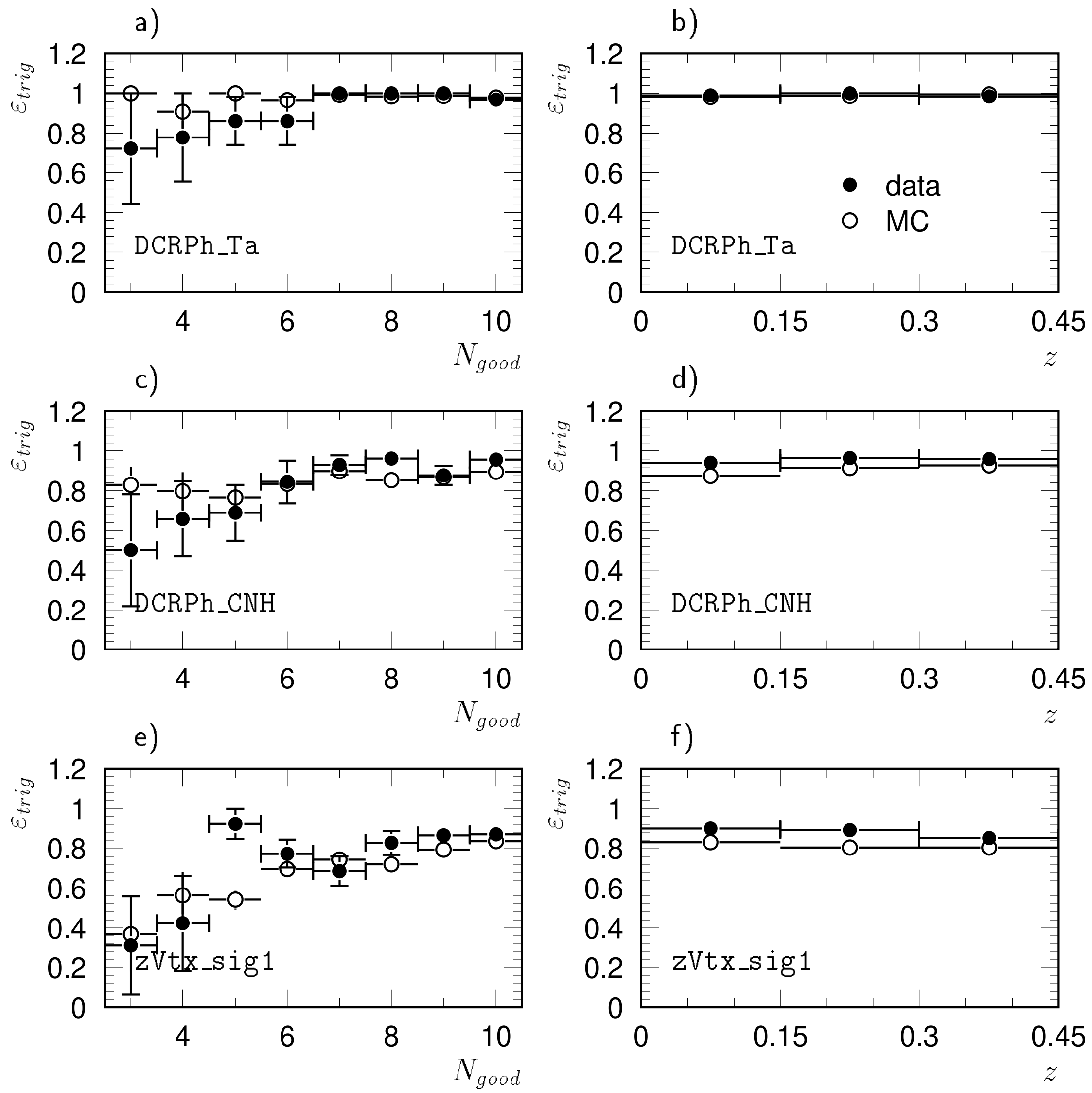

Figure 4.17: *Trigger efficiencies of the track trigger elements* DCRPh_Ta, DCRPh_CNH *and* zVtx_sig1 *as a function of the number of good tracks N_{good} (left). The trigger efficiencies as a function of the elasticity z for the same trigger elements are shown on the right.*

Subtrigger S56 includes the combination `SPCLe_IET>1||SPCLe_IET_Cen_2` of SpaCal trigger elements. It covers the outer and inner region of the electromagnetic SpaCal and has a low energy threshold. In figure 4.18 a) the efficiency of this combination is studied as a function of the energy of the most energetic electromagnetic cluster in the SpaCal. For very small energies (below 2 GeV) the trigger is not efficient. Furthermore the Monte Carlo simulation does not agree with the data in this region. Therefore a validation of `SPCLe_IET>1||SPCLe_IET_Cen_2` using an electromagnetic cluster in the SpaCal with an energy deposit $E_{Cluster} > 2.5\,\mathrm{GeV}$ is required. The efficiency of the validated trigger element combination is studied as a function of the elasticity z and the polar angle $\vartheta_{Cluster}$ of the most energetic electromagnetic cluster in the SpaCal (fig. 4.18 b,c). Except for the highest z bin, where only very few events with SpaCal clusters exist, good agreement between data and simulation is found.

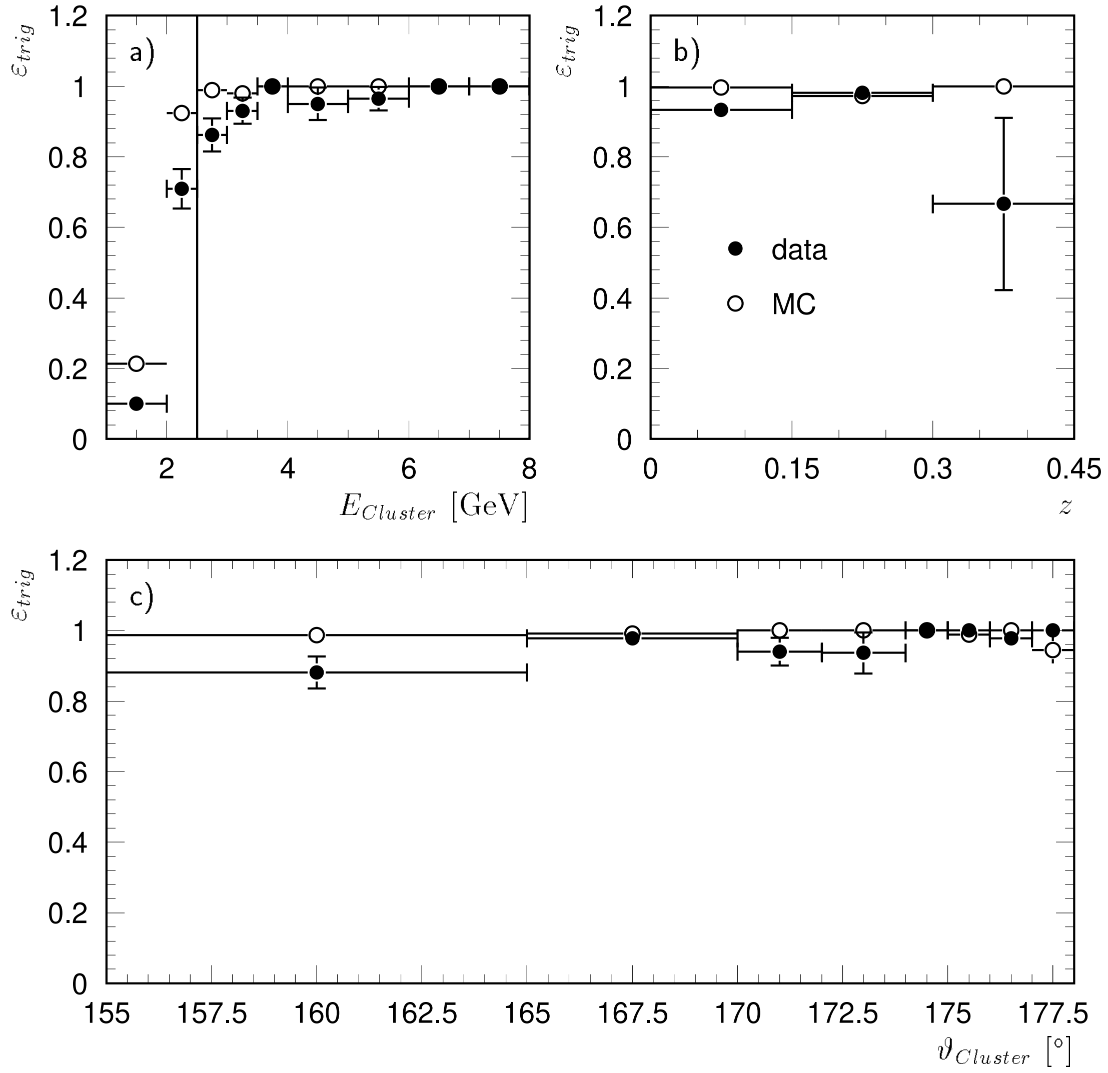

Figure 4.18: *a) Trigger efficiency of* `SPCLe_IET>1||SPCLe_IET_Cen_2` *as a function of the energy $E_{Cluster}$ of the most energetic electromagnetic cluster in the SpaCal. Efficiency of the same trigger as in a) requiring $E_{Cluster} > 2.5\,\mathrm{GeV}$ as a function of b) z and c) the polar angle $\vartheta_{Cluster}$ of the most energetic electromagnetic cluster in the SpaCal.*

The efficiencies of the trigger elements of the instrumented iron are studied using events containing exactly one track in the central muon detector. All selection cuts except the photoproduction requirement are imposed. An additional cut against cosmic ray muons is not needed because of the transverse momentum of the J/ψ candidate (the selection cut is $p_{t,\psi}^2 > 1\,\mathrm{GeV}^2$). In figure 4.19 the efficiencies of the combination `Mu_Bar||Mu_ECQ` and the trigger element `Mu_Any` are displayed as a function of the polar angle ϑ_μ and the momentum p_μ of the muon identified in the central muon detector. Good agreement between data and the combination of the EPJPSI-direct and EPJPSI-resolved simulations is seen in ϑ_μ. The reason for the smaller efficiency of `Mu_Any` at low momenta in the data

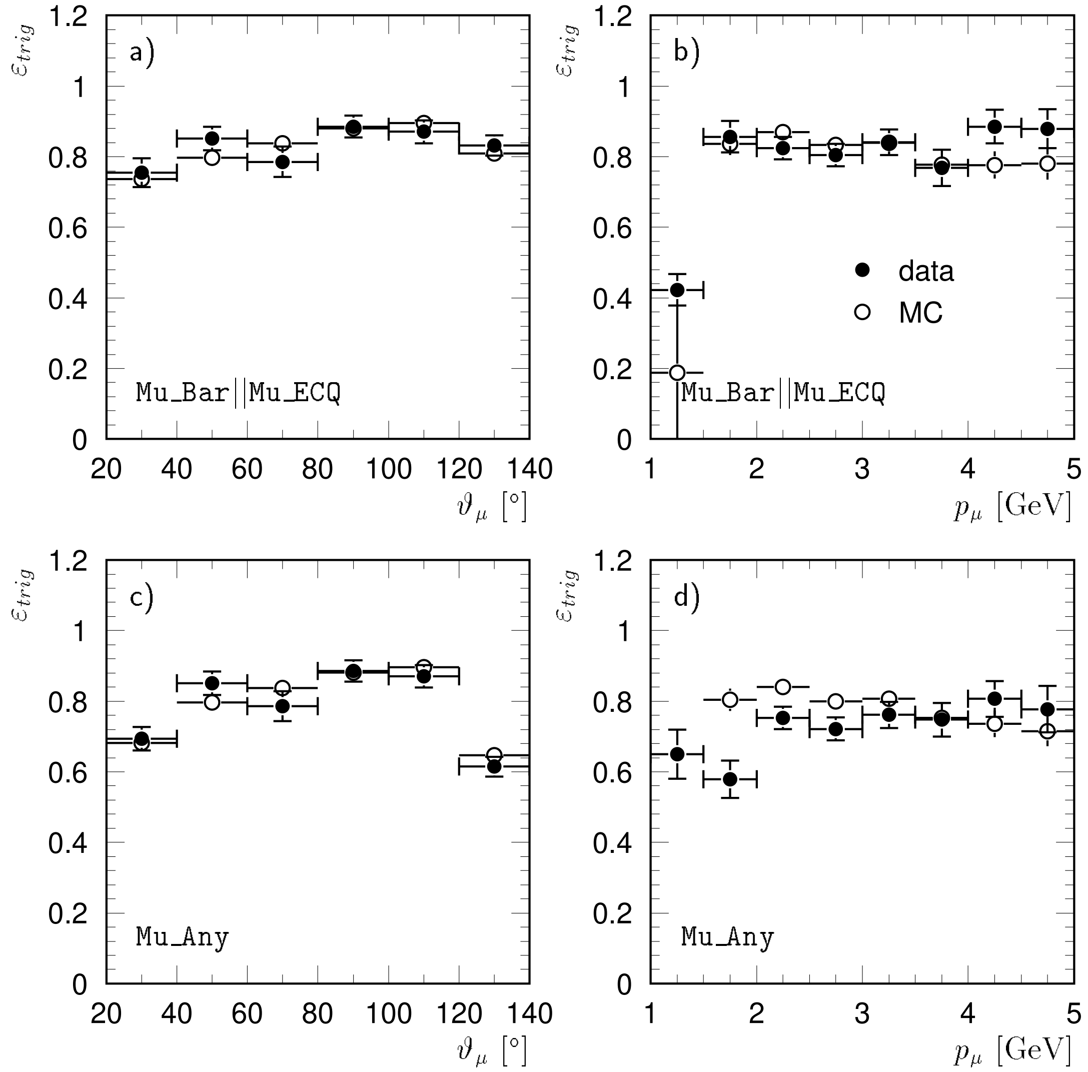

Figure 4.19: *The trigger efficiency of the combinations of trigger elements a)* `Mu_Bar||Mu_ECQ` *and c)* `Mu_Any` *as a function of the polar angle ϑ_μ of the muon identified in the instrumented iron. The trigger efficiency as a function of the momentum p_μ of the muon for the same trigger elements is shown in b) and d). A two component simulation (EPJPSI-resolved and EPJPSI-direct, open circles) is compared with the data (filled circles).*

is a different ϑ_μ distribution originating from background events in the inner endcaps of the CMD.

Level 1 Prescaling

The effect of prescaling on trigger level L1 is more important for the low z analysis than for medium z. Since subtrigger S56 always has a prescale factor of 1, also in trigger phase 1, phase 1 is included for this analysis. Subtriggers S19 and S22 have prescale factors of up to 1000 in phase 1. The weighting with the integrated luminosity results in a maximum value of the mean prescale of S19 and S22 of about 1.2 in 1997. In total, the mean weight of all events in all data taking periods is 1.08.

Trigger Level 4

The efficiency of the L4 trigger verification in 1996 and 1997 is compatible with the values obtained in the medium z analysis for S19 and S22: $\varepsilon_{\mathrm{L4,S19}} = 82.4\% \pm 1.2\%$ (medium z $84.6\% \pm 1.3\%$) and $\varepsilon_{\mathrm{L4,S22}} = 97.9\% \pm 0.8$ ($97.2\% \pm 0.5\%$). This is expected, because no dependence of the L4 efficiency on the properties of the triggering muon is found. The L4 verification efficiency for S56 is shown in figure 4.20. A total value of $\varepsilon_{\mathrm{L4,S56}} = 97.9\% \pm 0.7\%$ is obtained. The inefficiency of the trigger verification for S19 is corrected in the Monte Carlo, for S22 and S56 it is treated as a systematic error.

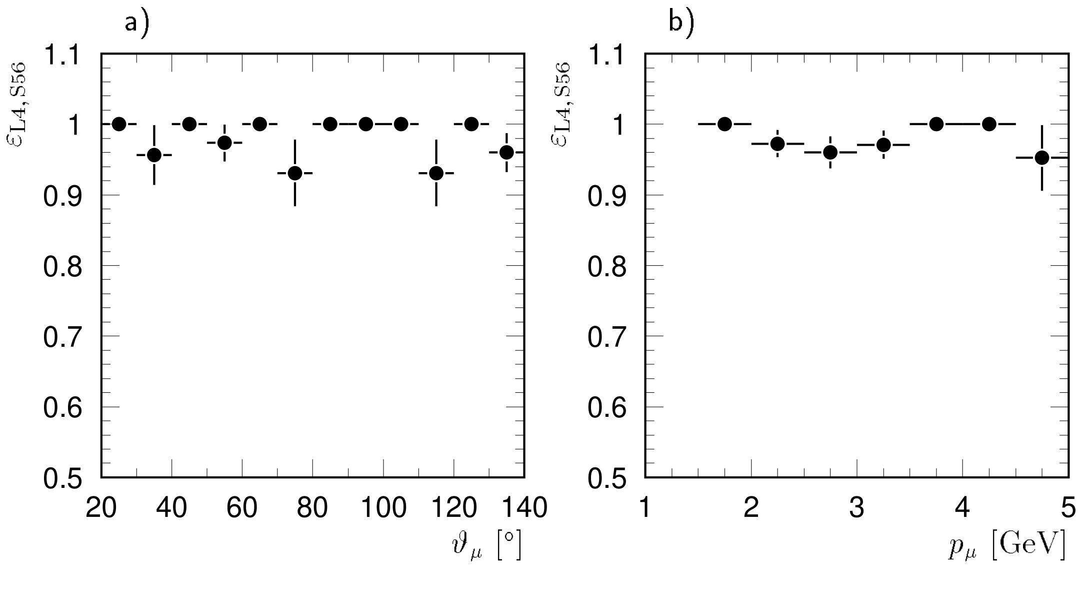

Figure 4.20: *Efficiency of the trigger verification on level 4 for* `S56` *in the data taking period 1997 as a function of a) the polar angle ϑ_μ and b) the momentum p_μ of the muon identified in the instrumented iron.*

In 1999 a total of eleven events are found which fulfil the selection cuts of the low z analysis but are not accepted by the high mass finder. Ten of these events were accepted by other 'final state finders' or a 'hard scale' and have a weight of 1, the other event was downscaled as 'soft physics' with weight 10. The resulting L4 efficiency is $\varepsilon_{\mathrm{L4}} = 98.4\% \pm 0.8\%$. This is again considered in the systematic error.

Total Trigger Efficiency

In figure 4.21 the total trigger efficiency is shown for a direct photon-gluon fusion and a resolved photon Monte Carlo simulation. It is studied for events passing all selection cuts as described above. The two types of Monte Carlo simulation show no significant systematic differences. In the region of high $W_{\gamma p}$ and very small z only very few events originating from direct photon-gluon fusion are found, therefore the statistical errors are rather large in these regions.

4.3.4 Selected Data Sample

The number of events which remain after applying the cuts described before are listed in table 4.3. The invariant mass spectrum of the muon pairs corresponding to the final selection (last row) is shown in figure 4.22. The unlike-sign pairs show a clear J/ψ signal, which is however not as prominent as in the medium z analysis. The unlike-sign spectrum is fitted with a function to be taken a superposition of a Gaussian for the J/ψ meson and a straight line for the non-resonant background up to a mass of 3.55 GeV. The J/ψ mass determined from this fit is again lower than the nominal value, but compatible within the rather large error. The width $\sigma_\psi = 90.3$ MeV which is again dominated by the momentum resolution of the tracking chambers is much broader than in the medium z case ($\sigma_\psi = 58.3$ MeV). The number of J/ψ mesons determined by the fit changes from 164 ± 26 to 121 ± 18 if the width of the Gaussian is fixed to the value found in the medium z analysis. The precise determination of the number of J/ψ mesons is described in chapter 6.

In figure 4.23, the rate of selected events per integrated luminosity is studied in $\sim 2\mathrm{pb}^{-1}$ bins of the integrated luminosity. Since the beginning of 1997 subtrigger S56 is used in addition to S19 and S22, which is expected to lead to a slightly higher rate. The reason for the rate increase from 1997 to 1999 could be due to the rewiring of the CJC, but also a generally higher background in 1999. During the data taking periods the rate is compatible with the expected constant behaviour.

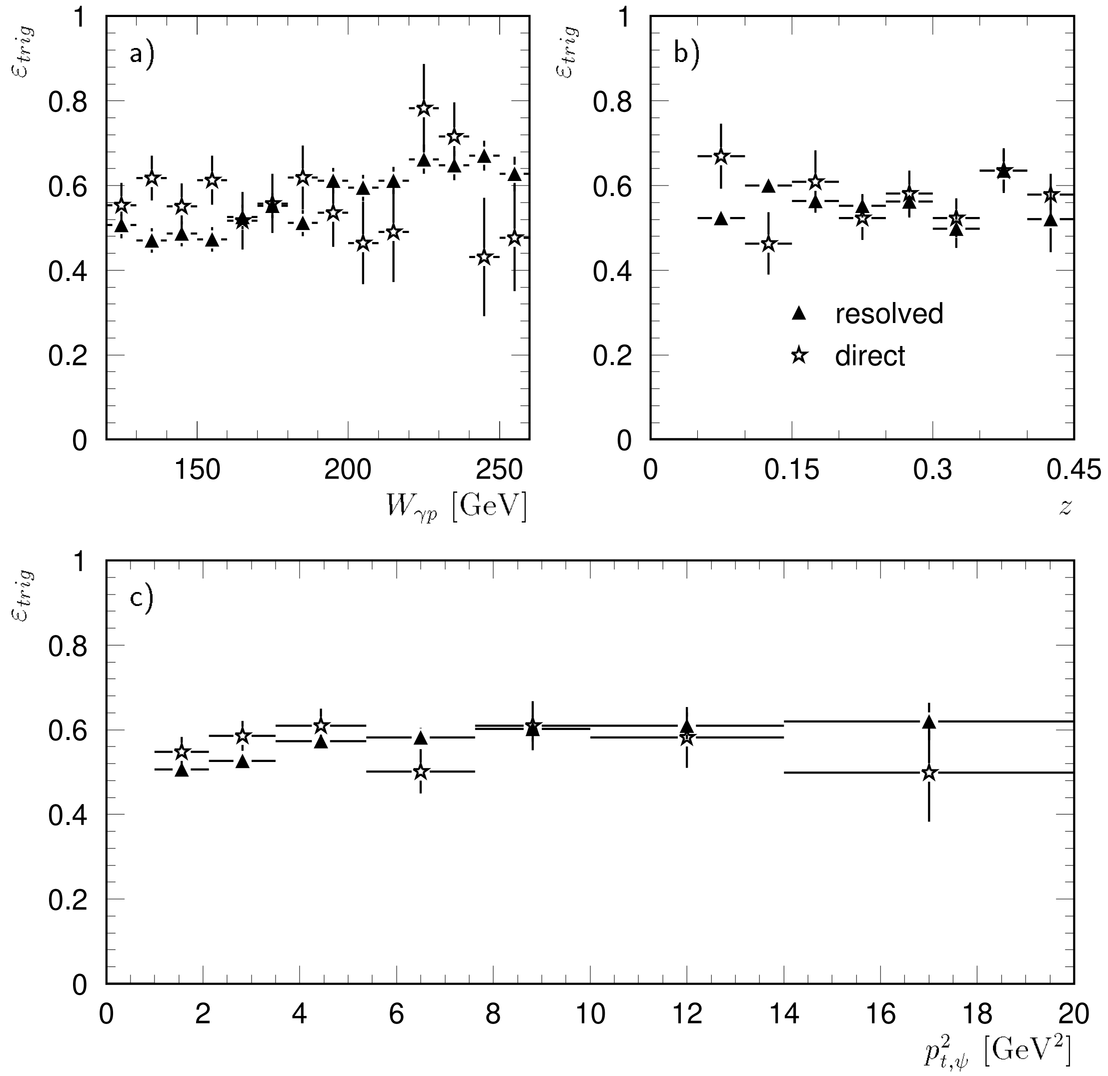

Figure 4.21: *Trigger efficiency in the kinematic region* $0.05 < z < 0.45$, $Q^2 < 1\,\mathrm{GeV}^2$, $120 < W_{\gamma p} < 260\,\mathrm{GeV}$ *and* $p_{t,\psi}^2 > 1\,\mathrm{GeV}^2$ *as a function of a)* $W_{\gamma p}$*, b)* z *and c)* $p_{t,\psi}^2$*. The efficiency is shown for the EPJPSI-resolved (triangles) and the EPJPSI-direct (stars) simulations.*

	1996	1997	1999 e^-	1999 e^+	sum
events on DST	23.2 mio.	31.0 mio.	17.3 mio.	21.9 mio.	93.4 mio.
class 24 / 16	1.3 mio.	2.2 mio.	1.9 mio.	0.9 mio.	6.3 mio.
≥ 2 muons, $M_{\mu\mu} > 2\,\mathrm{GeV}$, HV & run selection	45442	91623	82678	75029	294772
$\mu^+\mu^-$, $p_\mu > 0.8\,\mathrm{GeV}$, $20° < \vartheta_\mu < 140°$	9656	17735	28007	23144	78542
photoproduction	7494	13501	24114	19838	64947
$\lvert z_{\mathrm{vertex}}\rvert < 40\,\mathrm{cm}$, $N_{good} \geq 3$, ≥ 1 muon id. in CMD	1053	2740	3037	2416	9246
$0.05 < z < 0.45$, $p^2_{t,\psi} > 1\,\mathrm{GeV}^2$	540	1269	1139	1028	3976
$2.9 < M_{\mu\mu} < 3.3\,\mathrm{GeV}$	119	280	235	254	888
$120 < W_{\gamma p} < 260\,\mathrm{GeV}$	388	902	777	717	2784
$2.9 < M_{\mu\mu} < 3.3\,\mathrm{GeV}$	83	195	159	171	608
trigger	263	572	517	458	1810
$2.9 < M_{\mu\mu} < 3.3\,\mathrm{GeV}$	58	131	110	120	419
prescale weighted	265.0	682.4	536.8	474.9	1959.1
$2.9 < M_{\mu\mu} < 3.3\,\mathrm{GeV}$	58.3	155.7	114.3	124.7	453.0

Table 4.3: *Numbers of selected events for the* **low z** *analysis 1996 to 1999.*

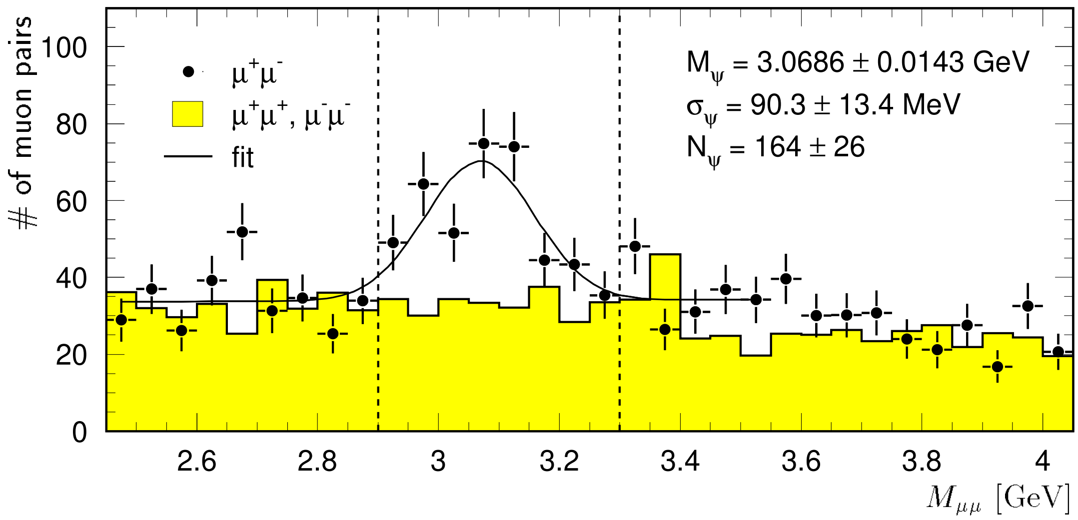

Figure 4.22: *The invariant mass distribution of the muon pairs for the low z selection. A clear J/ψ signal is seen in the unlike-sign pairs. The unlike-sign spectrum is fitted with a Gaussian for the J/ψ mesons plus a straight line for the non-resonant background. The fitted values for the J/ψ mass and width and for the number of J/ψ mesons are given.*

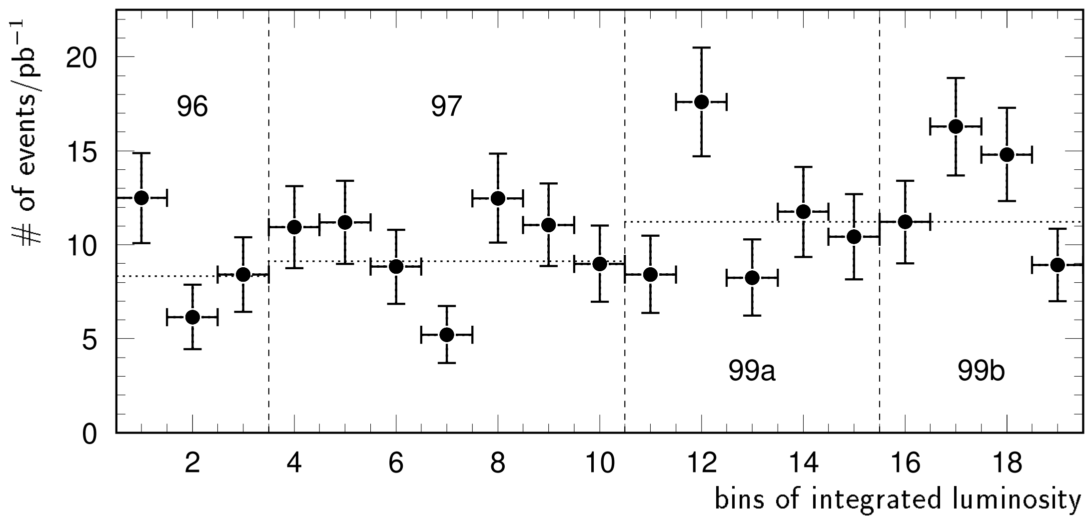

Figure 4.23: *The number of selected events per integrated luminosity in* $\sim 2\,\mathrm{pb}^{-1}$ *bins. Only events with unlike-sign muon pairs in the J/ψ mass region* $2.9 < M_{\mu\mu} < 3.3\,\mathrm{GeV}$ *are used. The different data taking periods are indicated by the dashed lines. The fits with a constant for periods with the same running conditions are represented as dotted lines.*

Chapter 5

J/ψ Photoproduction at Medium z

In this chapter the results for the photoproduction of J/ψ mesons in the region $0.3 < z < 0.9$ are discussed. The first section describes the determination of the number of J/ψ mesons in the data and the background subtraction. The Monte Carlo simulations of direct photon-gluon fusion (EPJPSI-direct) and resolved photon processes (EPJPSI-resolved) are then normalized and compared to the data. The two component simulation is used to extract cross sections. In previous analyses the systematic error was simply estimated by the remaining differences between the corrected simulation and the data. In view of smaller statistical errors a more thorough investigation is performed here. After the bin centre corrections, single and double differential cross sections are presented and compared to previous data and theoretical predictions. In the last section decay angular distributions are analysed.

5.1 Background Subtraction

After the selection chain described in the previous chapter, a significant non-resonant background in the invariant mass distribution is still observed. This background consists mainly of muon candidate pairs, where one or both particles are hadrons mis-identified as muons. Therefore it depends on the number of charged particles in the event which is strongly correlated with z, but also with $W_{\gamma p}$. For this reason the following procedure is used to determine the number of J/ψ mesons:

1. In each analysis bin the invariant mass spectrum of the unlike-sign muon pairs is fitted with a function taken to be a superposition of a Gaussian for the J/ψ signal and a linear function for the non-resonant background. Since the number of events used in each analysis bin is comparatively small, the size of the bins in the mass distribution has to be large (the order of the width of the Gaussian). Therefore the position of the peak and the width of the Gaussian are determined by a fit to the complete data sample, where the bin size can be much smaller (fig. 4.11).

2. The number of J/ψ mesons is calculated by counting the number of muon pairs in the mass window $2.9 < M_{\mu\mu} < 3.3\,\mathrm{GeV}$ and subtracting the non-resonant background obtained from the fit described under 1. This method is not as sensitive to the shape and the width of the peak as the number of events under the Gaussian obtained from the fit. The numbers obtained directly from the fit are usually smaller than the ones obtained from the method outlined. This is probably due to the fact that the detector components involved in the measurements of the tracks have different momentum and angular resolutions. It is not expected that one Gaussian describes the shape of the peak perfectly and the broader tails are not taken into account completely in the fit. As an example, the number of J/ψ mesons from the fit is compared to the method outlined above for different elasticities z in table 5.1 and figure 5.1. The corresponding tables for $W_{\gamma p}$, $p_{t,\psi}^2$ and x_g can be found in appendix D (tables D.1 to D.3). The differences are, however, not larger than the statistical error.

3. The statistical error of the total number of muon pairs in the mass window is used as estimate for the error of the number of J/ψ mesons. For the comparison the error from the fit is listed in the third column of table 5.1.

z	N_ψ	N_ψ fit	ΔN_ψ
$0.30 - 0.45$	99 ± 13	85 ± 12	14
$0.45 - 0.60$	154 ± 14	147 ± 13	7
$0.60 - 0.75$	187 ± 14	185 ± 14	2
$0.75 - 0.90$	179 ± 14	178 ± 14	1

Table 5.1: *The number of J/ψ mesons in bins of the elasticity z after imposing a cut $p_{t,\psi}^2 > 1\,\mathrm{GeV}^2$ on the transverse momentum of the J/ψ meson. In addition to the values determined with the background subtraction method (N_ψ) the numbers obtained directly from the fitted Gaussian (N_ψ fit) and the differences (ΔN_ψ) are given. For the calculation of the statistical errors see text.*

5.2 Comparison with Simulations

In order to extract cross sections the measured distributions have to be corrected for the acceptance and efficiency of the selection discussed in the previous chapter. This is done with the help of the simulation which has been cross-checked with the data. The generator EPJPSI will be used. This method relies on the simulation being in reasonable agreement with the data. Since direct and resolved photon processes may contribute to the production of J/ψ mesons at medium z the normalization of the simulation of both contributions (EPJPSI-direct and EPJPSI-resolved) will be determined. A comparison of this two component simulation with data will then be presented.

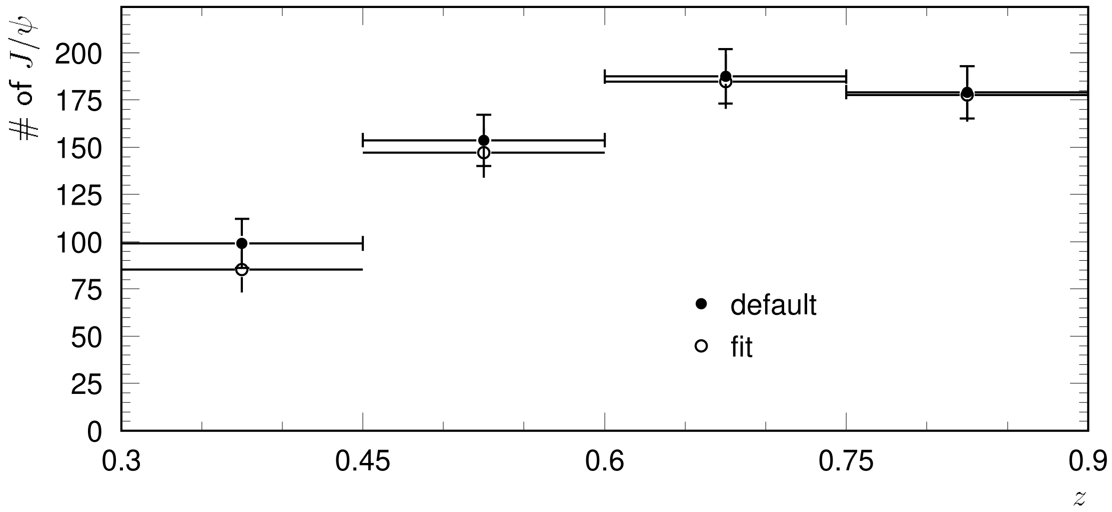

Figure 5.1: *Comparison of the number of J/ψ mesons in bins of the elasticity z after imposing a cut on the transverse momentum of the J/ψ candidate $p_{t,\psi}^2 > 1\,\mathrm{GeV}^2$. The black points show the values determined with the background subtraction method as described in the text, the open circles the ones obtained directly from the fitted Gaussian.*

5.2.1 Reweighting of $p_{t,\psi}^2$

As already mentioned in the selection chapter, the transverse momentum distribution of the J/ψ meson in the direct photon-gluon fusion simulation does not agree with the one observed in the data (fig. 5.2, dashed line). This is not surprising since the generator EPJPSI is a leading-order program and the $p_{t,\psi}^2$ spectrum is much harder in next-to-leading order calculations than in leading order [15]. The simulation is therefore reweighted on an event-by-event basis according to the value of $p_{t,\psi}^2$. In order to determine the weighting function the ratio of data to simulation is fitted with an exponential[1]. This gives a good description in the region $p_{t,\psi}^2 > 1\,\mathrm{GeV}^2$ (fig. 5.2, full line). All the distributions for the simulation which follow include the reweighting.

5.2.2 Normalization of Simulations

The variable which allows the best distinction between direct and resolved photon processes is the elasticity z. Resolved photon processes are expected to contribute only below $z \lesssim 0.4$. In the elasticity region above $z \gtrsim 0.4$ the simulation of direct photon-gluon fusion can be normalized. At very high z background from diffractive J/ψ production is expected. This is nearly completely removed by the requirement $z < 0.9$. J/ψ mesons originating from the decay of $\psi(2s)$ mesons which are produced in elastic and proton dissociative processes are significantly reduced by a cut $p_{t,\psi}^2 > 1\,\mathrm{GeV}^2$. The simulation of the direct process (EPJPSI-direct) is therefore normalized to the sum of the events in

[1]The slope of the exponential is 0.1, and the normalization , 1/1.7, is chosen to keep the total number of events in the simulation roughly constant. The maximum weight is about 7.

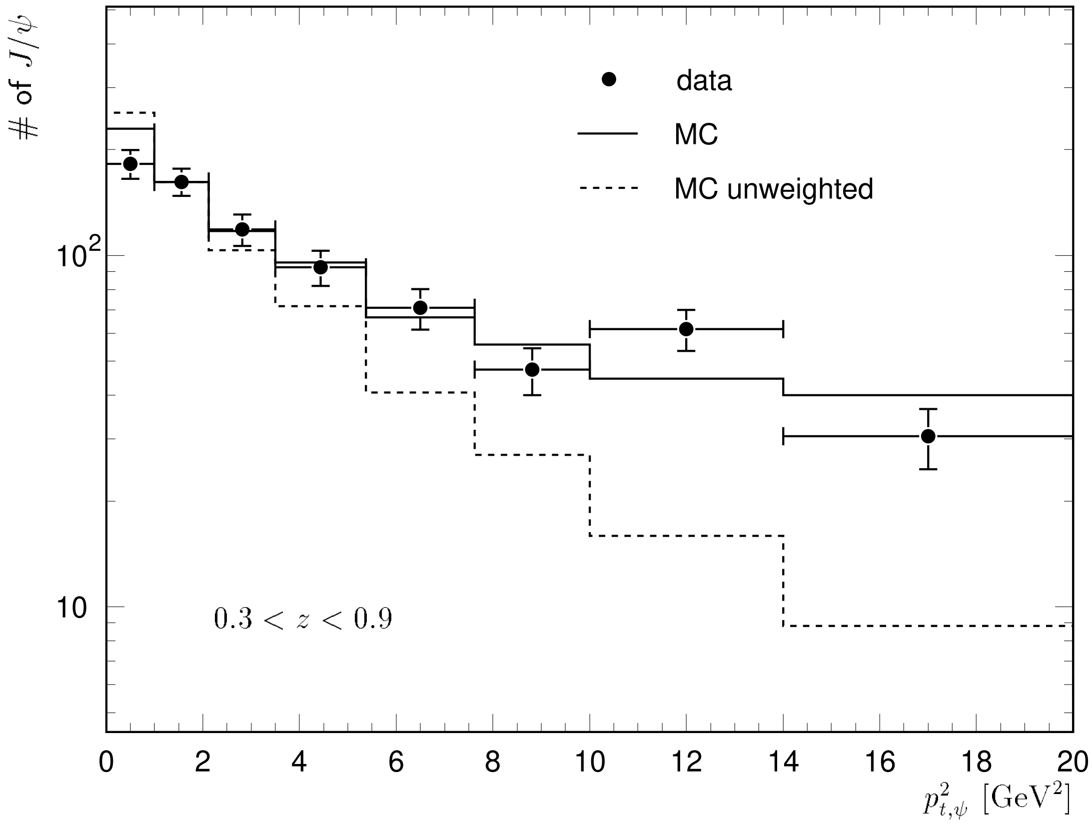

Figure 5.2: *Comparison of the transverse momentum squared of the J/ψ meson in the region $0.3 < z < 0.9$ between data (circles) and the direct photon-gluon fusion simulation before (dashed line) and after (full line) reweighting. The histograms for the simulation are normalized to the second bin of the data.*

the region $z > 0.45$ after applying the cut $p^2_{t,\psi} > 1\,\mathrm{GeV}^2$. The normalization factor is ~ 2.2, compatible with the expected k factor for direct photon-gluon fusion in the Colour Singlet Model [15]. One has to keep in mind, however, that the size of this factor depends on the normalization in the $p^2_{t,\psi}$ reweighting process. The normalization of the resolved photon simulation (EPJPSI-resolved) is determined for the low z analysis in section 6.2.1. It is assumed to be independent of z, and the normalization factor 0.8 is used also for the medium z region. The normalized two component simulation as a function of z is shown in figure 5.3 in comparison with the data. The contribution from resolved photon processes in the region $z > 0.45$ is found to be less than 1%, and in the lowest z bin ($0.3 < z < 0.45$) it amounts to 5%.

5.2.3 Distributions of Observables

After the reweighting of the transverse momentum of the J/ψ meson in the EPJPSI-direct simulation and the normalization of the two components, the simulation is in reasonable agreement with the data (fig. 5.4). The $W_{\gamma p}$ distribution, which is sensitive to the gluon

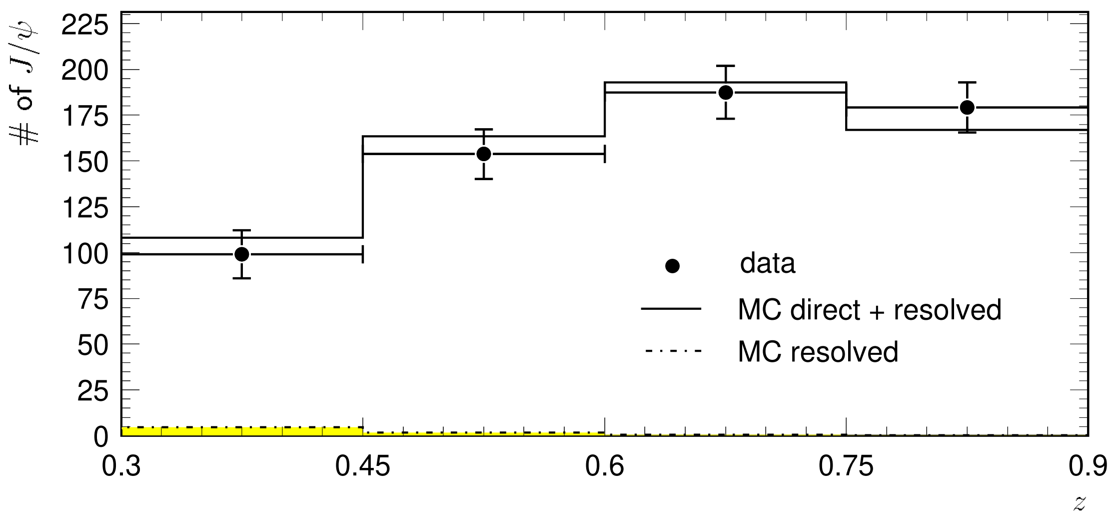

Figure 5.3: *Comparison of the elasticity distribution for $p_{t,\psi}^2 > 1\,\mathrm{GeV}^2$ between data (points) and the sum of the normalized simulations of direct and resolved photon processes (full line). The contribution from resolved photon processes is shown as a shaded histogram.*

density in the proton, has the same shape in the data and the simulation. The polar angle ϑ_ψ is correlated with the polar angle ϑ_μ of the decay muons, both of which have a maximum in the backward region of the detector. The muon momentum p_μ shows two peaks, one at low values originating from particles identified in the calorimeter and one around 2 GeV arising from muons reaching the instrumented iron.

The $p_{t,\psi}^2$ distributions in the low ($0.3 < z < 0.6$), intermediate ($0.6 < z < 0.75$) and high ($0.75 < z < 0.9$) elasticity regions are also in reasonable agreement between data and simulation (fig. 5.5 a – c). At high values of $p_{t,\psi}^2$ the numbers of J/ψ mesons in the data are very small, therefore more statistics would clearly improve this double differential measurement. The $p_{t,\psi}^2$ distribution for higher elasticities, $z > 0.9$, is shown in figure 5.5 d). The simulation lies clearly below the data due to missing diffractive contributions. The behaviour of the data, however, is similar to the other z regions. This means that high z events wrongly reconstructed at 'too small' z would have only a very small effect on the measured shape of the $p_{t,\psi}^2$ distribution.

5.3 Systematic Errors

The systematic errors are listed in table 5.2. The dominant contributions are due to uncertainties in the description of the data by the simulation which were discussed in chapter 4. The sources of the systematic error will be discussed in the following item by item.

The error of the track reconstruction efficiency is (as in previous analyses) conservatively

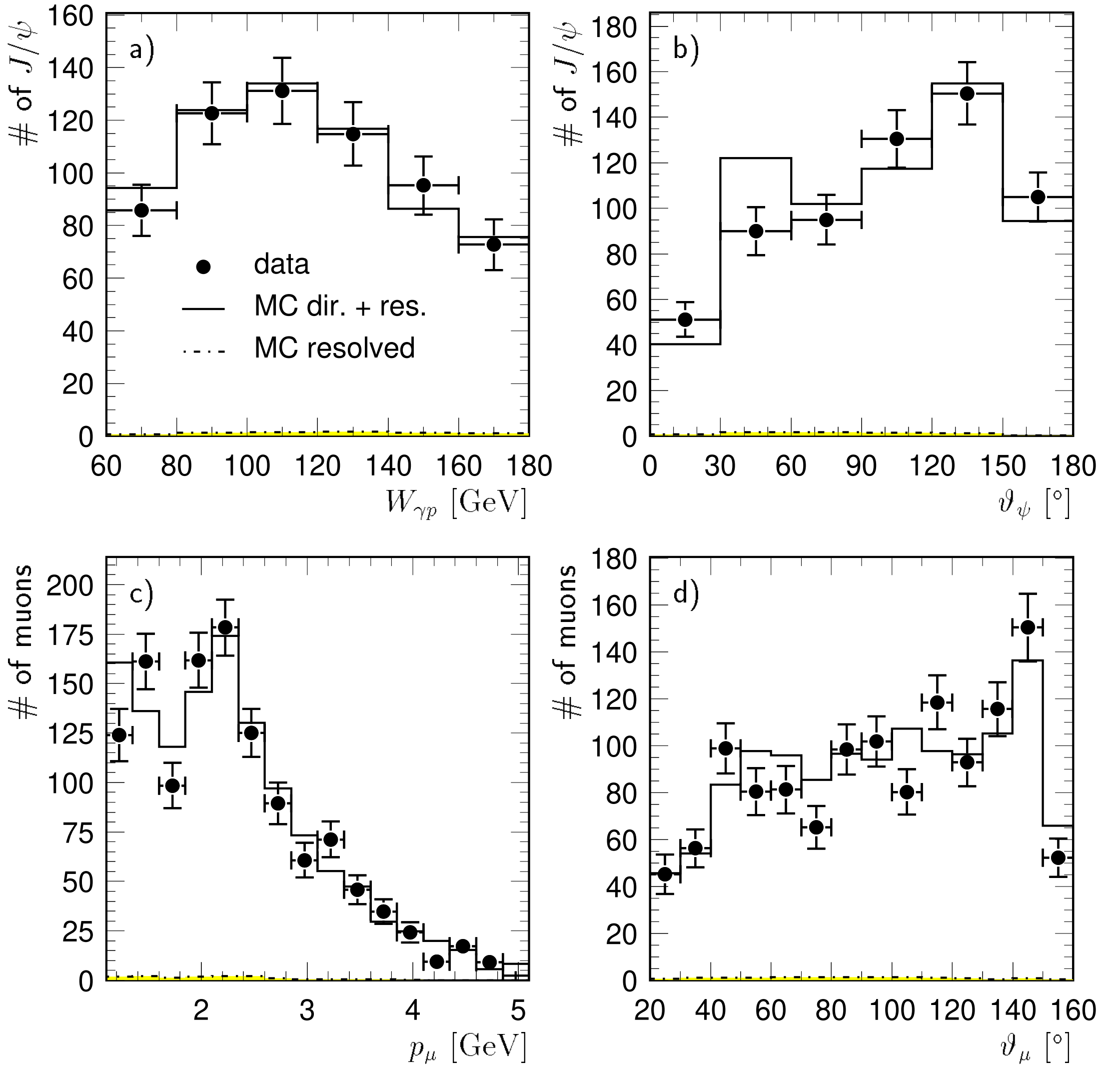

Figure 5.4: *Comparison of data and the normalized simulation (EPJPSI-direct + EPJPSI-resolved) for a)* $W_{\gamma p}$ *and b) the polar angle* ϑ_ψ *of the* J/ψ *meson. For the distribution of c) the momentum* p_μ *and d) the polar angle* ϑ_μ *of the decay muons a sideband subtraction method is used. All distributions are restricted to the range* $0.3 < z < 0.9$ *and* $p_{t,\psi}^2 > 1\,\mathrm{GeV}^2$.

estimated to be 2% per track, resulting in an error of 6% for at least three reconstructed tracks.

After correcting the muon identification probability in the LAr calorimeter no systematic deviation between data and simulation is found (section 4.2.2). It is not possible to repeat the analysis without the requirement of identified muons in order to calculate the systematic error of the muon identification efficiency. Therefore the remaining differences in the identification efficiency as a function of ϑ_μ (fig. 4.3) are used to estimate the uncertainty. Since some statistical fluctuations are expected and should not be included in a systematic error, only half of the differences are used. The systematic error δ is calculated as weighted quadratic average of half of the differences of the efficiency in the

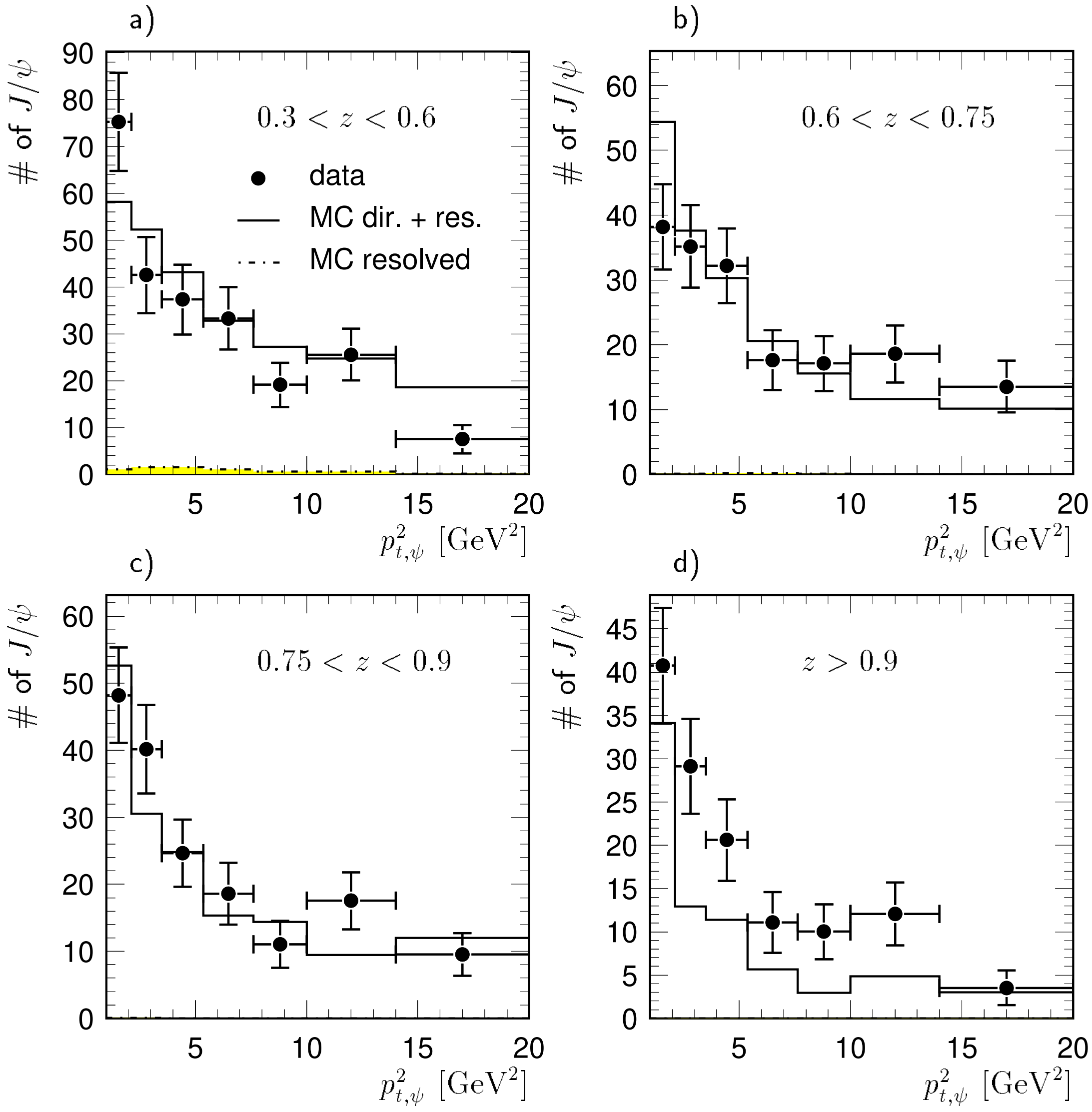

Figure 5.5: *a) – c) Comparison of data and the normalized simulation (EPJPSI-direct + EPJPSI-resolved) for $p^2_{t,\psi}$ in the three analysis regions of the elasticity z. In d) the distribution for higher values of z is shown.*

data ε_{data} and the simulation ε_{MC}:

$$\delta = \sqrt{\sum_{bins} N_i \left(\frac{\varepsilon_{data,i} - \varepsilon_{MC,i}}{2}\right)^2 \bigg/ \sum_{bins} N_i}$$

The result is 4.0% for the identification in the CMD, 1.3% in the LAr calorimeter or the Central Muon Detector and 4.2% for the quadratic sum of both. As a cross-check the full differences are added linearly resulting in −0.2% for the CMD and −1.1% for the LAr or the CMD. This means that the muon identification in the simulation is slightly more efficient than in the data.

For the iron trigger efficiency the problem is similar to the muon identification probability: There are no subtriggers which do not include CMD trigger elements that collected enough

source	amount
track reconstruction	6%
muon identification	4.2%
L1 iron trigger efficiency	3.0%
L1 track trigger efficiency	3.8%
L2NN efficiency average (z dependent)	2.4% ($-4.5\% \ldots + 6.7\%$)
L4 trigger efficiency	3%
parton density functions	2%
diffractive background $p_{t,\psi}^2 > 1\,\mathrm{GeV}^2$ ($p_{t,\psi}^2 < 1\,\mathrm{GeV}^2$)	2% (28%)
luminosity	1.5%
branching ratio	1.7%
total	10.2%

Table 5.2: *Sources of the systematic error. The uncertainty of the L2NN efficiency is taken into account as a function of the elasticity z, for the other distributions the average value is used. The diffractive background of 28% in brackets is only relevant for the lowest bin in the $p_{t,\psi}^2$ distribution. All other variables are studied in the kinematic range $p_{t,\psi}^2 > 1\,\mathrm{GeV}^2$.*

events to allow a cross-check. Therefore the weighted quadratic average of half of the differences in the trigger efficiency as a function of ϑ_μ, resulting in 3.0%, is used as systematic error. The linear sum would result in -2.1%.

The different `zVtx` and `DCRPh` trigger elements in subtrigger S15 and in the combination S19||S22 provide the possibility to estimate the systematic error. Since the trigger elements in S15 (`DCRPh_Thigh` and `zVtx_Mu_D`) tend to have higher efficiencies in the simulation than in the data (figures 4.5 and 4.6) the cross sections determined with the simulated efficiency of S15 are expected to be smaller than the true values. The track trigger elements in S19||S22 (`DCRPh_CNH` and `zVtx_sig1`) have lower values in the simulation than in data. Therefore the cross sections determined with S19||S22 are expected to be larger. This means that the true cross sections are expected to lie between those determined with the different trigger conditions, and the differences between the cross sections determined with S15 and those determined with S19||S22 are expected to be larger than the differences to the true values. All single differential cross sections are therefore determined with S19||S22 for the whole data sample to estimate the uncertainty of the efficiency ot the track trigger elements. The comparison to the 'standard' results, which are obtained with S19||S22 in 1996 and the first part of 1997 and with S15 afterwards, shows no statistically significant differences (fig. 5.8 a). The relative differences are added in quadrature and divided by the number of bins. The fact that only a part of the data sample used for this procedure has a different trigger condition is taken into account by scaling the values with the ratio of the total luminosity to the luminosity for S15. The resulting estimate of the systematic error due to the track trigger elements is 3.8%.

In order to estimate the systematic error arising from the neural network validating subtrigger S15 on trigger level 2, the simulated efficiency of the net is reweighted to match the elasticity distribution of the data (fig. 4.8) and the analysis is repeated. The effect on the cross section as a function of $W_{\gamma p}$ and $p_{t,\psi}^2$ is small (less than 2.4% in all bins). The differential cross section $\mathrm{d}\sigma/\mathrm{d}z$ decreases by 4.5% at low z values and is increased by 6.7% at high z values. A similar trend is observed if the analysis is repeated with S19||S22 as subtriggers without a L2NN condition for the whole data sample (fig. 5.8). The algorithm of the neural net validating subtrigger S15 is the same in the simulation as in the data and it is not clear to what extent the differences in the efficiency are caused by background in the data. Therefore the reweighted efficiency is only used to estimate the systematic error.

All efficiencies of trigger level 4 which are not corrected for in the simulation are above 97% (see section 4.2.3). A systematic error of 3% is assumed.

The influence of different parton density functions (PDFs) on the geometrical acceptance is studied with the direct photon-gluon fusion simulation, where the standard PDF for the proton, MRS(A'), was replaced by the functions GRV98 LO, CTEQ5L or MRST LO which have been obtained more recently than MRS(A'). In figure 5.6 a) the acceptances and b) their differences relative to the acceptance obtained with MRS(A') are shown. Nearly all deviations are compatible with zero within the statistical error. A systematic error of 2% is assigned to cover possible differences.

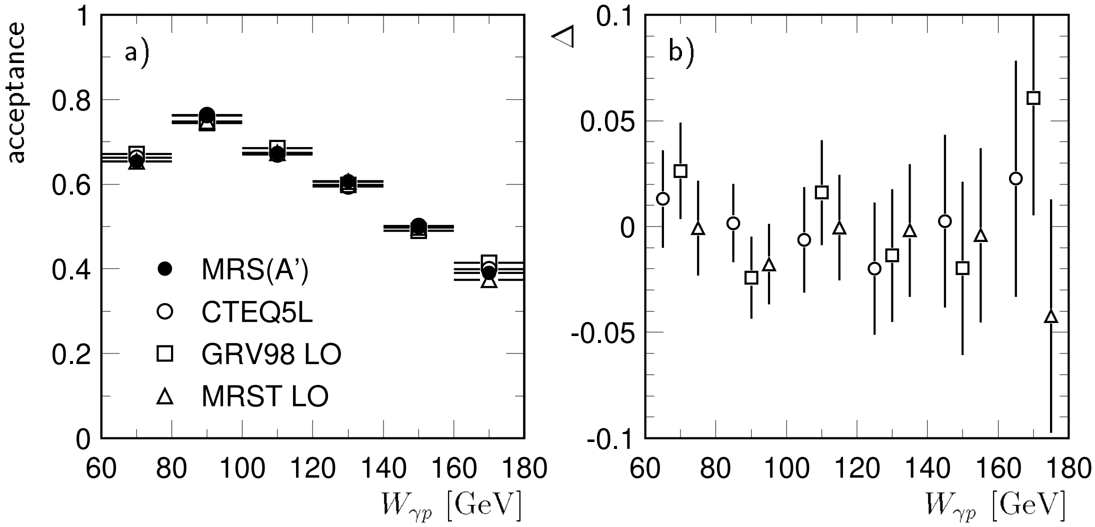

Figure 5.6: *a) Geometrical acceptance as a function of $W_{\gamma p}$ for different parton density functions. b) Difference $\Delta = (\mathsf{acc} - \mathsf{acc}_{\mathsf{MRS(A')}})/\mathsf{acc}_{\mathsf{MRS(A')}}$ relative to the acceptance obtained with MRS(A').*

For the background from diffractive processes J/ψ and $\psi(2s)$ mesons which have been produced elastically and proton dissociatively are considered. While only very few diffractively produced J/ψ mesons pass the selection, the cascade decay of the $\psi(2s)$ contributes significantly. Under the assumption that the diffractive $\psi(2s)$ cross section is $\sigma_{\psi(2s)} = 0.15 \times \sigma_{J/\psi}$ [53] and the trigger efficiency is at most 65% (in order not to rely on the trigger simulation, compare fig. 4.10) a contribution of 28% to the number of selected J/ψ mesons at $p_{t,\psi}^2 < 1\,\mathrm{GeV}^2$ is obtained. Therefore the final analysis is carried out in the region $p_{t,\psi}^2 > 1\,\mathrm{GeV}^2$, where this background is estimated to be only 2%. The diffractive events are concentrated in the highest z bin. No correction is applied.

In the Colour Singlet Model the contribution from the cascade decay of inelastically produced $\psi(2s)$ mesons is expected to be 15% which was confirmed experimentally [63]. Since this process is very difficult to distinguish from J/ψ production in photon-gluon fusion it is not corrected for.

The error of the luminosity measurement is taken from [57]. For the branching ratio and its error the particle data group [8] value $BR(J/\psi \to \mu\mu) = (5.88 \pm 0.10)\%$ is used. These errors affect only the normalization.

5.4 Bin Centre Determination

If a cross section varies rapidly over a bin, the measured (mean) cross section will in principle not be equal to the expected value at the centre of the bin. This would only be the case for an infinitesimal bin or for a linear dependence. In order to compare the measured cross sections with theoretical predictions corrected bin centres are determined in this analysis. The treatment of $W_{\gamma p}$ is different from the other variables and is discussed first.

In the case of the photon-proton centre-of-mass energy $W_{\gamma p}$ the fact that the photon flux $f_{\gamma/e}$ depends on y and therefore on $W_{\gamma p}$ has to be considered. For a bin $W_1 \leq W_{\gamma p} \leq W_2$ with bin centre $\langle W_{\gamma p} \rangle$ the following equation is valid:

$$\sigma_{\gamma p}(\langle W_{\gamma p} \rangle) = \int_{W_1}^{W_2} \mathrm{d}W\, f_{\gamma/e}(W)\, \sigma_{\gamma p}(W) \Big/ \int_{W_1}^{W_2} \mathrm{d}W\, f_{\gamma/e}(W) \; . \tag{5.1}$$

In order to solve this equation an assumption on $\sigma_{\gamma p}(W)$ has to be made. Here a functional form $\sigma_{\gamma p}(W) \propto W^{\delta}$ is assumed and a value of $\delta = 0.68$ is found to fit the data. The resulting corrected bin centres are listed in table D.4. The correction is always small, i.e. less than 1 GeV for a bin width of 20 GeV. Larger values of δ reduce this effect, since the influence of the photon flux is partially compensated.

The photon flux depends only on $W_{\gamma p}$ and Q^2 and does not influence the bin centre of any other observable such as $p_{t,\psi}^2$ and z. Therefore the bin centre for any variable x can be determined using the following equation:

$$\frac{\mathrm{d}\sigma_{\gamma p}}{\mathrm{d}x}(\langle x \rangle) = \frac{1}{x_2 - x_1} \int_{x_1}^{x_2} \mathrm{d}x\, \frac{\mathrm{d}\sigma_{\gamma p}}{\mathrm{d}x}(x) \; . \tag{5.2}$$

Again the functional form of $\mathrm{d}\sigma_{\gamma p}/\mathrm{d}x$ is needed to solve this equation. In the case of the elasticity z a linear function fits the data well (see figure 5.9 a), which means that no correction compared to the nominal bin centre is needed. The theoretical prediction in the Colour Singlet Model also shows no strong dependence on z. Large Colour Octet contributions at high z, which do not fit HERA data, could change this behaviour (section 2.3.3).

One possibility for the bin centre correction in the transverse momentum squared $p_{t,\psi}^2$ of the J/ψ meson is an exponential function which was used to correct the $p_{t,\psi}^2$ distribution in the simulation. An exponential function, however, only fits the data on detector level. After the acceptance and efficiency corrections the sum of at least two exponentials is needed to describe the data. For the bin centre determination a function of the form $a \cdot (p_{t,\psi}^2)^n$ is used instead. The result of the fit is $n = -1.55 \pm 0.05$. For $p_{t,\psi}^2 = 0$ this fit function has a pole resulting in an unphysically corrected bin centre of $p_{t,\psi}^2 = 0$ for the bin starting at $p_{t,\psi}^2 = 0$. Since this bin is not used for a comparison with theoretical curves, the nominal bin centre is taken (figure 5.9 b).

5.5 Cross Sections as Functions of $W_{\gamma p}$, z, $p_{t,\psi}^2$ and x_g

The differential electron-proton cross section as a function of any variable x is calculated from the number of J/ψ mesons N_ψ according to

$$\frac{\mathrm{d}\sigma_{ep}}{\mathrm{d}x} = \frac{N_\psi(x)}{\Delta x \cdot \varepsilon_{sel}(x) \cdot \varepsilon_{trig}(x) \cdot BR \cdot \mathcal{L}} ,$$

where Δx is the bin width, ε_{sel} the selection efficiency (including the acceptance) and ε_{trig} the trigger efficiency in the bin. These numbers can be found in appendix D for all distributions. BR denotes the branching ratio $J/\psi \to \mu^+\mu^-$ and $\mathcal{L}$ the integrated luminosity. The electron-proton cross sections are converted into photon-proton cross sections according to formula 2.9.

$W_{\gamma p}$ Dependence

The total photoproduction cross section for inelastic J/ψ production (including J/ψ mesons originating from the decay of inelastically produced $\psi(2s)$ mesons) in the kinematic region $Q^2 < 1\,\mathrm{GeV}^2$, $0.3 < z < 0.9$ and $p_{t,\psi}^2 > 1\,\mathrm{GeV}^2$ is shown as a function of $W_{\gamma p}$ in figure 5.7. A preliminary measurement of the ZEUS collaboration in a similar range ($0.4 < z < 0.9$) is also shown [64] and reasonable agreement is found. Due to the restricted z range the ZEUS measurement is expected to be about 10% lower than this analysis. This is not observed, but compatible within the errors. The theoretical predictions in the next-to-leading order Colour Singlet Model (CSM) with a charm quark mass of $m_c = 1.4\,\mathrm{GeV}$ also show reasonable agreement with the data. A correction factor of 1.25 is recommended by the author Krämer to account for relativistic corrections and

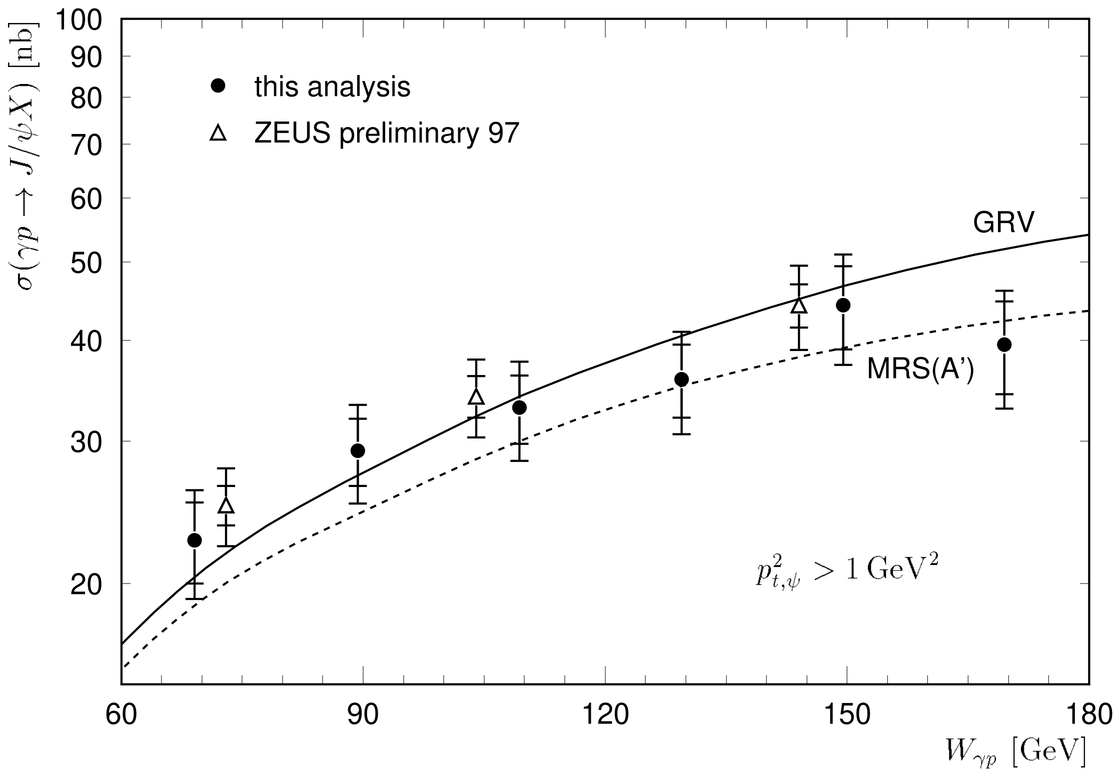

Figure 5.7: *Total cross section as a function of $W_{\gamma p}$ for inelastic J/ψ photoproduction in the region $0.3 < z < 0.9$. For comparison a preliminary measurement of the ZEUS collaboration in a very similar range ($0.4 < z < 0.9$) and the theoretical predictions of the Colour Singlet Model in next-to-leading order calculated with two different proton parton density functions are shown [15].*

contributions from inelastic $\psi(2s)$ production. The factor is not included since it would deteriorate the agreement with the data. With the assumption of a mass dependence of the cross section as in leading order, $\sigma \propto 1/m_c^3$, the correction factor is cancelled by a change in the charm mass to $m_c = 1.51\,\mathrm{GeV}$. The shape of the cross section reflects the gluon density inside the proton. Shown are the predictions for the parameterization MRS(A') resulting in the slowest increase with $W_{\gamma p}$ and GRV resulting in the steepest increase. The data tend to rise even more slowly than MRS(A') but the errors are too large to exclude GRV.

z and $p_{t,\psi}^2$ Dependence

The differential photoproduction cross sections as functions of the elasticity z and the transverse momentum squared of the J/ψ meson $p_{t,\psi}^2$, integrated over the range $60 < W_{\gamma p} < 180\,\mathrm{GeV}$, are compared to previous preliminary H1 measurements in figure 5.8. Since data of the years 1996 and 1997 were used for these measurements, this analysis is an extension and the comparison is a consistency check. The cross sections determined in this analysis are in good agreement with the preliminary analysis of the data taking periods 1996 and 1997 only. The difference between the present analysis and the preliminary one as a function of z is compatible with being of statistical nature. An analysis of 1999 data alone does not result in significantly higher cross sections than for the total data sample. This is confirmed by the agreement in the transverse momentum squared $p_{t,\psi}^2$. In addition a cross check with the subtrigger combination S19||S22 (without S15), which was used to estimate the influence of the track trigger elements and of the neural net validating S15 for the systematic error, is shown in figure 5.8 a).

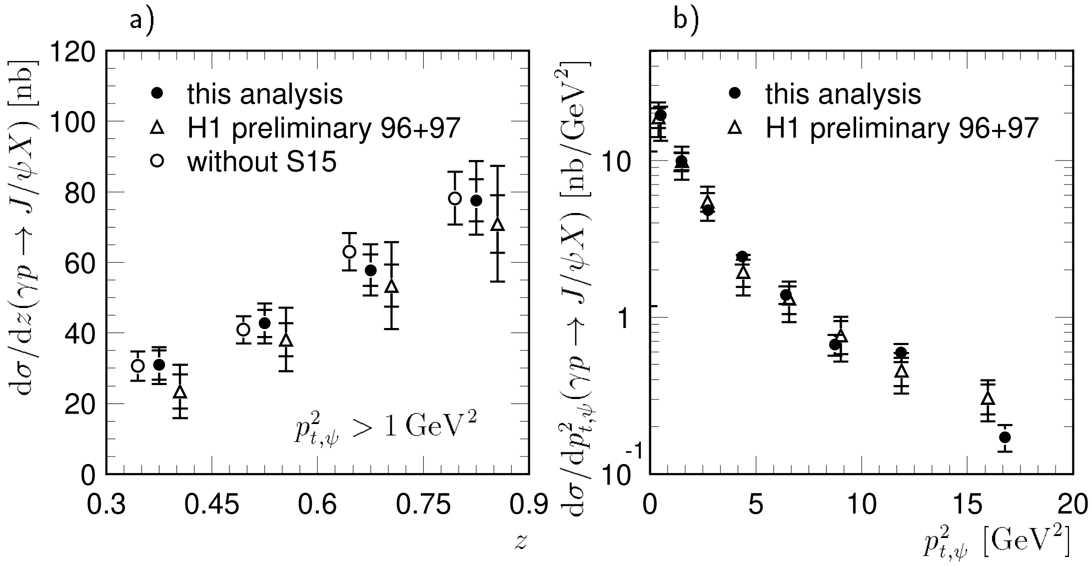

Figure 5.8: *a) Differential cross section* $\mathrm{d}\sigma/\mathrm{d}z$ *for inelastic* J/ψ *photoproduction in the region* $p_{t,\psi}^2 > 1\,\mathrm{GeV}^2$, *integrated over the range* $60 < W_{\gamma p} < 180\,\mathrm{GeV}$. *The cross sections determined in this analysis (filled circles) are plotted at the nominal bin centre, the values of the analysis of 1996 and 1997 data (triangles) are shifted 0.03 to the right. The open circles (shifted 0.03 to the left) show the result of this analysis, if the trigger S15 is replaced by S19 and S22 for all data taking periods. b) Differential cross section* $\mathrm{d}\sigma/\mathrm{d}p_{t,\psi}^2$ *for inelastic* J/ψ *photoproduction, integrated over the range* $60 < W_{\gamma p} < 180\,\mathrm{GeV}$.

The differential photoproduction cross section as a function of the elasticity z, integrated over the range $60 < W_{\gamma p} < 180\,\mathrm{GeV}$, is shown in figure 5.9 a) together with a preliminary measurement of the ZEUS collaboration integrated over the range $50 < W_{\gamma p} < 180\,\mathrm{GeV}$ [65]. The two measurements agree well. Due to the different $W_{\gamma p}$ region the mean $W_{\gamma p}$ of the ZEUS measurement is lower. This is expected to reduce the cross sections only by about 6% (with the assumption of $\sigma_{\gamma p} \propto W_{\gamma p}^{\delta}$ and $\delta = 0.68$ as in section 5.3). The Colour Singlet Model at next-to-leading order is able to describe the data reasonably well, while the leading-order prediction is about a factor 2 too low. No hint for a steep rise at high z is found which was expected from the first calculations in the Colour Octet Model.

The differential photoproduction cross section as a function of $p_{t,\psi}^2$, again integrated over the range $60 < W_{\gamma p} < 180\,\mathrm{GeV}$, is shown in figure 5.9 b). For the first bin, $p_{t,\psi}^2 < 1\,\mathrm{GeV}^2$, the nominal bin centre is used (see section 5.4), and because of the large amount of background expected from the cascade decay of diffractively produced $\psi(2s)$ mesons an

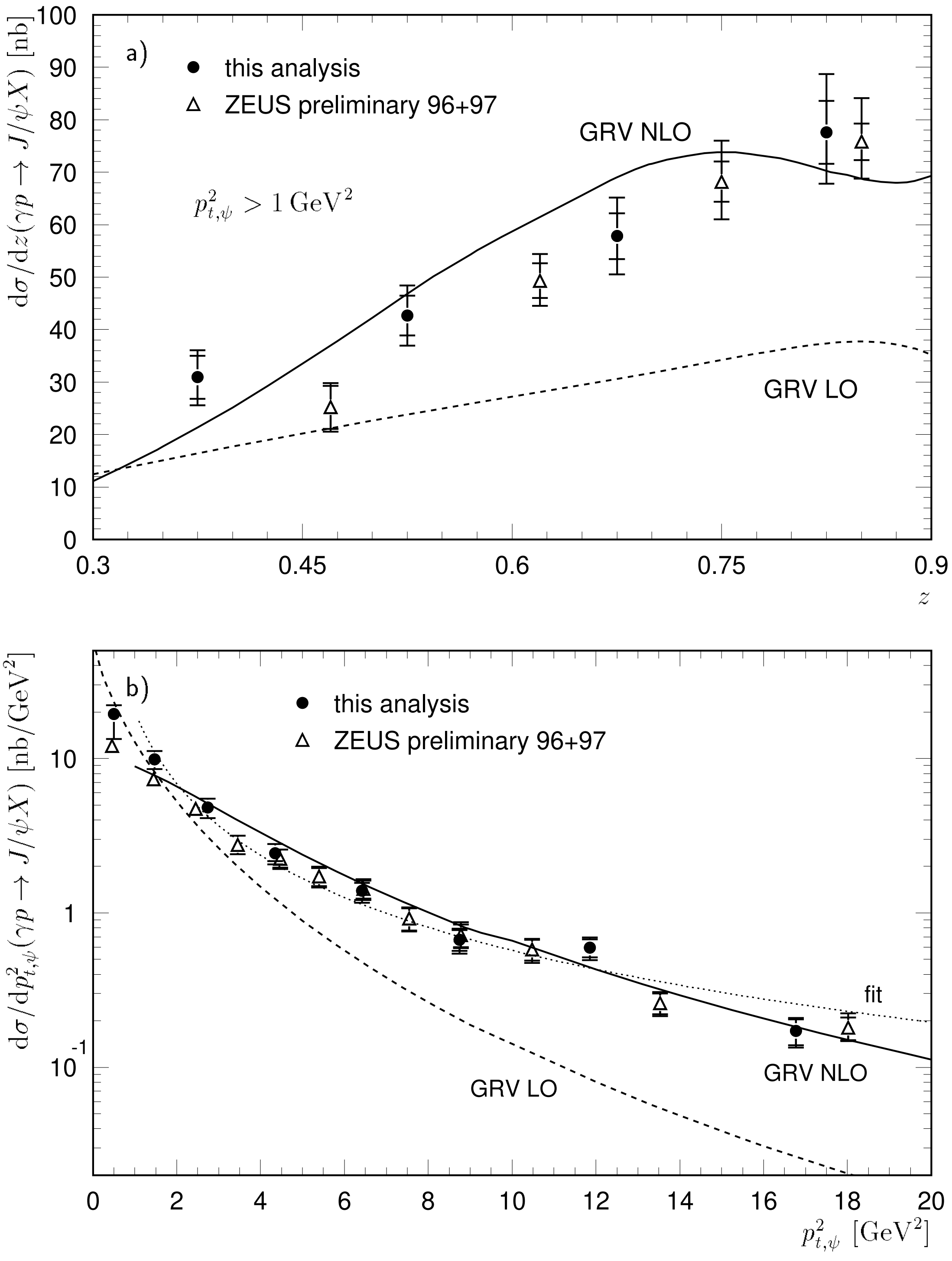

Figure 5.9: *Differential cross sections a)* $\mathrm{d}\sigma/\mathrm{d}z$ *in the region* $p_{t,\psi}^2 > 1\,\mathrm{GeV}^2$ *and b)* $\mathrm{d}\sigma/\mathrm{d}p_{t,\psi}^2$ *in the region* $0.3 < z < 0.9$ *for inelastic* J/ψ *photoproduction, integrated over* $60 < W_{\gamma p} < 180\,\mathrm{GeV}$. *For comparison a preliminary measurement of the ZEUS collaboration in a very similar range* ($50 < W_{\gamma p} < 180\,\mathrm{GeV}$ *and* $0.4 < z < 0.9$) *and theoretical predictions of the Colour Singlet Model in leading order (dashed line) and next-to-leading order (full line) calculated with the corresponding GRV parton density functions are shown. The dotted line in b) is a fit of the form* $a \cdot (p_{t,\psi}^2)^n$ *yielding* $n = -1.55 \pm 0.05$ *(only statistical errors considered).*

asymmetric systematic error is determined. The data are compared to a preliminary measurement of the ZEUS collaboration in the kinematic region $0.4 < z < 0.9$ and $50 < W_{\gamma p} < 180\,\text{GeV}$ [65]. For $p_{t,\psi}^2 > 1\,\text{GeV}^2$ good agreement is found, at lower transverse momentum squared the agreement is slightly worse. In this region the distinction between inelastically and diffractively produced J/ψ mesons is difficult. The next-to-leading order calculation in the CSM describes the data in the region, where it can be applied ($p_{t,\psi}^2 > 1\,\text{GeV}^2$), whereas in this case not only the normalization, but also the shape of the leading-order curve are not in agreement with the data. A fit of the form $a \cdot (p_{t,\psi}^2)^n$ gives a reasonable description of the data and is also shown in figure 5.9 b). The resulting $n = -1.55 \pm 0.05$ will be used for comparison with the double differential cross sections in the next section.

x_g Dependence

One aim of the analysis of inelastic J/ψ photoproduction in the medium z range is the determination of the gluon density. The differential cross section as a function of the logarithm of the gluon fractional momentum x_g inside the proton is shown in figure 5.10. x_g is reconstructed according to the leading order formula 3.5. The kinematic region is $0.3 < z < 0.9$ and $p_{t,\psi}^2 > 1\,\text{GeV}^2$, integrated over $60 < W_{\gamma p} < 180\,\text{GeV}$. For comparison predictions of the EPJPSI Monte Carlo generator for the proton parton densities MRS(A') and GRV98 LO are shown. Since the transverse momentum squared of the J/ψ meson is used to reconstruct x_g (see section 3.4), it is expected that the reweighting in $p_{t,\psi}^2$ which is needed to achieve agreement of EPJPSI-direct with the data also changes the x_g behaviour. The prediction of EPJPSI for MRS(A') is therefore shown in figure 5.10 with and without reweighting in $p_{t,\psi}^2$. The k factors are used to adjust the normalization to the data.

The EPJPSI 'prediction' for MRS(A') with the $p_{t,\psi}^2$ dependent reweighting is in good agreement with the data, while the predictions without reweighting are too high at small x_g and too low at large x_g for both parton density functions. The differences in shape between GRV98 LO and MRS(A') before reweighting are smaller than the effect of reweighting in $p_{t,\psi}^2$. Due to this sensitivity to $p_{t,\psi}^2$ it is at present not possible to distinguish the proton parton densities from the x_g distribution. Since x_g is reconstructed from $W_{\gamma p}$, z and $p_{t,\psi}^2$ a simulation where all these quantities are in agreement with data is needed to profit from the additional sensitivity of the x_g distribution to the gluon density compared to $W_{\gamma p}$.

Comparison with CASCADE

In figure 5.11 the predictions of the Monte Carlo simulation programs CASCADE and EPJPSI are compared to the total photoproduction cross section as a function of $W_{\gamma p}$ and the differential cross sections as functions of z and $p_{t,\psi}^2$. Both simulation programs calculate cross sections according to the Colour Singlet Model in leading order. The most important differences are the unintegrated (k_t dependent) gluon density inside the proton which is used in CASCADE and the relativistic corrections implemented only in EPJPSI (for details of the two generators see chapter 3). Only direct photon-gluon fu-

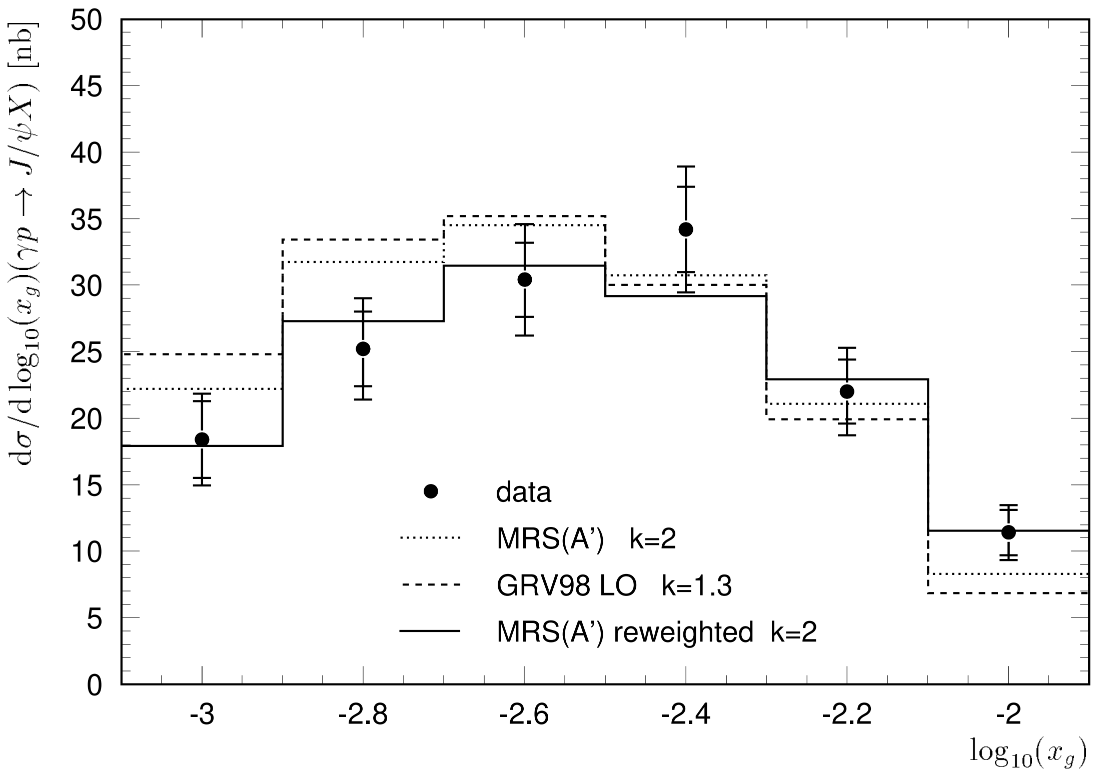

Figure 5.10: *Differential cross section* $\mathrm{d}\sigma/\mathrm{d}\log_{10}(x_g)$ *for inelastic* J/ψ *photoproduction in the region* $0.3 < z < 0.9$, $p_{t,\psi}^2 > 1\,\mathrm{GeV}^2$ *integrated over* $60 < W_{\gamma p} < 180\,\mathrm{GeV}$. *For comparison predictions of the EPJPSI Monte Carlo generator for the proton parton densities MRS(A') (dotted) and GRV98 LO (dashed) are shown. The full line is the 'prediction' of EPJPSI with MRS(A'), if the* $p_{t,\psi}^2$ *dependent reweighting (see section 5.2.1) is applied.*

sion is considered. The EPJPSI curves are multiplied by a k factor of 2 to facilitate the comparison with the data. The difference in normalization can be explained by missing next-to-leading order contributions and by the uncertainty in the charm mass. The $p_{t,\psi}^2$ dependent reweighting (section 5.2.1) is **not** applied. The rise towards high z is described by EPJPSI, while CASCADE undershoots the data (fig. 5.11 a). Relativistic corrections, which are not implemented in CASCADE, are expected to contribute mainly in this region.

In order to facilitate the comparison the CASCADE predictions for the other variables are multiplied by a k factor of 1.5 although it is not clear if the relativistic corrections change the dependence of the cross section on other variables than z. The data show the same dependence on $W_{\gamma p}$ as EPJPSI but the errors are too large to exclude a flat behaviour as predicted by CASCADE (fig. 5.11 b). A better description of the $p_{t,\psi}^2$ dependence of the cross section is given by CASCADE (fig. 5.11 c). To depict the discrepancy more clearly the ratio of the differential cross sections in the data and the simulation is plotted in figure 5.11 d) bin by bin normalized in the fourth $p_{t,\psi}^2$ bin. For CASCADE this ratio is flat, while EPJPSI shows a clear rise. The transverse momentum of the gluon inside the proton in CASCADE leads to this better agreement of the $p_{t,\psi}^2$ dependence with the

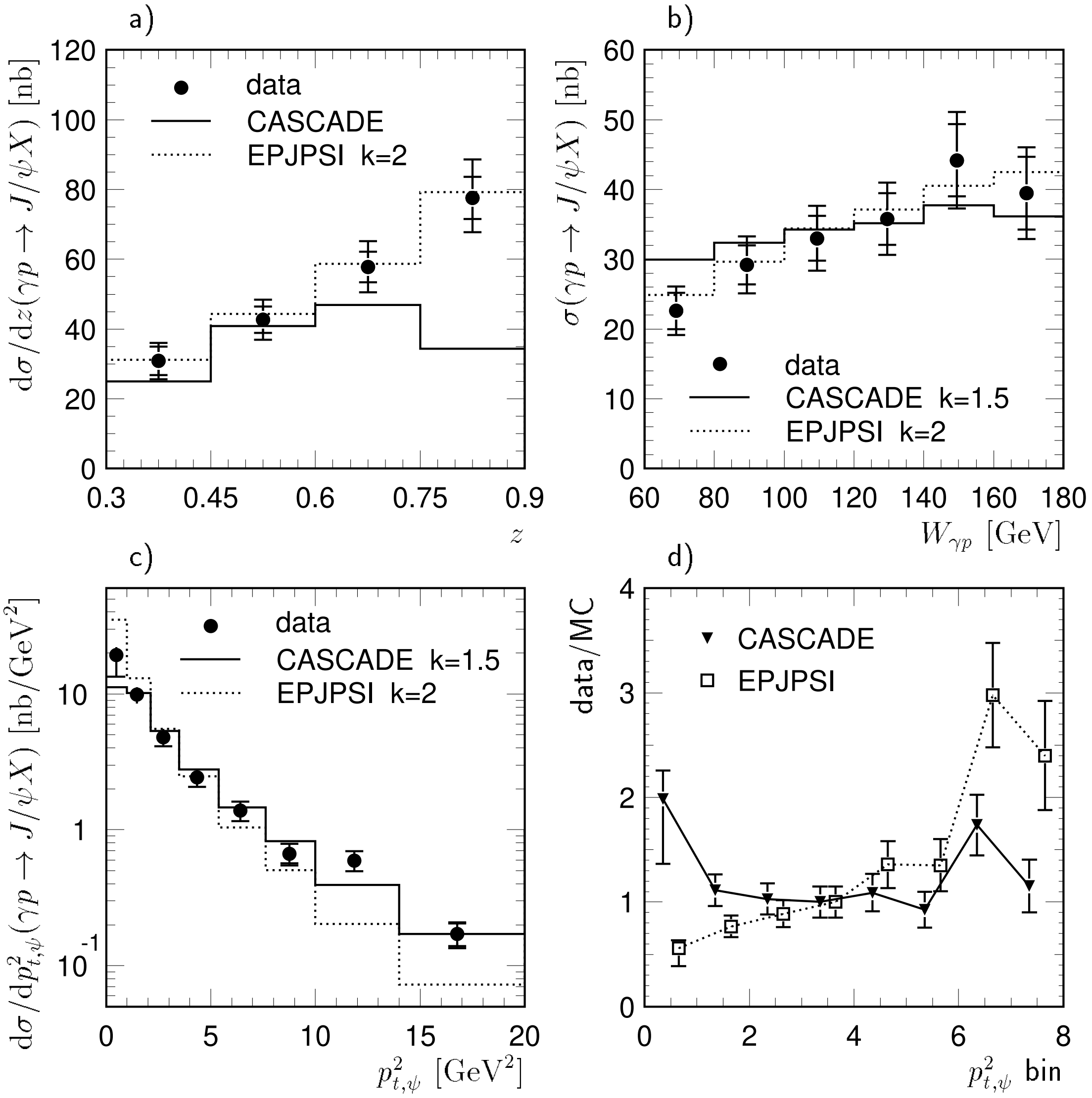

Figure 5.11: *a) The differential cross section as a function of z. The data (filled circles) are compared to predictions of the MC generators CASCADE (full line) and EPJPSI (dotted line, multiplied with $k = 2$). b) The total cross section as a function of $W_{\gamma p}$ and c) the differential cross section as a function of $p^2_{t,\psi}$ in comparison with the predictions of CASCADE ($k = 1.5$) and EPJPSI ($k = 2$). d) The ratio of data over simulation as a function of the $p^2_{t,\psi}$ bin, normalized to the fourth bin. The total error is shown.*

data, but due to the missing relativistic corrections the z dependence of the data is not described.

5.6 Double Differential Cross Sections in $p^2_{t,\psi}$ and z

A measurement of the double differential cross section in $p^2_{t,\psi}$ and z could help to clarify whether different production mechanisms with different $p^2_{t,\psi}$ dependences dominate in various z ranges. The data sample is therefore split into a low ($0.3 < z < 0.6$), medium ($0.6 < z < 0.75$) and high ($0.75 < z < 0.9$) z region. Contributions from Colour Octet states are expected at high z, while resolved photon processes might change the $p_{t,\psi}^2$ dependence in the low z region.

The double differential cross sections in the three elasticity regions are shown in figure 5.12, together with fits of the form $a \cdot (p_{t,\psi}^2)^n$. Values for the exponent n range between -1.25 and -1.73, a difference which corresponds to more than five times the statistical error of the fit (table 5.3). The value of n, however, is strongly dependent on the highest bin in $p_{t,\psi}^2$, which is statistically limited. To estimate the influence of the last bin the fits are repeated without this bin (last column of table 5.3). Then the largest difference corresponds to three times the fit error.

z region	exponent n	n for $p_{t,\psi}^2 < 14.0\,\mathrm{GeV}^2$
$0.30 - 0.60$	-1.64 ± 0.09	-1.43 ± 0.11
$0.60 - 0.75$	-1.25 ± 0.09	-1.20 ± 0.11
$0.75 - 0.90$	-1.73 ± 0.09	-1.54 ± 0.11
$0.30 - 0.90$	-1.55 ± 0.05	-1.41 ± 0.06
$0.05 - 0.45$	-1.28 ± 0.15	

Table 5.3: *The exponents of fits of the form $a \cdot (p_{t,\psi}^2)^n$ to the double differential cross sections as a function of $p_{t,\psi}^2$ in three elasticity regions. In the last column the highest $p_{t,\psi}^2$ bin was omitted in the fit. For comparison, the results obtained for the single differential cross sections in the medium and the low z analyses are listed in the last two rows.*

For comparison also fits with a fixed exponent $n = -1.55$ which is obtained from the single differential cross section are shown in figure 5.12. For the low and high elasticity region this fit agrees rather well with the data but in the medium z range the data show clearly a harder behaviour. This is confirmed by the fit without the last bin which results in a similar n value as the fit in the whole $p_{t,\psi}^2$ region. This behaviour might suggest that different production mechanisms than direct photon-gluon fusion change the $p_{t,\psi}^2$ behaviour in the low and high elasticity regions.

The EPJPSI simulation of direct photon-gluon fusion predicts only a very weak dependence of the $p_{t,\psi}^2$ behaviour on the elasticity. With increasing z the decrease with $p_{t,\psi}^2$ gets slightly steeper. In the data the smallest contributions from other processes than photon-gluon fusion are expected in the medium z region. At high z the observed steeper decrease could be a result of background from diffractive processes which are known to show such a steeper behaviour at $p_{t,\psi}^2 \lesssim 1.2\,\mathrm{GeV}^2$; at high $p_{t,\psi}^2$ a preliminary measurement from the ZEUS collaboration found a $p_{t,\psi}^2$ dependence in proton dissociation of $n = -1.7 \pm 0.2 \pm 0.2$ [66]. The colour octet contributions from the $[\underline{8}, {}^3P_0]$ and $[\underline{8}, {}^1S_0]$ states which are expected at high z show in leading order a slightly harder behaviour than the colour singlet prediction [30].

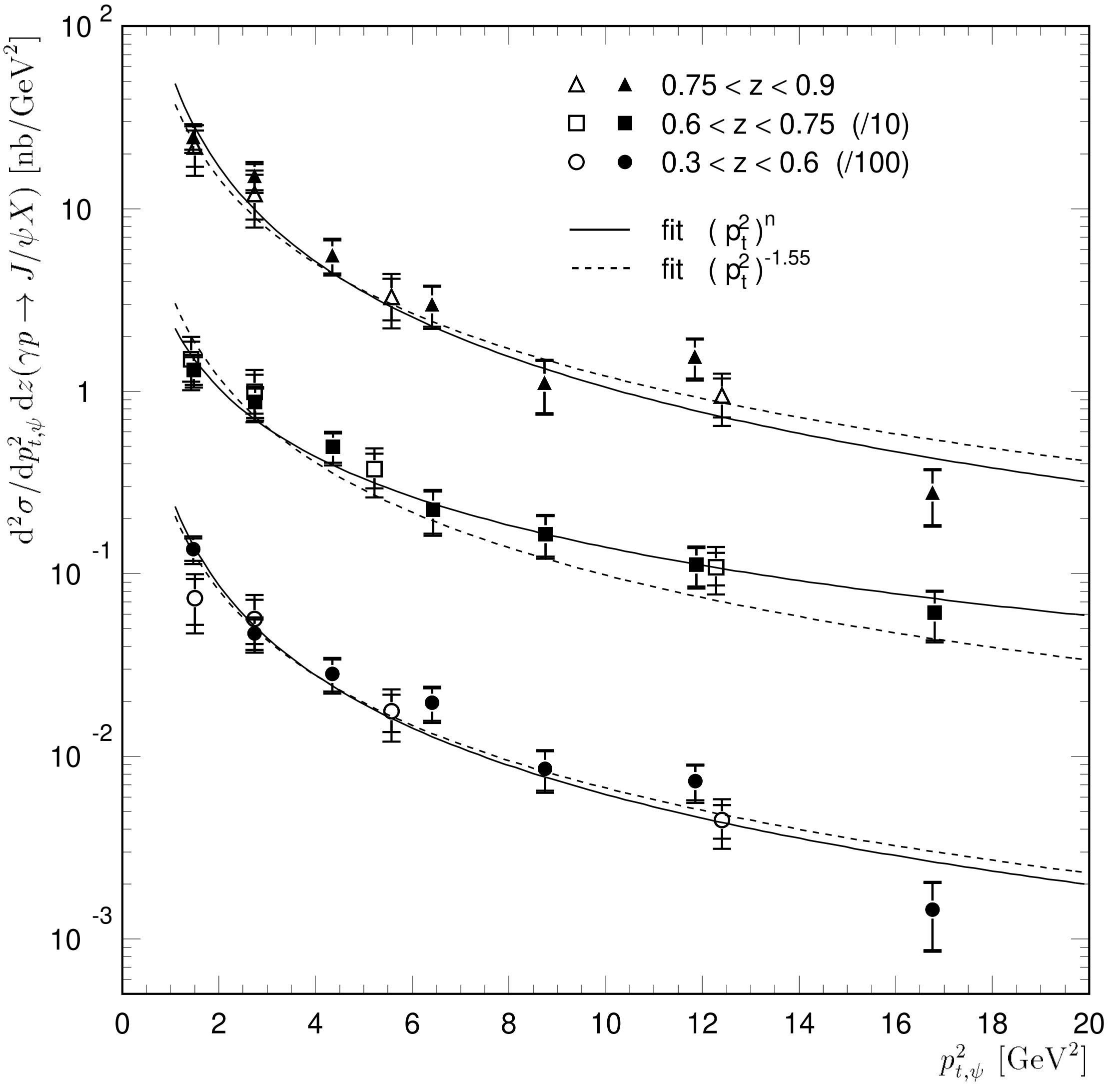

Figure 5.12: *The double differential cross section* $\mathrm{d}^2\sigma/\mathrm{d}p_{t,\psi}^2\,\mathrm{d}z$ *for inelastic* J/ψ *photoproduction integrated over the range* $60 < W_{\gamma p} < 180\,\mathrm{GeV}$. *In addition to the cross sections determined in this analysis (full symbols) the results of previous analyses using 1996 and 1997 data (open symbols) are shown. The full lines are fits of the form* $a \cdot (p_{t,\psi}^2)^n$ *(only the statistical errors are considered), for the dashed lines the exponent was fixed to be* $n = -1.55$*, as obtained for the single differential cross section.*

At low z contributions from processes with resolved photons are expected whose $p_{t,\psi}^2$ dependence has not been measured at HERA so far. The EPJPSI prediction is, however, even harder than for direct photon-gluon fusion, in contrast to what the data may indicate. In the analysis in the elasticity region $0.05 < z < 0.45$ which is presented in the next chapter the contributions from processes with resolved photons are expected to be much higher than in the low z bin ($0.3 < z < 0.6$) here. There the fit to the differential cross section as a function of $p_{t,\psi}^2$ yields $n = -1.28 \pm 0.15$, comparable to the medium z bin here. This implies that the fit result in the low z bin could be a statistical fluctuation. More statistics that allows for a finer binning at high $p_{t,\psi}^2$ is clearly needed to settle the question, whether there is a change in the $p_{t,\psi}^2$ dependence with z and whether different production mechanisms are the cause.

5.7 Decay Angle Distributions

Another possibility of distinguishing different production mechanisms is to investigate the polarization parameters λ and ν which can be determined from the angular distributions of the J/ψ decay muons (for the definitions see chapter 2). λ is expected to be nearly zero in the region $0.1 \lesssim z \lesssim 0.7$ and to rise towards higher elasticities. In the Colour Octet Model this rise should be smaller than in the CSM where it should reach $\lambda = 1$ at $z = 1$. The CSM predicts ν values near 0.5 in the range $0.1 \lesssim z \lesssim 0.7$ falling to 0.0 at $z = 1$. The COM prediction is lower everywhere with values between -1 and 0.0 at $z = 1$, depending on the choice of the Colour Octet Matrix Elements (see section 2.3.3).

The polarization parameters are determined in the regions $0.3 < z < 0.6$ and $0.6 < z < 0.9$. At $\cos\vartheta^* \approx \pm 1$ one of the decay muons has nearly the opposite direction to that of the J/ψ meson in the photon-proton centre-of-mass system. This leads to a small muon momentum in the laboratory frame and thus to a drop in the acceptance (fig. 5.13 a). The analysis region is therefore restricted to $|\cos\vartheta^*| < 0.75$. In addition the bins in $\cos\vartheta^*$ are chosen to be of different sizes to account for the varying acceptance. If the J/ψ production and decay planes fall together ($\varphi^* \approx 0\,°$ or $\varphi^* \approx \pm 180\,°$), the transverse momentum of one of the muons relative to the J/ψ meson is opposite to the transverse momentum of the J/ψ meson relative to the incoming proton. This also leads to a small transverse muon momentum in the laboratory frame and to a drop in the acceptance (fig. 5.13 b). Since the differential cross section $\mathrm{d}\sigma/\mathrm{d}\varphi^*$ is proportional to the sum of a constant and a term $\frac{\nu}{3}\cos 2\varphi^*$, for small numbers of bins a better sensitivity for ν is achieved by analysing the absolute value $|\varphi^*|$ instead of φ^*.

The comparison of the decay angle distributions between the data and the unpolarized simulation shows reasonable agreement (fig. 5.14 a – d). The measured polarization parameters λ and ν are therefore expected to be compatible with zero. The differential cross section $\mathrm{d}\sigma/\mathrm{d}\cos\vartheta^*$ is fitted with a function proportional to $1 + \lambda\cos^2\vartheta^*$ (fig. 5.14 e). This function is also used to determine the corrected bin centre, which is independent of λ. λ values of 1.00 ± 0.81 in the low z region and 1.10 ± 0.59 at high z are obtained. Positive values are preferred, but within the large errors both are compatible with zero. The expected rise towards high z cannot be resolved within the present precision. In the case of the azimuthal angle φ^* (fig. 5.14 f) the function fitted, $b \cdot (1 + \frac{\lambda}{3} + \frac{\nu}{3}\cos 2|\varphi^*|)$, depends on λ. This results in an additional uncertainty in ν. The central value for ν is determined by fixing λ to the value of the corresponding ϑ^* fit. The error of ν depending on λ is determined by changing λ within one standard deviation of the ϑ^* fit and calculating the difference in ν. The values for ν are compatible with unpolarized J/ψ mesons in both z regions, but with a tendency to negative values (table 5.4). This result agrees with the CSM and the COM, but with the present statistics it is not possible to resolve the small differences between the CSM and the COM.

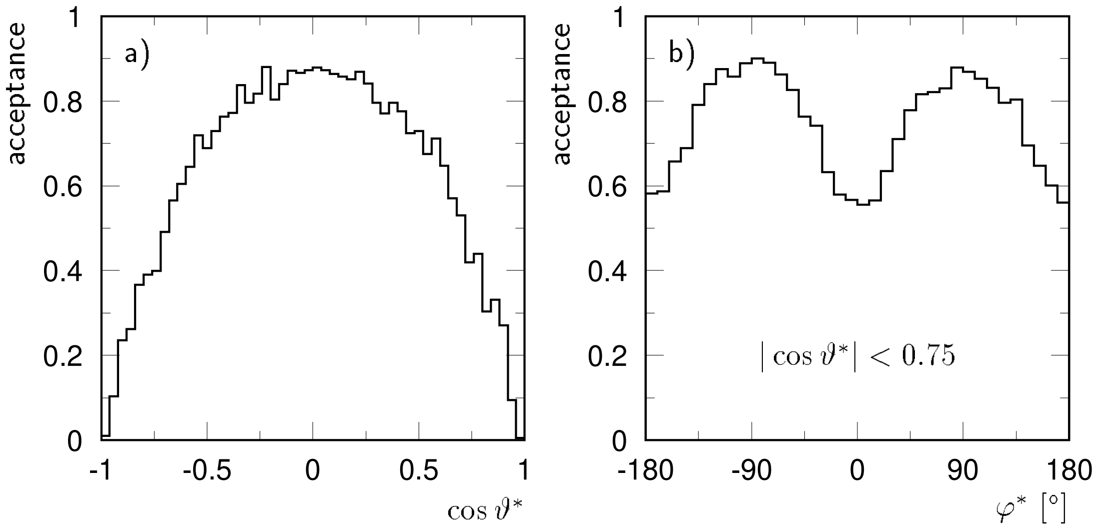

Figure 5.13: *The acceptance of* $20° < \vartheta_\mu < 160°$ *and* $p_\mu > 1.1\,\mathrm{GeV}$ *as a function of a)* $\cos\vartheta^*$ *and b)* φ^* *for a direct photon-gluon fusion simulation with* $E_p = 820\,\mathrm{GeV}$. *The kinematic region covered is* $Q^2 < 1\,\mathrm{GeV}^2$, $60 < W_{\gamma p} < 180\,\mathrm{GeV}$, $0.3 < z < 0.9$ *and* $p_{t,\psi}^2 > 1\,\mathrm{GeV}^2$.

	λ	ν
$0.3 < z < 0.6$	1.00 ± 0.81	$-0.58 \pm 0.56 \pm 0.12$
$0.6 < z < 0.9$	1.10 ± 0.59	$-0.52 \pm 0.39 \pm 0.08$

Table 5.4: *The fitted polarization parameters* λ *and* ν *in two regions of the elasticity* z. *The first error is the error resulting from fitting the decay angular distributions including the statistical errors only. Since the relative normalization of the constant to the* φ^**-dependent term, which is relevant for the measurement of* ν, *depends on* λ, *a second uncertainty for* ν *is determined by varying* λ *by one sigma.*

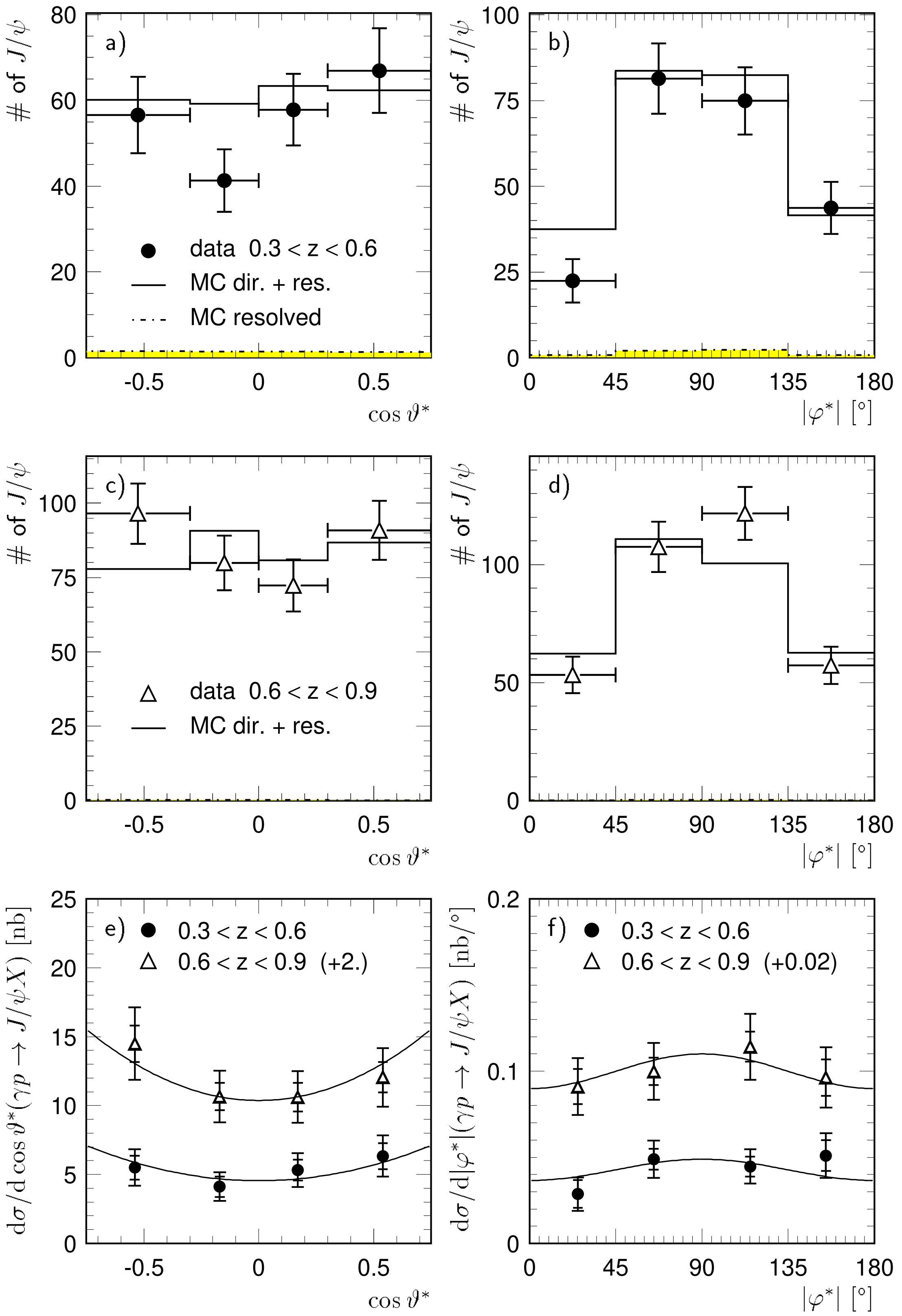

Figure 5.14: *Comparison of data and simulation (direct + resolved) for a), c)* $\cos\vartheta^*$ *and b), d)* $|\varphi^*|$ *in two regions of the elasticity* z *for* $p_{t,\psi}^2 > 1\,\mathrm{GeV}^2$ *and* $|\cos\vartheta^*| < 0.75$. *The differential cross sections* $\mathrm{d}\sigma/\mathrm{d}\cos\vartheta^*$ *and* $\mathrm{d}\sigma/\mathrm{d}|\varphi^*|$ *are shown in e) and f) where the data in the high* z *region are offset for clarity. The curves are fits of the form* $a\cdot(1+\lambda\cos^2\vartheta^*)$ *and* $b\cdot(1+\frac{\lambda}{3}+\frac{\nu}{3}\cos 2|\varphi^*|)$. *Only the statistical errors are considered in the fits.*

Chapter 6

J/ψ Photoproduction at Low z

The results for J/ψ photoproduction in the kinematic region $0.05 < z < 0.45$, $120 < W_{\gamma p} < 260\,\mathrm{GeV}$ and $p_{t,\psi}^2 > 1\,\mathrm{GeV}^2$ are presented in this chapter. After a short description of the calculation of the number of selected J/ψ mesons, the contributions of the two components of the simulation, EPJPSI-direct and EPJPSI-resolved, are determined and compared with the data. The systematic errors are then estimated, and single differential cross sections are presented.

6.1 Background Subtraction

In the region of low elasticities the non-resonant background increases compared to the medium z range due to the increasing number of charged particles which can be misidentified as muons. This becomes most evident in the invariant mass distribution in the lowest z bin (fig. 6.1 a). In addition, the J/ψ meson is produced at small polar angles ϑ_ψ, since the momentum transferred from the beam electron to the J/ψ meson is small. Therefore, the decay muons also tend to lie in the forward region of the detector where the momentum resolution is not as good as in the central part. Since the detector resolution dominates the observed width of the J/ψ peak, it is expected that this width decreases with increasing z. The present statistics, however, only allows a rather coarse binning of the mass distributions in each analysis bin of z, where the determination of the width would lead to very large errors. Thus the same procedure as in the medium z analysis is used:

- In each analysis bin the invariant mass spectrum of the unlike-sign muon pairs is fitted with a function to be taken the superposition of a Gaussian with fixed mean and width for the J/ψ signal and a linear function for the non-resonant background.

- The number of J/ψ mesons is calculated by counting the number of muon pairs in the mass window $2.9 < M_{\mu\mu} < 3.3\,\mathrm{GeV}$ and subtracting the non-resonant background obtained from the background fit.

- The statistical error of the total number of muon pairs in the mass window is used as an estimate for the error of the number of J/ψ mesons.

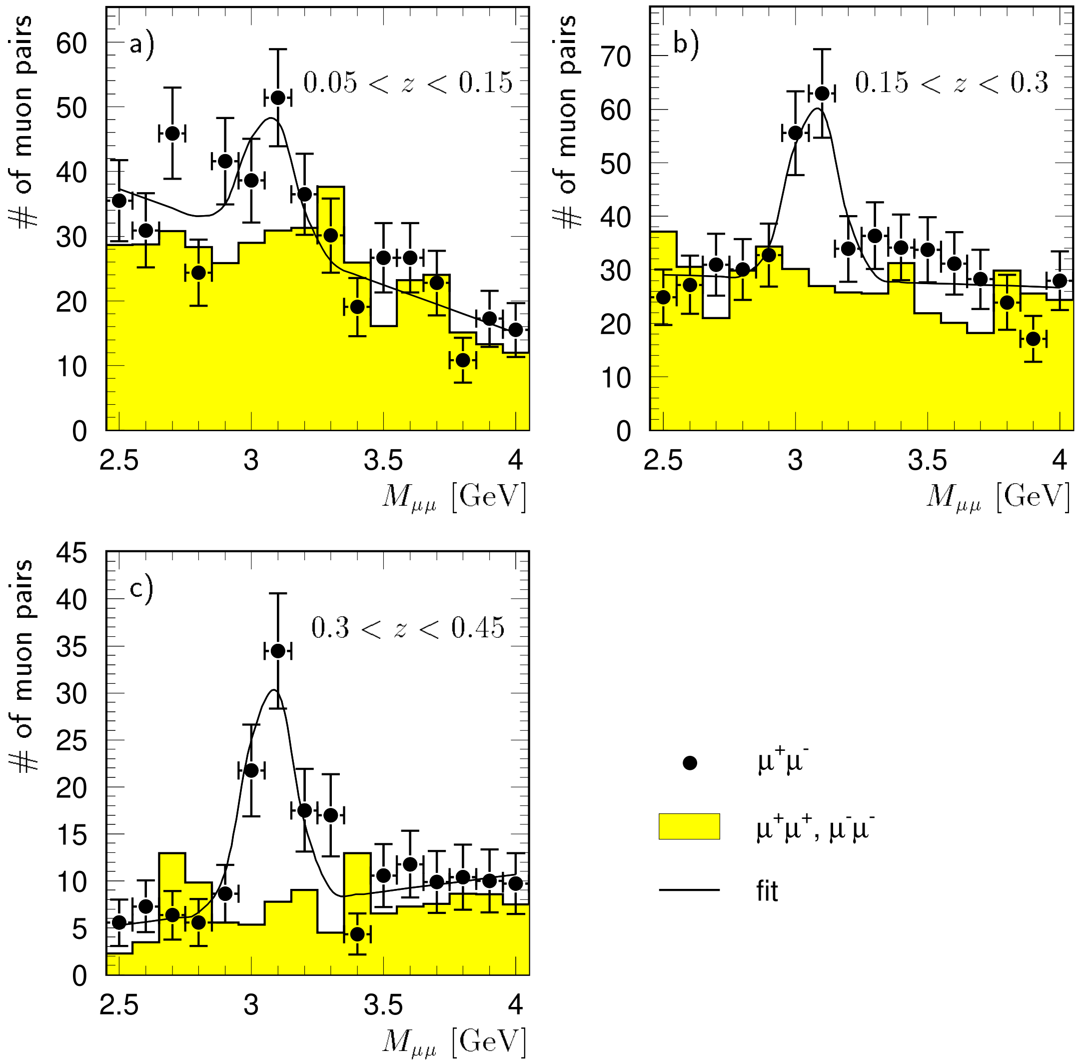

Figure 6.1: *Mass distributions in bins of the elasticity z for $p_{t,\psi}^2 > 1\,\mathrm{GeV}^2$ and $120 < W_{\gamma p} < 260\,\mathrm{GeV}$.*

6.2 Comparison with Simulations

For the extraction of cross sections the data have to be corrected for the acceptance and efficiency of the selection discussed in chapter 4. These probabilities are determined with a two component simulation (EPJPSI-direct with MRS(A') as proton PDF and EPJPSI-resolved with MRS(A') as proton PDF and GRV92 LO as photon PDF). After the description of the normalization of the two components a comparison of the simulation with the data is presented. As regards possible contributions from other processes see chapter 3 and section 6.3.

6.2.1 Normalization of Simulations

The normalization of the direct contribution was determined after the $p_{t,\psi}^2$-dependent reweighting (section 5.2.1) in the kinematic region $0.45 < z < 0.9$, $60 < W_{\gamma p} < 180\,\mathrm{GeV}$ and $p_{t,\psi}^2 > 1\,\mathrm{GeV}^2$ (section 5.2.2). In this region no significant contributions from other processes, either resolved photon processes or diffraction, are expected. A factor of ~ 2.2 was found to describe the data. The $p_{t,\psi}^2$ dependent reweighting and the same normalization factor are also applied to the direct photon-gluon fusion simulation in the low z region. The contribution of resolved photon processes is then added to the direct simulation to match the total number of events in the z distribution of the low z analysis ($0.05 < z < 0.45$). The resulting z distribution is in good agreement with the data (fig. 6.2 a). The normalization factor for the resolved photon simulation is ~ 0.8.

6.2.2 Distributions of Observables

In figure 6.2 the two component Monte Carlo simulation is compared with the data. The $W_{\gamma p}$ distribution (fig. 6.2 b) is in good agreement with the data. In the highest $W_{\gamma p}$ bin, the contribution of the resolved processes is clearly larger than in the lower $W_{\gamma p}$ range. With the present statistics it is not possible to distinguish whether the resolved photon contribution also has a harder $p_{t,\psi}^2$ behaviour than expected in the simulation (fig. 6.2 c). EPJPSI-resolved is therefore not reweighted. In figure 6.2 d) the polar angle ϑ_ψ of the J/ψ meson is shown. Reasonable agreement between the simulation and the data is observed. While the J/ψ mesons produced in direct photon-gluon fusion are concentrated in the central part of the detector, those originating from resolved photon processes tend to lie in the forward region.

For the normalization of the EPJPSI-resolved simulation the assumption is made, that the normalization of EPJPSI-direct which is determined in the medium z region is also valid at low z. If this assumption is correct the addition of the EPJPSI-resolved simulation clearly improves the agreement of data and simulation in the normalization.[1] The shape of the z and the $W_{\gamma p}$ distribution are in better agreement with the data for the two component simulation than for EPJPSI-direct alone.

The result of the normalization procedure is that about a quarter of the J/ψ mesons in this analysis are produced in resolved photon processes. In the two lower elasticity bins, $0.05 < z < 0.3$, resolved photon processes contribute a third of the J/ψ mesons. An independent consistency check is provided by the observation that about 10% of the events in this analysis are accepted by subtrigger S56 which contains a SpaCal condition.

[1] If the normalization of EPJPSI-direct would be determined in a reduced z region, such as $0.45 < z < 0.75$, to avoid possible contributions from diffractive processes at high z, the contribution from EPJPSI-resolved would be increased.

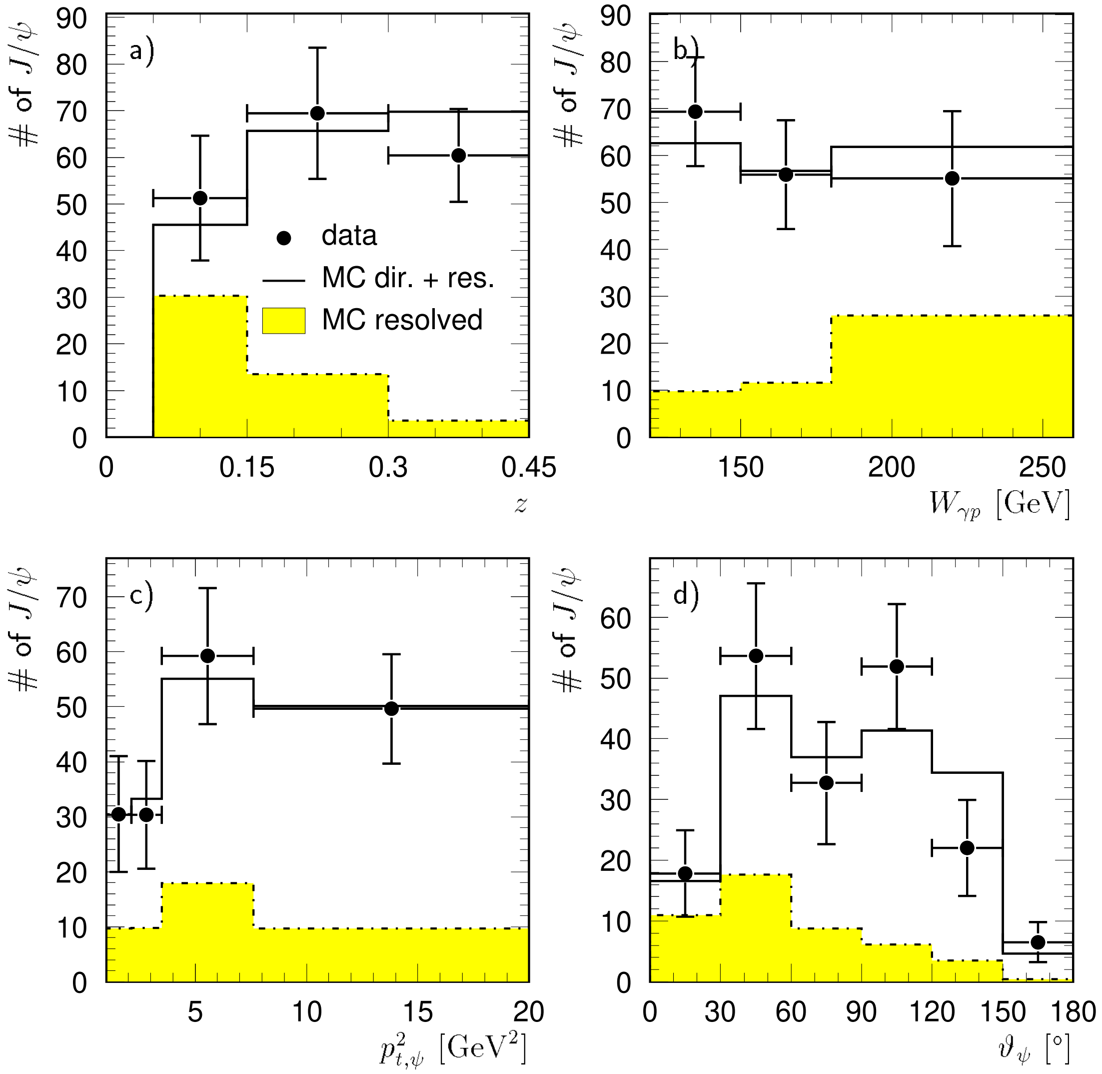

Figure 6.2: *Comparison of data and the two component simulation (EPJPSI-direct + EPJPSI-resolved) for a) the elasticity z, b) $W_{\gamma p}$, c) $p_{t,\psi}^2$ and d) the polar angle ϑ_ψ of the J/ψ meson. All distributions are restricted to the range* $0.05 < z < 0.45$ *and* $p_{t,\psi}^2 > 1\,\mathrm{GeV}^2$.

From the simulation about half of the events with resolved photons are expected to have a photon remnant detected in the SpaCal.

6.3 Systematic Errors

A list of the systematic errors is given in table 6.1. As in the medium z region large contributions are due to uncertainties in the description of the data by the simulation which were discussed in chapter 4. In addition the background from other production processes increases the systematic error. The sources will be discussed in the following item by item.

source	amount
track reconstruction	6%
reconstruction of z	5%
muon identification	6.2%
L1 iron trigger efficiency	2.0%
L1 track & SpaCal trigger efficiency	9.7%
L4 trigger efficiency	3%
parton density functions	5% (10%)
background from B-meson decays	−14%
luminosity	1.5%
branching ratio	1.7%
total	+15.4% (+17.7%) −20.8% (−22.5%)

Table 6.1: *Sources of the systematic error. The values in brackets refer to the lowest $W_{\gamma p}$ bin.*

As in the medium z analysis the error on the track reconstruction is estimated to be 2% per track, resulting in 6% for at least three reconstructed tracks.

The cross sections will be derived in an interval $0.05 < z < 0.45$. Since the resolution is about 0.02 at low z the influence of the z reconstruction is estimated by varying the lower z cut by ± 0.01. In addition to the expected shift by 2.5%, variations of about 5% are observed.

For the muon identification efficiency no systematic deviation between the data and the simulation is found after correcting the identification probability in the LAr calorimeter (fig. 4.15). To estimate a systematic error, the weighted quadratic average of half of the remaining differences between data and simulation as a function of $\vartheta_\mu$is used. The resulting error is 5.7% for the identification in the CMD, 2.4% in the LAr calorimeter or CMD and 6.2% for the quadratic sum of both. As a cross check the full differences are added linearly resulting in +4.7% for the CMD and +3.5% for the LAr or the CMD. This means that the identification in the simulation is in total more efficient than in the data. In the medium z analysis, in the momentum and polar angular range $20° < \vartheta_\mu < 160°$ and $p_\mu > 1.1\,\mathrm{GeV}$ instead of $20° < \vartheta_\mu < 140°$ and $p_\mu > 0.8\,\mathrm{GeV}$, the identification in the simulation is less efficient than in the data.

For the L1 trigger efficiencies the contributions of the different subtriggers have to be considered separately, since S56 is made up from different trigger elements compared to S19||S22. About 10% of all events in the low z analysis are accepted by S56. Therefore the total systematic error is calculated as a weighted sum of the errors of the trigger elements of S56 and of S19||S22. These errors of the trigger elements are estimated as follows.

Since no systematic deviation is found for the iron trigger elements (fig. 4.19), half of the differences in the trigger efficiency as a function of the polar angle between data and simulation are used to estimate the systematic error. The quadratic sum is 2.3% for `Mu_Any` (S56) and 2.0% for `Mu_Bar||Mu_ECQ` (S19||S22). The linear sum of the full differences would have been −1.3% for `Mu_Any` and 0.8% for `Mu_Bar||Mu_ECQ`.

For the track and SpaCal trigger elements a small systematic shift cannot be excluded (fig. 4.17, 4.18). Therefore the quadratic sum of the full differences is used to estimate the systematic errors. This results in 7% for `SPCLe_IET`, 1% for `DCRPh_Ta` (S56), 6% for `DCRPh_CNH` and 8% for `zVtx_sig1` (S19||S22).

All efficiencies of trigger level 4 which are not corrected for in the simulation are above 97% (see section 4.3.3). A systematic error of 3% is assumed.

In the simulation of the resolved processes the photon parton density function (PDF) enters in addition to the proton PDF. Since the photon PDF is not so well known as the proton PDF, the influence of different photon PDFs on the geometrical acceptance is studied. For the proton the 'standard' PDF MRS(A') is used. For the photon GRV92 LO [41] is taken as reference in figure 6.3 because it fits a previous H1 measurement with dijet events [67]. It was replaced by the more recent functions GAL [48] and SAS1D [49], which both show a slower rise towards small x_γ than GRV92 LO. In figure 6.3 the acceptance calculated with the LAC1 [50] PDF is shown in addition, an old function which is known to be too steep [67]. The biggest differences in the acceptance are found in the first $W_{\gamma p}$ bin, where an error of 10% is assumed. For other observables like z, and in the higher $W_{\gamma p}$ region, the differences are covered by an error of 5%.

In the following three different production mechanisms for J/ψ mesons which are considered as background sources for this analysis are discussed. The J/ψ mesons originating from the decay of B-mesons are considered in the systematic error since they show a different dependence e.g. on z than the J/ψ production in direct photon-gluon fusion or in gluon-gluon fusion with resolved photons (see chapter 3). The contributions from χ_c and $\psi(2s)$ decays are estimated but not included in the systematic error because they show a very similar dependence as the corresponding process where the J/ψ is produced directly.

The background from the decay of B-mesons is estimated with the simulation package EPJPSI (see chapter 3). For the normalization the total $b\bar{b}$ cross section measured by H1 [43] is used. It is assumed that the B particles decay into a J/ψ with a branching ratio of 1.16% ([8], B admixture). In order not to rely on the simulation of the trigger efficiency which has not been checked, a mean trigger efficiency of 65% is used. This leads to a fraction of 14% of the J/ψ mesons in this analysis resulting from the decay of B-mesons. The shapes of the distributions for J/ψ mesons originating from B-meson decay differ from those of EPJPSI-direct and EPJPSI-resolved separately, but are in agreement with the shape of the sum of both simulations and with the data as shown in figure 6.2. This means that it cannot be excluded that the cross sections for direct photon-gluon fusion and gluon-gluon fusion with resolved photons are lower by a constant fraction and there is a third component, the B-meson decay. A fraction of 14% is therefore included in the systematic error.

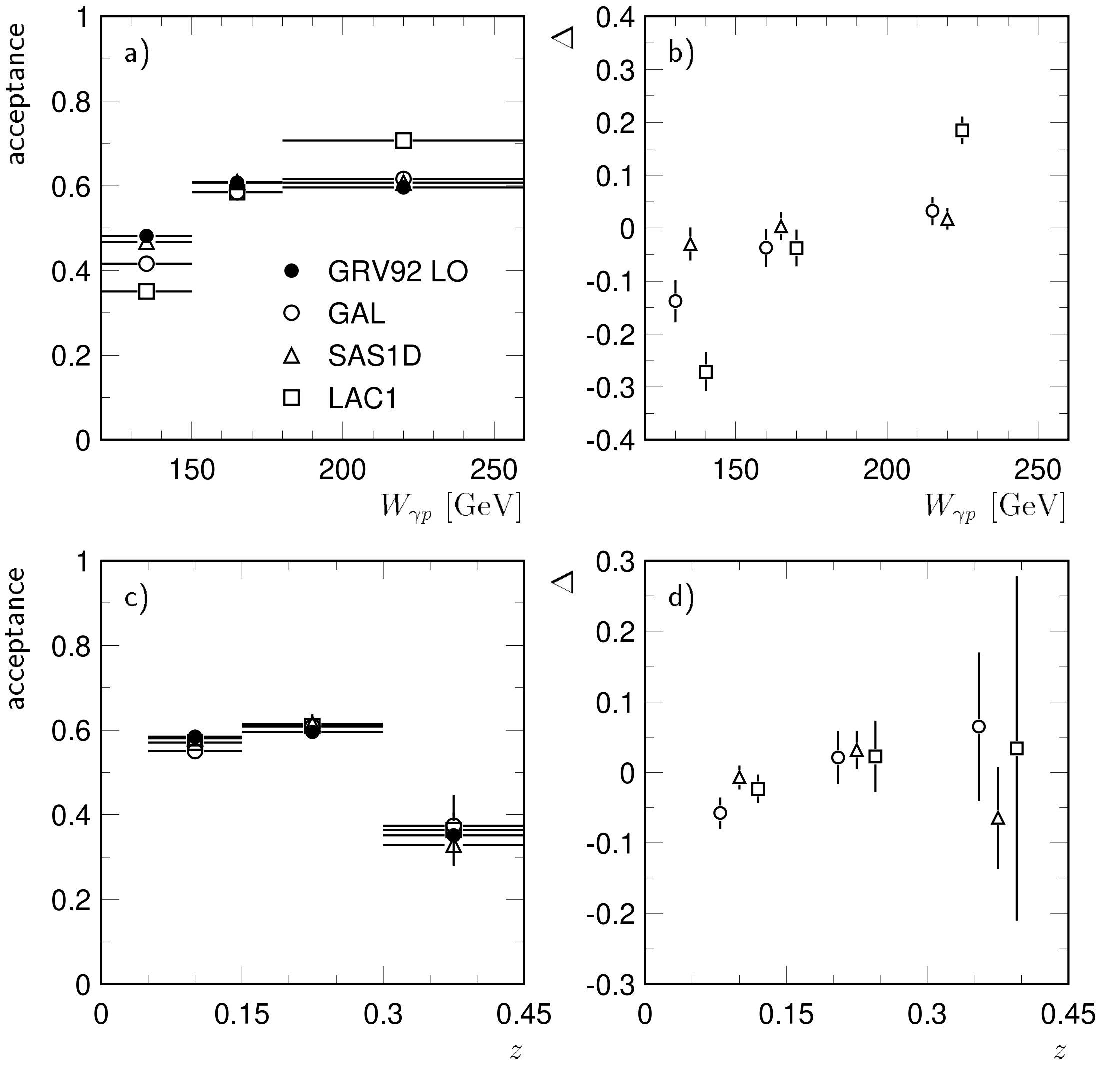

Figure 6.3: *Comparison of the geometric acceptance as a function of $W_{\gamma p}$ (a,b) and z (c,d) for a resolved photon Monte Carlo simulation with different photon parton densities. In a) and c) the acceptance is shown, in b) and d) the difference $\Delta = (\mathsf{acc} - \mathsf{acc}_{\mathsf{GRV92LO}})/\mathsf{acc}_{\mathsf{GRV92LO}}$ relative to the acceptance obtained with GRV92 LO (the points are shifted for clarity). The proton PDF is MRS(A') in all cases.*

A further source of background is the decay of χ_c mesons which is, however, not considered in the systematic error. The χ_c mesons are produced in resolved photon processes and can decay into a J/ψ meson and a low-energy photon (see chapter 3). In the detector such events are hard to distinguish from events in which the J/ψ is formed in the gluon-gluon fusion process. The total electron-proton cross section for χ_c mesons with $p_{t,\chi}^2 > 1\,\mathrm{GeV}^2$ calculated by EPJPSI is $\sigma(ep \to \chi_c X) = 0.598 \pm 0.010\,\mathrm{nb}$. With the branching ratios from [8] and considering only events fulfilling $p_{t,\psi}^2 > 1\,\mathrm{GeV}^2$ this corresponds to $\sigma(ep \to \chi_c X \to J/\psi X) = 0.093\,\mathrm{nb}$. The result for J/ψ mesons originating from a gluon-gluon fusion with $p_{t,\psi}^2 > 1\,\mathrm{GeV}^2$ is $\sigma(ep \to J/\psi X) = 1.29\,\mathrm{nb}$ (both calculated for a proton beam energy of $E_p = 920\,\mathrm{GeV}$). This means that χ_c mesons are expected to contribute a background of about 7% to the J/ψ mesons in resolved photoproduction. Neither this background will be subtracted nor the expected contribution of about 15% from $\psi(2s)$ decays since both contributions are expected to show very similar dependences as the corresponding processes where the J/ψ meson is produced directly.

The error of the luminosity measurement is taken from [57]. For the branching ratio and its error the particle data group [8] value $BR(J/\psi \to \mu\mu) = (5.88 \pm 0.10)\%$ is used. These errors affect only the normalization.

6.4 Cross Sections as Functions of $W_{\gamma p}$, z and $p_{t,\psi}^2$

The cross sections in the region of low z are presented as functions of the photon-proton energy $W_{\gamma p}$, the elasticity z and the transverse momentum squared of the J/ψ meson $p_{t,\psi}^2$. For a comparison the prediction of the Monte Carlo generator EPJPSI for direct photon-gluon fusion and resolved photon processes is used. Since the simulation is used as a theoretical prediction the $p_{t,\psi}^2$-dependent reweighting is not applied, neither for the direct nor for the resolved cross sections. The only adjustment is a k factor of 2 for the direct contribution. For the differential cross section as a function of z a prediction of Kniehl and Kramer [25] is also compared to the data. Other theoretical predictions for inelastic J/ψ production at HERA such as [30] are calculated for a fixed value of $W_{\gamma p} = 100\,\text{GeV}$ and are therefore not comparable to the data, which cover the range $120 < W_{\gamma p} < 260\,\text{GeV}$.

$W_{\gamma p}$ Dependence

The total photoproduction cross section for inelastic J/ψ production in the kinematic region $Q^2 < 1\,\text{GeV}^2$, $0.05 < z < 0.45$ and $p_{t,\psi}^2 > 1\,\text{GeV}^2$ is shown in figure 6.4 as a function of $W_{\gamma p}$. For comparison, the cross section determined in the medium z analysis ($0.3 < z < 0.9$), where nearly no contributions from resolved photon processes are expected, is also shown. The prediction of EPJPSI for direct photon-gluon fusion with a scale factor of 2 is found to describe the data well. After also applying the same k factor to the prediction for direct photon-gluon fusion in the low z region, the sum of the predictions for both processes is in agreement with the measurement at low z. Since the dependence on $W_{\gamma p}$ is very similar for the two production mechanisms, no direct evidence for resolved photon contributions can be inferred from this distribution.

z Dependence

The differential photoproduction cross section as a function of the elasticity z, integrated over the range $120 < W_{\gamma p} < 260\,\text{GeV}$, is in good agreement with the sum of the EPJPSI predictions for the two production processes (fig. 6.5 a). While the cross section for direct photon-gluon fusion falls towards low z, the data show a flat behaviour indicating contributions from processes with resolved photons, which increase toward low z and contribute 80% at $z < 0.15$ with the chosen normalizations. The measurement in the lowest z bin is, however, compatible with zero within $2.7\,\sigma$ of the total error ($3.8\,\sigma$ of

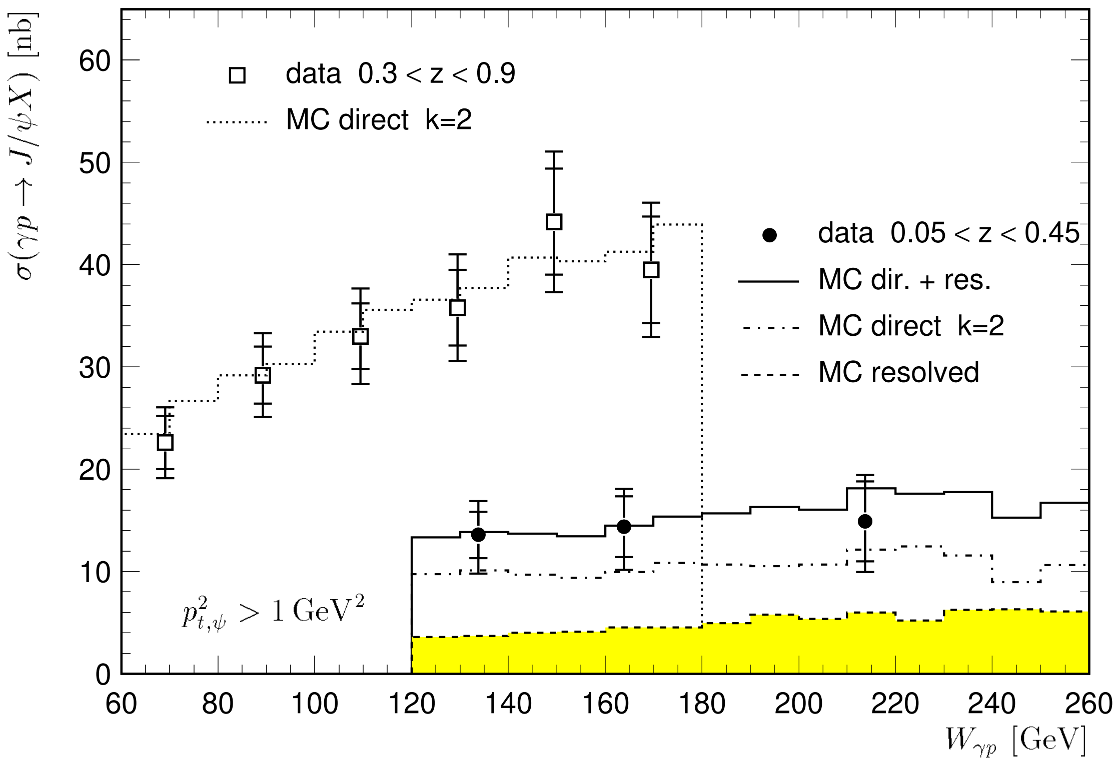

Figure 6.4: *Total cross section as a function of* $W_{\gamma p}$ *for inelastic* J/ψ *photoproduction in the region* $0.05 < z < 0.45$ *(filled circles). The lines are predictions of the Monte Carlo Generator EPJPSI. The dashed line shows the prediction of the resolved photon simulation, the dash–dotted line the contribution of direct photon-gluon fusion simulation multiplied with a k factor of* 2 *and the full line the sum of both. The size of the k factor is determined in the region of the medium z analysis* $0.3 < z < 0.9$ *(data: open squares, simulation: dotted line).*

the statistical error). On the other hand there is a clear J/ψ signal in this bin and a background fluctuation resulting in this signal is rather unlikely. The data in the lowest z bin is compatible with the normalized direct simulation within $2.2\,\sigma$ of the total error ($3.1\,\sigma$ of the statistical error). It has, however, not been measured up to now if the EPJPSI prediction for direct photon-gluon fusion is reliable at these very low elasticities. No conclusive statement on resolved photon processes is therefore possible.

In figure 6.5 b) the same data are shown in comparison with a theoretical prediction by Kniehl and Kramer [25] in a slightly different kinematic range ($130 < W_{\gamma p} < 250\,\mathrm{GeV}$). The calculation includes Colour Singlet (CS) and Colour Octet (CO) terms for the direct as well as the resolved processes. For the colour octet contributions rough estimates of higher order effects were made when extracting the Colour Octet Matrix Elements from the CDF data. The CTEQ5M parton density function was chosen for the proton and the GRV92 HO parton density function was chosen for the photon. α_s is evaluated from the two-loop formula with $\Lambda^{(4)} = 326\,\mathrm{MeV}$ resulting in values $\alpha_s \approx 0.21 \ldots 0.25$. The renormalization and factorization scales in the $\overline{MS}$ scheme are set to the transverse mass $m_t = \sqrt{4m_c^2 + p_t^2}$. The authors suggest a substantial k factor, and $k = 3$ is found to agree with the data. The CO contributions to the resolved photon processes clearly improve this agreement when compared to just the CS processes alone.

In the comparison between figures 6.5 a) and b) a difference in normalization of the CSM prediction for resolved photon processes is obvious. The average of the prediction in figure 6.5 b) for the lowest z bin is about 3 nb (without the k factor), while it is about 30 nb for EPJPSI (fig. 6.5 a). There are several differences in the calculations which are responsible for this effect. Since the cross section is $\mathcal{O}(\alpha_s^3)$, the different calculation of α_s has a large impact, up to a factor 3. The coupling of the J/ψ meson to the $c\bar{c}$ pair is calculated with the next-to-leading order formula for the leptonic decay width in EPJPSI, but with the leading order formula by Kniehl and Kramer. This results in an additional

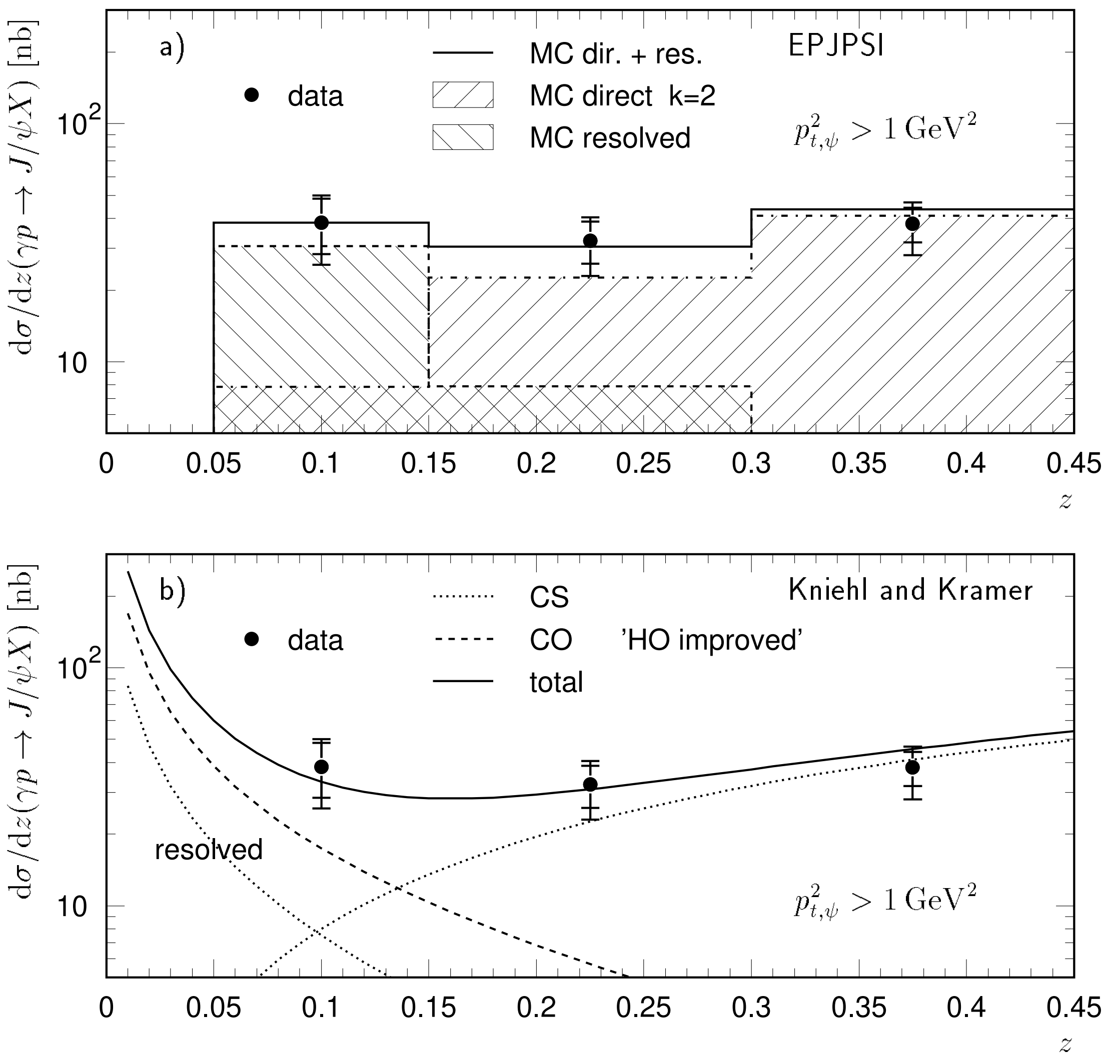

Figure 6.5: *Differential cross section as a function of the elasticity z in the region $p_{t,\psi}^2 > 1\,\mathrm{GeV}^2$, integrated over the range $120 < W_{\gamma p} < 260\,\mathrm{GeV}$, compared a) with the sum of the predictions of a resolved and a scaled direct simulation (EPJPSI) and b) with a theoretical prediction by Kniehl and Kramer [25] multiplied by a k factor of 3 (see text).*

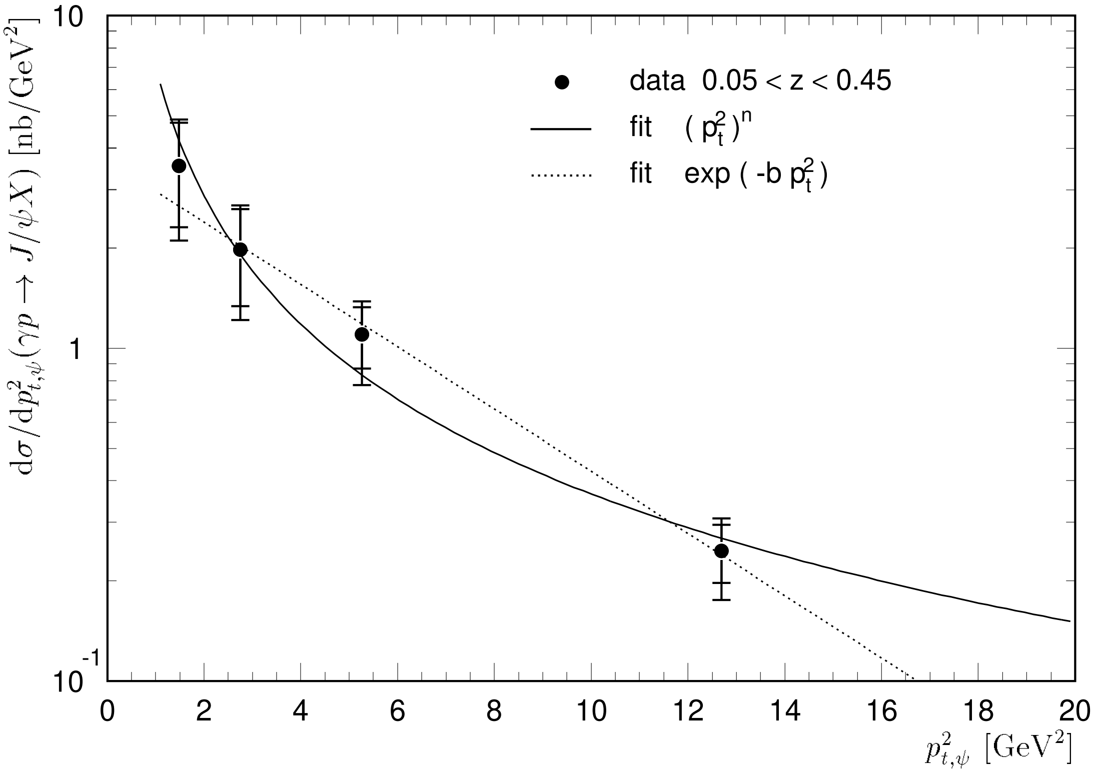

Figure 6.6: *Differential cross section* $\mathrm{d}\sigma/\mathrm{d}p^2_{t,\psi}$ *for inelastic* J/ψ *photoproduction in the region* $0.05 < z < 0.45$ *integrated over* $120 < W_{\gamma p} < 260\,\mathrm{GeV}$. *In addition two fits of the forms* $a_1 \cdot (p^2_{t,\psi})^n$ *(full line) and* $a_2 \cdot e^{-b \cdot p^2_{t,\psi}}$ *(dotted line) are shown. Only the statistical errors are considered in the fits.*

factor 2. The relativistic corrections and the leading order photon parton density function in EPJPSI can increase the cross section by about 30% each. The CTEQ5M proton parton density function is very similar to MRS(A') in the relevant x_g range. In total the effects account for a factor 10, in agreement with the difference which is found.

$p^2_{t,\psi}$ Dependence

The differential cross section $\mathrm{d}\sigma/\mathrm{d}p^2_{t,\psi}$ is shown in figure 6.6 together with two fits of different functional forms. The first fit is of the form $a_1 \cdot (p^2_{t,\psi})^n$ like the one used for the double differential analysis in the medium z region (section 5.6). The resulting value $n = -1.28 \pm 0.15$ is slightly lower than the one obtained in the medium z region ($n = -1.55 \pm 0.05$), but compatible within errors. In addition a fit of the form $a_2 \cdot e^{-b \cdot p^2_{t,\psi}}$ is shown, which agrees much better with the low z data, but does not describe the results of the medium z analysis. The result is $b = 0.22 \pm 0.03$.

From the simulation small differences in the slope parameter b are expected between direct and resolved photon processes. In order to illustrate the $p^2_{t,\psi}$ dependence of the simulation, the ratio of the two components of the simulation to the data is plotted in figure 6.7 separately. For the direct photon-gluon fusion the distributions with and without the $p^2_{t,\psi}$ dependent reweighting (see section 5.2.1) are shown. The simulation of direct and resolved photon processes both show a steeper decrease than the data. Using exponential fits the differences in the slopes b are $\Delta b = -0.070 \pm 0.032$ for direct photon-gluon fusion and $\Delta b = -0.046 \pm 0.028$ for gluon-gluon fusion with resolved photons. After the $p_{t,\psi}^2$ dependent reweighting the direct photon-gluon fusion simulation is in agreement with the data ($\Delta b = +0.019 \pm 0.032$).

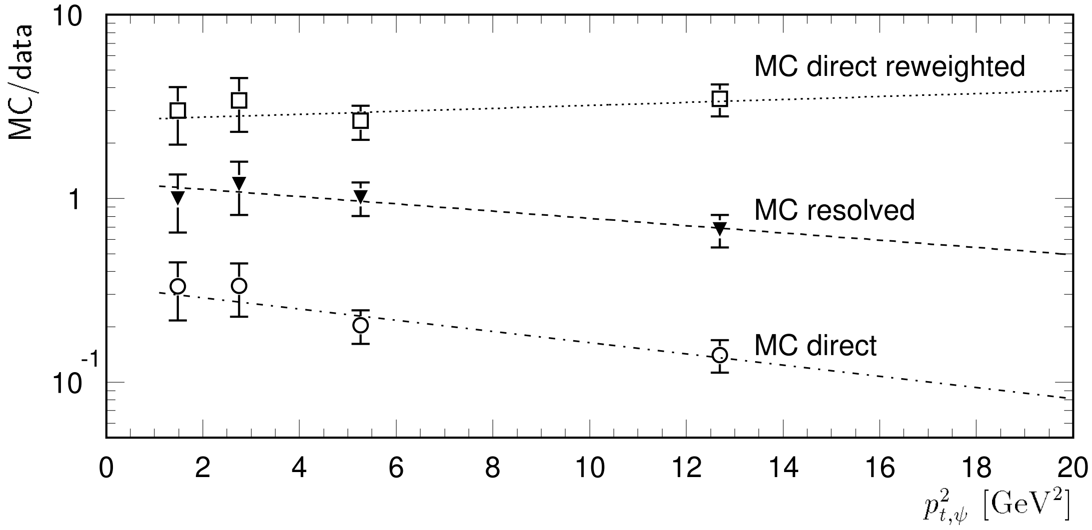

Figure 6.7: *The points represent the ratio of three sets of simulations to the data of figure 6.6* ($\mathrm{d}\sigma/\mathrm{d}p_{t,\psi}^2$) *including only statistical errors. The predictions of EPJPSI for direct photon-gluon fusion and gluon-gluon fusion with resolved photons are shown separately. In addition the ratio for the direct process with the* $p_{t,\psi}^2$ *dependent reweighting is plotted. The normalization is arbitrary. Fits with exponential functions are shown.*

Conclusions and Outlook

In this thesis, an analysis of the photoproduction (corresponding to $Q^2 < 1\,\mathrm{GeV}^2$) of J/ψ mesons at medium and low elasticities z was presented. The muonic decay channel was used to select the J/ψ mesons. The data have been collected with the H1 detector at the electron-proton collider HERA and correspond to an integrated luminosity of about $40\,\mathrm{pb}^{-1}$. The data could be described by a two component Monte Carlo simulation of direct photon-gluon fusion (after reweighting the $p_{t,\psi}^2$ distribution) and gluon-gluon fusion with resolved photons. This simulation was used to correct the data for detector effects.

In the medium z range the total photoproduction cross section as a function of the photon-proton centre-of-mass energy $W_{\gamma p}$ and the single differential cross sections as functions of the elasticity z, the transverse momentum squared of the J/ψ meson $p_{t,\psi}^2$ and the fractional gluon momentum inside the proton x_g are extracted. The kinematic range is $0.3 < z < 0.9$, $60 < W_{\gamma p} < 180\,\mathrm{GeV}$ and $p_{t,\psi}^2 > 1\,\mathrm{GeV}^2$. The contribution from the decay of $\psi(2s)$ mesons produced inelastically is included in the data. The results are found to be in agreement with previous H1 and ZEUS measurements. A comparison with theoretical predictions in the next-to-leading order Colour Singlet Model yields good agreement for $W_{\gamma p}$, $p_{t,\psi}^2$ and z. For the gluon density in the proton a function which is slowly rising towards small x_g like MRS(A') [1] is preferred. Although the statistical and systematic errors are significantly reduced compared to previous H1 analyses, they are too large to exclude a steeper gluon density function such as GRV98 LO [45]. Due to large uncertainties arising from missing higher order terms in Colour Octet Model predictions and possible transverse momenta of the initial state partons no final statement on colour octet contributions is possible.

The double differential cross section in $p_{t,\psi}^2$ and z shows a hint for a steeper decrease of the data with $p_{t,\psi}^2$ at low and high z than at medium z. With the analysed statistics it is, however, difficult to judge whether this z-dependence has its origin in different production mechanisms in the analysed z bins or is a fluctuation.

A study of the decay angle distributions of inelastically produced J/ψ mesons in two elasticity regions, $0.3 < z < 0.6$ and $0.6 < z < 0.9$, is presented. The precision of the data is not sufficient to allow any conclusion on a dependence of the polarization parameters λ and ν on z. The distributions are compatible with unpolarized J/ψ production within the errors.

In the region of the low elasticities, $0.05 < z < 0.45$, an analysis which aims to measure the contributions from resolved photon processes to J/ψ photoproduction is presented. The total photoproduction cross section as a function of $W_{\gamma p}$ and the differential cross sections as functions of z and $p_{t,\psi}^2$ in the kinematic region $120 < W_{\gamma p} < 260\,\mathrm{GeV}$ and $p_{t,\psi}^2 > 1\,\mathrm{GeV}^2$ are extracted. The decay of $\psi(2s)$ and χ_c mesons produced inelastically is included in the data. Contributions from resolved photon processes improve the agreement of the simulation and of theoretical predictions with the data compared to using only direct photon-gluon fusion which, without additional contribution, would be rather poor. The errors of data and theoretical prediction are, however, too large to draw a definitive conclusion. Due to the fact, that a variation of the photon gluon density, of the strong coupling α_s and of a few further model parameters can change the colour singlet prediction of the resolved photon processes by an order of magnitude, no statement on colour octet contributions is possible.

For both analyses presented here an increase of the integrated luminosity would be a clear improvement. In the medium z region the double differential cross sections are limited by statistics, as well as the entire low z analysis. During the data taking period 2000 H1 recorded about 50 inverse picobarn of physics data. The integrated luminosity from 1996 to 2000 amounts to about 90 inverse picobarn, which is twice the amount used for the present analysis. Due to the higher proton beam energy and the increased acceptance at high $W_{\gamma p}$ since 1999, data collected during the year 2000 will probably allow an extension of the kinematic regions in $W_{\gamma p}$.

In future a major luminosity upgrade program which has been in progress since autumn of the year 2000 will increase the instantaneous luminosity by about a factor five. The challenge for the analysis of photoproduction events will be the triggering since the trigger conditions have to be based on the hadronic final state and the increased input rate demands more restrictive trigger conditions.

A better resolution of the elasticity z would allow a finer binning and a more detailed analysis in the medium z region. This may be hard to achieve since a lot of effort was already used to obtain the present resolution.

In both elasticity regions the production of J/ψ mesons via other processes in addition to direct photon-gluon fusion and gluon-gluon fusion with resolved photon leads to uncertainties in the cross section determination. J/ψ mesons originating from the decay of $\psi(2s)$ mesons produced inelastically are estimated to contribute about 15%. Since they are hard to distinguish experimentally from the 'directly' produced J/ψ mesons they are usually considered in the theoretical predictions. At present only two preliminary measurements from the H1 and ZEUS collaborations exist that confirm the value of 15%, however with large errors.

The contributions from the decay of B and χ_c mesons have only been estimated for the low z region. There are two analyses in progress which attempt to measure J/ψ production via the decay of B-mesons with the help of the central silicon tracker and via χ_c decay by reconstructing the low-energy photon. A measurement of these cross sections could improve the estimate of the error or could be used to subtract the contributions from the decay of other mesons.

In order to distinguish colour octet from colour singlet contributions a Monte Carlo simulation of the colour octet processes would be very useful. In particular differences in the final state originating from the soft gluons could be studied. It might also be interesting to see if relativistic corrections would improve the agreement between the CASCADE predictions and the data. Other Monte Carlo generators such as HERWIG [68] could be used to cross-check the efficiency determination and to study model dependences.

Further theoretical effort is needed for an improvement of the determination of the Colour Octet Matrix Elements at the Tevatron which would allow more precise predictions for photoproduction and deep inelastic scattering at HERA. Calculations in next-to-leading order for the hadroproduction of J/ψ mesons could clarify how much impact the higher orders have on the $p_{t,\psi}^2$ dependence of the cross section and whether the resulting Colour Octet Matrix Elements are compatible with the HERA measurements.

Appendix A

Iron Trigger Timing Efficiency

In the context of this analysis a method was developed to determine the 'timing efficiency' of the iron trigger on the basis of DST data. Several effects are included in this efficiency. The pure timing efficiency is the probability that the trigger element is set in the correct bunch crossing if the iron layer coincidence condition is fulfilled. It takes into account the fact that the hits of four successive bunch crossings are used for the track reconstruction in the instrumented iron, but only two successive bunch crossings are used for the triggering. Additional inefficiencies are introduced by imperfections of the hardware and are also taken into account by the determination of the 'timing efficiency' with the method presented here.

In DST data only very limited information is available about tracks in the instrumented iron. These are the coordinates of the first hit (in x, y, z or r, ϑ, φ coordinates), the hit layers, a momentum estimate, the angular direction of the track and its timing. The information about single hits, especially which modules they are in, is not stored on DST. The granularity of the trigger information is also very coarse (forward inner endcap, forward outer endcap, barrel, backward outer endcap or backward inner endcap), the module which caused the trigger is not available.

To determine the 'timing efficiency' the selection is based on events for which exactly one track is reconstructed in the instrumented iron. The events have to be accepted by an iron-independent L4 verified subtrigger. A cut rejecting cosmic ray muons is applied because these events have a different timing structure than muons originating from ep interactions. The method which is used to determine the 'timing efficiency' is divided into three steps:

1. The first hit of the iron track is used to assign the track to a module. This is done using the nominal position of the modules. Some regions in the barrel, where the muon boxes overlap two modules, are excluded.

2. The hit layers of the track have to fulfil the layer coincidence condition of the iron trigger in this module. Other events are excluded.

3. The 'timing efficiency' is the ratio of the events, where the iron trigger element, which corresponds to the module with the track, is set, and the total number of events with tracks in this module.

This efficiency is stored module by module in the ITTE bank and is used to take into account all other efficiencies relevant for the iron trigger besides the single layer efficiency of the limited streamer tubes in the simulation.

Appendix B

L4 Class 16

Class 16 consists of 6 subclasses (AOPEN, ATWOMU, ATWOEL, AJPSI, 2ELEC and 2PRONG) which cover the elastic and inclusive production of heavy vector mesons decaying leptonically as well as inclusive muons for beauty measurements. Two subclasses (ATWOEL and 2ELEC) are designed for the electron channel and therefore not explained here. 2PRONG requires no lepton identification but exactly two central tracks which makes it inefficient for the presented analyses. The most relevant subclasses are AJPSI, AOPEN and ATWOMU. Their requirements are as follows. For cuts which differ in $99e^-$ and $99e^+$ running the $99e^+$ value is given in brackets. The track and muon identification criteria are listed afterwards in table B.1.

AJPSI : muonic decay of inelastically produced J/ψ

- ≥ 2 muons identified in the CMD, FMD or LAr (for LAr $\vartheta > 20\,[18]^\circ$) with good associated inner track (see table B.1)
- $M_{\mu\mu} > 2\,\mathrm{GeV}$
- [$\sum Q_c^i \geq 5$ for events without CMD or FMD muons]
- [cosmic ray filter]

AOPEN: inclusive muons

- ≥ 1 muon identified in the CMD ($N_{layers} \geq 6$ for endcaps) or FMD with good associated inner track
- central muon ($\vartheta \geq 20\,[18]^\circ$): $p_t > 2.0\,[1.5]\,\mathrm{GeV}$
- forward muon ($\vartheta < 20\,[18]^\circ$): $p > 5.0\,\mathrm{GeV}$ and ($\vartheta > 15^\circ$ or FMD muon)
- [$N_{KTKX} \geq 4$]

ATWOMU: muonic decay of elastically produced heavy vector mesons

- ≥ 1 muon identified in the CMD, FMD or LAr ($Q_c = 3$) with good associated inner track [$\vartheta_\mu > 18^\circ$ or $p_\mu > 4.0\,\mathrm{GeV}$ or FMD + CMD identification]

- ≥ 1 vertex fitted track (quality criteria only asked for FTD tracks) [with central track ($\vartheta > 18°$): $p > 0.7\,\mathrm{GeV}$ or forward track ($\vartheta < 18°$): $p > 4.0\,\mathrm{GeV}$]
- $M_{\mu\,track} > 2\,\mathrm{GeV}$
- $N_{KTKX} \leq 5$
- [cosmic ray filter]

Inner Track Criteria	
only vertex fitted tracks with $\lvert z_0 - z_{nom}\rvert \leq 40\,\mathrm{cm}$, $p \geq 0.8\,[0.7]\,\mathrm{GeV}$	and
• central tracks: $R_{start} \leq 50\,\mathrm{cm}$	
• forward tracks: $R_0 \leq 10\,\mathrm{cm}$	and
$\chi^2_{trackfit}/\mathrm{NDF} \leq 10.0$	and
$\chi^2_{vertexfit}/\mathrm{NDF} \leq 50.0$	and
$N_{planar\,segments} \geq 1$	and
$N_{segments} \geq 2$ for $\theta < 20°$	and
$p \geq 1.0\,\mathrm{GeV}$ **or** $p_t \geq 0.150\,\mathrm{GeV}$	
• combined tracks: no additional cuts	
Muon Identification in the Central Muon Detector	
only iron tracks linked to a 'good' inner track with $P(\chi^2) \geq 0.0001$	and
($N_{layers} \geq 6/2/3$ and $i_{first\,layer} \leq 5/5/8$ (FEC/barrel/BEC)) or l_{save}	and
• barrel: $\rho < 100\,\mathrm{cm}$ if $N_{layers} > 6$	and
$z_0 \leq 100\,\mathrm{cm}$ if $N_{strip} > 1$	
• endcaps: $\rho_x < 100\,\mathrm{cm}$ if $N_{strip} > 1$	and
$\rho_y < 100\,\mathrm{cm}$	
Muon Identification in the LAr Calorimeter	
at least *normal* quality ($Q_c \geq 2$)	
Muon Identification in the Forward Muon Detector	
$-400 < zvx < 300\,\mathrm{cm}$ and $IQ \leq 2$	

Table B.1: *Selection criteria of class 16 in the data taking period 1999 for tracks reconstructed in the tracking detectors and for the muon identification. In the cases where different cuts were used in 99e$^-$ and 99e$^+$ running the 99e$^+$ value is given in brackets.*

The variables used for class 16 in the online classification are:

- ϑ: polar angle of a vertex fitted track
- $M_{\mu\mu}$, $M_{\mu\,track}$: invariant mass of two muons or of a muon and a vertex fitted track

- Q_c: μ quality in the LAr [for $99e^+$ the cuts for the identification are relaxed in comparison to the offline values]
- p, p_t: momentum, transverse momentum of a vertex fitted track
- N_{KTKX}: number of rows of the KTKX bank, this is one more than the number of vertex fitted tracks in the event
- z_0: z coordinate of a (non vertex fitted) track at the point of closest approach
- z_{nom}: z coordinate of the nominal interaction point
- R_{start}: radial distance of the first hit to the z axis
- R_0: radial distance of a non vertex fitted track to the nominal vertex
- $\chi^2_{trackfit}$: χ^2 of the track fit to the hits in the tracking detectors
- $\chi^2_{vertexfit}$: χ^2 of the fit of the track to the the primary event vertex
- NDF: number of degrees of freedom
- $N_{planar\,segments}$: number of hit planar segments in the FTD
- $N_{segments}$: number of hit radial and planar Segments in the FTD
- N_{layers}: number of hit streamer tube layers in the instrumented iron (excluding the muon boxes)
- $i_{first\,layer}$: first hit streamer tube layer in the instrumented iron (excluding the muon boxes)
- l_{save}: $|\kappa| < 0.001$ or $N_{KTKX} < 6$ or extrapolated inner track hits gap in iron, where κ is the curvature of the inner track
- N_{strip}: number of hit strip layers in the instrumented iron
- ρ, ρ_x, ρ_y: radial distance of the extrapolated iron track to the primary event vertex and its x and y component
- z_0: z coordinate at the iron track starting point
- zvx: intersection of extrapolated FMD track and z axis
- IQ: quality of track fit in the FMD (1 ... 5=good ... bad)

Appendix C

Lee West Track and Muon Selection

C.1 Track Selection

combined tracks			forward tracks		
p_t	$>$	$0.150\,\mathrm{GeV}$	p_t	$>$	$0.150\,\mathrm{GeV}$
ϑ	$>$	$0.0°$	ϑ	$>$	$6.0°$
	$<$	$180.0°$		$<$	$25.0°$
R_{start}	$<$	$50.0\,\mathrm{cm}$	R_0	$<$	$10.0\,\mathrm{cm}$
$\chi^2_{FTD\,CTD\,link}$	$<$	50.0	$\chi^2_{trackfit}$	$<$	10.0
$\chi^2_{vertexfit}$	$<$	50.0	$\chi^2_{vertexfit}$	$<$	25.0
σ_p/p	$<$	1	σ_p/p	$<$	1
$\lvert DCA\rvert$	$<$	$5.0\,\mathrm{cm}$	$N_{planar\ segments}$	$\geq$	1
central tracks			$N_{segments}$	$\geq$	2
p_t	$>$	$0.150\,\mathrm{GeV}$	p	$>$	$0.500\,\mathrm{GeV}$
ϑ	$>$	$20.0°$			
	$<$	$160.0°$			
R_{start}	$<$	$50.0\,\mathrm{cm}$			
$\lvert DCA\rvert$	$<$	$2.0\,\mathrm{cm}$			
track length	$>$	$10.0\,\mathrm{cm}$ for $\vartheta < 150°$			
track length	$>$	$5.0\,\mathrm{cm}$ for $\vartheta > 150°$			
$RPTPHTH$	$=$	1.0			

Table C.1: *Track selection cuts*

C.2 Muon Selection

forward endcap			backward endcap		
ρ_x	$<$	100 cm	ρ_x	$<$	100 cm
ρ_y	$<$	100 cm	ρ_y	$<$	100 cm
N_{layers}	$\geq$	6	N_{layers}	$\geq$	3
$i_{first\,layer}$	$\leq$	5	$i_{first\,layer}$	$\leq$	8
$i_{last\,layer}$	$\geq$	6	$i_{last\,layer}$	$\geq$	3
barrel			**calorimeter muons**		
ρ	$<$	100 cm	μ *quality* Q_c	$\geq$	2
z_0	$<$	100 cm	*separation angle*	$>$	12°
N_{layers}	$\geq$	2			
$i_{first\,layer}$	$\leq$	5			
$i_{last\,layer}$	$\geq$	2			

Table C.2: *Muon selection cuts*

Most variables used for the track and muon selection are already explained in appendix B for the online classification. Additional variables are:

- DCA: distance of closest approach to the primary event vertex
- σ_p/p: relative error of the momentum measurement
- track length: difference between the radius at the end of the track and that at the start
- $RPTPHTH$: variable used to remove unreliable parts of central tracks which were split into two parts by reconstruction problems
- $i_{last\,layer}$: last hit streamer tube layer in the instrumented iron
- *separation angle*: minimal distance of two muons identified in the calorimeter

Appendix D

Tables for Medium z

$W_{\gamma p}$ [GeV]	N_ψ	N_ψ fit	ΔN_ψ
$60.0 - 80.0$	86 ± 10	84 ± 10	2
$80.0 - 100.0$	123 ± 12	120 ± 12	3
$100.0 - 120.0$	131 ± 13	129 ± 12	2
$120.0 - 140.0$	115 ± 12	109 ± 12	6
$140.0 - 160.0$	95 ± 11	90 ± 11	5
$160.0 - 180.0$	73 ± 10	68 ± 9	5

Table D.1: *Numbers of J/ψ mesons in bins of $W_{\gamma p}$ after imposing a cut $p_{t,\psi}^2 > 1\,\mathrm{GeV}^2$ on the transverse momentum of the J/ψ meson. In addition to the values determined with the background subtraction method (N_ψ) the numbers obtained directly from the fitted Gaussian (N_ψ fit) and the differences between the methods (ΔN_ψ) are given .*

$p_{t,\psi}^2$ [GeV^2]	N_ψ	N_ψ fit	ΔN_ψ
$0.000 - 1.000$	182 ± 17	178 ± 16	4
$1.000 - 2.125$	162 ± 14	154 ± 14	8
$2.125 - 3.500$	119 ± 12	116 ± 12	3
$3.500 - 5.375$	95 ± 11	90 ± 11	5
$5.375 - 7.625$	71 ± 9	70 ± 9	1
$7.625 - 10.000$	47 ± 7	49 ± 7	-2
$10.000 - 14.000$	62 ± 8	55 ± 8	7
$14.000 - 20.000$	31 ± 6	31 ± 6	0

Table D.2: *Numbers of J/ψ mesons in bins of $p_{t,\psi}^2$.*

$\log_{10}(x_g)$	N_ψ	N_ψ fit	ΔN_ψ
-3.1 – -2.9	51 ± 8	50 ± 8	1
-2.9 – -2.7	108 ± 12	100 ± 12	8
-2.7 – -2.5	139 ± 13	135 ± 13	4
-2.5 – -2.3	137 ± 13	133 ± 12	4
-2.3 – -2.1	99 ± 11	96 ± 11	3
-2.1 – -1.9	51 ± 7	46 ± 7	5

Table D.3: *Numbers of J/ψ mesons in bins of* $\log_{10}(x_g)$

$W_{\gamma p}$ [GeV]	$\langle W_{\gamma p} \rangle$	ε_{sel} [%]	ε_{trig} [%]	σ_{ep} [nb]	$\Phi_{\gamma/e}$	$\sigma_{\gamma p}$ [nb]
$60.0 - 80.0$	69.3	15.6	41.4	0.577 ± 0.065	0.0255	$22.6 \pm 2.6 \pm 2.3$
$80.0 - 100.0$	89.4	19.6	51.3	0.530 ± 0.051	0.0181	$29.2 \pm 2.8 \pm 3.0$
$100.0 - 120.0$	109.5	23.2	54.8	0.448 ± 0.043	0.0136	$33.0 \pm 3.2 \pm 3.4$
$120.0 - 140.0$	129.6	21.7	61.4	0.375 ± 0.039	0.0105	$35.8 \pm 3.7 \pm 3.7$
$140.0 - 160.0$	149.6	18.5	61.0	0.366 ± 0.043	0.0083	$44.2 \pm 5.2 \pm 4.5$
$160.0 - 180.0$	169.6	18.2	66.5	0.262 ± 0.035	0.0066	$39.5 \pm 5.2 \pm 4.0$

Table D.4: *Overview over the numbers used to determine the total photoproduction cross section as a function of $W_{\gamma p}$. The selection efficiency includes the geometrical acceptance. For the electroproduction cross section only the statistical error is given.*

z	$\langle z \rangle$	ε_{sel} [%]	ε_{trig} [%]	$\mathrm{d}\sigma_{ep}/\mathrm{d}z$ [nb]	$\mathrm{d}\sigma_{\gamma p}/\mathrm{d}z$ [nb]
$0.30 - 0.45$	0.375	20.4	55.1	2.56 ± 0.34	$30.9 \pm 4.1 \begin{array}{l} +3.1 \\ -3.4 \end{array}$
$0.45 - 0.60$	0.525	23.4	53.9	3.53 ± 0.31	$42.7 \pm 3.8 \begin{array}{l} +4.3 \\ -4.3 \end{array}$
$0.60 - 0.75$	0.675	19.3	58.8	4.78 ± 0.37	$57.8 \pm 4.4 \begin{array}{l} +5.9 \\ -5.8 \end{array}$
$0.75 - 0.90$	0.825	16.1	50.2	6.41 ± 0.49	$77.6 \pm 6.0 \begin{array}{l} +9.3 \\ -7.7 \end{array}$

Table D.5: *Overview over the numbers used to determine the differential photoproduction cross section as a function of z.*

$p_{t,\psi}^2$ [GeV^2]	$\langle p_{t,\psi}^2 \rangle$ [GeV^2]	ε_{sel} [%]	ε_{trig} [%]	$\mathrm{d}\sigma_{ep}/\mathrm{d}p_{t,\psi}^2$ [nb/GeV^2]	$\mathrm{d}\sigma_{\gamma p}/\mathrm{d}p_{t,\psi}^2$ [nb/GeV^2]
$0.000 - 1.000$	0.50	9.7	51.1	1.60 ± 0.15	$19.4 \pm 1.8 \begin{array}{l} +2.0 \\ -5.8 \end{array}$
$1.000 - 2.125$	1.47	14.2	54.3	0.815 ± 0.072	$9.86 \pm 0.87 \pm 1.01$
$2.125 - 3.500$	2.74	17.2	55.1	0.397 ± 0.041	$4.81 \pm 0.50 \pm 0.49$
$3.500 - 5.375$	4.35	19.0	57.5	0.201 ± 0.023	$2.43 \pm 0.27 \pm 0.25$
$5.375 - 7.625$	6.42	21.4	55.9	0.115 ± 0.015	$1.39 \pm 0.18 \pm 0.14$
$7.625 - 10.000$	8.74	27.8	56.2	0.0553 ± 0.0085	$0.669 \pm 0.103 \pm 0.068$
$10.000 - 14.000$	11.86	29.2	46.7	0.0492 ± 0.0066	$0.595 \pm 0.079 \pm 0.061$
$14.000 - 20.000$	16.77	31.3	49.8	0.0142 ± 0.0028	$0.172 \pm 0.033 \pm 0.018$

Table D.6: *Overview over the numbers used to determine the differential photoproduction cross section as a function of $p_{t,\psi}^2$.*

$\log_{10}(x_g)$	$\langle\log_{10}(x_g)\rangle$	ε_{sel} [%]	ε_{trig} [%]	$\mathrm{d}\sigma_{ep}/\mathrm{d}\log_{10}(x_g)$ [nb]	$\mathrm{d}\sigma_{\gamma p}/\mathrm{d}\log_{10}(x_g)$ [nb]
-3.1 – -2.9	-3.0	12.5	58.6	1.52 ± 0.24	$18.4 \pm 2.9 \pm 1.9$
-2.9 – -2.7	-2.8	17.7	63.7	2.09 ± 0.23	$25.2 \pm 2.8 \pm 2.6$
-2.7 – -2.5	-2.6	19.8	60.7	2.51 ± 0.24	$30.4 \pm 2.8 \pm 3.1$
-2.5 – -2.3	-2.4	20.1	52.4	2.82 ± 0.26	$34.2 \pm 3.2 \pm 3.5$
-2.3 – -2.1	-2.2	23.9	49.4	1.82 ± 0.20	$22.0 \pm 2.4 \pm 2.2$
-2.1 – -1.9	-2.0	26.1	45.2	0.941 ± 0.137	$11.4 \pm 1.7 \pm 1.2$

Table D.7: *Overview over the numbers used to determine the differential photoproduction cross section as a function of* $\log_{10}(x_g)$

$0.3 < z < 0.6$						
$p^2_{t,\psi}$ [GeV^2]	$\langle p^2_{t,\psi}\rangle$ [GeV^2]	N_ψ	ε_{sel} [%]	ε_{trig} [%]	$\mathrm{d}^2\sigma_{ep}/\mathrm{d}p^2_{t,\psi}\,\mathrm{d}z$ [nb/GeV^2]	$\mathrm{d}^2\sigma_{\gamma p}/\mathrm{d}p^2_{t,\psi}\,\mathrm{d}z$ [nb/GeV^2]
1.000 – 2.125	1.47	75 ± 10	15.9	53.7	1.13 ± 0.1571	$13.7 \pm 1.9 \pm 1.4$
2.125 – 3.500	2.74	43 ± 8	19.5	58.8	0.390 ± 0.0750	$4.72 \pm 0.91 \pm 0.48$
3.500 – 5.375	4.35	37 ± 7	20.5	60.1	0.234 ± 0.0468	$2.84 \pm 0.57 \pm 0.29$
5.375 – 7.625	6.41	33 ± 7	24.5	54.0	0.162 ± 0.0325	$1.96 \pm 0.39 \pm 0.20$
7.625 – 10.000	8.74	19 ± 5	29.0	56.9	0.0707 ± 0.0174	$0.855 \pm 0.211 \pm 0.087$
10.000 – 14.000	11.85	26 ± 5	31.3	49.1	0.0603 ± 0.0130	$0.730 \pm 0.157 \pm 0.074$
14.000 – 20.000	16.77	8 ± 3	33.8	44.8	0.0120 ± 0.0048	$0.145 \pm 0.058 \pm 0.015$

Table D.8: *Overview over the numbers used to determine the double differential photoproduction cross sections in bins of* $p^2_{t,\psi}$ *for* $\mathbf{0.3 < z < 0.6}$.

$0.6 < z < 0.75$						
$p^2_{t,\psi}$ [GeV^2]	$\langle p^2_{t,\psi} \rangle$ [GeV^2]	N_ψ	ε_{sel} [%]	ε_{trig} [%]	$\mathrm{d}^2\sigma_{ep}/\mathrm{d}p^2_{t,\psi}\,\mathrm{d}z$ [nb/GeV^2]	$\mathrm{d}^2\sigma_{\gamma p}/\mathrm{d}p^2_{t,\psi}\,\mathrm{d}z$ [nb/GeV^2]
1.000 − 2.125	1.48	38 ± 7	15.2	59.5	1.09 ± 0.19	$13.1 \pm 2.3 \pm 1.3$
2.125 − 3.500	2.75	35 ± 6	18.4	55.9	0.721 ± 0.130	$8.73 \pm 1.58 \pm 0.89$
3.500 − 5.375	4.36	32 ± 6	22.0	55.2	0.410 ± 0.074	$4.96 \pm 0.89 \pm 0.51$
5.375 − 7.625	6.43	18 ± 5	19.5	62.4	0.186 ± 0.049	$2.25 \pm 0.59 \pm 0.23$
7.625 − 10.000	8.75	17 ± 4	24.3	62.6	0.137 ± 0.034	$1.66 \pm 0.41 \pm 0.17$
10.000 − 14.000	11.87	19 ± 4	26.3	55.2	0.0927 ± 0.0219	$1.12 \pm 0.26 \pm 0.11$
14.000 − 20.000	16.80	14 ± 4	24.7	52.0	0.0508 ± 0.0151	$0.615 \pm 0.182 \pm 0.063$

Table D.9: *Overview over the numbers used to determine the double differential photoproduction cross sections in bins of* $p^2_{t,\psi}$ *for* $\mathbf{0.6 < z < 0.75}$.

$0.75 < z < 0.9$						
$p^2_{t,\psi}$ [GeV^2]	$\langle p^2_{t,\psi} \rangle$ [GeV^2]	N_ψ	ε_{sel} [%]	ε_{trig} [%]	$\mathrm{d}^2\sigma_{ep}/\mathrm{d}p^2_{t,\psi}\,\mathrm{d}z$ [nb/GeV^2]	$\mathrm{d}^2\sigma_{\gamma p}/\mathrm{d}p^2_{t,\psi}\,\mathrm{d}z$ [nb/GeV^2]
1.000 − 2.125	1.47	48 ± 7	12.1	50.3	2.04 ± 0.30	$24.7 \pm 3.6 \pm 2.5$
2.125 − 3.500	2.73	40 ± 7	13.9	48.9	1.25 ± 0.21	$15.1 \pm 2.5 \pm 1.5$
3.500 − 5.375	4.35	25 ± 5	14.7	56.2	0.461 ± 0.094	$5.57 \pm 1.14 \pm 0.57$
5.375 − 7.625	6.41	19 ± 5	18.4	52.6	0.248 ± 0.061	$3.00 \pm 0.74 \pm 0.31$
7.625 − 10.000	8.74	11 ± 3	29.6	49.6	0.0920 ± 0.0290	$1.11 \pm 0.35 \pm 0.11$
10.000 − 14.000	11.85	18 ± 4	28.1	35.5	0.128 ± 0.031	$1.55 \pm 0.37 \pm 0.16$
14.000 − 20.000	16.76	10 ± 3	34.8	57.6	0.0230 ± 0.0076	$0.278 \pm 0.093 \pm 0.028$

Table D.10: *Overview over the numbers used to determine the double differential photoproduction cross sections in bins of* $p^2_{t,\psi}$ *for* $\mathbf{0.75 < z < 0.9}$.

Appendix E

Tables for Low z

$W_{\gamma p}$ [GeV]	N_ψ	N_ψ fit	ΔN_ψ
$120.0 - 150.0$	69 ± 12	62 ± 11	7
$150.0 - 180.0$	56 ± 12	59 ± 11	-3
$180.0 - 260.0$	55 ± 14	58 ± 14	-3

Table E.1: *Numbers of J/ψ mesons in bins of $W_{\gamma p}$*

z	N_ψ	N_ψ fit	ΔN_ψ
$0.05 - 0.15$	51 ± 13	46 ± 13	5
$0.15 - 0.30$	69 ± 14	76 ± 14	-7
$0.30 - 0.45$	60 ± 10	54 ± 10	6

Table E.2: *Numbers of J/ψ mesons in bins of z*

$p_{t,\psi}^2$ [GeV^2]	N_ψ	N_ψ fit	ΔN_ψ
$1.000 - 2.125$	30 ± 11	26 ± 10	4
$2.125 - 3.500$	30 ± 10	27 ± 9	3
$3.500 - 7.625$	59 ± 12	62 ± 12	-3
$7.625 - 20.000$	50 ± 10	48 ± 10	2

Table E.3: *numbers of J/ψ in bins of $p_{t,\psi}^2$*

$W_{\gamma p}$ [GeV]	$\langle W_{\gamma p}\rangle$	ε_{sel} [%]	ε_{trig} [%]	σ_{ep} [nb]	$\Phi_{\gamma/e}$	$\sigma_{\gamma p}$ [nb]
120.0 – 150.0	133.8	24.9	55.9	0.202 ± 0.034	0.0149	$13.6 \pm 2.3 \begin{array}{l} +2.4 \\ -3.1 \end{array}$
150.0 – 180.0	163.9	27.0	55.4	0.151 ± 0.031	0.0105	$14.4 \pm 3.0 \begin{array}{l} +2.2 \\ -3.0 \end{array}$
180.0 – 260.0	213.7	15.3	60.1	0.243 ± 0.063	0.0163	$14.9 \pm 3.9 \begin{array}{l} +2.3 \\ -3.1 \end{array}$

Table E.4: *Overview over the numbers used to determine the total photoproduction cross section as a function of* $W_{\gamma p}$

z	$\langle z\rangle$	ε_{sel} [%]	ε_{trig} [%]	$\mathrm{d}\sigma_{ep}/\mathrm{d}z$ [nb]	$\mathrm{d}\sigma_{\gamma p}/\mathrm{d}z$ [nb]
0.05 – 0.15	0.100	23.3	55.7	1.60 ± 0.42	$38.4 \pm 10.0 \begin{array}{l} +5.9 \\ -8.0 \end{array}$
0.15 – 0.30	0.225	24.5	57.1	1.34 ± 0.27	$32.3 \pm 6.5 \begin{array}{l} +5.0 \\ -6.7 \end{array}$
0.30 – 0.45	0.375	17.7	58.1	1.59 ± 0.26	$38.1 \pm 6.3 \begin{array}{l} +5.9 \\ -7.9 \end{array}$

Table E.5: *Overview over the numbers used to determine the differential photoproduction cross section as a function of* z

$p^2_{t,\psi}$ [GeV^2]	$\langle p^2_{t,\psi}\rangle$ [GeV^2]	ε_{sel} [%]	ε_{trig} [%]	$\mathrm{d}\sigma_{ep}/\mathrm{d}p^2_{t,\psi}$ [nb/GeV^2]	$\mathrm{d}\sigma_{\gamma p}/\mathrm{d}p^2_{t,\psi}$ [nb/GeV^2]
1.000 – 2.125	1.48	14.0	53.1	0.148 ± 0.051	$3.54 \pm 1.23 \begin{array}{l} +0.55 \\ -0.74 \end{array}$
2.125 – 3.500	2.75	19.1	56.9	0.0824 ± 0.0266	$1.98 \pm 0.64 \begin{array}{l} +0.30 \\ -0.41 \end{array}$
3.500 – 7.625	5.26	22.5	56.6	0.0456 ± 0.0095	$1.10 \pm 0.23 \begin{array}{l} +0.17 \\ -0.23 \end{array}$
7.625 – 20.000	12.70	27.3	58.1	0.0103 ± 0.0021	$0.246 \pm 0.049 \begin{array}{l} +0.038 \\ -0.051 \end{array}$

Table E.6: *Overview over the numbers used to determine the differential photoproduction cross section as a function of* $p^2_{t,\psi}$

Bibliography

[1] A.D. Martin, R.G. Roberts, W.J. Stirling, *Phys. Lett.* **B354** (1995) 155

[2] H1 Collaboration, I Abt et al., *Nucl. Instrum. Methods* **A386** (1997) 310, *Nucl. Instrum. Methods* **A386** (1997) 348

[3] S. Egli et al., *Calculating event weights in case of downscaling on trigger levels 1-4*, Internal H1-Note H1-04/97-517

[4] H. Itterbeck et al., *Improvement of the Trigger Timing of the H1 Digital Muon System*, Internal H1-Note H1-02/95-427

[5] S. Mohrdieck, *Neuronaler Netzwerk-Trigger für Myonen im H1-Detektor bei HERA*, Diploma Thesis, Hamburg (1997)

[6] P. Merkel, H1 internal information (1997)

[7] C.F. von Weizsäcker, Z. Phys. **88** (1934) 612;
E.J. Williams, Phys. Rev. **45** (1934) 729;
V.M. Budnev et al., Phys. Rep. **15** (1975) 181;

[8] Particle Data Group, D.E. Groom et al., *Eur. Phys. J.* **C15** (2000) 1

[9] G. Zweig, CERN-TH-412 (1964)

[10] J.J. Aubert et al., *Phys. Rev. Lett.* **33** (1974) 1404

[11] J.E. Augustin et al., *Phys. Rev. Lett.* **33** (1974) 1406

[12] C.-H. Chang, *Nucl. Phys.* **B172** (1980) 425

[13] E.L. Berger, D. Jones, *Phys. Rev.* **D23** (1981) 1521

[14] R. Baier, R. Rückl, *Phys. Lett.* **B102** (1981) 364, *Nucl. Phys.* **B201** (1982) 1, *Z. Phys.* **C19** (1983) 251

[15] M. Krämer, *Nucl. Phys.* **B459** (1996) 3

[16] H1 Collaboration, S. Aid et al., *Nucl. Phys.* **B472** (1996) 3

[17] ZEUS Collaboration, J. Breitweg et al., *Z. Phys.* **C76** (1997) 599

[18] NMC, D. Allasia et al., *Phys. Lett.* **B258** (1991) 493

[19] EMC, J. Ashman et al., *Z. Phys.* **C56** (1992) 21

[20] CDF Collaboration, F. Abe et al., *Phys. Rev. Lett.* **79** (1997) 572, *Phys. Rev. Lett.* **79** (1997) 578

[21] E. Braaten et al., *Phys. Lett.* **B333** (1994) 548; M. Cacciari and M. Greco, *Phys. Rev. Lett.* **73** (1994) 1586

[22] G.T. Bodwin, E. Braaten, G.P. Lepage, *Phys. Rev.* **D51** (1995) 1125

[23] P. Cho, A.K. Leibovich, *Phys. Rev.* **D53** (1996) 150, *Phys. Rev.* **D53** (1996) 6203

[24] B. Cano-Coloma and M.A. Sanchis-Lozano, *Nucl. Phys.* **B508** (1997) 753,

[25] B. Kniehl and G. Kramer, *Eur. Phys. J.* **C6** (1999) 493

[26] M. Krämer, Preprint hep-ph/9707449 (1997), Talk presented at the Ringberg Workshop *New Trends in HERA Physics*

[27] CDF Collaboration, T. Affolder et al., Preprint hep-ex/0004027 (2000), submitted to Phys.Rev.Lett.

[28] M. Beneke, M. Krämer, *Phys. Rev.* **D55** (1997) 5269

[29] E. Braaten, B.A. Kniehl, J. Lee, *Phys. Rev.* **D62** (2000) 094005

[30] M. Beneke, M. Krämer and M. Vänttinen, *Phys. Rev.* **D57** (1998) 4258

[31] K. Sridhar, A.D. Martin and W.J. Stirling, *Phys. Lett.* **B438** (1998) 211

[32] P. Hägler, R. Kirschner, A. Schäfer, L. Szymanowski and O.V. Teryaev, Preprints hep-ph/0004263 (2000) and hep-ph/0008316 (2000)

[33] F. Yuan and K. Chao, *Phys. Rev.* **D63** (2001) 034006

[34] H1 Collaboration, S. Aid et al., *Nucl. Phys.* **B463** (1996) 3;
ZEUS Collaboration, J. Breitweg et al., *Eur. Phys. J.* **C2** (1998) 247

[35] ZEUS Collaboration, M. Derrick et al., *Phys. Lett.* **B377** (1996) 259

[36] ZEUS Collaboration, J. Breitweg et al., *Z. Phys.* **C75** (1997) 215;
H1 Collaboration, C. Adloff et al., *Phys. Lett.* **B483** (2000) 23

[37] J. Meyer, *Guide to simulation program H1SIM*, H1 internal software manual (1991)

[38] *GEANT – Detector Description and Simulation Tool*, CERN Program Library Long Writeup W5013; R. Brun, R. Hagelberg, M. Hansroul and J.C. Lassalle, CERN-DD-78-2-REV

[39] H. Jung, *Monte Carlo Generator EPJPSI for J/ψ mesons in high energy γp, ep, μp, $p\bar{p}$ and pp collisions*, http://www-h1.desy.de/~jung/epjpsi.html; Proceedings 'Physics at HERA', Eds. W. Buchmüller, G. Ingelman, 1488 (1991)

[40] H. Plothow-Besch, *PDFLIB: Proton, Pion and Photon Parton Density Functions, Parton Density Functions of the Nucleus, and α_s Calculations*, Users's Manual, Version 8.04, CERN Program Library Long Writeup W5051, 2000; H. Plothow-Besch, Int. J. Mod. Phys. **A10** (1995) 2901

[41] M. Glück, E. Reya and A. Vogt, *Phys. Rev.* **D46** (1992) 1973, *Phys. Rev.* **D45** (1992) 3986

[42] T. Sjöstrand, *PYTHIA 5.7 and JETSET 7.4: Physics and manual*, Preprint hep-ph/9508391 (1995)

[43] H1 Collaboration, C. Adloff et al., *Phys. Lett.* **B467** (1999) 156

[44] H. Jung, D. Krücker, C. Greub, D. Wyler, *Z. Phys.* **C60** (1993) 721

[45] M. Glück, E. Reya and A. Vogt, *Eur. Phys. J.* **C5** (1998) 461

[46] CTEQ Collaboration, H.L. Lai et al., *Eur. Phys. J.* **C12** (2000) 375

[47] A.D. Martin, R.G. Roberts, W.J. Stirling and R.S. Thorne, *Eur. Phys. J.* **C4** (1998) 463

[48] H. Abramowicz, E. Gurvich and A. Levy, *Phys. Lett.* **B420** (1998) 104

[49] G.A. Schuler and T. Sjöstrand, *Phys. Lett.* **B376** (1996) 193

[50] H. Abramowicz, K. Charchula and A. Levy, *Phys. Lett.* **B269** (1991) 458

[51] H. Jung and G.P. Salam, Preprint hep-ph/0012143 (2000)

[52] B. List, *Diffraktive J/ψ-Produktion in Elektron–Proton–Stößen am Speicherring HERA*, Diploma Thesis, Berlin (1993)

[53] H1 Collaboration, C. Adloff et al., *Phys. Lett.* **B421** (1998) 385

[54] Dirk Schmidt, Dissertation in preparation

[55] F. Jacquet, A. Blondel, *Proceedings of the workshop: Study for an ep facility in Europe*, DESY 79-048 (1979) 391

[56] L. Wilden, *Inelastic Photoproduction of J/ψ Mesons at HERA*, Diploma Thesis, Hamburg (1998)

[57] S. Levonian, H1 internal information (2000)

[58] L. West, *How to use the Heavy Flavour Working Group Track, Muon and Electron Selection Code*, H1 internal software manual (2000)

[59] B. Naroska, S. Schiek and G. Schmidt, *Lepton Identification in the H1 Detector at Low Momenta*, Internal H1-Note H1-05/97-518 (1997)

[60] G. Schmidt, *Untersuchung der diffraktiven Photoproduktion von J/ψ -Mesonen im H1-Detektor bei HERA*, Dissertation, Hamburg, Internal report DESY F11/F22-97-02 (1997)

[61] A. Meyer, *Charmonium Production in deep inelastic scattering at HERA*, Dissertation, Hamburg, Internal report DESY-Thesis-1998-012 (1998)

[62] K. Krüger, *Inelastische Produktion von J/ψ-Mesonen am Speicherring HERA*, Diploma Thesis, Hamburg (1997)

[63] H1 Collaboration, C. Adloff et al., Contributed Paper 157aj, International Europhysics Conference on High Energy Physics (EPS-HEP99), Tampere, Finland (1999)

[64] ZEUS Collaboration, J. Breitweg et al., Contributed Paper 814, XXIX International Conference on High Energy Physics (ICHEP98), Vancouver, Canada (1998)

[65] ZEUS Collaboration, J. Breitweg et al., Contributed Paper 851, XXXth International Conference on High Energy Physics (ICHEP2000), Osaka, Japan (2000)

[66] ZEUS Collaboration, J. Breitweg et al., Contributed Paper 884, XXXth International Conference on High Energy Physics (ICHEP2000), Osaka, Japan (2000)

[67] H1 Collaboration, C. Adloff et al., *Phys. Lett.* **B483** (2000) 36

[68] G. Marchesini et al., *Comput. Phys. Commun.* **67** (1992) 465

Danksagung

An dieser Stelle sollen diejenigen Erwähnung finden, die zum Gelingen dieser Doktorarbeit beigetragen haben. Dabei handelt es sich natürlich um eine subjektive Auswahl:

Frau Prof. Dr. Naroska danke ich für die hervorragende Betreuung während der Doktorarbeit und die Begutachtung dieser Dissertation. Herrn Prof. Dr. Büßer danke ich für die Erstellung des Zweitgutachtens.

Felix, Andreas und Duncan haben sich um die Lesbarkeit der Arbeit verdient gemacht, sowohl was die Physik als auch das Englisch angeht. Natürlich liegen eventuell verbliebene Fehler allein an mir.

Durch das freundliche Arbeitsklima vergingen drei Jahre und drei Monate viel schneller als gedacht, und dafür möchte ich mich bei allen (Ex-)Mitgliedern sowohl der Myon- als auch der FPS-Gruppe herzlich bedanken. Die Diskussionen innerhalb und außerhalb der Kaffee-(Tee-)runde haben immer wieder bei der Lösung von physikalischen und Computer-Problemen geholfen. Aber auch "unphysikalische" Themen sind dabei nie zu kurz gekommen.

Meiner Familie, insbesondere meinen Eltern und meinem Freund Helge, danke ich für ihre Geduld und Unterstützung in allen Lebenslagen.